Epitaxial growth and properties of AlGaN-based UV-LEDs on Si(111) substrates

Dissertation
zur Erlangung des akademischen Grades

doctor rerum naturalium
(Dr. rer. nat.)

genehmigt durch die Fakultät für Naturwissenschaften
der Otto-von-Guericke-Universität Magdeburg

von M.Sc. Phannee Saengkaew

geb. am 07.03.1974 in Phrae, Thailand

Gutachter: Prof. Dr. Alois Krost
Prof. Dr. Axel Hoffmann

eingereicht am: 24.03.2010
verteidigt am: 08.07.2010

"Alle Kinder haben die märchenhafte Kraft,
sich in alles zu verwandeln,
was immer sie sich wünschen".

"All children possess the magic power of being able
to change themselves into what they wish".

Jean Cocteau

Abstract

An increasing demand for bright and efficient ultraviolet light emitting diodes (UV-LEDs) is generated by numerous applications such as biochemical sensors, purification and sterilization, and solid-state white lighting. $Al_xGa_{1-x}N$ is a promising material to develop UV-LEDs due to the direct wide-bandgap material for emission wavelengths in the UV range and the capability of n- and p-type doping. To develop UV-LEDs on Si substrates is very interesting for low-cost UV-light sources since the Si substrate is available at low cost, in large-diameter size enabling the integration with well-known Si electronics.

This work presents the first crack-free AlGaN-based UV-LEDs on Si(111) substrates by MOVPE growth. This AlGaN-based UV-LED on Si(111) substrate consists of $Al_{0.1}Ga_{0.9}N$:Si layers on LT-AlN/HT-AlN SL buffer layers and an active layer of GaN/$Al_{0.1}Ga_{0.9}N$ MQWs followed by Mg-doped (GaN/$Al_{0.1}Ga_{0.9}N$) superlattices and GaN:Mg cap layers. It yields a ~350 nm UV electroluminescence at room temperature and a turn-on voltage in a range of 2.6 - 3.1 V by current-voltage (I-V) measurements.

The novel LT-AlN/HT-AlN superlattice buffer layers efficiently improve the crystalline quality of $Al_xGa_{1-x}N$ layers and compensate a thermal tensile strain in $Al_xGa_{1-x}N$ layers after cooling as observed by in-situ curvature measurements. The dislocation density could be reduced from 8.4×10^{10} cm^{-2} in the AlN-based SLs to 1.8×10^{10} cm^{-2} in the $Al_{0.1}Ga_{0.9}N$ layers as determined by cross-sectional transmission electron microscopy (TEM) measurements.

Crack-free $Al_xGa_{1-x}N$ layers grown on these LT-AlN/HT-AlN superlattices with $0.05 \le x \le 0.65$ are achieved on Si substrates with good crystalline, optical, and electrical properties. The best crystalline quality of $Al_{0.1}Ga_{0.9}N$ is obtained with ω-FWHMs of the (0002) and (10-10) reflections of ~700 and ~840 arcsec, respectively. The good optical qualities of $Al_{0.1}Ga_{0.9}N$ and $Al_{0.65}Ga_{0.35}N$ are presented with a low yellow luminescence and narrow near-bandgap emissions at 330 and 240 nm, respectively as determined by cathodoluminescence (CL) measurements. The maximum electron concentration of 2.6×10^{18} cm^{-3} in *n*-type $Al_{0.1}Ga_{0.9}N$:Si layers and a hole concentration of 2.4×10^{17} cm^{-3} of Mg-doped GaN/$Al_{0.1}Ga_{0.9}N$ superlattices are achievable.

These high-quality $Al_xGa_{1-x}N$ materials with good optical and electrical properties are the main factors to accomplish AlGaN-based UV-LEDs on Si(111) substrates. It is demonstrated that it is also a promising approach to achieve deep UV-LEDs on Si substrates with a higher Al content layers.

Abstract

Auf Grund zahlreicher Anwendungsmöglichkeiten, zum Beispiel als biochemische Sensoren, in der Reinigung und der Sterilisation, aber auch als weißlichtemittierende Halbleiter besteht eine wachsende Nachfrage nach hellen und effizienten Lichtemittern für den ultravioletten Spektralbereich (UV-LEDs). Als direkter Halbleiter mit einer großer Bandlücke für Emissionswellenlängen im UV-Bereich und mit der Möglichkeit der n- und p-Dotierung stellt $Al_xGa_{1-x}N$ ein vielversprechendes Material für die Fertigung von UV-LEDs dar. Für die Entwicklung von kostengünstigen UV-Lichtquellen ist Silizium als Substratmaterial sehr interessant, denn Si-Substrate sind preiswert und mit großen Durchmessern erhältlich, und UV-LEDs auf Si-Substraten lassen sich in die wohlbekannte Si-Elektronik integrieren.

Die vorliegende Arbeit präsentiert die ersten rissfreien AlGaN-basierten UV-LEDs, die mittels metallorganischer Gasphasenepitaxie (MOVPE – Metal Organic Vapor Phase Epitaxy) auf Si(111)-Substraten gewachsen wurden. Diese AlGaN-basierten UV-LEDs auf Si(111)-Substraten bestehen aus $Al_{0.1}Ga_{0.9}N$:Si Schichten auf LT-AlN/HT-AlN SL Pufferschichten und aktiven GaN/$Al_{0.1}Ga_{0.9}N$ MQWs gefolgt von einer Mg-dotierten (GaN/$Al_{0.1}Ga_{0.9}N$) Übergitterstruktur und einer GaN:Mg Deckschicht. Mittels Elektrolumineszenz konnte bei Raumtemperatur eine Strahlung von etwa 350 nm ermittelt werden und mittels einer Strom-Spannungskennlinie eine Einsetzspannung im Bereich von 2.6 – 3.1 Volt.

Durch einen neuartigen Puffer, der aus einem LT-AlN/HT-AlN-Mehrschichtsystem besteht, konnte die kristalline Qualität der $Al_xGa_{1-x}N$-Schichten effektiv verbessert werden. Desweiteren konnte mittels in-situ Krümmungsmessungen eine Kompensation der nach der Abkühlung thermisch induzierten tensilen Verspannung beobachtet werden. Die Reduktion der Versetzungsdichte von 8.4×10^{10} cm^{-2} in den AlN-basierten SL auf 1.8×10^{10} cm^{-2} in den $Al_{0.1}Ga_{0.9}N$ Schichten wurde mittels Transmissionselektronenmikroskopie (TEM) an Querschnitten ermittelt.

Rissfreie $Al_xGa_{1-x}N$-Schichten, die mittels solcher LT-AlN/HT-AlN–Übergitter mit Aluminiumkonzentrationen von $0.05 \le x \le 0.65$ auf Si-Substraten gewachsen wurden zeigten gute kristalline, optische und elektrische Eigenschaften. So erreichte die beste kristalline Qualität eine $Al_{0.1}Ga_{0.9}N$-Schicht mit Halbwertsbreiten der ω-Scans von ~700 Bogensekunden (arcsec) am (0002)-Bragg-Reflex und ~840 arcsec am (10-10)-Bragg-Reflex. In Kathodolumineszenzuntersuchungen (CL) zeigte sich an Hand einer geringen Intensität der gelben Defektlumineszenz und einer schmalen bandkantennahen Emission des $Al_{0.1}Ga_{0.9}N$ bei 330 nm und des $Al_{0.65}Ga_{0.35}N$ 240 nm eine gute optische Qualität. Die höchste

Elektronenkonzentration von 2.6×10^{18} cm^{-3} in *n*-dotierten $Al_{0.1}Ga_{0.9}N$:Si Schichten und eine Löcherkonzentration von 2.4×10^{17} cm^{-3} in Mg-dotierten GaN/$Al_{0.1}Ga_{0.9}N$-Übergittern waren erreichbar.

Dieses hochqualitative $Al_xGa_{1-x}N$ mit guten optischen und elektrischen Eigenschaften ist der wichtigste Faktor um AlGaN-basierende UV-LEDs auf Si(111) Substraten zu gewinnen. Es wird gezeigt, dass es ein vielversprechender Ansatz ist, tief-UV-LEDs auf Si-Substraten zu bekommen mit Schichten, die höhere Al-Konzentrationen enthalten.

Acknowledgements

I would like to express my gratitude to the people who have helped and supported me to realize this work.

My sincere thanks go to:

- Prof. Dr. Alois Krost for giving me this challenging topic and the opportunity to work in his research group, for his worthy advices and discussions throughout the years, for pushing me to accomplish this research within a limited time and for his expression of “It is not a problem but it is a chance.” It is a really big chance for me.
- Prof. Dr. Axel Hoffmann for kindly accepting to referee this work.
- Prof. Dr. Jürgen Christen for his worthy advices and discussions in the optical properties and for the facilities of optical instruments in his research group.
- Priv.-Doz. Dr. Armin Dadgar for training and giving me the knowledge to grow the valuable samples by MOVPE, for his useful advices and discussions throughout the years, for giving me the sessions to pursue my wonderful investigations in his laboratory, for his understanding my problems and especially for kindly correcting and commenting my dissertation.
- Dr. Jürgen Bläsing for training and giving me the knowledge to characterize the samples by XRD, for his valuable advices and discussions, for his nice listening to me about my problems, for nice general talks during working in his laboratory and especially for wonderful dinners with Bläsing’s family. “See you later, alligator”.
- Dipl.-Phys. Barbara Bastek for her worthy CL measurements of my several samples, for her useful discussions and especially for her best to give me the good results from some difficult samples and Dr. Frank Bertram for his useful advices and discussions.
- Dipl. Phys. Annette Diez for her nice assistance in a MOVPE laboratory, for teaching me to prepare Si-wafers, for her AFM measurements and especially for her helpfulness in my first trouble year.
- Dr. Hartmut Witte for his useful advices and discussions in the electrical properties and for the facilities of electrical instruments in his laboratory.
- Dipl.-Phys. Kay-Michael Günther and Miss Antje Rohrbeck for their AFM measurements, hall measurements and CV measurements of my several samples and especially for their nice attempt to get the beautiful AFM images.
- Dr. Thomas Hempel for his valuable SEM images and discussions and for his nice general talks during doing the measurements.

- Dr. Peter Veit for his worthy TEM measurements and reports, for his nice cooperation and discussions and Mrs. Petra Kremz for her supreme sample preparations.
- Mr. Thomas Fey for his fast EL measurements and for his nice cooperation and Azzurro semiconductor AG for a needle probe to measure these EL measurements.
- Dipl.-Phys. Matthias Wieneke for his kind assistance to do PL measurements, for his nice discussions about working problems and for his nice translation to German.
- Mr. Mathias Müller for his assistance to make metal contacts of my LED samples.
- Dr. Fabian Reiher, Dr. Antje Reiher and Dipl.-Phys. Christoph Hums for their nice friendship and for their generous helpfulness in my first trouble year.
- My all co-workers for a nice smile and greeting and the pleasure of working in Germany.

I also would like to express my gratitude to my dear parents for giving me their great love, their endless support, for their providing me to be a good learner, and especially for their taking care of my lovely children during pursuing my doctoral study. I am also indebted to my dear grandparents and my nice family for their love, sympathy and encouragement. My big thanks go to my dear husband with my all heart for giving me to have a concentrated time to do my research with his patience, love and never-ending support and for his sympathy and encouragement when I am in trouble.

Finally, I would like to acknowledge the scholarship from Deutscher Akademischer Austausch Dienst (DAAD) during doing this work and attending German courses. I am also indebted to SFB787 for a financial support to contribute my research work in conferences in Switzerland and Korea. I also acknowledge King Mongkut's University of Technology North Bangkok (KMUTNB) for giving me a worthy time to attend Otto-von-Guericke University Magdeburg, Germany.

Phannee Saengkaew
Magdeburg, Germany
March 2010

Contents

* * *

Chapter 1

Introduction

Group III nitrides and their compounds are attractive semiconductor materials for high-power, high-frequency and high-temperature electronic applications due to their excellent structural properties and high thermal and chemical stability as compared to other group III-V compound semiconductors. Optoelectronic devices such as visible light emitting diodes (LEDs), InGaN-based LEDs for green light and GaN-based LEDs for blue light are successfully achieved due to the direct bandgap of group-III-nitrides and the capabilities of *n*-and *p*-doping of GaN. After the realization of *p*-type conductivity with Mg-doped GaN, Amano and co-workers demonstrated the first GaN *p-n* junction blue LED in 1989 [Aman89]. An AlGaN/GaN-based LED with an efficiency (η_{ext}) of 1.5% was achieved in 1992 by Akasaki *et al* [Akas92] and in 1993 a high-brightness GaN blue LED with an efficiency of ~ 2.7% was commercialized [Naka94].

In the short wavelength regime bright and efficient UV-light sources are required for many applications in various fields such as medical instruments, biochemical sensors, purification and sterilization, solid-state white lighting, and high capacity data storage systems [Khan05, Zuka02]. As applied in research labs for analytical instrumentation, UV and deep-UV lights have, e. g., been used for absorbance, fluorescence and spectroelectrochemical measurements in a planar flow-through cell [Dasg03]. Compared to conventional UV-light sources ultraviolet light emitting diodes (UV-LEDs) are a very attractive alternative due to their compact designs, low heat generation, low current consumption, high performance and high energy efficiency as compared to traditional light sources.

Similar to InGaN- and GaN-based LEDs, $Al_xGa_{1-x}N$ is the material of choice to develop UV-LEDs due to the wide bandgap energies of $Al_xGa_{1-x}N$ with $0 \leq x \leq 1$ ranging from 3.4 eV for GaN to 6.2 eV for AlN corresponding to the wavelength range from 360 to 200 nm. However, to achieve high-quality $Al_xGa_{1-x}N$ epilayers with high conductivity is challenging especially with increasing Al content due to a lower crystalline quality and a higher activation energy of the dopants.

The first high-power UV-LED on SiC substrates was fabricated by Nishida and co-workers in 1999 [Nish99]; in 2001, they achieved a 10-mW AlGaN-based LED using *n*-type and *p*-type $Al_{0.14}Ga_{0.86}N/Al_{0.18}Ga_{0.82}N$ short-periods superlattices below and above the AlGaN/AlGaN QWs emitting light of 352 nm [Nish01a, Nish01b].

Hirayama and co-workers demonstrated 333 nm $Al_{0.03}Ga_{0.97}N/Al_{0.25}Ga_{0.75}N$ MQWs of UV-LED with *p*-type $GaN/Al_{0.25}Ga_{0.75}N$ superlattices on SiC in 2000 [Kino00]. More recently, efficient InAlGaN-based LEDs with quaternary InAlGaN QWs with emission wavelengths of 290-375 nm have been developed [Hira04, Hira05, Fuji08a, Fuji08b]. It was proposed that the carriers captured into the In-segregated region in quaternary InAlGaN QWs recombine radiatively before being trapped in nonradiative centers by defects similar to the effect obtained in InGaN QWs [Hira05]. Moreover, efficient UV-LEDs on sapphire with AlGaN-QWs emitting at 231–261 nm by using a low threading dislocation density AlN buffer template with a NH_3 pulse-flow technique and a thin quantum well about 1-3 nm [Hira04] were obtained. Recently, 222–282 nm AlGaN and InAlGaN-based UV-LEDs on high-quality AlN buffers on sapphire were demonstrated [Hira08, Hira09].

Khan and Adivarahan *et al* [Khan01, Adiv01b] have achieved 305-340 nm UV-LEDs on sapphire that consisted of AlInGaN/AlInGaN MQWs with varying compositions by using pulsed atomic layer epitaxy (PALE), *p*-type Mg-doped AlGaN/AlGaN superlattices and *n*-type AlGaN/AlGaN superlattices (with the In/Si co-doping approach) on *n*-type $Al_{0.22\text{-}0.36}GaN$. They further improved their LED structures in light extraction and current spreading [Zhan02b, Adiv04, Wu04, Bile05, Sun04a, Sun04b, Khan05]. In 2006 matrix addressable micro-pixel AlGaN based 280 nm deep UV LEDs were developed [Wu06]. Recently, Adivarahan *et al* have reported the first RT operation of a 280 nm emission monolithic deep UV LED lamp with a record dc power of 42 mW at 1 A and a RT lifetime in excess of 1500 h when biased at 400 mA with an output power of 22 mW [Adiv09].

As a challenging investigation of UV-LEDs for numerous applications, there are several reports on Al(In)GaN-based and AlGaN UV-LEDs [Han98, Iida04, Niki05, Knei06, Niki08]. Furthermore, Taniyasu *et al.* achieved AlN-based UV-LEDs with an emission wavelength of 210 nm with an output power ~0.02 µW at 40 mA and V_D of 5 V for the PIN LED and 3.8 V for the MIS LED on SiC substrate by using AlN/AlGaN superlattices to enhance the average both *n*-and *p*-type carrier concentrations of 10^{18} cm^{-3}. The external quantum efficiency (η_{ext}) was estimated to about 10^{-6} % [Tani06, Tani08]. Especially optimized growth parameters for the QW structure and the methods to reduce TDD in $Al_xGa_{1-x}N$ layers such as In-adding are the most common approaches to fabricate UV-LEDs.

One important requirement of UV-LEDs is their price. This is the main reason to develop UV-LEDs on Si substrates since Si substrates are available at low cost in large-diameters enabling the fabrication of low-cost UV-light sources and also enabling the integration with Si electronics.

Even though $Al_xGa_{1-x}N$ epilayers grown on Si substrates will suffer from a large lattice mismatch and a large difference in thermal expansion coefficients.

In 1998, Guha and co-workers [Guha98a, Guha98b] started to demonstrate the first LEDs on Si substrates consisting of *p*-$Al_{0.05-0.09}$GaN/ undoped GaN/ *n*-$Al_{0.05-0.09}$GaN layers with emission wavelengths at ~360 nm. Since then no research groups further developed UV-LEDs on Si substrate. Until now, the development of LEDs on Si substrates is mostly based on InGaN/GaN MQWs for green and blue light emission as presented in *table 1.1*. The present performance of blue InGaN-based LEDs on Si substrates has been successfully improved to similar values as devices grown on conventional substrates as sapphire by Lattice Power [Latweb1]. In early 2010, the 1 mm and 0.5 mm size products have been introduced to the general market [Latweb1, Latweb2].

Krost and Dadgar *et al* [Kros02, Dadg00, Dadg03] investigated and solved the cracking problem of GaN layers on Si substrates and improved the GaN quality. They have achieved InGaN/GaN-QW-based blue LED on Si substrates with (111), (001) and (110) orientations [Dadg01, Schu06, Reih09].

Meanwhile high-performance AlGaN-based UV-LEDs on other substrates as sapphire and SiC are investigated but there are no reports on Si substrates up to now.

As expected similar to the success of InGaN/GaN-based LEDs on Si substrates, AlGaN-based UV-LEDs on Si substrates are a promising approach to enable the fabrication of low-cost UV-LEDs for the increasing requirement of the future. Therefore this work aims to develop $Al_{0.1}Ga_{0.9}N$-based UV-LEDs on Si(111) substrates by developing suited seeding and buffer layers which improve the crystalline quality and to *n*-and *p*-type dope AlGaN layers for diode operation.

The fundamentals of the materials used and of LEDs are described in chapter 2 followed by a description of MOVPE growth technique and the characterization techniques used in chapter 3. Chapter 4 describes the experimental results of $Al_xGa_{1-x}N$ growth with Al content up to 65% on Si(111) substrate as followed by chapter 5 describing strain engineering of AlN interlayers to grow thick, crack-free $Al_xGa_{1-x}N$ layers. The growth of *p*- and *n*-type layers and of a full crack-free LED structure and its properties are described in Chapter 6.

Table 1.1 Developments of group III-nitride based LEDs on Si substrates

Year	LEDs on Si substrates	Emission wavelenght (nm)	Output power (mW)	Turn-on voltage (Volt)	Forward voltage (Volt)	Demonstrated by	Reference	Note
1998	GaN/AL$_{0.15}$Ga$_{0.85}$N violet and UV-LEDs	~420 , ~360	-	4.5–6.5	12 V at 14-65 mA	Guha *et al.*	[Guha98a]	MBE
	UV-LEDs with organic dye based color converters	~360 , ~530, ~600	-	-	-		[Guha98b]	
1999	Blue In$_{0.22}$Ga$_{0.78}$N/GaN-MQW LEDs	465	-	4 V	8 V at 20 mA	Tran *et al.*	[Tran99]	
2000	Blue In$_{0.22}$Ga$_{0.78}$N/GaN-MQW LEDs	465	-	3.2 V	20 V at 35 mA	Yang *et al.*	[Yang00]	MBE/MOVPE
2001	Blue InGaN/GaN-MQW LEDs	467	-	2.5 V	4.5 ~ 6.5 V at 20 mA	Dadgar *et al.*	[Dadg01]	
	Green InGaN/GaN-MQW LEDs	508	0.006 mW at 20 mA	6.8 V	10.7 V at 20 mA	Feltin *et al.*	[Felt01]	
2002	Blue InGaN/GaN-MQW LEDs	455	0.15 mW at 20 mA	2.8 V	~ 4.5 V at 20 mA	Dadgar *et al.*	[Dadg02]	
	Green InGaN/GaN-MQW LEDs	505	0.02 mW at 20 mA	4 V	~ 7 V at 20 mA	Egawa *et al.*	[Egaw02a]	lifetime>500 h
	Blue and green InGaN/GaN-MQW LEDs	478, (505)	0.018 mW at 20 mA	~3V	~ 4.1 V at 20 mA	Egawa *et al.*	[Egaw02b]	
2003	Blue InGaN/GaN-MQW LEDs	498	0.42 mW at 20 mA	-	-	Dadgar *et al.*	[Dadg03]	
2005	In$_{0.17,\,0.23}$GaN/In$_{0.01}$Ga$_{0.99}$N-MQW LEDs	475	1.5-2 mW at 20 mA	~3 V	3.8 - 4.1 V at 20 mA	Egawa *et al.*	[Egaw05]	
	Blue and green In$_{0.4}$Ga$_{0.6}$N/GaN-MQW LEDs and emitted white light with yellow phosphor	430, 490	0.5-0.7 mW at 20 mA	~ 4-6 V	~ 4-6 V at 20 mA	Shin *et al.*	[Shin05]	lifetime>500 h
2006	InGaN/GaN-MQW LEDs on Si(001)	490	-	-	-	Schulze *et al.*	[Schu06]	
	Blue InGaN/GaN-MQW LEDs (with a Si-substrate lift-off)	456 (lateral LED) 466 (vertical LED)	0.76 mW (lateral) at 20 mA 2.8 mW (vertical) at 20 mA	2.5 V (both)	3.65, 3.85 (lateral) 3.45, 4.21 (vertical) at 20, 60 mA	Chuanbing *et al.*	[Chua06]	lateral LED (grown on Si) vertical LED (bonded on Si)
2007	InGaN/GaN LEDs on nanoscale SOI	485 on bulk Si 530 on SOI	-	~3 V	~4 V at 20 mA	Tripathy *et al.*	[Trip07]	
	Blue InGaN/GaN-MQW LEDs	-	1.5 mW	-	3.5 (horizontal) 4.8 (vertical)	Hsu *et al.*	[Hsu07]	
	Blue LEDs on patterned Si substrates	453	0.7 mW at 20 mA	4.3	-	Zhang *et al.*	[Zhang07]	
2008	InGaN/GaN microdisk LEDs on SOI	487 on bulk Si 496 on SOI	-	~3.5 V	~5 V at 6 mA	Tripathy *et al.*	[Trip08]	
	InGaN LEDs with AlInN/GaN DBR	~ 455-475	~0.013 mW with DBR, ~0.003 mW without DBR, at 20 mA	-	-	Ishikawa *et al.*	[Ishi08]	
	Blue InGaN/GaN-MQW LEDs on 150 mm Si(001)	456	-	2.8 V	-	Schulze *et al.*	[Schu08]	
	Blue InGaN/GaN-MQW LEDs on Si(110)	428	0.072 mW at 300 mA	~2.5-3.5 V	3.5 V at 20 mA	Damilano *et al.*	[Dami08]	MBE
2009	Green and blue InGaN/GaN-MQW LEDs	455 - 510	1.2 mW at 50 mA	~2.5 V	<3.5 V at 20 mA	Zhu *et al.*	[Zhu09a, Zhu09b]	
	Bluish InGaN/GaN-MQW LEDs on Si(110)	485	-	-	-	Reiher *et al.*	[Reih09]	
	High-power blue InGaN-based LEDs on Si(111) (with a Si-substrate lift-off) and emitted white light with YAG phosphor	453	458 mW at 350 mA (1x1 mm) 74.8 mW at 60 mA (0.5x0.5 mm)	~2.5 V	~3.3 V at 20 mA	Lattice Power	[Latweb1,Latweb2]	lifetime>500 h

Chapter 2

Fundamental properties of AlGaN, Si substrate and LED principle

The aims of this work are to investigate and develop AlGaN-based UV LEDs on Si substrate. The fundamental properties of AlGaN and Si and the principle of LEDs will be provided to know the important parameters of the investigations. In this chapter, the structural and electronic properties of AlGaN will be described conceptually, e.g. chemical bonding, crystal structure, bandgap energy and polarization etc. Afterwards the structural and other properties of Si substrate will be summarized including the surface preparation and special problems in epitaxial growth on Si substrate. Lastly, the general principle of LEDs such as a *p-n* junction, radiative transition and Quantum Confined Stark Effect (QCSE) in quantum-well structure and doping for *n*- and *p*- type conductivity will be explained. In addition, current-voltage characteristics and definitions of efficiencies of LEDs will be included in this chapter.

2.1 Structural properties

In this section, chemical bonding and crystal structure of group III nitrides will be explained to comprehend their structural properties.

2.1.1 Chemical Bonding

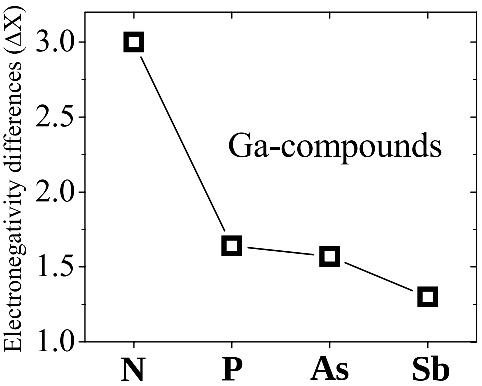

Figure 2.1 The electronegativity differences of Ga–group V compounds [Pödö96]

$Al_xGa_{1-x}N$ is a group III nitride compound as a ternary alloy of AlN and GaN. Group III nitrides and their compounds are special attractive semiconductor materials for high-power electronic applications due to some excellent structural properties. In comparison to other group III-V compound semiconductors (for example GaAs, InP), the group III nitrides have a group III-nitrogen covalent bond with stronger ionic component due to the basic properties of nitrogen atom the smallest and the most electronegative group V element. As a result, the electrons involved in such covalent bond are attracted by the stronger coulomb potential of the nitrogen atomic nucleus leading to the strong ionicity of the metal nitrogen bond compared to that of other group V bonds. As seen in *Fig.2.1* data from [Pödö96], GaN has the largest electronegativity difference of all Ga-group V compounds corresponding to the strongest ionic bond of nitride compounds. Additionally, lattice parameters for the nitrides are significantly reduced due to the small covalent radius of N (0.7 Å, compared with 1.10 Å for P, 1.18 Å for As, 1.36 Å for Sb). This induces high bond energies of group III nitrides implied to high melting temperatures as compared with group III arsenides as shown in *Fig.2.2 (right).* The bond energy between group III atoms and nitrogen atoms reveal large variations from the strongest bond energy of E_B (Al-N) = 2.88 eV to E_B (Ga-N) = 2.2 eV and E_B (In-N) = 1.93 eV of the binary AlN, GaN and InN, respectively. This can explain the highest thermal stability of AlN with a melting point of approximately 3200°C and 2500°C of GaN whereas the InN melting point is at about 550°C as shown in *Fig. 2.2 (center).* Similarly, these variations influence the wide bandgap characteristics of the group III nitrides as their bandgap energy vary from 6.2 eV (AlN) to 3.4 eV (GaN) and 0.8 eV (InN) as shown in *Fig. 2.2 (left).*

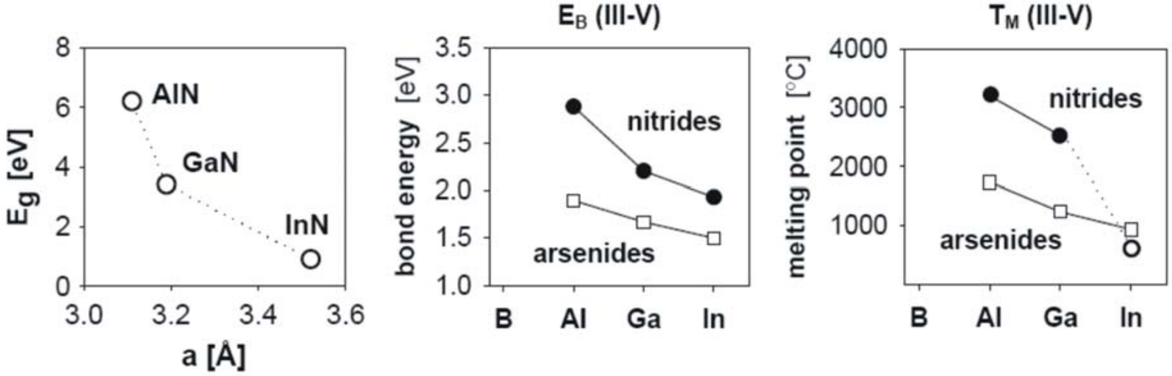

Figure 2.2 Physical and chemical properties of group III nitrides. Band gap energy (E_g) as a function of lattice parameter (left), binary bond energies for group III nitrides and arsenides (center), the melting points of group III nitrides and arsenides (right) [Kell03].

In brief, these properties provide the group III nitrides more stable thermally and chemically and well suitable for high-power, high-frequency and high-temperature electronic applications.

2.1.2 Crystal structure

Group III nitrides are categorized into three crystal structures i.e. wurtzite (Wz), zincblende (ZB) and rocksalt structures. In rocksalt or NaCl structure (with space group $Fm\overline{3}m$ in Hermann-

Mauguin notation and O_h^5 in Schoenflies notation), they can be possibly grown only under very high pressures of 22.9 GPa for AlN, 52.2 GPa for GaN and 12.1 GPa for InN. Thus, rocksalt group III nitrides cannot be produced by any epitaxial growth [Mork08]. In cubic zincblende structure or *β*-phase (with space group $F\overline{4}3m$ in Hermann-Mauguin notation and T_d^2 in Schoenflies notation), they are metastable structures and can be stabilized under specific growth conditions such as on some suitable substrates [Mork08].

In hexagonal wurtzite structure or *α*-phase (with space group $P6_3mc$ in Hermann-Mauguin notation and C_{6v}^4 in Schoenflies notation), group III nitrides and their alloys have the thermodynamically most stable structure. The primitive unit cell or unit cell of hexagonal wurtzite structure is a parallelepiped with a basis of four atoms, two group III atoms and two nitrogen atoms as depicted in *Fig.2.3(left).* Each atom in the structure can be seen as located at the center of a tetrahedron with its four nearest atomic neighbors of the other type at the four corners of the tetrahedron as depicted in *Fig.2.3(right).*

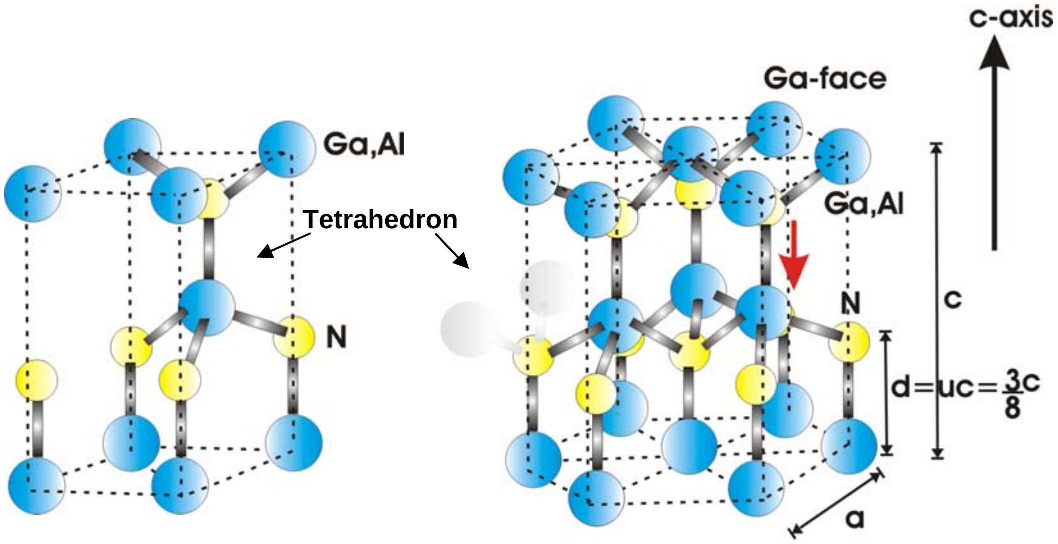

Figure 2.3 Unit cell of wurtzite structure of (Ga,Al)N (left) and wurtzite structure of (Ga,Al)N (right)

The wurtzite structure consists of two interpenetrating hexagonal close packed (HCP) sublattices, one of group III-atom lattice and another of nitrogen-atom lattice. Each lattice displaces from the other along the *c*-axis ideally by 3/8 of the cell height, (3/8*c*), related to *u*-parameter. The stacking sequence of orientations of bi-atomic group III-nitrogen (0001) planes is an AaBb-AaBb-AaBb sequence whereas capital letters corresponding to the group III atoms and small letters to the nitrogen atoms. Thus, atoms in the first and third plane of each type are directly aligned with each other. Unlike the zincblende structure, the stacking sequence of (111) planes is an AaBbCc-AaBbCc-AaBbCc sequence in the <111>direction as will be discussed in section 2.5 of Si(111) substrate. Since the zincblende (β-phase) and wurtzite (*α*-phase) structures of group III nitrides slightly differ in the stacking sequence, the coexistence of both structure-types is possible and leads to stacking faults in epitaxial layers.

The parameters to characterize the wurtzite lattice are the edge length of basal-plane hexagonal (a), the height of hexagonal (c) and the internal parameter (u) of the cation-anion bond length ratio along the c-axis in a unit of c as shown in *Fig.2.3 (right).* In an ideal wurtzite crystal, the c/a ratio is 1.6330 and u-parameter is 0.375 as shown in Table 2.1. These values of each nitride crystal are different because of different metal cations and bond lengths and no one has the ideal-wurtzite parameters. This is important to determine the strength of polarization in all nitride crystals.

Table 2.1 Lattice parameters, c/a ratios and u-parameters of the ideal wurtzite and group III nitrides after [Zimm08].

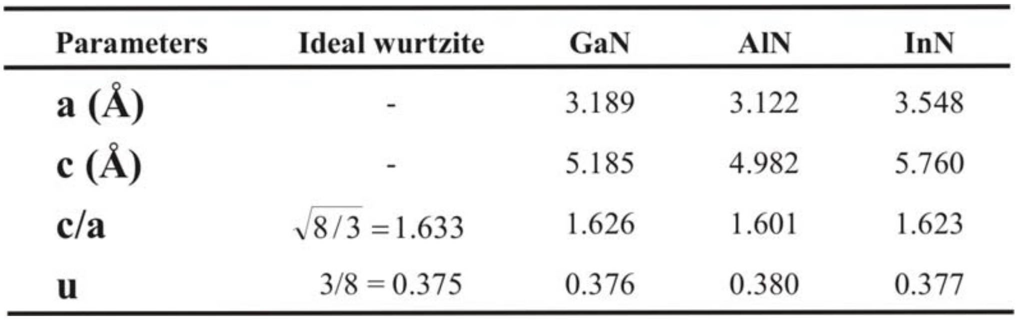

Parameters	Ideal wurtzite	GaN	AlN	InN
a (Å)	-	3.189	3.122	3.548
c (Å)	-	5.185	4.982	5.760
c/a	$\sqrt{8/3} = 1.633$	1.626	1.601	1.623
u	$3/8 = 0.375$	0.376	0.380	0.377

2.2 Electronic properties

The electronic properties as bandgap structure, polarization and band discontinuity and two-dimension carrier gas of heterostructure of group III nitrides will be briefly introduced in this section.

2.2.1 Bandgap structure

The band structure of group III nitrides is a direct bandgap by the conduction band minimum and the valence band maximum lay at the center of the Brillouin zone (Γ point). Bandgap energy (E_g) is nearly equal to a distance between them. *Figure 2.4(left) and (right)* present the calculated band structure near Γ point of wurtzite GaN [Chen96] and AlN [Li03], respectively. The electric and optical properties are generally governed by this local *E-k* relationship. *k* is the wavevector related to the direction of electron motion in the crystal. Unlike a structure with high symmetry such as FCC, the wurtzite hexagonal structure with low symmetry strongly affects the band structure, in particular, the valence band. The valence bands in hexagonal are split into three separate subbands representing as $\Gamma 9$, $\Gamma 7$, and $\Gamma 7$ of the C_{6v} point group. As explained above, the bonding in group III nitrides is a mixed ionic and covalent bond. The mixed ionic-covalent bonds can be imagined as a superposition of two extreme cases. In case of ionicity, an electron transfer from group III to N gives an ionic structure group $III^{+}N^{-}$ such as $Ga^{+}N^{-}$. In case of covalence, the electron transfer from N to group III leaves both group III and N with four electrons in the outer shell. Due to this mixing of *s*- and *p*-wavefunctions, this allows forming *sp^3*-hybrid orbitals similar to that of group IV Si and Ge and splitting into two *sp^3*-subbands as bonding and antibonding orbitals to equilibrate a bonding distance [Ibac03].

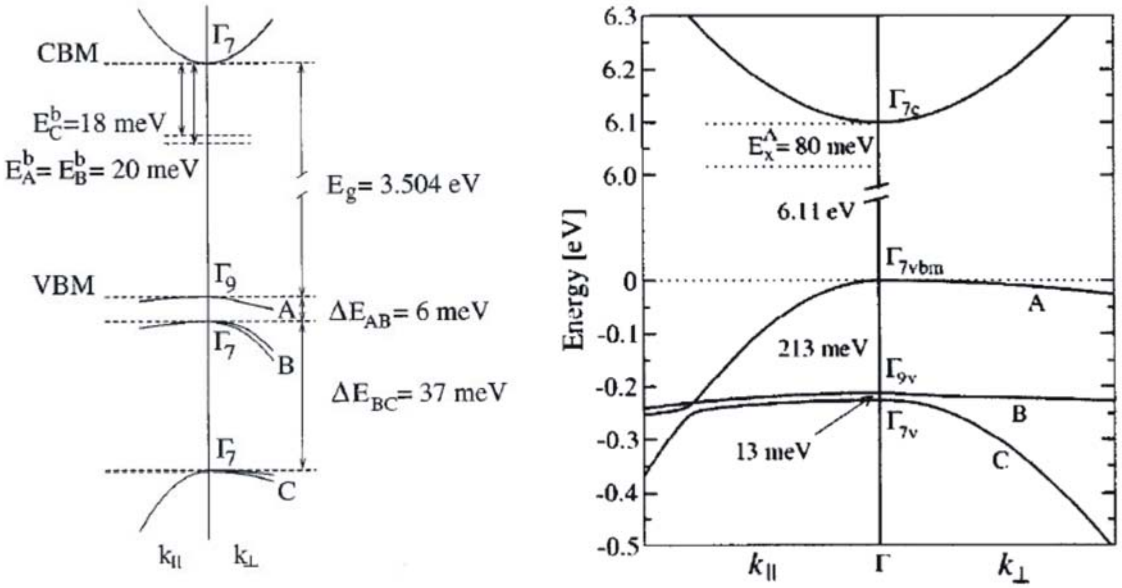

Figure 2.4 Calculated band structure near the Γ point of wurtzite GaN (left) [Chen96] *and AlN (right)* [Li03].

Otherwise, the three hole bands are labelled as HH (heavy), LH (light) and CH (crystal-field split-off). Their gap sizes strongly depend on temperature. With increasing temperature, lattice parameters are distorted as an increasing in-plane lattice parameter due to a thermal expansion. As a result, the bandgap will be smaller with respect to a reducing in the *sp^3*-subband splitting.

In a case of ternary alloy bandgap, a bandgap of $Al_xGa_{1-x}N$ is given by the composition-weighted average of GaN and AlN bandgaps with a non-linear term as a bowing parameter (*b*) and it can be expressed by

$$E_{gap}(Al_xGa_{1-x}N) = (1-x)E_{gap}(GaN) + xE_{gap}(AlN) + b\cdot x\cdot(1-x) \qquad \text{Eq.2.1}$$

Usually the measurement of bowing parameters studied on the bandgap and Al-content of AlGaN is complicated by strains in layers. There are many reports of various bowing parameters from -0.8 eV (upward bowing) to +2.6eV (downward bowing) [Mork08]. However the most notable bowing parameter is 1.0 eV for the entire compositional range [Yun02].

Theoretical lattice parameters of ternary can be predicted by Vegard's law of the composition-weighted average of the GaN and AlN parameters given i.e.

$$a,c_{(AlxGa1\text{-}x\ N)} = (1\text{-}x)a,c_{(GaN)} + x\ a,c_{(AlN)}$$

as can be alternatively expressed by

$$a_{Al_xGa_{1-x}N} = 3.1986 - 0.0891x\ \text{Å} \qquad \text{and}$$

$$c_{Al_xGa_{1-x}N} = 5.2262 - 0.2323x\ \text{Å} \qquad \text{Eq.2.2. [Amba02]}$$

2.2.2 Polarization of group III nitrides

The origin and effect of spontaneous and piezoelectric polarizations of group III nitrides will be briefly explained and the band discontinuity and two dimension carrier gas of heterostructure will be also introduced in this section. More details about polarization in group III nitrides can be found in references [Mork08, Amba98, Amba99].

A. Spontaneous and piezoelectric polarizations

Group III atoms are bonded with nitrogen atoms by their strong ionicity-covalent bonds in a tetrahedral form, along the c-axis of wurtzite structure without inversion symmetry. The covalent bond with stronger ionicity acted as a localized polarization will result in macroscopic polarization in the crystal structure [Amba98, Amba99]. In a simple model, it can be assumed that the planes containing group III atoms carry a positive charge and the planes of nitrogen atoms carry a negative charge. This results in electrical dipoles along the c-axis due to no inversion symmetry or dipole annihilation along this direction in the wurtzite group III nitrides. As a result, strong macroscopic spontaneous polarizations occur along the c-axis and then the basal or (0001) planes are the primary polar planes. By the non-centrosymmetric wurtzite structure, group III-nitrides will have two distinct faces of group III (Ga, Al or In)-face and N-face

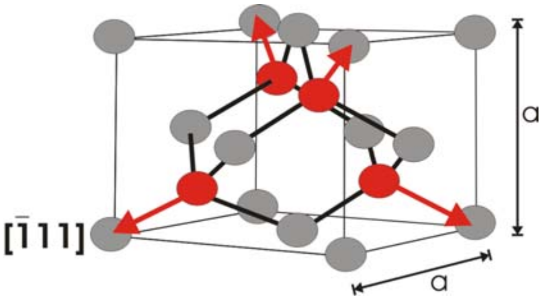

Figure 2.5 Sum of the microscopic dipoles resulting no spontaneous polarization for the zincblende structure.

with two different polarities as a group III-polarity or $[0001]$ polarity, and an N-polarity or $[000\bar{1}]$ polarity depending on the growth direction of the *c*-axis. The group III-polarity or $[0001]$ polarity is defined by a polarization vector pointing from the anion (N atoms) to the nearest cation (group III atoms) along the longitudinal bond as depicted with a red downward vector opposite the growth direction of the *c*-axis in *Fig.2.3,* corresponding to group III element on the top position of the {0001} basal plane of the wurtzite structure as called group III-faced. On the other hand for the N-polarity or $[000\bar{1}]$ polarity or N-faced, the opposite polarity is in upward direction parallel to the *c*-axis growth direction as will be shown in *Fig.2.6(above).* In brief, the strong ionicity of chemical bonding, non-centrosymmetric structure and the polarity are responsible for the strong macroscopic spontaneous polarization effects that appear in the wurtzite group III nitrides along the *c*-direction. Meanwhile in zincblende crystals the dipoles along the four equivalent <111> directions as the primary polar planes cause the annihilation and then the total polarization field is zero as shown schematically in *Fig.2.5*.

However, in reality the group III-face can be either group III-terminated or N-terminated. The termination type or the Ga- or N-polarity significantly affects not only the surface morphology but also many physical characteristics such as impurity incorporation and electrical properties [Stut01]. The Ga- or N-polarity can be determined by the choice of substrate and the growth process, especially the initial stages of it [Stut01]. Typically, group III nitrides grown by MOVPE or HVPE will exhibit the group III-face with a better quality than the N-face grown by MBE. Nevertheless the N-face GaN also is applied in some devices as HEMT [Raja05, Wong08].

In principle, the polarization in wurtzite group III nitrides is categorized into two types as spontaneous and piezoelectric polarizations. For ***spontaneous polarization,*** this polarization effect occurs in the equilibrium lattice of the group III nitrides at zero strain due to non inversion symmetry [Smit93, Bern97]. Theoretically, the spontaneous polarization of the typical group III nitrides is always along the $[000\bar{1}]$ direction as shown in *Fig.2.3(right)* and *Fig.2.7(above).*

When stress is applied to the group III-nitride lattice, lattice parameters *c* and *a* of the relaxed structure will be changed to accommodate the stress. As a result, the polarization strength will be changed due to a changing of the bond length (*d*). This additional polarization occurring in the strained group III nitrides is called ***piezoelectric polarization*** and adds to the spontaneous polarization [Smit93, Bern97]. The relation of lattice parameter changing is governed by Poisson's law as

$$\frac{c-c_0}{c_0} = -2\frac{C_{13}}{C_{33}}\left(\frac{a-a_0}{a_0}\right) \qquad \text{Eq.2.3}$$

whereas c_0, a_0 are relaxed lattice constants and C_{13}, C_{33} are elastic stiffness constants (can be found in references [Mork08, Amba98]). So, piezoelectric polarization can be written as

$$P_{PE} = 2\frac{a-a_0}{a_0}\left(e_{31} - e_{33}\frac{C_{13}}{C_{33}}\right) \qquad \text{Eq.2.4}$$

whereas e_{31}, e_{33} are strain or piezoelectric constants in references [Mork08, Amba98].

However, Eq.2.3 is valid only in the linear regime for small strain values. It defines the piezoelectric tensor through the change in polarization induced only by variations of lattice constants a and c [Amba98]. For more detailed calculations, taking more parameters as alloy compositions into account leads to the nonlinearities in piezoelectric polarization [Mork08].

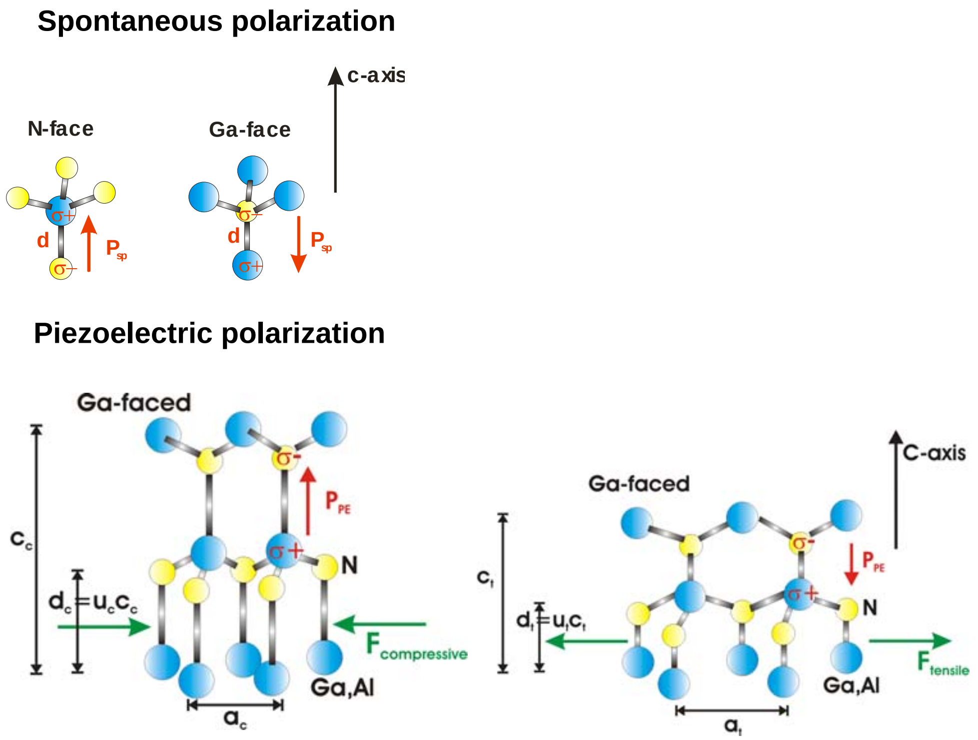

Figure 2.6 Spontaneous polarization (above) and piezoelectric polarizations due to compressive stresses (left) and tensile stresses (right) after [Mork08,Zimm08]

When group III nitride is under biaxial ***compressive stress***, the a-lattice constant will be smaller and the c-lattice constant will be larger resulting in an increased bond length (d) and an increased c/a ratio approaching to the ideal lattice ratio. This also will reduce the total polarization strength of the nitride crystal because the piezoelectric polarization will occur in opposite direction of the spontaneous polarization as depicted in *Fig.2.6(left)*. In contrast to the nitride crystal under ***tensile stress***, the *a*-lattice constant will be larger and the *c*-lattice constant will be smaller reducing the *c/a* ratio far away from the ideal ratio leading to enhance the total polarization because the piezoelectric and spontaneous polarizations will happen in the same direction as shown in *Fig.2.6 (right)*.

B. Effects of strain and polarization

Both compressive and tensile strains are able to distort lattice constants and modify a band structure as a bandgap shift related to changing total polarizations. As an important result, their electrical and optical properties will be changed in both negative and positive effects depending on applications.

For example in the positive case of the tensile strained $Al_xGa_{1-x}N$ grown on thick GaN layers as $Al_xGa_{1-x}N$/GaN heterostructures, their large lattice mismatch causes $Al_xGa_{1-x}N$ materials under tensile stress and a piezoelectric polarization along the same direction of the spontaneous polarization. This increased polarization is applied in high-electron mobility transistors (HEMTs) to create ***two-dimension electron gas (2DEG)***. More details of $Al_xGa_{1-x}N$/GaN heterostructures will be discussed in section 2.2.3.

For instance in the negative case of the strained-induced polarization fields within a quantumwell structure of optoelectronic device, this built-in electric field within the strained quantumwell will lead to a spatial separation of electron and hole wavefunctions and a ***Quantum-Confined Stark Effect (QCSE)*** resulting in a decreased recombination efficiency and a red-shift of emission. This will limit the performance of the optoelectronic devices. More details of QCSE will be discussed in section 2.6.2.

2.2.3. Semiconductor heterostructures

The layer structures of electronic devices are commonly developed from heterostructures of different semiconductor materials, e.g. n-channel or p-channel for HEMTs , quantumwell structures for LEDs and superlattice structures for DBR of LDs etc. With a heterostructure, their band structures will discontinue near the interface leading to the changes of electrical and optical properties in many ways for example charge transport across the interface and carrier confinement or optical confinement in quantum wells. In this section, a band discontinuity and a concept of two possible types of two-dimension carrier gases in heterostructures will be discussed. More detailed information about semiconductor heterostructures applied in devices can be found in [Miti99].

A. Band discontinuity

The discontinuities or offsets in the conduction and valence band edges of heterostructure semiconductors significantly influence the electrical and optical properties of heterostructure devices. To determine their expected band discontinuities is an important step to design heterostructure devices and a strain-induced piezoelectric polarization also taken in account.

In principle, the conduction band discontinuity, ΔE_C, is equal to the difference in electron affinity, χ, of the two semiconductors [Ibac03] i.e. $\Delta E_C = \chi_{\mathrm{II}} - \chi_{\mathrm{I}} = \Delta\chi$ and $\Delta E_g = \Delta E_C + \Delta E_V$. So, the valence band offset is given by $\Delta E_V = \Delta E_g - \Delta\chi$, whereas ΔE_g and ΔE_V are the bandgap and valence band discontinuities, respectively.

In fact, these predicted discontinuities with this model are very different from the experimental measured values. Martin et al. reported that the valence band discontinuity of GaN/AlN is 0.70±0.24 eV and suggested the ratio of conduction-to-valence band discontinuity is about 75:25 of the ΔE_g and the first approximated band discontinuity for ternary alloys of $\mathrm{Al}_x\mathrm{Ga}_{1-x}\mathrm{N}$ assumed by linear varying with Al composition [Mart96]. Hang and co-worker studied $\mathrm{Al}_x\mathrm{Ga}_{1-x}\mathrm{N}$/GaN band discontinuities by PL measurements and achieved the relation of bandgap, conduction and valence band discontinuities with Al fraction (x) as

$\Delta E_g = 1.05x + 7.62x^2, \ \pm 0.02x$, $\quad \Delta E_C(x) = 0.6x + 5.05x^2, \ \pm 0.03x$, and

$\Delta E_V(x) = \Delta E_g(x) - \Delta E_C(x) = 0.45x + 2.57x^2, \ \pm 0.05x$ and the ratio of conduction-to-valence band discontinuity is about 65:35 [Hang01].

B. Two-dimensional carrier gas in heterostructures

When one semiconductor is grown on another semiconductor, the band structures of these two semiconductors with discontinuities or offsets of their conduction and valence bands will adjust themselves to each other until their Fermi levels are the same resulting in a bending of the bands. However, this affects only the structure near a interface and the structure far from the interface their Fermi levels remain unchanged in both sides. In the simple schematic of band structures to explain a concept as shown in *Fig.2.7*, the higher bandgap semiconductor I with a negative doping or a Fermi level close to the conduction band is under tensile stresses by the larger in-plane lattice of semiconductor II such as AlGaN on GaN for examples of this structure applied in devices can be seen in [Adiv05, Chen07, Fieg07, Schu07, Wu04YF], AlN on AlGaN/GaN [Iman98, Kawa98] and AlGaN with higher Al composition on GaN/AlGaN with lower Al composition [Cord05]. At the interface, the conduction band of semiconductor II falls below the Fermi level and electrons will be transferred from semiconductor I and leave the positive charges in the semiconductor I. This will enhance the ionization of donors in the semiconductor I due to compensating the accumulated charges by the ionized donors. This will occur in the confined local area or the strong localization at the interface resulting in the formation of quantum states in the direction perpendicular to the interface and the electrons can move freely parallel to the interface as called ***two dimensional electron gas (2DEG)*** as shown in *Fig.2.7*.

In addition to the effects of band-structure alignment, the polarization effects have to be considered. As a reason, their lattice mismatch respecting to their piezoelectric polarizations enables to enhance an accumulation of carriers besides the spontaneous polarization. This principle is commonly used as the conductive channel for HEMT devices. The carriers from the dopants in the high bandgap material lead to a higher mobility of carriers in the channels due to a lower impurity scattering. For $Al_xGa_{1-x}N$/GaN heterostructures, $Al_xGa_{1-x}N$ with a higher Al content will induce larger polarizations and this effect on the formation of 2DEG will become stronger as shown in *Fig.2.8* [Amba98]. With such a structure, the carrier density could be enhanced to 1.2×10^{13} cm^{-2} and the mobility of 1290 cm^2/Vs at room temperature [Lund04]. Therefore, $Al_xGa_{1-x}N$/GaN heterostructures are widespread structures for applications in high frequency, high power HEMT devices.

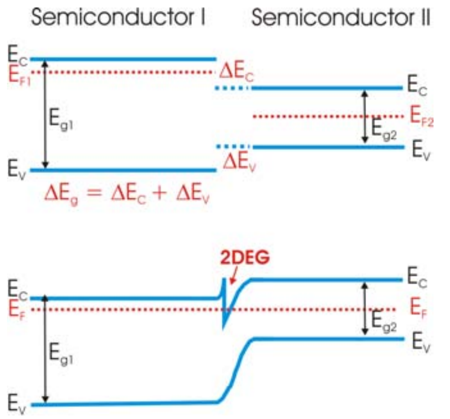

Figure 2.7 Schematic of band diagrams of two isolated semiconductors (above), and heterostructures (below)

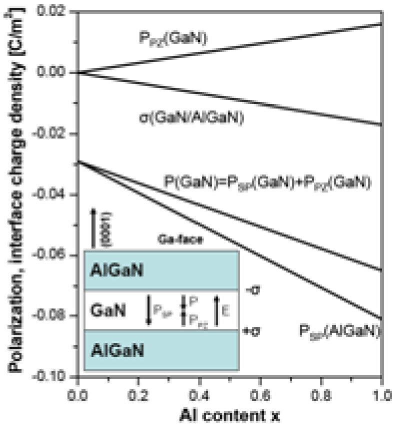

Figure 2.8 Polarization (P) of AlGaN/ GaN/AlGaN heterostructure as function of the Al content x [Amba98].

In another case of two dimension hole gas (2DHG), although the formation of 2DHG as the conductive channel applied in the devices has not yet been widespread and is more complicated and difficult for a device structure than the n-channel devices, to explain a basic principle to form 2DHG

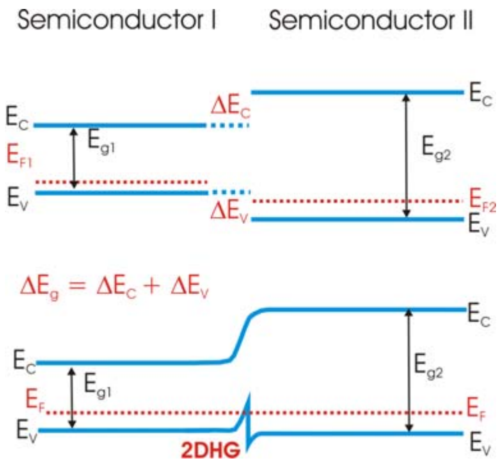

Figure 2.9 Schematic of band diagram of two isolated semiconductors (above), and heterostructures (below)

in heterostructures the simple schematic of band structures is presented in *Fig.2.9*. In this simple model of both semiconductor with a positive doping or a Fermi level close to the valance band, the smaller bandgap semiconductor I is under compressive stresses by the smaller in-plane lattice of semiconductor II such as InGaN on GaN for p-channel HFET [Zimm04, Zimm08], GaN on AlGaN [Lin06], a comparison of AlGaN/GaN with GaN/AlGaN/GaN [Heik03], both 2DEG and 2DHG presences in GaN/AlGaN/GaN heterostructure [Mitc08], AlGaN/GaN on AlN substrate [Acar08], and AlInN/AlN/GaN/AlN [Tasl10]. At the interface, the Fermi level of semiconductor II closes to the valence band of semiconductor I and holes will be transferred from semiconductor I and leave the negative charges in the semiconductor I. This will enhance the ionization of acceptors in the semiconductor I due to compensating the accumulated charges. As the strong localization at the interface the quantum states in the direction perpendicular to the interface will be formed and allow the holes to move freely parallel to the interface as called ***two dimensional hole gas (2DHG)*** as shown in *Fig.2.9*. With expecting to be similar to 2DEG, 2DHG will depend on the effects of the band-structure alignment and the polarization effects. Hackenbuchner and co-workers [Hack01, Maje04] presented from the calculated model that the most important parameter to impact on 2DHG is the induced polarizations and other factors e.g. the widths of wells and barriers the temperature, and the Mg concentration profile play a minor role.

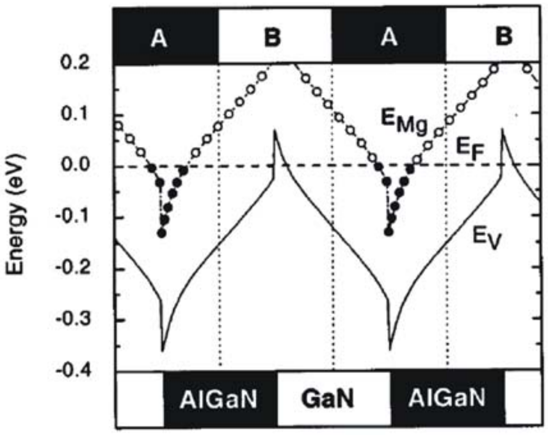

Figure 2.10 Calculated band structure of Mg doped GaN/$Al_{0.2}Ga_{0.8}N$ showing the Mg ionization energy pulled down below than Fermi level to enhance the hole density [Kozo99].

However, this principle is very beneficial to apply in p-type superlattice structures to enhance a hole density for p-type conductivity of group-III-nitride LEDs [Kozo99a,Kozo99b, Goep00, Schub96, Saxl99] as shown in *Fig.2.10*. As well the p-type conductivity of LED structures in this work is achieved by Mg-doped GaN/AlGaN superlattices and more details about experimental results will be discussed in Chapter 6.

2.3 *Misfit dislocations*

In case of homoepitaxial growth, pseudomorphic epilayers grown on the lattice-matched substrate will be nearly relaxed as shown in *Fig.2.11(a)*. In general case of heteroepitaxial growth, pseudomorphic epilayers grown on the lattice-mismatched substrate will be strained by two types of compressive or tensile strains depending on in-plane lattice constant of the substrate as compared to the relaxed in-plane lattice constant of layers. If the relaxed a-lattice constant of layers is larger than that of the substrate, the growing layers are compressive strained (*Fig.2.11(c)*).

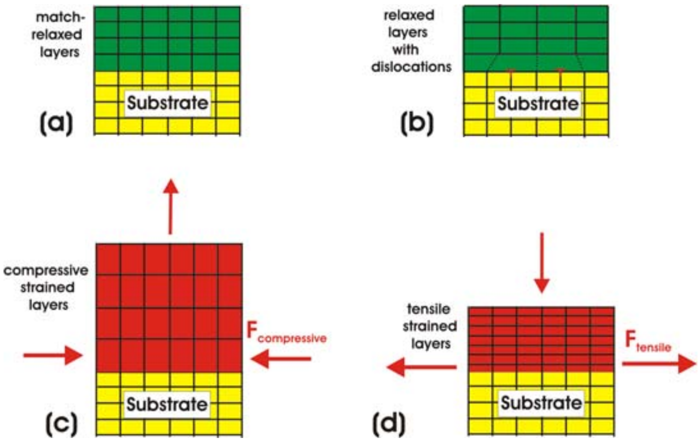

Figure 2.11 Ralaxed epilayers with lattice match (a) and with misfit dislocations (b) and pseudomorphic grown layers with compressive strain (c) and tensile strain (d).

Otherwise the relaxed a-lattice constant of the layers is smaller in the case of tensile strained (*Fig.2.11(d)*). When further growing, the strain energy will be higher with increasing layer-thickness. Until the thickness is thicker than a critical thickness, h_C, the strain will be partially relaxed or minimized by forming dangling bonds and creating defects or rows of defects known as ***misfit dislocations*** as shown in *Fig.2.11(b)*. Misfit dislocations are interfacial defects occurred between the layer and the substrate interface. These misfit dislocations are required to relief strain and generally will not thread up into the layer. However, threading dislocations in layers can be originated from the network of these misfit dislocations.

The in-plane strain ε_{xx} resulting from the lattice mismatch is given by

$$\varepsilon_{xx} = \frac{a_{sub} - a_{epi}}{a_{epi}}$$

Eq.2.5

where a_{sub} and a_{epi} are the lattice constants of the substrate and the epilayers, respectively and the strain in the growth direction is given by

$$\varepsilon_{ZZ} = -2\left(\frac{C_{13}}{C_{33}}\right)\varepsilon_{xx} \qquad \text{Eq.2.6}$$

where C_{13} and C_{33} are the elastic stiffness constants of the films.

The critical thickness [Matt74] is defined by

$$h_C = \frac{b}{2\pi f}\frac{1-\nu\cos^2\alpha}{(1+\nu)\cos\lambda}\left(\ln\frac{h_C}{b}+1\right) \qquad \text{Eq.2.7}$$

where b = the relevant Burger's vector, f = the mismatch strain. ν = Poisson's ratio, α = the angle between $\vec{b}$ and the dislocation, λ = the angle between the slip direction and the direction in film plane perpendicular to the line of intersection of the slip plane and the interface [Matt74, Scho09].

Alternatively, The critical thickness has been found to follow an empirical formula [Sze07] given by

$$h_C \approx \frac{a_{epi}}{2\varepsilon_{mismatch}} \approx \frac{a_{epi}^2}{2\left|a_{epi}-a_{sub}\right|} \qquad \text{Eq.2.8}$$

A typical number for the critical thickness, from a mismatch of 2% and an a_{epi} of 5Å, is about 10 nm [Sze07].

2.4 Silicon substrate

Due to excellent physical properties, crystalline quality, doping capability, thermal stability, large-diameter wafer, low cost and high possibility to integrate with Si-microelectronics for group III-nitride based devices, silicon is the most attractive substrate. Although, silicon is a most perfect crystal and its surface can be prepared with extremely smooth finish as compared to other substrate materials as sapphire and silicon carbide, the quality of group III-nitrides on silicon has been lower than that on sapphire or silicon carbide, due to large lattice mismatch (e.g. -17% for GaN), different thermal expansion coefficient (e.g. 6.8×10^{-6} K^{-1} of AlN [Figg09], 6.0×10^{-6} of GaN [Rode05] and 3.9×10^{-1} of Si [Mazu09] at 1000K) and the tendency to form amorphous Si_xN_y at the surface [Dadg03, Ishi98, Kros02, Kuku08, Wan01, Will98]. Nevertheless, GaN-based devices on Si substrates have been successfully demonstrated such as LEDs on Si (111) [Dadg02, Dadg03, Egaw05, Guha98a, Guha98b, Mo05, Li06, Zhan07], LEDs on Si(110) [Dami08, Reih09], LEDs on Si(001) [Schu06, Schu07, Schu08], and other devices on Si substrates such as FETs [Schu07, Vesc02, John04], HEMTs [Arul05], gaseous chemical sensors [Semo01, Thak07], and photodiodes [Bush04, Wang07].

2.4.1 Silicon structure and properties

Silicon crystallizes in a diamond structure with the space group of $Fd\overline{3}m$ (No.227) in the cubic-crystal family as shown in *Fig.2.12(left)*. Otherwise it can be described as two interpenetrating fcc structures or sublattices that are displaced relative to one another along the main diagonal of the cube or the [111] direction as depicted in *Fig.2.12(right)* [Ibac03]. The position of the origin of the second fcc sublattice, expressed in terms of the basis vectors, is $\left(\frac{1}{4},\frac{1}{4},\frac{1}{4}\right)$ in *Fig 2.12(left)* or α-position in *Fig 2.13(right)*. Thus, each Si atom in a tetrahedral configuration is surrounded by four equi-distant nearest neighbors lying at the corners with a distance of $\frac{\sqrt{3}}{4}a$, where a = 0.5431 nm and the distance of a central atom from the base of its tedrahedron of neighbors is $\frac{1}{4}$ of the total height of tetrahedron [Ibac03]. The separation of closed-packed layers in the fcc structure is $\frac{\sqrt{3}}{3}a$ with the stacking sequence of the close-packed (111) planes of ABCABC…… and αβγαβγ...... of the second fcc sublattice as shown in *Fig 2.12(right)*.

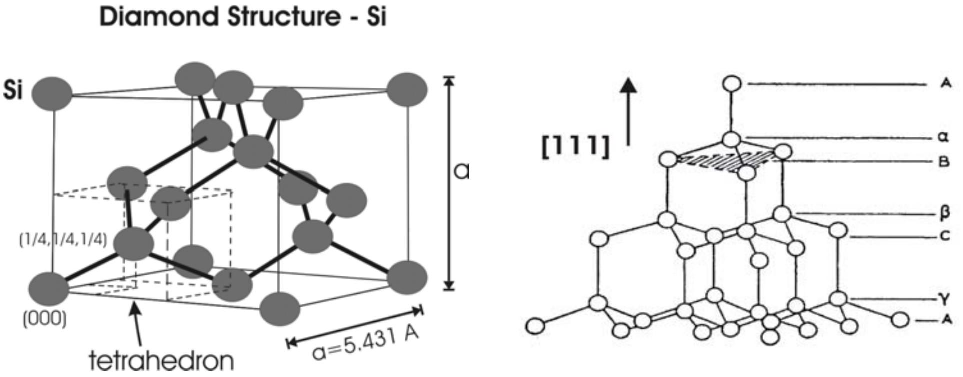

Figure 2.12 Diamond structure of Si and the side view along the [111] direction showing the close-packed plane [Omar90].

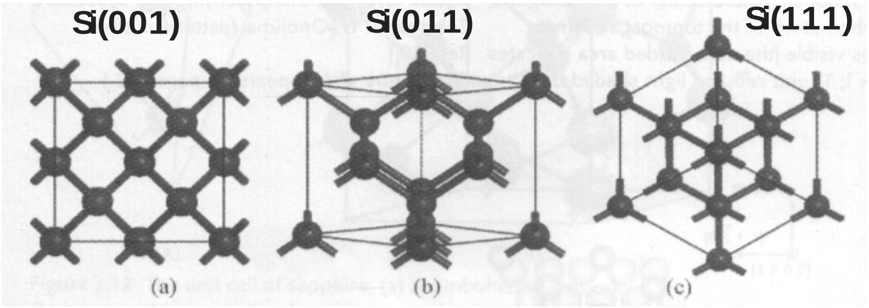

Figure 2.13 The perspective view along (a) the [001] (b) [011] (c) [111] directions of a Si cell [Mork08].

Therefore, the Si(111) orientation with the three-fold surface symmetry is generally preferred as the substrate plane for the wurtzite phase of GaN or group III-nitride growth rather than other planes such as Si(100) and Si(011). The perspective views along the [001], [011], [111] directions are presented in *Fig. 2.13*. Also, Si(001) is employed for GaN growth with a predominantly cubic structure but the growth with both phases of wurtzite and cube are frequently detected with a large number of extended defects [Basu94, Lei91, Lei92, Mork08]. Schulz and co-worker reported that the wurtzite GaN grown on Si(100) are different orientations depending on the buffer layer details with c-direction of GaN being on the (001) surface of Si or r-plane of GaN being oriented parallel to the Si surface [Schu04, Reih08]. However, the quality of GaN grown on Si substrates with (111), (100) and (011) orientations has been improved until devices have been demonstrated as mentioned before. The general properties of Si are summarized in *Table 2.2* [Kuku08]. More details about the other properties, doping and manufacturing of Si wafer can be seen in a handbook of semiconductor silicon technology [Omar90].

Table 2.2 The properties of silicon at room temperature [Kuku08].

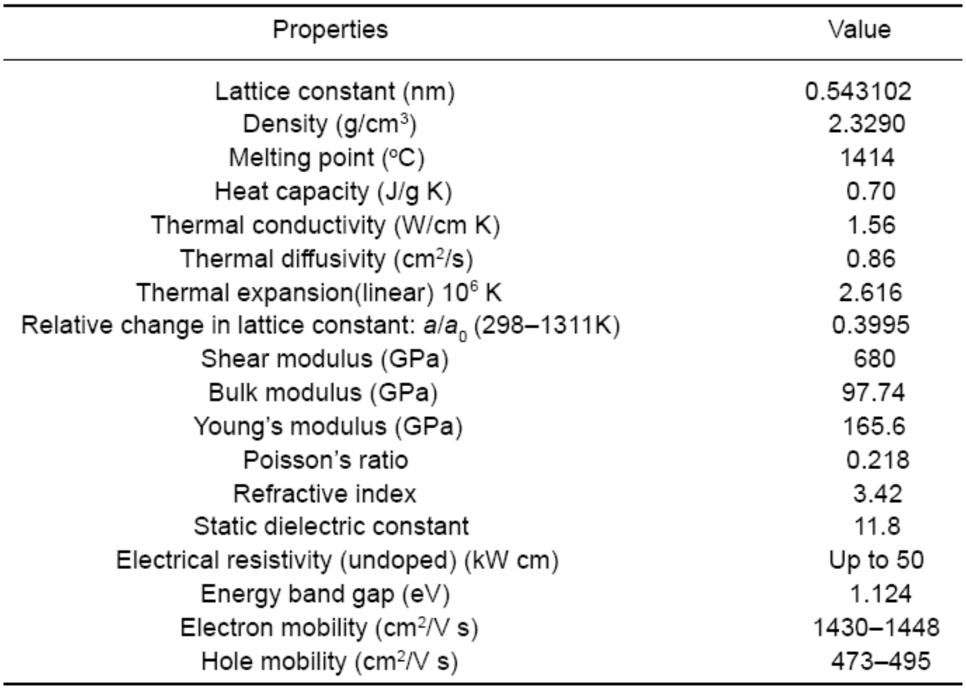

Properties	Value
Lattice constant (nm)	0.543102
Density (g/cm^3)	2.3290
Melting point (^{o}C)	1414
Heat capacity (J/g K)	0.70
Thermal conductivity (W/cm K)	1.56
Thermal diffusivity (cm^2/s)	0.86
Thermal expansion(linear) 10^6 K	2.616
Relative change in lattice constant: a/a_0 (298–1311K)	0.3995
Shear modulus (GPa)	680
Bulk modulus (GPa)	97.74
Young's modulus (GPa)	165.6
Poisson's ratio	0.218
Refractive index	3.42
Static dielectric constant	11.8
Electrical resistivity (undoped) (kW cm)	Up to 50
Energy band gap (eV)	1.124
Electron mobility (cm^2/V s)	1430–1448
Hole mobility (cm^2/V s)	473–495

2.4.2 Surface preparation of Si

When bare silicon is exposed to the atmosphere, it reacts almost immediately with oxygen or moisture in the air and forms a thin layer (about 10 to 20 Å) of silicon dioxide (SiO_2), called native oxide on the silicon surface and silicon dioxide is a dense material that fully covers the silicon surface [Omar90]. The thickness of the native oxide is enough to stop further oxidation or other chemical reactions with Si atoms at room temperature. To use Si substrate for epitaxy, silicon dioxide and other contaminations on the surface will interfere with deposition of adatoms to grow epitaxial layers. Therefore, a basic requirement of epitaxy is an atomically clean surface just prior to beginning deposition [Omar90]. This will be accomplished through some combination of pre-cleans outside the reactor and in-situ cleans done in the reactor.

In this work, the Si-substrate surface is cleaned by wet chemical etching before loading into the reactor. The Si substrate will be firstly cleaned for removal of small-size dust particles from the surface by dipping in propanol (isopropyl alcohol) with an ultrasonic cleaning. Next, to remove the organic contaminants on the surface, Si wafer is immersed in a mixture solution of diluted sulfuric acid ($H_2SO_4 + H_2O$) and hydrogen peroxide (H_2O_2) with a mixing ratio of 3:1:1 of H_2SO_4:H_2O:H_2O_2 for 1 minute and porous oxides will be formed [Grun91, Itan93]. Afterwards, the Si wafer is immersed in hydrofluoric acid (HF 5%) for 30 s to remove the resulting oxide layers from the surface and to terminate the Si surface with H-atoms or hydrogenation of surface dangling bonds [Mork08, Grun91]. During the chemical cleaning steps, the wafer is rinsed in deionized water for a while for pH = 7. The cleaning process is preformed 2 times. The Si-H bonds will be broken up at ~425°C in the reactor [Reih08, Dabr00] to provide an atomically cleaned Si surface for epitaxy.

2.4.3 Special problems in epitaxial growth on Si substrate

Heteroepitaxy growth of group III-nitrides on Si substrate suffers from some obstacles as large lattice mismatch, different thermal expansion coefficient. In addition, the amorphous Si_xN_y tends to be formed by a reaction between Si and group III-N species at the surface [Stev94, Lui03] and a meltback etching by a reaction between Si and Ga atoms at the surface and even through the growing layers [Dadg02v, Kros02a,Kros02b].

- To prevent the amorphous Si_xN_y and a meltback etching

The problem of nitridization at the Si surface is proposed to be overcome by the Al pre-deposition to cover the Si surface with a few Al monolayers and later NH_3 is switched on to form an AlN seed or nucleation layer [Clam06, Chen01, Dadg02v]. Meltback etching occurs only high growth temperatures due to a fast reaction between Ga and Si [Grau00, Chen00]. It is proposed to reduce this problem by using thick Al-rich seed and buffer layers because of high Al-N bonding energy or alternatively forming SiC on the Si wafer [Dadg02v]. Therefore, there is no meltback etching problem in $Al_xGa_{1-x}N$ growth for this work, even growth of $Al_{0.05}Ga_{0.95}N$.

- To reduce misfit dislocations

The problem of misfit between Si substrate and group III-nitride layer is typically solved by introducing a nucleation layer or seeding layer and buffer layers deposited first on the Si substrate to adjust or compromise most of lattice mismatch between the layer and substrate, providing a better lattice match and improving the orientation of the subsequent layers grown on them. Commonly, LT-AlN and HT-AlN are employed for the seeding and buffer layers to grow GaN and its compounds due to smaller grain size [Jang02, Cont08, Keya04, Kros04, Zami00, Lahr00] as well as a standard parameter of AlN seeding layer for our group's samples of the *c*-axis growth direction on Si substrate. Furthermore, using superlattice buffer layers is an approach to reduce the dislocation density due to enabling to bend the dislocation propagation away from the growth direction, combine and terminate dislocations etc. [Zhan02a, Sun05, Mura07]. In general, AlN is also used for one part of superlattice buffer layers of AlN/GaN SLs and AlGaN/AlN SLs and also AlGaN/GaN SLs to grow GaN on Si substrate [Felt01, Dadg01, Schu06] as well as in this work using LT-AlN/HT-AlN SLs to improve $Al_xGa_{1-x}N$ quality with Al composition upto 65% [Saen09a, Saen09b]. In principle, efficient buffer layers can help to reduce not only the dislocation density but also to compensate tensile strain after cooling.

- To compensate tensile strain after cooling to avoid cracks

To grow thick GaN layers on Si (111) is required in order to achieve better electrical and structural properties but cracks appearing in layers when exceeding 1 μm because of lower thermal expansion coefficient of Si more than two times of that of GaN involving to the strong stresses initiated in layers, and this results in cracking of GaN layers at cooling [Etzk01, Folls98, Roma06]. In principle, this problem will be avoided by inserting various interlayers between the GaN or AlGaN layers grown on Si substrates in order to reduce thermally-induced tensile strain such as LT-AlN interlayers [Aman98, Dadg00, Reih03, Lui07, Luo08], HT-AlN IL [Weng07], HT-GaN IL for InAlGaN [Wu04J] and AlN-based SL intermediate layers [Felt01, Jang03]. LT-AlN interlayers are grown with relaxed growth and HT-AlN interlayers with pseudomorphic growth [Bläs02]. Therefore GaN or AlGaN layers grown on the LT-AlN interlayers are grown under compressive interlayer-induced strain that compensates the thermally-induced tensile strain.

More details the seeding and buffer layers for GaN grown on Si substrate can be found in [Dadg02v, Dadgo3a, Kros02a, Kros02b]. In this work, to improve the quality of $Al_{0.1}Ga_{0.9}N$ on Si(111) substrate, these problems are also required to overcome. Therefore, the seed layer and buffer layers are optimized and more details of experimental results will be discussed in chapter 4 and 5.

2.5 Principle of LEDs

Light emitting diodes (LEDs) or electroluminescent diodes which are optoelectronic devices, consist of a *p*-type and *n*-type region, just like a regular *p-n* diode. But they are particularly designed that the radiative recombination dominates to produce a photon or electroluminescence whose wavelength depends on the bandgap of semiconductors. This radiative recombination process of electrically injected electrons and holes from *p*-type and *n*-type regions occurs efficiently in the active region of LEDs. The principle of LEDs such as a *p-n* junction, radiative transition and Quantum Confined Stark Effect in quantumwell structure, and doping of n- and p-type conductivity will be briefly described in this section to comprehend the factors of the designed LED structure. The current-voltage characteristics and the definitions of LED efficiencies will be introduced conceptually. More details can be found in references [Rose02, Schub03, Sze85, Sze07].

2.5.1 *P-n* junction

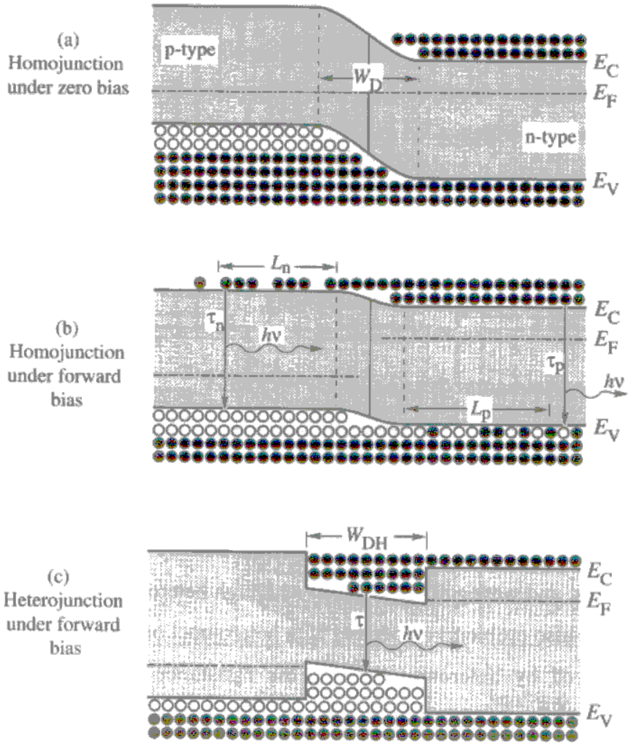

Figure 2.14 A p-n homojunction under zero bias (a) and under forward bias (b), and a p-n heterojunction under forward bias (c) [Schub03].

The basic structure of LEDs is a *p-n* junction. In the *p–n* junction, the Fermi energy in the *p*-region is much lower than that in the *n*-region. The Fermi energy of both regions will change in order to adjust to the same energy level as shown in *Fig.2.14(a)* by decreasing in the *n*-type region and increasing in the *p*-type region. Therefore, electrons near the *p–n* junction or interface can diffuse into the *p*-region and the holes can also diffuse into the *n*-region. While electrons diffuse, they leave ionized donors as fixed ions with positive charges. Analogously, holes near the *p–n* interface diffused into the *n*-region will leave negative ionized acceptors in the *p*-region. Electrons and holes transfer from one side to the other as called ***minority carriers*** and they will attract and eliminate each other in a process of ***recombination***. This causes free-carrier depletion from the two sides of the *p–n* interface to form a space charge region or depletion region or transition region in where uncompensated ionized dopant ions remain. Then the ionized dopant ions with the opposite charges will create a built-in electric field or diffusion voltage (V_D) over the depletion region given by

$$V_D = \frac{kT}{e} \ln \frac{N_A N_D}{n_i^2} \qquad \text{Eq.2.9}$$

where T is absolute temperature, k is Boltzmann's constant, n_i is the intrinsic carriers density, N_D and N_A are donor and acceptor concentrations. In a condition of an abrupt *p-n* junction, all dopants are assumed to be fully ionized and no compensation by unintentional impurities and defects. Thus a free-electron concentration is given by $n = N_D$ and a free-hole concentration by $p = N_A$.

Meanwhile the diffusion process generates the space charge region but the electric field generated by the space charge tends to counteract the diffusion to balance the Fermi energy. The average length an electron travels through the p-type region before recombining is the diffusion lengths given by

$$L_n = \sqrt{D_n \tau_n} \ \text{ for electrons and similarly for holes, } L_p = \sqrt{D_p \tau_p} \qquad \text{Eq.2.10}$$

where $D_n = \frac{kT}{e}\mu_n$ and $D_p = \frac{kT}{e}\mu_p$ are the electron and hole diffusion constants, τ_n and τ_p are the electron and hole minority carrier lifetimes, and μ_n and μ_p are the electron and hole mobility, respectively. The width of the depletion region can be written as

$$W_D = \sqrt{\frac{2\varepsilon}{e}(V - V_D)\left(\frac{1}{N_A} + \frac{1}{N_D}\right)} \qquad \text{Eq.2.11}$$

where $\varepsilon = \varepsilon_r \varepsilon_0$ is the dielectric permittivity of semiconductor and V is the bias voltage.

When a positive terminal is applied to the *p*-type region and a negative terminal to the *n*-type region as a forward bias, the holes in the p-type region and the electrons in the n-type region are repelled towards the junction resulting to reduce the width of the depletion region or lower the potential barrier. The narrow depletion width will allow electrons and holes to readily cross the junction and diffuse into another region near their neutral regions. This corresponds to a reduced electrical resistance and then a current flow through the diode from electrons flowing through the n-region to the junction and holes flowing in the opposite direction. Consequently, they will recombine in the vicinity of the junction and emit some light as shown in *Fig.2.14(b).*

2.5.2 Quantum-well structure

The luminescence in the *p-n* junction diode is produced from radiative recombination of minority carriers in the depletion and diffusion regions under forward bias. Due to the long diffusion length of homojunction in order of a micrometer, the recombination will occur over a large region with a strong effect on the minority-carrier concentration. Therefore, double-heterostructure is designed as a sandwich structure by a thin layer of smaller bandgap semiconductor in the middle of two layers of larger bandgap semiconductor to confine carriers in the active layer as presented in *Fig.2.14(c)*. In this double-heterojunction configuration of the central undoped layer bound by layers of opposite types, the number of excess carriers can be significantly increased and the radiative recombination lifetime will be shortened resulting to more-efficient radiative recombination [Sze07]. Furthermore, if the thickness of the central layer is reduced to the range of de Broglie wavelength of the carriers or until to the size of free exciton Bohr radius around 2.8 nm for GaN well, a quantum well is formed and the energy within the well is quantized in discrete levels. In a case of QW, electrons and holes can only move freely in two dimensions within the finite potential barriers that are determined by the band structure offset of two semiconductors. Therefore, the main factors influencing the quantized energies are the potential-barrier height and the well width.

2.5.2.1 Radiative transitions

In direct-bandgap semiconductors, radiative recombination primarily occurs at $k = 0$, the same wavenumber of the conduction and valence bands. In indirect-bandgap semiconductors, the recombination process will occur at the different wavenumber and require a phonon to assist according to the energy and momentum conservations. This results in a lower interaction probability of the direct-bandgap semiconductor. Besides the radiative recombination, non-radiative recombination such as trap-assisted recombination will be able to occur if there are deep-level defects in the semiconductor.

In *Fig.2.15*, schematic shows basic recombination transitions of electron-hole in a semiconductor as classified into 3 group as follows.

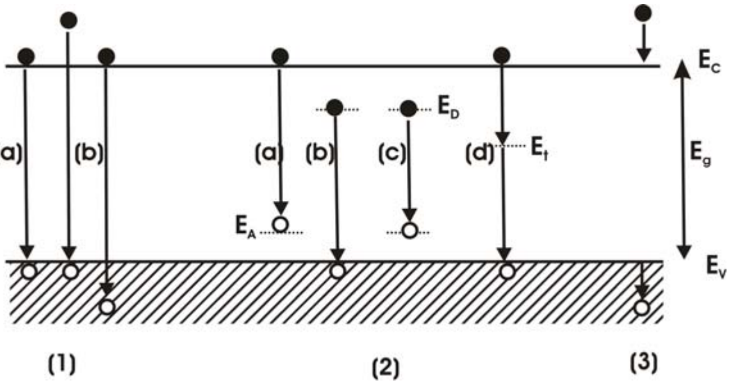

Figure 2.15 Basic recombination transitions in semiconductor after [Sze07].

The first group, label (1), is *the interband transition*

(a) intrinsic emission with the *near bandgap energy*

(b) high-energy emission of energetic or hot carriers or *avalanche emission*.

The second group, (2), is the transitions involving *chemical impurities* or *physical defects*,

(a) conduction band to acceptor-type defect,

(b) donor-type defect to valance band,

(c) donor-type to acceptor defect (*pair emission*), and

(d) band-to-band via deep-level traps.

The third group, (3), is *the intraband transition* of hot carriers or *deceleration emission* or *Auger process*.

However, there are not all transitions to occur in the same material or under the same conditions. Except Auger process, all transitions will emit light with different wavelengths depending on the energy-level differences. In an efficient luminescent material, the radiative recombination of interband transitions (a) in (1) emitting light with the near bandgap energy will be predominant over non-radiative processes. This process is a spontaneous recombination of electron-hole pairs as required for LEDs.

According to a conservation of momentum, the optical transition between valence and conduction bands for direct band gap is given by

$$h\upsilon = \left(E_C + \frac{\overline{h}^2 k^2}{2m_e^*} \right) - \left(E_V - \frac{\overline{h}^2 k^2}{2m_h^*} \right) = E_g + \frac{\overline{h}^2 k^2}{2m_r^*} \qquad \text{Eq.2.12}$$

This is the joint dispersion relation and m_r^* is the reduced effective mass by $\frac{1}{m_r^*} = \frac{1}{m_e^*} + \frac{1}{m_h^*}$ [Sze07].

A joint density of states can be obtained as

$$N_J(E) = \frac{\left(2m_r^*\right)^{3/2}}{2\pi^2 \overline{h}^3} \sqrt{E - E_g} \qquad \text{Eq.2.13}$$

By the Boltzmann distribution, the distribution of carriers is

$$F(E) = e^{\left(-\frac{E}{kT}\right)} \qquad \text{Eq.2.14}$$

So, ***the spontaneous emission rate*** is proportional to the product of the density of states of Eq.2.13 and the probability of corresponding carriers of Eq.2.14**,** and it can be generally written in the form

$$I(E = h\upsilon) \propto \sqrt{E - E_g} \cdot e^{\left(-\frac{E}{kT}\right)} \qquad \text{Eq.2.15}$$

As presented in *Fig.2.16*, the spectrum of spontaneous emission has a threshold energy of E_g, the maximum of $E_g + \frac{kT}{2}$, and a FWHM of the spectrum of 1.8kT as can be given in wavelength of a spectrum width by

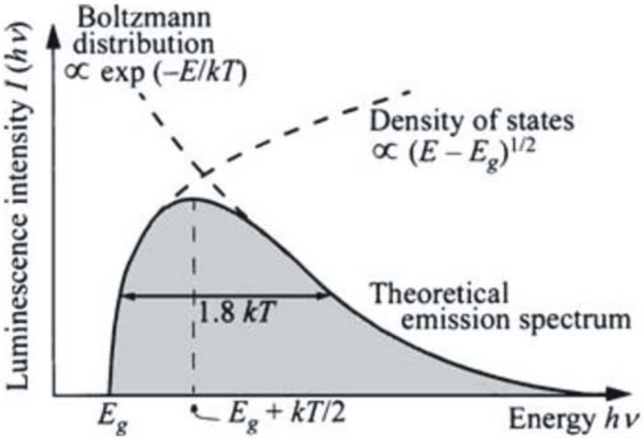

Figure 2.16 Theoretical spectrum of spontaneous emission of an LED [Sze07].

$$\Delta\lambda \approx \frac{1.8kT\lambda^2}{hc}$$

Eq.2.16

where c is the velocity of light. For example, in the middle of the visible spectrum, the emission spectrum width is ~10 nm. Otherwise, the radiative recombination rate is simply expected to be directly proportional to the product pn of the free electron concentration, n, and the free hole concentration, p.

2.5.2.2 Quantum Confined Stark Effect (QCSE)

As discussed in section 2.2.2, group III-nitride heterostructures including quantumwell structures will undergo with both spontaneous and piezoelectric polarizations described along the c-axis growth direction. The strong polarizations or internal electrostatic fields within the quantumwell layers can result in a sheet carrier density at each side of the interface. The internal electrical fields will change the potential-well shape into triangular shape allowing the reduced energy states in quantumwells due to decreasing the difference in the electron and hole energy levels and the quantum confinements. This energy reduction is a redshift of the emission wavelength as known ***Quantum Confined Stark Effect (QCSE).*** In addition, the spatial separation of the electron and hole wavefunctions causes a reduction in the radiative recombination efficiency due to a reduction in transition probability [Amba98, Amba99]. Consequently, the radiative decay time is prolonged due to the reduced oscillator strength for recombination. Both effects will be stronger when the well thickness and lattice mismatch increase due to increasing total polarization. One of promising approaches to reduce some polarizations in QW layers along the c-axis growth direction is slightly n-type doping in barrier layers in order to compensate the polarization charges by electrons and ionized donors [Kino00]. For example, the calculated band profiles of (5 nm GaN)/(10 nm $Al_{0.1}Ga_{0.9}N$) quantum wells with QCSE show the spatial separation of the electron and hole wavefunctions and a reduction of luminescence energy as revealed in *Fig.2.17(a)* with a comparison to flat-band profiles without internal electric fields of non-polar QW structure *(b)*.

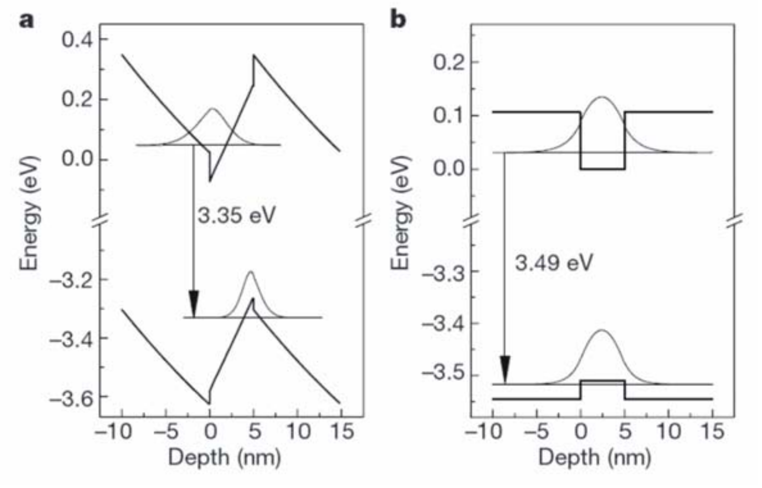

Figure 2.17 Calculated band profiles of (5 nm GaN)/(10 nm $Al_{0.1}Ga_{0.9}N$*) QWs with a QCSE and poor electron–hole overlap* ***(a)*** *and flat-band profiles without internal electric fields of non-polar QWs* ***(b)*** [Walt00].

2.5.3 *N*- and *p*-type semiconductors

One of basic requirements of LEDs is an injection of electrons and holes into an active layer for radiative recombination. Therefore, electrons and holes in cladding layers of the active layer are yielded by an intentional addition of impurities or dopant atoms into a lattice of a host semiconductor as called ***doping***. The doping is classified into two types as negative and positive conductivities depending on the type of dopants to produce free carriers in the semiconductor. The dopant atoms that give or donate an electron are called ***donors*** and called ***acceptors*** for creating a hole. After the dopants accommodate in the semiconductor, they will form energy states within the bandgap of the semiconductor as a donor state and an acceptor state. When a donor state is ionized by donating an electron, it will be positive and it is neutral when occupied. In the other case, an ionized acceptor state is negative by accepting an electron and it will be neutral when empty. Mostly the ionization energy of dopant states is analyzed by use of the simplest calculation based on the hydrogen-atom model [Sze07].

Ionization energy or activation energy of dopants

The ionization energy of a hydrogen atom is given by

$$E_n^H = \frac{m_0 e^4}{2\left(4\pi\varepsilon_0 \hbar\right)^2}\frac{1}{n^2} \qquad \text{Eq.2.17}$$

and $E_1^H = 13.6 \quad eV$. The ionization energy of a donor ($E_d = E_C - E_D$) in a semiconductor lattice can be obtained by replacing m_0 by *the conductivity effective mass of electrons* of $m_{ce} = \dfrac{3}{\left(\dfrac{1}{m_1^*} + \dfrac{1}{m_2^*} + \dfrac{1}{m_3^*}\right)}$ and replacing ε_0 by the permittivity of the semiconductor, ε_S.

So, the ionization energy of the donor is given by

$$E_d = \left(\frac{\varepsilon_0}{\varepsilon_S}\right)^2 \frac{m_{ce}}{m_0} E_H \qquad \text{Eq.2.18}$$

Analogously, the acceptor ionization energy, ($E_a = E_A - E_V$), can be calculated by using *the conductivity effective mass of holes*. In fact, this simple hydrogen-atom model certainly cannot account for the detailed ionization energy, particularly the deep levels in semiconductor. So far, n-type and p-type group III nitrides are accomplished commonly by Si- and Mg-doping and their donor and acceptor activation energies in GaN are reported about 8-28 meV [Tani02, Götz96, Hack94] and 150-250 meV [Mire98,Li02,Tana94], respectively and the donor and acceptor activation energies in AlN of 86 or 250-320 meV [Tani02,Tani04,Zeis00] and the acceptor activation energies of 510 [Nam03], 630 [Tani02] and 465 to 758 meV (from calculations [Mire98]), respectively. These values show that the ionization energies of acceptors in both GaN and AlN are much larger than those of donors to explain a lower effective *p*-type activation than *n*-type activation greatly and both ionization energies of donors and acceptors in GaN are smaller than in AlN explaining that donors and acceptors in GaN are activated much more effective than in AlN. Although AlN has naturally insulating properties with a large difficulty in *n*- and *p*-type doping, *n*-type AlN with Si-doping could yielded the electron concentration of ~10^{15} [Bori05, Tani02] to 7.4×10^{17}cm^{-3} [Ive05] and p-type AlN with Mg-doping could yielded the hole concentration of ~10^{10} cm^{-3} [Tani06]. Nevertheless, Taniyasu *et al.* [Tani06] developed AlN-based LED with a wavelength of 210 nm on SiC substrate by using AlN/AlGaN superlattices to enhance both *n*-and *p*-type conductivity successfully.

For Si- and Mg-doping in Al$_x$Ga$_{1-x}$N, both ionization energies of Si and Mg increase with a higher Al content from 8 to 86 meV for Si in Al$_x$Ga$_{1-x}$N with $0 \le x \le 1$ [Tani02] as shown in *Fig.2.18* and from 150 to 320 meV (396 meV with considering the mobility variation) for Mg in Al$_x$Ga$_{1-x}$N with $0 \le x \le 0.7$ [Li02,Naka05] as presented in *Fig.2.19*.

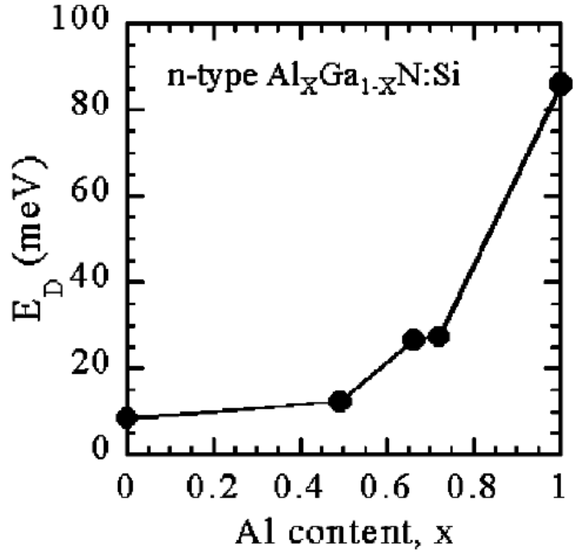

Figure 2.18 The activation energy of Si in $Al_xGa_{1-x}N$ as a function of x [Tani02]

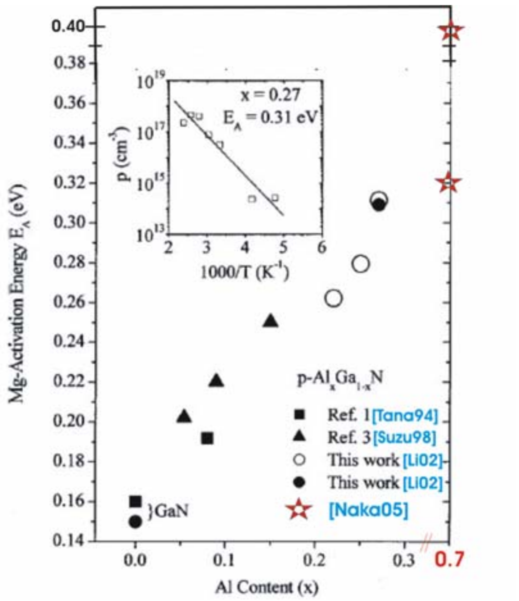

Figure 2.19 The activation energy of Mg in $Al_xGa_{1-x}N$ as a function of x after [Li02]

The doping limits in semiconductors

In addition to the ionization energy, ***the solubility limit*** of substitutional dopants in the host semiconductor also governs the achievable range of carrier concentrations by intentional doping. With a higher physical size and chemical similarity between the dopants and the host atoms, the solubility will be higher and it will be easier for the dopants to replace the host atoms [Zhang02]. However, if no dopant exists in nature that closely resembles the host atom, it will be difficult for example the difficulty in *p*-type GaN resulting from the low solubility of Mg dopants or the reasonably high solubility with the low fraction on the desired atomic sites [Wall04]. Moreover, ***the self-compensation*** by the spontaneous creation of intrinsic defects e.g. the formation of cation vacancies in n-type semiconductors also can limit the doping efficiency as involves a charge transfer from the dopants to the defects or from the defects to the dopant atoms [Zhang02]. At higher dopant concentrations, the higher difficulty in doping is caused by the self-compensation mechanism. Furthermore, there are more effects enabling to reduce the doping efficiency e.g. the formation of the *DX* and *AX* centers and the dopants being on the wrong lattice positions or forming undesired clusters etc. More details can be seen in a reference [Zhang02].

Carrier concentration in doped semiconductors

When electrons or carriers can move freely back and forth along one direction in the semiconductor, these movements can be explained by standing-wave oscillations with the wavelength related to their momentum or energy [Sze85]. The density of allowed energy states per unit volume as called ***the density of states***, $N(E)$, is given by

$$N(E) = 4\pi\left(\frac{2m_n}{h^2}\right)^{3/2}\sqrt{E} \text{ or } N(E) = 4\pi\left(\frac{2m_e^*}{h^2}\right)^{3/2}\sqrt{E} \qquad \text{Eq.2.19}$$

where $m_n = m_e^*$ = the effective mass, h = Planck's constant.

The electron density, $n(E)$, in an energy range is defined by the product of the density of allowed energy stated per unit volume and the probability of occupying that energy range, $F(E)$, as given by

$$n = \int_0^{E_{top}} n(E)dE = \int_0^{E_{top}} N(E)F(E)dE \qquad \text{Eq.2.20}$$

Thus, the probability that an electronic state with energy E occupied by an electron is given by

$$F(E) = \frac{1}{1+\exp^{\left(\frac{E-E_F}{kT}\right)}} \qquad \text{Eq.2.21}$$

This is called ***Fermi-Dirac distribution function***.

where *k*=Boltzmann constant , *T*= the absolute temperature and E_F =Fermi level.

Eventually, the electron density in the conduction band is given by

$$n = N_C \exp^{\left(-\frac{E_C-E_F}{kT}\right)} \qquad \text{Eq.2.22}$$

The electron density in the conduction band is given by

$$p = N_V \exp^{\left(-\frac{E_F-E_V}{kT}\right)} \qquad \text{Eq.2.23}$$

where N_C and N_V are *the effective density of states in the conduction band* and *the effective density of states in the valence band*, respectively.

At room temperature, the Fermi level of an intrinsic semiconductor generally lies very close to the middle of the band. So the intrinsic carrier density is obtained by

$$np = n_i^2 \qquad \text{Eq.2.24}$$

This is called ***the mass action law*** and By taking Eq.2.22 and Eq.2.23 in Eq.2.24,

$$n_i^2 = N_C N_V \exp^{\left(-\frac{E_g}{kT}\right)} \qquad \text{Eq.2.25}$$

Or

$$n_i = \sqrt{N_C N_V} \exp^{\left(-\frac{E_g}{2kT}\right)} \qquad \text{Eq.2.26}$$

where $E_g = (E_C - E_V)$ bandgap energy

For shallow dopants in the semiconductors and in the condition of ***complete ionization***, the electron density is equal to the ionized donors as can be written by $n = N_D$

From Eq.2.26, $$E_C - E_F = kT\ln\left(\frac{N_C}{N_D}\right) \qquad \text{Eq.2.27}$$

Similarly, for shallow acceptor,

$$p = N_A \quad \text{and} \quad E_F - E_V = kT\ln\left(\frac{N_V}{N_A}\right) \qquad \text{Eq.2.28}$$

In briefly, the electron density is given by

$$n = N_C \exp^{\left(-\frac{E_C - E_F}{kT}\right)} \quad \text{or} \quad n = n_i \exp^{\left(\frac{E_F - E_i}{kT}\right)} \qquad \text{Eq.2.29}$$

and the hole density is given by

$$p = N_V \exp^{\left(-\frac{E_F - E_V}{kT}\right)} \quad \text{or} \quad p = n_i \exp^{\left(\frac{E_i - E_F}{kT}\right)} \qquad \text{Eq.2.30}$$

In case of both donors and acceptors presence simultaneously, the Fermi level must adjust itself to preserve charge neutrality i.e. the total negative charges (electrons and ionized acceptors) must equal to the total positive charges (holes and ionized donors).

$$n + N_A = p + N_D \qquad \text{Eq.2.31}$$

From Eq.2.24 for n-type semiconductor $$p_n = \frac{n_i^2}{n_n} \qquad \text{Eq.2.32}$$

The subscript n refers to the n-type semiconductor (electron is the majority carrier)

For p-type semiconductor $$n_p = \frac{n_i^2}{p_p} \qquad \text{Eq.2.33}$$

The subscript p refers to the p-type semiconductor (hole is the majority carrier)

Generally, the magnitude of the net impurity concentration $|N_D - N_A|$ is large than the intrinsic carrier concentration n_i

Therefore, from Eq.2.31 the electron density for n-type semiconductor is given by

$$n_n \approx N_D - N_A \quad \text{if } N_D > N_A \qquad \text{Eq.2.34}$$

Similarly, the hole density for p-type semiconductor is given by

and $$p_p \approx N_A - N_D \quad \text{if } N_A > N_D \qquad \text{Eq.2.35}$$

In fact, to determine the carrier density in semiconductors is more complex and has to take the ionization at deep levels in account.

Doping of $Al_xGa_{1-x}N$

As known well, it is not difficult to achieve n-type group III nitrides due to unintentional impurity acting as donors in undoped layers. However, it will be more difficult to obtain high n-type conductivity in $Al_xGa_{1-x}N$ layers with a high Al composition up to AlN layers respecting to larger activation energy and their self-compensation mechanism as mentioned before. Nevertheless, Si-doped $Al_xGa_{1-x}N$ layers with $0.42 \le x \le 1$ are able to be activated effectively with a decreasing electron concentration from ~10^{20} to 10^{15} cm^{-3} as depicted in *Fig.2.20*.

Higher impurity such as oxygen and carbon with a higher Al content can form a donor complex (*DX*) converting a shallow donor into a deep level so that intentional donors of Si atoms will undergo with a higher ionization energy resulting in more difficult to donate free electrons [Bori05, McCl98, Stam98, Götz96b, Zhang02] as presented in *Fig.2.21*. Additionally the increasing Al vacancies as acceptor-like defects will act to compensate the intentional Si donors with an increasing Si doping.

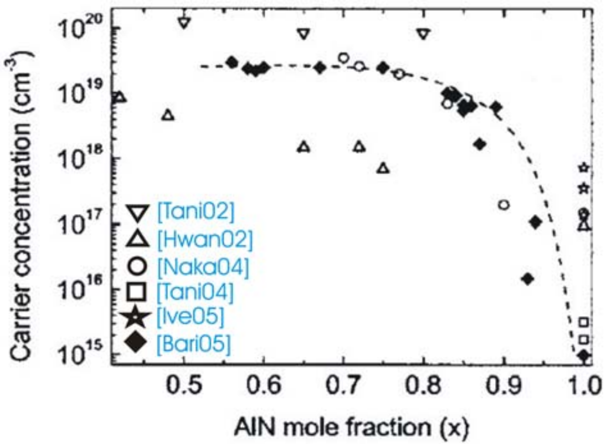

Figure 2.20 The electron concentration in $Al_xGa_{1-x}N$ as a function of x [Bori05].

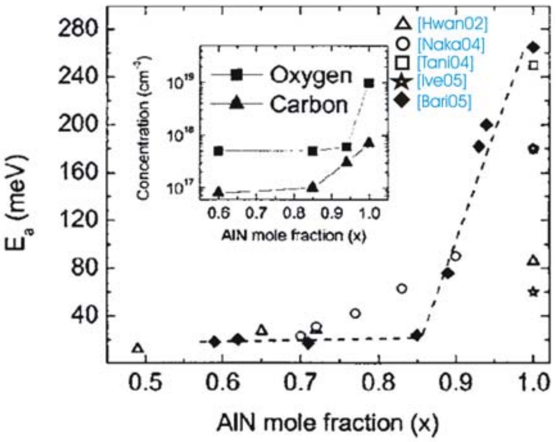

Fig.2.21 The Si activation energy in $Al_xGa_{1-x}N$ as compared to the concentrations of O and C (inset) as a function of x [Bori05].

In addition to a uniform doping with optimization of growth parameters, there are various proposed approaches to enhance *n*-type conductivity in Si-doped $Al_xGa_{1-x}N$ layers with a high Al content up to pure AlN such as co-doping with other dopants e.g. Indium [Adiv01a, AlTa08, Cantu03], delta doping [Cont02, Heik03, Kim03, Xin04] and with doped short-period superlattice structures [Nish03, Niki03, Kips03, Tani06].

In case of p-type conductivity by Mg doping, the activation energy of Mg in $Al_xGa_{1-x}N$ is quite high about 150 meV and higher with a higher Al content as discussed before. This results in Mg-doped GaN or $Al_xGa_{1-x}N$ remaining in the freeze-out region with an incomplete activation of acceptors or low activation efficiency at room-temperature [Tana94, Stam98]. Subsequently, low free-hole concentration in layers leads to a low conductivity or a high resistivity in layers. Due to the large ionization energy, the resulting hole concentration of Mg incorporated in concentrations up to $\sim10^{20}$ cm^{-3} is only $\sim10^{18}$ cm^{-3} meaning to only ~1% of Mg atoms ionized at room temperature [Neug96, Wall04]. Although the Mg concentration is increased beyond 10^{20} cm^{-3}, the hole concentration turns to a saturation and then decreases due to the limited solubility [Wall04, Kozo00] and the maximum hole concentration of mid 10^{17} to $\sim10^{18}$ cm^{-3} [Nagam08].

Moreover, the acceptor energy state of Mg will be compensated by hydrogen or hydrogen passivation to form a neutral complex of $(Mg\text{-}H)^0$ as a big obstacle of valence-electron promotion into the acceptor state in order to form free-holes [Aman89, Götz96a, Ohba94, Naka92a, Neug95, Vech92]. Therefore, Mg doping in GaN layers will be mostly activated to form free-holes by a thermal annealing in an environment with a lack of hydrogen such as in N_2 ambient at 600-700°C and higher for $Al_xGa_{1-x}N$ [Götz96a, Naka92b, Nagam08, Obat04] or in O_2 ambient at 400-900°C and high temperature for $Al_xGa_{1-x}N$ [Nakag04, Kuo02, Koid99, Hull00, Nagat09]. In addition, there are other methods to activate Mg-doped layers such as a low-energy electron-beam irradiation (LEEBI) treatment [Aman89, Gelh03], a microwave treatment [Chan01], a radio frequency (RF) treatment [Take01], and a laser treatment [Cheng01, Lin04].

However, there are notable approaches applied to accomplish *p*-type group III nitrides by Mg doping such as delta doping [Simb07], co-doping, and valence-band modulation by using strained superlattice structures.

By using Mg-doped superlattice structures, particularly short-period superlattices, both valence bands related to their acceptor activation energies are modulated for the same Fermi level. Due to the heterostructure and the piezoelectric fields, parts of the valence band are pulled down to below the Fermi level resulting in an enhancement of the acceptor ionization. The use of SLs to enhance the acceptor ionization was first proposed by Schubert *et al.* [Schub96] without considering the polarization field. In a later publication, Kozodoy et al. [Kozo99] proposed a model to show that the polarization field would enhance the effect of valence-band modulation. Saxler et al. [Saxl99] concluded that the effective activation energy in AlGaN:Mg is reduced by the use of Mg-doped GaN/AlGaN SLs. Although the presence of barriers for conduction of an SLs probably reduces the vertical conductivity, Zhu et al. [Zhu02] reported that the SL structure can reduce the vertical resistance in AlGaN/GaN LED structures. Up to now, this technique of short-period SLs is applied to successfully develop UV-LEDs in many groups [Hira08, Kips03, Niki05, Sumi08, Tani06, Wu06].

For instance, in Mg-doped $Al_xGa_{1-x}N$/GaN superlattices, large internal electric fields in $Al_xGa_{1-x}N$ and GaN layers are generated by the spontaneous and piezoelectric polarizations with corresponding directions. In case of Ga-face or (0001) surface polarity, the resulting electric fields point towards the substrate in the $Al_xGa_{1-x}N$ layers and towards the growth surface in the GaN layers. As an effect of the polarizations, the band bending forms an oscillation of the valence band edge. At one side of the GaN layer is below the Fermi level allowing valence electrons in the GaN valence band to transfer to the Mg acceptor states in the adjacent $Al_xGa_{1-x}N$ layer. This indicate to the formation of a two-dimensional hole gas at the GaN/$Al_xGa_{1-x}N$ interface as mentioned in section *2.2.3*. The high density of free-holes at the interface will be much larger than the average carrier concentration from a bulk layer.

2.5.4 The current-voltage characteristics of LEDs

The principle of current-voltage (I-V) characteristic of LEDs will be explained in this section and more details can be found in reference [Schub03]. The current-voltage (I-V) characteristic of a *p-n* junction diode is described by ***the Shockley equation*** with cross-section area A is given by

$$I = eA\left(\sqrt{\frac{D_p}{\tau_p}}\frac{n_i^2}{N_D} + \sqrt{\frac{D_n}{\tau_n}}\frac{n_i^2}{N_A}\right)\left(e^{eV/kT} - 1\right) \qquad \text{Eq.2.36}$$

where D_n and D_p are the electron and hole diffusion constants and τ_n and τ_p are the electron and hole minority carrier lifetimes, respectively, I and V are current and voltage of the diode, N_A and N_D are the acceptor and donor density, respectively and n_i is the intrinsic carrier density.

For reverse bias conditions, the diode current saturates (I_S)and this constant current is given by the constant factor in front of the exponential function in Eq.2.36 as

$$I_S = eA\left(\sqrt{\frac{D_p}{\tau_p}}\frac{n_i^2}{N_D} + \sqrt{\frac{D_n}{\tau_n}}\frac{n_i^2}{N_A}\right) \qquad \text{Eq.2.37}$$

So, the diode I-V equation of Eq.2.36 can be written as

$$I = I_S\left(e^{eV/kT} - 1\right) \qquad \text{Eq.2.38}$$

For forward bias conditions, $V >> \frac{kT}{e} \Rightarrow \left(e^{eV/kT} - 1 \right) \approx e^{eV/kT}$

So, Eq.2.36 can be rewritten as

$$I = eA\left(\sqrt{\frac{D_p}{\tau_p}} N_A + \sqrt{\frac{D_n}{\tau_n}} N_D \right) e^{e(V - V_D)/kT} \qquad \text{Eq.2.39}$$

where the diffusion voltage $V_D = \frac{kT}{e} \ln \frac{N_A N_D}{n_i^2}$

This equation shows the relation of current (I) and diode voltage (V) as a exponential function meaning to the strongly increasing current with approaching of the diode voltage to the diffusion voltage ($V \approx V_D$). This voltage is called ***threshold voltage***, $V_{th} \approx V_D$

At the zero bias,

$$eV_D - E_g + (E_F - E_V) + (E_C - E_F) = 0 \qquad \text{Eq.2.40}$$

Due to $E_C - E_F << E_g$ and $E_F - E_V << E_g$, Eq.2.40 can be rewritten as

$$eV_D - E_g = 0 \quad \Rightarrow \quad V_{th} \approx V_D \approx \frac{E_g}{e} \qquad \text{Eq.2.41}$$

As seen in *Fig.2.22*, the real threshold voltage or turn-on voltage is smaller than $\frac{E_g}{e}$ which expected from the theoretical I-V characteristic of the Shockley equation as

$$I = I_S e^{eV/n_{ideal}kT} \qquad \text{Eq.2.42}$$

where the ideality factor $n_{ideal} = 1$ for a perfect diode.

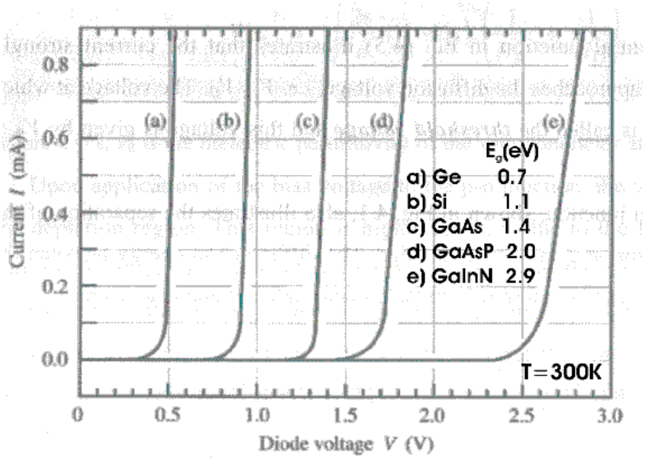

Figure 2.22 I-V characteristics of p-n junctions made from different semiconductors [Schub03].

For real diodes, the ideality factor is typically $n_{ideal} = 1.1 - 1.5$, higher as $n_{ideal} = 2.0$ for group III-arsenide and phosphide, and $n_{ideal} = 6.0$ for GaN/GaInN diodes [Rhod88]. This feature of group III nitrides is due to several reasons as large band gap discontinuities cause an additional voltage drop, the less-mature contact technology for nitride materials, the low p-type conductivity in bulk GaN, and a parasitic voltage drop in the n-type buffer layers [Schub03].

In addition, due to unwanted parasitic resistance of LEDs, the I-V equation will be rewritten as

$$I - \frac{(V - IR_S)}{R_p} = I_S e^{e(V - IR_S)/n_{ideal} kT} \qquad \text{Eq.2.43.}$$

For $R_p \to \infty$ and $R_S \to 0$ this equation reduces to the Shockley equation of Eq.2.42 where R_S, series resistance can originate from excessive contact resistance or the resistance of the neutral regions and a parallel resistance, R_p, from any channel that bypasses the p-n junction (this bypass can be caused by damaged regions of the p-n junction or by surface imperfections). *Figure 2.23* shows the effect of a series resistance and a parallel resistance (shunt) on the I-V characteristic of the p-n junction diode.

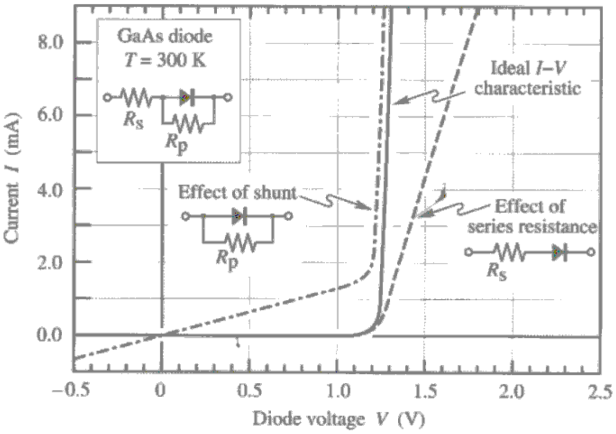

Figure 2.23 Effect of a series resistance and a parallel resistance (shunt) on the I-V characteristic [Schub03].

Evaluating **the parallel resistance** can be performed near the origin of the I-V diagram where $V << \frac{E_g}{e}$. For this range, the p-n junction current can be neglected and the parallel resistance is given by

$$R_p = \left. \frac{dV}{dI} \right|_{near \ \ origin} \qquad \text{Eq.2.44}$$

(typically $R_p >> R_S \Rightarrow R_S$ can be neglected for this case).

Evaluating **the series resistance** can be performed at a high voltage where $V >> \frac{E_g}{e}$. For sufficiently large voltages, the diode I-V characteristic becomes linear and the series resistance is given by

$$R_S = \left. \frac{dV}{dI} \right|_{at \ \ voltages \ \ exceeding \ \ turn-on} \qquad \text{Eq.2.45}$$

However, it may not be practical to evaluate the diode resistance at high voltages due to device heating effects.

When $R_p \to \infty$, Eq.2.43 can be rewritten as

$$I = I_S e^{e(V-IR_S)/n_{ideal}kT} \qquad \text{Eq.2.46}$$

by differentiating V with respect to I, it yields

$$\frac{dV}{dI} = R_S + \frac{n_{ideal}kT}{e}\frac{1}{I}$$

or

$$I\frac{dV}{dI} = R_S I + \frac{kT}{e} \qquad \text{Eq.2.47}$$

for $n_{ideal} = 1$.

The series resistance of the diode is obtained as the slope of a $(I\frac{dV}{dI})$-versus-(I) plot (*Fig.2.24)*.

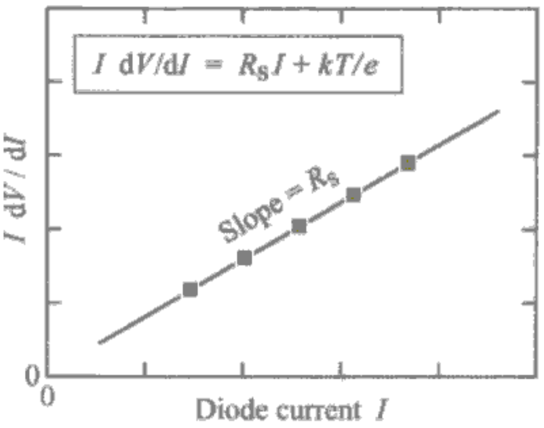

Figure 2.24 the $(I\frac{dV}{dI})$*-versus-*(I) *plot to evaluate the diode series resistance as the slope* [Schub03].

2.5.5 Definitions of LED efficiencies

In this section, the definitions of LED efficiencies were summarized and more details can be found in [Sze07].

Internal Quantum Efficiency

Internal Quantum Efficiency is the efficiency of converting carrier current to photons, defined as

$$\eta_{in} = \frac{\text{number of photon emitted internally}}{\text{number of carriers passing junction}} \qquad \text{Eq.2.48}$$

Otherwise, the internal quantum efficiency is the fraction of the injected carriers that combined radiatively to the total recombination rate and it can be written as

$$\eta_{in} = \frac{R_r}{R_r + R_{nr}} = \frac{\tau_r}{\tau_r + \tau_{nr}} \qquad \text{Eq.2.49}$$

where R_r are R_{nr} the radiative and nonradiative recombination rates, τ_r and τ_{nr} are their associated radiative and nonradiative lifetimes, respectively.

External Quantum Efficiency

External quantum efficiency is also called ***extraction efficiency*** defined as

$$\eta_{ex} = \frac{\text{number of photons emitted externally}}{\text{number of carriers passing junction}} = \eta_{in}\eta_{op} \qquad \text{Eq.2.50}$$

Optical Efficiency

Optical Efficiency that focused on the device optical paths and optical interfaces can be simply given by the fraction of the solid angle of the light-escape cone to the total solid angle from a point source,

$$\eta_{op} = \frac{\text{solid angle of light - escape cone}}{4\pi} = \frac{1}{2}\left(1-\cos\theta_c\right) \approx \frac{1}{4}\frac{\bar{n}_o^2}{\bar{n}_S^2} \qquad \text{Eq.2.51}$$

where $\theta_c = \sin^{-1}\left(\frac{\bar{n}_o}{\bar{n}_S}\right) \approx \frac{\bar{n}_o}{\bar{n}_S}$, θ_c is the critical angel, and $\bar{n}_o, \bar{n}_S$ are the refractive indexes of the ambient and semiconductors, respectively. $\eta_{op} \approx 2\%$ for a typical semiconductor LED with planar surface.

Power Efficiency

The power efficiency is simply defined as the ratio of the light power output to the electrical power input,

$$\eta_P = \frac{\text{optical power out}}{\text{electrical power in}} = \frac{\text{number of photons emitted externally} \times \text{h}\upsilon}{\text{I} \times \text{V}} \qquad \text{Eq.2.52}$$

$$= \frac{\text{number of photons emitted externally} \times \text{h}\upsilon}{\text{number of carriers passing junction} \times \text{q} \times \text{V}}$$

Due to $qV \approx h\upsilon$, it follows that $\eta_P \approx \eta_{ex}$.

Luminous Efficiency

The luminous efficiency normalizes the power efficiency by a factor that is related to the eye sensitivity. The brightness of light output is measured by the luminous flux (in lumens).

$$\eta_{lu} = \frac{\text{luminous flux}}{\text{electrical power in}} = \frac{L_0 \int V(\lambda) P_{op}(\lambda) d\lambda}{IV} \text{ lm/W} \qquad \text{Eq.2.53}$$

where L_0 is a constant with a value of 683 lm/W, $V(\lambda)$ the relative eye sensitivity function normalized to unity for the peak at $\lambda = 555nm$, and $P_{op}(\lambda)$ the power spectrum of the radiation output. The maximum luminous efficiency has a value of 683 lm/w.

Chapter 3

The principle of MOVPE and characterization methods

An AIXTRON 200/4 RF-S MOVPE machine equipped with a home-built in-situ optical reflectivity monitor was used to grow AlGaN layers and develop AlGaN-based LED structures on Si substrates. During MOVPE growth, in-situ measurements of the wafer bow during growth are required for strain engineering. The samples are characterized ex-situ for their crystalline quality, electrical and optical properties by various methods. The crystalline quality is mainly characterized by x-ray diffractometry (XRD). The surface morphologies are investigated by atomic force microscopy (AFM), field emission scanning electron microscopy (FE-SEM) and Nomarski microscopy. Transmission electron microscopy (TEM) is employed for investigating the microstructure in cross-section, the dislocation density and precise thickness. To characterize the optical properties, luminescence microscopy as cathodoluminescence (CL), photoluminescence (PL) and electroluminescence (EL) are applied to optimize quantum-well structures. For electrical properties, capacitance-voltage (C-V) measurements are used to determine the carrier density of n- and p-type samples. Current-voltage (I-V) measurements and electroluminescence (EL) microscopy are performed to characterize full LED structures. In this chapter, the basic principle of MOVPE, an overview of MOVPE growth of AlGaN and the precursors will be briefly described. Further details can be found in Stringfellow's book [Stri89] and elsewhere [Herm04, Quay08, Mork08]. Furthermore, the principles of all characterization methods applied in this work are shortly summarized in this chapter.

3.1 Basic principle of MOVPE

Metal-organic vapor phase epitaxy (MOVPE) is a method to grow layers on a substrate from precursor molecules in a non-equilibrium condition. The MOVPE growth system basically consists of 4 main parts as the gas and metalorganic precursor systems, the reaction chamber, the heating system and the exhaust and low pressure pumping system. Typically, trimethyl-gallium (TMGa) and trimethyl-aluminium (TMAl) from bubblers are applied for metalorganic (MO) sources or precursors of Ga and Al, respectively, and. Mass flow controllers (MFC) and pressure controllers to control the accurate flow rate of metalorganic sources into a reactor. In order to exactly control the vapor pressure of the liquid metalorganic precursors, the bubblers are maintained in a thermal bath at a constant temperature between melting and boiling points such as 0°C for TMGa and 17°C for TMAl. The vapor partial pressure or the equilibrium vapor pressure of metalorganic precursor depends on this bubbler temperature and the relation can be expressed as

$$P_{partial,MO} = 10^{\left(a-\frac{b}{T}\right)} \times \frac{1013.25}{760} \text{ mbar} \qquad \text{Eq.3.1}$$

where a and b are vapor pressure parameters depending on the metalorganic precursor, T is the bubbler temperature. For TMGa kept at 0°C, the vapor partial pressure is 90 mbar and 9.6 mbar for TMAl at 17°C. The vapor partial pressures of available metalorganic sources are given as a function of temperature by the chemical manufacturer and can be also found in reference [Stri89].

A carrier gas as H_2 or N_2 flows through the bubblers and ideally saturates with the vapor of the metalorganic precursor. This flow is transported together with gaseous group V precursors as NH_3 to the reactor where a heated substrate is placed to form a layer from the precursor gases. The process is usually performed at reduced pressure which is maintained by a vacuum pumping. The reactor's wall is cold by a cooling water. The heated substrate on the susceptor over a heater is the hottest zone. During growth, the susceptor is rotated in order to enhance the layer homogeneity. A scheme of a MOVPE system and the reactor are shown in *Fig.3.1*.

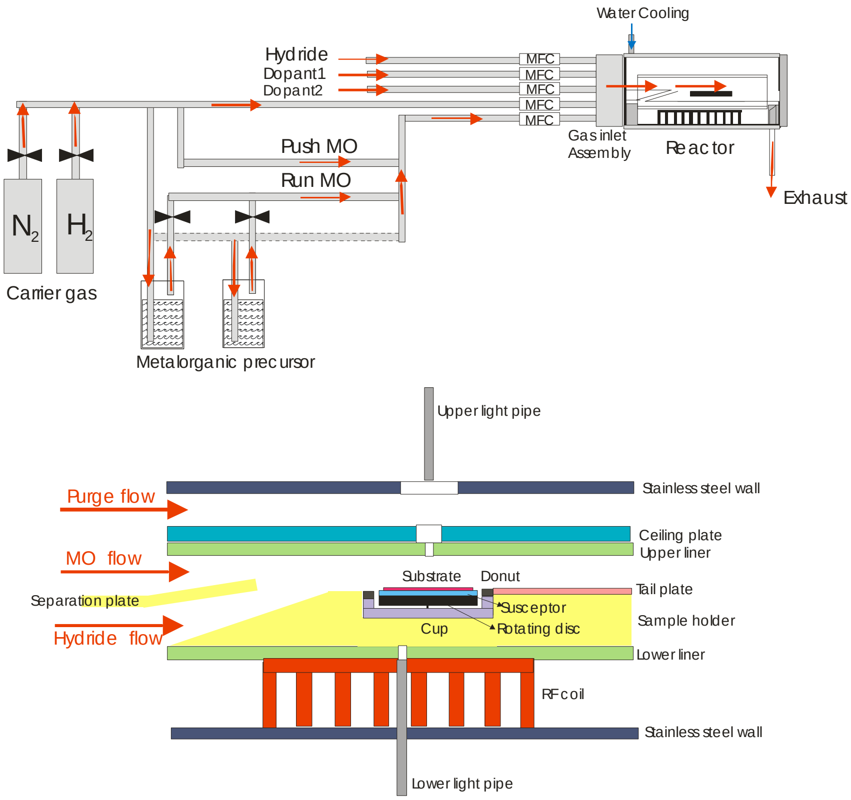

Figure 3.1 Schematics of a basic MOVPE system (above) and a reactor (below) after [Schubweb]

The molar flow rate or mass transport rate of metalorganic precursors into the reactor controlled by the MFC given in unit of sccm (standard cubic centimeter a minute) is regulated by the molar fraction of metalorganic vapor resulting from changing the metalorganic vapor partial pressure, $P_{partial,MO}$. With an increasing bubbler temperature, the metalorganic vapor pressure increases. The molar flow rate of metalorganic precursors by MFC can be expressed as

$$F_{M,MO} = \frac{P_{partial,MO}}{P_{total}} F_{M,total} \qquad \text{Eq.3.2}$$

By using the ideal-gas equation,

$$F_{M,total} = \frac{P_{atm} F_{V,total}}{RT} = 0.0446 F_{V,total} \qquad \text{Eq.3.3}$$

So, the molar flow rate of metalorganic precursors can be expressed as

$$F_{M,MO} = 0.0446 \frac{P_{partial,MO}}{P_{total}} F_{V,total} \quad \text{or} \quad F_{M,MO} = 0.0446 \frac{P_{partial,MO}}{P_{MFC}} F_{V,MFC} \qquad \text{Eq.3.4}$$

where $F_{M,MO}$ is the molar flow rate of the MO precursor (moles per minute), $F_{V,MO}$ is the volume flow rate of the MO precursor (in sccm), R is the ideal-gas constant, R = 8.3146 J/(mol K), T is the standard temperature (273 K), $P_{partial,MO}$ and P_{total} are the vapor partial pressure of the MO precursor and the total pressure of the gas mixture (in mbar), $F_{V,total}$ is the total volume flow rate of the gas mixture, $P_{total} \approx P_{partial,carrier} \approx P_{MFC}$ and $F_{V,total} \approx F_{V,MFC}$. In fact, the MFC measures the heat capacity of the mass flowing through itself and calculate in a volume of gas at standard temperature and pressure [AdEnweb].

A general reaction to grow group-III-nitride layers can be simply written without a complicated MOVPE process given by Eq.3.5.

$$R_3M\,(g) + NH_3\,(g) \rightarrow MN\,(s) + 3RH\,(g) \qquad \text{Eq.3.5}$$

where R is an organic radical of methyl (CH_3) or ethyl (C_2H_5), M is a metal from group III alkyls.

In fact, the MOVPE process is very complex with many parallel and series reaction steps simultaneously involving homogeneous and heterogeneous reactions of group III- and group V-source molecules. Epitaxial growth relates to surface processes such as adsorption and desorption of chemical species and surface migration. The precursor molecules are transported by the carrier gas as H_2 or N_2 to undergo decomposition reactions in the gas phase at the heated zone of the reactor. Resulting species diffuse from a boundary layer to a growing surface and adsorb at favored energy sites such as edges, kinks and steps on the surface. They will diffuse along the surface before the final incorporation reactions and the resulting product will be incorporated by forming a new bond to grow the film. Also, the species can desorb from the surface or react with other surface species. Gaseous byproducts desorb from the surface and diffuse in the carrier gas away from the deposition zone towards the reactor exhaust. Schematic steps of the MOVPE growth process are shown in *Fig.3.2*.

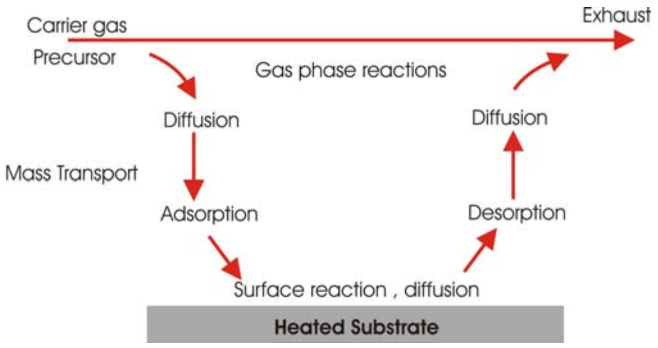

Figure 3.2 Schematic of MOVPE growth process after [wikiweb].

Thermal decomposition or pyrolysis of gaseous species as NH_3 and volatile metalorganic radicals is the most common chemical reaction for MOVPE growth. The processes of MOVPE growth are governed by **thermodynamics** as a main driving force to contribute desired deposition materials for epitaxial growth, **kinetics** or chemical surface reactions, and **mass transport** for diffusion and hydrodynamics of molecular species. Stringfellow categorized the key processes in MOVPE growth as shown in *Table 3.1*.

Table 3.1 Key processes in MOVPE growth after [Stir89].

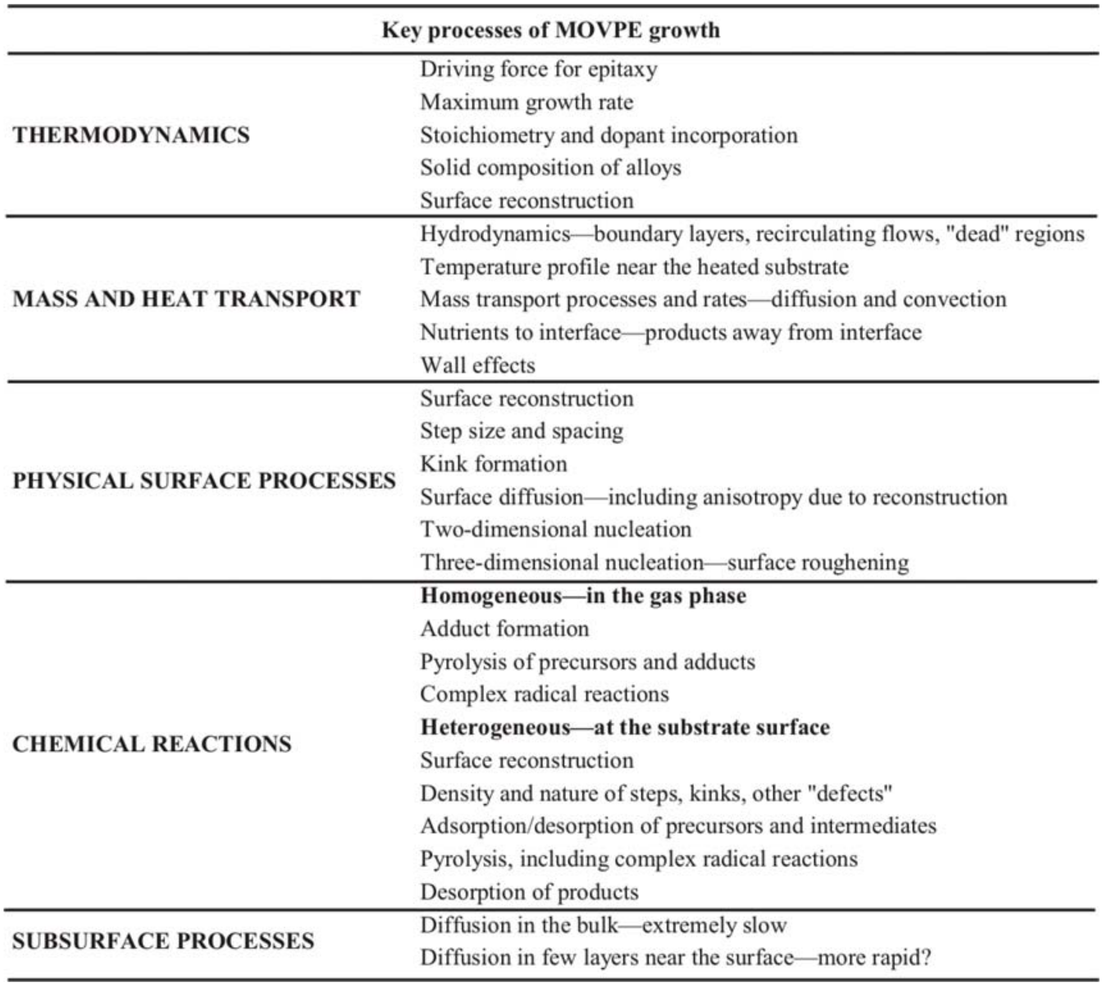

Key processes of MOVPE growth	
THERMODYNAMICS	Driving force for epitaxy Maximum growth rate Stoichiometry and dopant incorporation Solid composition of alloys Surface reconstruction
MASS AND HEAT TRANSPORT	Hydrodynamics—boundary layers, recirculating flows, "dead" regions Temperature profile near the heated substrate Mass transport processes and rates—diffusion and convection Nutrients to interface—products away from interface Wall effects
PHYSICAL SURFACE PROCESSES	Surface reconstruction Step size and spacing Kink formation Surface diffusion—including anisotropy due to reconstruction Two-dimensional nucleation Three-dimensional nucleation—surface roughening
CHEMICAL REACTIONS	**Homogeneous—in the gas phase** Adduct formation Pyrolysis of precursors and adducts Complex radical reactions **Heterogeneous—at the substrate surface** Surface reconstruction Density and nature of steps, kinks, other "defects" Adsorption/desorption of precursors and intermediates Pyrolysis, including complex radical reactions Desorption of products
SUBSURFACE PROCESSES	Diffusion in the bulk—extremely slow Diffusion in few layers near the surface—more rapid?

For series reactions, the slowest step will control the overall reaction rate but the fastest reaction will control the overall reaction rate resulting from a sum of the individual reaction rates for parallel reactions. In an exothermic process the MOVPE growth rate is given by an Arrhenius equation $k = A\exp^{\left(-\frac{E_a}{RT}\right)}$, where k is the rate constant, A is the pre-exponential factor, E_a is the activation energy, R is the gas constant and T is the absolute temperature. From a relation of the growth rate and the reciprocal temperature, there are three growth temperature regimes as depicted in *Fig.3.3*. In the range of lower temperatures, chemical kinetic or surface reactions are slower than mass transport and limit the overall growth rate thus this range is called **kinetic limited regime**. With increasing temperature, the rate increases steeply until a range of intermediate temperatures is reached where the surface reactions are faster and mass transport limits the overall rate. This region where gas diffusion to and away from the surface determines growth and the rate is nearly constant is called **mass transport limited regime**. In the **thermodynamic limited regime** at high temperatures**,** thermodynamics limits the growth rate which decreases with increasing temperature. Here gas-phase pyrolysis of the hydrides becomes dominant and solid particles can form without being deposited on the substrate. Therefore, spontaneous gas phase nucleation, deposition on the reactor wall, and higher desorption rate of the reactant species disturb the desired deposition and reduce the growth rate.

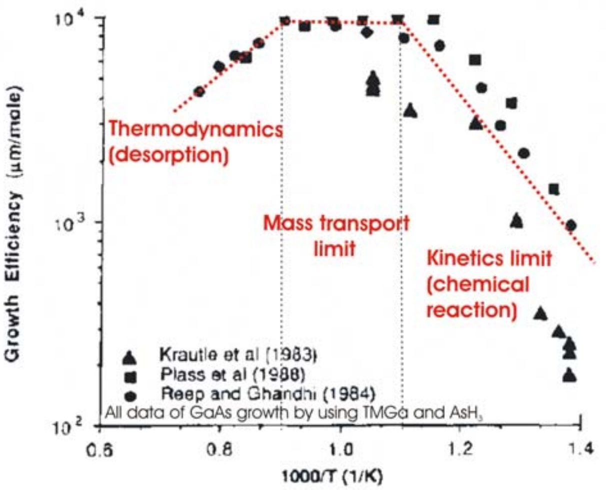

Figure 3.3 Temperature dependence of MOVPE growth rate after [Stri89].

In addition to the temperature dependence, there are other parameters influencing the overall growth rate. In the case of kinetic limitation, the surface plays a role as an initial orientation or surface treatments of the substrate need to be considered. For the case of mass transport the total flow rate, flow velocity and reactor pressure are be important. At high temperatures, the growth rate decreases due to depletion routes as adducts formation and enhanced reactor wall depositions, reactor geometry, gas inlet design and time residence also do have an impact on growth.

3.2 MOVPE growth of $Al_xGa_{1-x}N$ and precursors

Here the chemical structure and properties of Al, Ga and N precursors including precursors for *n*- and *p*-doping will be briefly explained in order to better understand the $Al_xGa_{1-x}N$-growth process and problems occurring in MOVPE systems. For more details on the influence of precursors and other growth parameters of the MOVPE system see references [Kalu03, Miho98, Miho99].

Aluminum precursor

Trimethylaluminium, $(CH_3)_3Al$ or TMAl, is employed as Al-precursor in MOVPE growth of $Al_xGa_{1-x}N$ or AlN. Its melting and boiling points are 15°C and 125°C, respectively and it is liquid at room temperature. It is a very strong electron acceptor or Lewis acid. Thus intermolecular bonds are easily formed by self-association forming a dimer molecule of $Al_2(CH_3)_6$. $(CH_3)_3Al$ is also air and water sensitive and spontaneously flammable due to the polar character of their Al-C bonds. The dimer structure is realized by forming CH_3 bridges between the aluminum atoms. As a result from the decomposition of methyl radicals, growth leads to carbon contamination of the layers. The structure of $Al_2(CH_3)_6$ is shown in *Fig.3.4*.

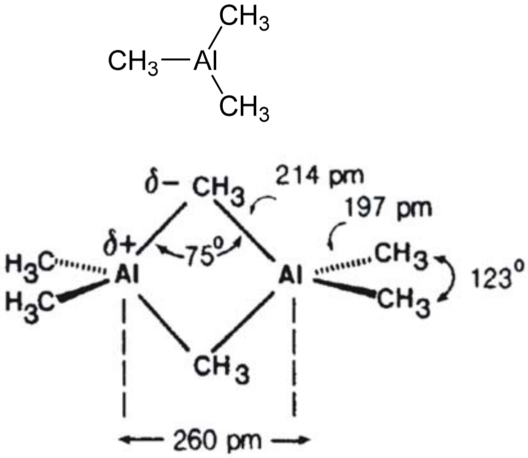

Figure 3.4 Schematic of $Al(CH_3)_3$ and $Al_2(CH_3)_6$ molecular structure [Kalu03].

Gallium precursors

Trimethylgallium, $(CH_3)_3Ga$ or TMGa, is commonly used as Ga-precursor and triethylgallium $(C_2H_5)_3Ga$ or TEGa in some cases. They are liquid at room temperature and melting and boiling points of TMGa are -15°C and 55.7°C, respectively. Ga and Al are group III metals with a large difference of their atomic properties such as atomic radius, ionization energy and electron affinity. Therefore, the chemical properties of gallium compounds are different from those of the aluminium compounds. Thus trialkylgallium R_3Ga compounds are less reactive and weaker electron acceptors than the analogous R_3Al compounds. This originates from different electronic configurations. Ga has a greater effective nuclear charge and a smaller atomic radius than Al (135 pm for Ga and 143 pm for Al) resulting in an anomalously high electronegativity value of Ga compared to Al [Kula03]. This affects the polarity of the Ga-C bonds presenting a lower polarity than the Al-C bonds and therefore the bond strength for Ga-C is weaker than for Al-C. In consequence, the R_3Ga compounds are not stabilized by dimerization as the R_3Al compounds and the R_3Ga are monomeric in vapor and liquid phases. In some cases triethylgallium $(C_2H_5)_3Ga$ or TEGa is used as Ga-precursor when lower carbon incorporation and an accurate thickness control, e.g., for quantum well structures is required. For the latter the lower vapor pressure enabling a low growth rate is responsible [Miho98, Miho99]. The schematic of the $(CH_3)_3Ga$ and $(C_2H_5)_3Ga$ molecular structures are shown in *Fig.3.5* and *Fig.3.6*, respectively.

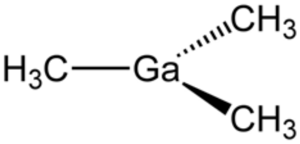

Figure 3.5 Schematic of $(CH_3)_3Ga$ molecular structure [wikiweb].

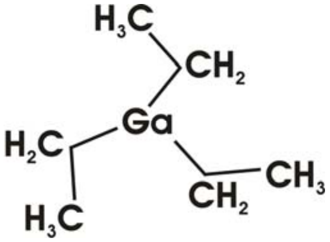

Figure 3.6 Schematic of $(C_2H_5)_3Ga$ molecular structure after [Safcweb].

Nitrogen precursor

Ammonia, NH_3, is gaseous at room temperature with melting and boiling points of -77.7°C and -33.3°C at 1013 hPa, respectively. It is formed in a trigonal pyramid (or tetrahedral geometry of NH_4^+) with five valence electrons; two *s*-electrons as a lone pair occupy one hybrid orbital of nitrogen and the other three *p*-electrons of the nitrogen form three s-p bonds with the 1s orbitals of the hydrogen atoms. This bonding leads to the high stability of NH_3 molecules even at high temperature explaining the poor cracking efficiency in typical MOVPE environments [Kula03]. Due to the lone pair, NH_3 acts as a Lewis base and interacts with metalorganic precursors, especially the strong Lewis-acid TMAl in gas phase to form adducts. To generate a sufficient amount of active nitrogen for layer growth, great amounts of NH_3 are required which are also lost from the growing layer due to the high volatility of nitrogen. Moreover, a thermal decomposition of NH_3 into N_2 and H_2 occurs in a very limited range of temperatures and pressures without a catalyst. The scheme of a NH_3 molecular structure is shown in *Fig.3.7*.

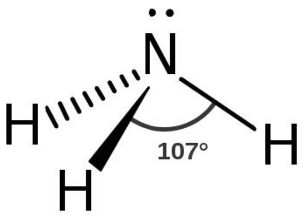

Figure 3.7 Schematic of NH_3 molecular structure [wikiweb].

N-dopant Precursors

Silane, SiH_4, is used as Si precursor for n-doping. Silane is a toxic and flammable gas with melting and boiling points of -185°C and -112°C, respectively. It has a general formula Si_nH_{2n+2}, with $n = 1, 2, 3$, and so on by covalent bonding in a tetrahedral geometry. SiH_4 is insoluble in water and slow hydrolysis. SiH_4 is a structural analogue of a saturated hydrocarbon (e.g. methan, CH_4). It is easily decomposed by oxygen due to the thermodynamically favoured bonding of Si-O as compared to Si-Si. Above 420°C, SiH_4 can decompose into Si and H_2. The scheme of the SiH_4 molecular structure is shown in *Fig.3.8*.

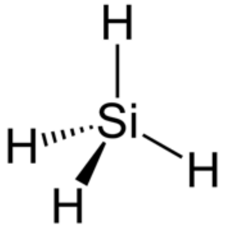

Figure 3.8 Schematic of SH_4 molecular structure [Wikiweb].

P-dopant Precursors

Figure 3.9 Schematic of $(C_5\ H_5)_2$ Mg molecular structure [Chemweb].

Bis cyclopentadienyl magnesium, $(C_5H_5)_2$ or Cp_2Mg, is commonly used as Mg precursor for the most effective p-dopant presently known for group III nitrides. Cp_2Mg is a white crystalline powder with high melting and boiling points of 176°C and 300°C, respectively, low vapor pressure or a low volatility of 0.043 torr at 25°C [Akzoweb]. To avoid any condensation in the piping of the MOVPE system and to achieve higher gas phase concentrations, the precursors are often kept above room temperature and the piping is heated to, e.g., 37°C [Beau97]. $(C_5H_5)_2Mg$ belongs to a group of organometallic compounds called metallocenes [Crab01]. The metallocenes with the general formula, $(C_5H_5)_2M$, consist of two cyclopentadienyl anions (Cp or $C_5H_5^-$) bound to a metal center (M) in the oxidation state II. The metal ion is sandwiched between two parallel cyclopentadienyl rings as a sandwich structure. The Cp_2Mg molecular structure is shown in *Fig.3.9*.

MOVPE growth of $Al_xGa_{1-x}N$

From the general form of the basic reaction in MOVPE process shown in Eq. 3.5, the general reactions for GaN, AlN and $Al_xGa_{1-x}N$ using the precursors $(CH_3)_3Ga$, $(CH_3)_3Al$ and NH_3, can be written as

$$(CH_3)_3Ga(g) + NH_3(g) \rightarrow GaN(s) + 3CH_4(g) \qquad \text{Eq.3.6}$$

$$(CH_3)_3Al(g) + NH_3(g) \rightarrow AlN(s) + 3CH_4(g) \qquad \text{Eq.3.7}$$

$$(x)(CH_3)_3Al(g) + (1-x)(CH_3)_3Ga(g) + NH_3(g) \rightarrow Al_xGa_{1-x}N(s) + 3CH_4(g) \quad \text{Eq.3.8}$$

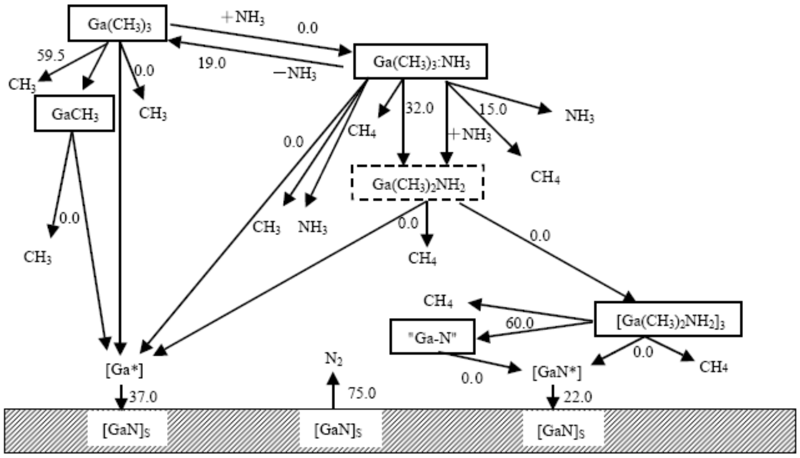

Figure 3.10 Schematic of the GaN deposition and reaction pathway [Hara01].

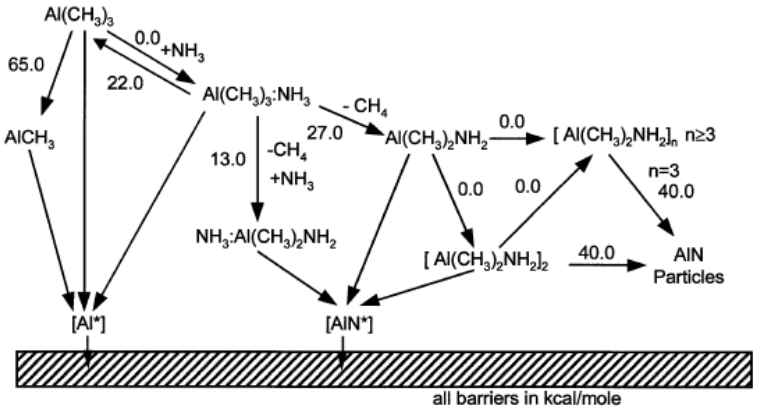

Figure 3.11 Schematic of the AlN deposition and reaction pathway [Miho98].

MOVPE chemistry is very complex and involves a number of gas phase and surface reactions as shown in *Fig.3.10* for a model of GaN growth and *Fig.3.11* for AlN growth. Although, there are many groups [Hara01, Hirak05, Kalu03, Miho98, Sun00] proposing the models of chemical reaction mechanism of group III nitrides, the fundamental understanding of the processes involved is still evolving and as such the reaction mechanism and the related kinetic rate parameters are poorly understood [Mork08]. Due to the chemical properties of TMAl as electron acceptors or Lewis acids and NH_3 as an electron donor or Lewis base, the chemical interaction between TMAl and NH_3 readily occurs to promote the formation of gas-phase adducts and these reactions are also observed for TMGa radicals but less dominantly than for TMAl radicals.

The reactions leading to Al-adducts can be written as

$$Al(CH_3)_3\,(g) + NH_3(g) \leftrightarrow Al(CH_3)_3{:}NH_3(s) \quad \text{Eq.3.9}$$

and the reactions to form Ga-adducts can be written as

$$Ga(CH_3)_3\,(g) + NH_3(g) \leftrightarrow Ga(CH_3)_3{:}NH_3(s) \quad \text{Eq.3.10}$$

These gas-phase adducts further react with other molecular species or radicals to produce AlN and GaN particles in the gas phase (in *Fig.3.11* and *Fig.3.10*, respectively). This is problematic for MOVPE growth of $Al_xGa_{1-x}N$ with a high Al content. Additionally, it is indicated that the final formation of dimer and trimer nano-particles plays a role in reducing the AlN growth rate at a typical MOVPE environment [Miho98, Crei04]. Thus to achieve MOVPE growth of $Al_xGa_{1-x}N$ with a high Al content, the elimination of gas-phase prereactions or parasitic reactions between NH_3 and metalorganic precusors is an important issue. By many groups [Khan05, CHChen96, Choi00, Kond04], the growth conditions of low pressure and low growth rate are suggested approaches to improve $Al_xGa_{1-x}N$ growth. Moreover, the other chemical properties of TMAl as high reactivity and air and water sensitivity lead to an oxygen contamination during $Al_xGa_{1-x}N$ growth. As another problem, with a strong chemical bonding of TMAl, Al adatoms have a higher sticking coefficient and lower surface mobility than Ga adatoms [Khan05]. All of these can explain the difficulty of growing high Al-content $Al_xGa_{1-x}N$ in MOVPE compared to GaN growth.

3.3 In-situ optical reflectivity measurement

This optical technique is applied to monitor epitaxial growth during the MOVPE process. The important values of growth rate and curvature of the growing samples provide the control of the growth quality. The interference of two light beams reflected from the surfaces of the substrate and growing epilayer is detected by an optical area detector. In this work, a He-Ne laser is used as a light source at 633 nm.

Growth rate and thickness

The growth rate and thickness of the epilayer can be directly calculated from interference pattern or intensity oscillations. The maximum of Fabry-Perot oscillations will occur at the thickness, *d* as

$$n \cdot d = (m) \cdot \frac{\lambda}{2} \qquad \text{Eq.3.11}$$

where $m > 1$ as integer and λ is the light wavelength and n the refractive index of the layer. Therefore, the growth rate μ_{gr} can be calculated from the interval between two of these maxima

$$\mu_{gr} = \frac{\lambda}{2n\Delta t} \qquad \text{Eq.3.12}$$

Curvature measurements

Not only the reflection intensity but also the distance between two light spots are monitored and this converted to the curvature value by this expression

$$\kappa = \frac{1}{R} \approx \frac{d_0 - d}{2d_0 \cdot L} \qquad \text{Eq.3.13}$$

where κ is the curvature, R is the curvature radius, d is the distance between the laser source and the detector, d_0 is the distance between two laser points on the surface and L is the distance of the detector and the surface [Reih08] as presented in *Fig.3.12*.

Consequently, the approximated stresses in each layer will be determined by the well-known Stoney's formula [Ston09, Freu03], in case for $h_f << h_S$ as

$$\kappa = \frac{6m\varepsilon_m h_f}{h_s^2}, \quad \text{or} \quad \kappa = \frac{6\sigma_f h_f}{M_s h_s^2} \qquad \text{Eq.3.14}$$

where $m = \frac{M_f}{M_s}$ and $\sigma_f = M_f \varepsilon_m$.

$M_f = \frac{E_f}{1-\nu_f}$, M_f is the biaxial modulus of layer, E_f = Young's modulus, ν_f = the Poisson ratio.

$M_s = \frac{E_s}{1-\nu_s}$, M_s = the biaxial modulus of substrate, ε_m = the biaxial mismatch strain between film and substrate, σ_f = the film stress in the growing epilayers at that time,

h_f =the film thickness at that time, h_s =the substrate thickness.

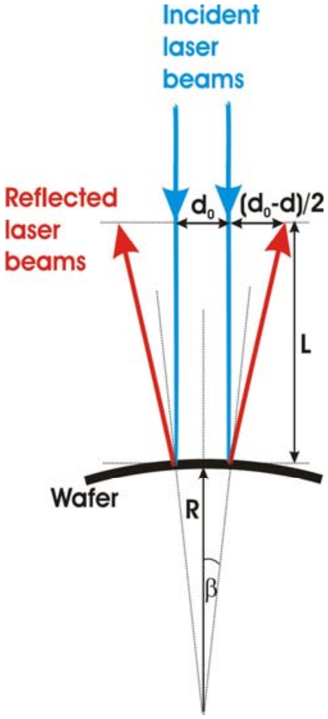

Figure 3.12 Reflection geometry of in situ curvature measurements after [Reih08]

For this case, the thickness of Si(111) substrates used is 500 µm.

Typically, when the samples are unloaded from the reactor, they are simply characterized by the naked eyed before an analysis with other characterization methods is applied. Typically, epilayers or thin films grown on Si substrate will appear clean and smooth as a mirror-like surface and with an appropriated thickness, interference fringes will be observed on the surface. Some common problems as chamber cleanliness or instability of the machine can strongly affect the surface appearance.

3.2. X-ray measurements

The crystalline quality of $Al_xGa_{1-x}N$ layers is characterized by x-ray measurements, a non-destructive method giving fast and precise results. Here, the basic principle of x-ray diffractometer and x-ray reflectivity used in this work are summarized.

3.2.1 High-resolution x-ray diffractometer

An x-ray diffractometer is a measuring instrument to characterize the structure of a crystal material from the diffraction patterns produced when a beam of x-rays interacts with it. A typical simple diffractometer consists of a source of radiation or x-ray tube, a monochromator to choose the wavelength, slits to adjust the shape of the beam, a sample holder, a detector and a goniometer to fine adjustment of the sample and the detector positions [Holy99, Klug74].

All x-ray diffraction techniques are based on the elastic scattering of x-rays from material structures that have long range order of a repeating pattern or arrangement. The comprehensive principle of x-ray diffraction from crystals is described by the dynamical theory of diffraction [Holy99]. For more detail of the dynamical theory of x-ray diffraction can be seen in [Auth01].

High resolution x-ray diffraction (HR-XRD) with a setup of parallel-beam optics is applied to characterize epitaxial layers, heterostructures and superlattice systems [Holy99, Krost96, Piet04]. From the diffraction patterns of reflected x-ray beam after interacting with a crystalline sample, the information on lattice parameters, composition, and uniformity of epitaxial layers, their thickness, strain state, relaxation and the crystalline quality related to their crystal orientations are obtained.
In principle, the diffraction of x-rays is described by **Bragg'law**,

$$n\lambda = 2 \cdot d_{hkl} \cdot \sin\theta_B \qquad \text{Eq.3.15}$$

whereas $n =$ an integer by the order, $\lambda =$ the wavelength of the x-rays,
$d_{hkl} =$ the distance between each hkl plane in atomic lattice, $2\theta_B =$ the angle between the incident x-ray and the diffracted x-ray or the detector as shown in *Fig 3.13*.

d_{hkl} of cubic crystal system is defined by:

$$d_{hkl} = \frac{a_0}{\sqrt{h^2 + k^2 + l^2}} \qquad \text{Eq.3.16}$$

where hkl = the Miller indices of the scattering planes, a_0 = the lattice constant.

The real lattice space for a hexagonal crystal system is given by:

$$d_{hkl} = \frac{1}{\sqrt{\frac{4}{3}\left(\frac{h^2+hk+k^2}{a^2}\right)+\frac{l^2}{c^2}}} \qquad \text{Eq.3.17}$$

where a and c are the in-plane and out-of-plane lattice constants, respectively.

At first, the origin of real lattice (000) is transferred to the origin of reciprocal lattice as the wavevector of incident x-rays ($\vec{k}_i = \frac{2\pi}{\lambda_i}$) and the scattering plane (hkl) to the wavevector of diffracted x-rays ($\vec{k}_s = \frac{2\pi}{\lambda_s}$) whereas λ_i, λ_s are the wavelengths of incident x-rays and diffracted x-rays, respectively. With the condition of elastic scattering of x-ray diffraction, the incident wavelength and diffraction wavelength are the same ($\lambda_i = \lambda_s$). So, the magnitude of the wavevectors of incident x-rays and diffracted x-rays are equivalent, $|k_i| = |k_s|$ and the difference between the wavevectors of diffracted and incident x-rays is denoted as a scattering vector ($\vec{Q}$),

$$(\vec{Q} = \Delta\vec{k} = \vec{k}_s - \vec{k}_i) \qquad \text{Eq.3.18}$$

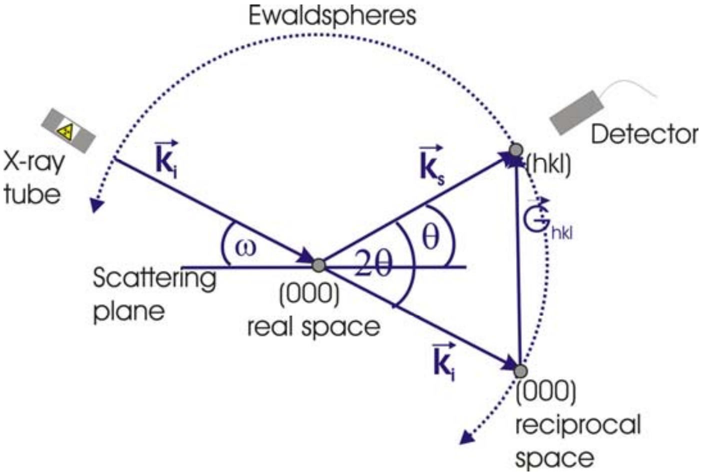

Figure 3.13 Schematic of the scattering geometry in real and reciprocal spaces

As represented in *Fig.3.13*, both wavevectors are placed on the surface of the reflection or scattering sphere known as **Ewald sphere** with a radius of $\frac{2\pi}{\lambda}$ and a real lattice at the center. The Ewald sphere is a geometric construction in reciprocal space as well as Bragg's law is a construction in a real space.

Secondly, the real scattering plane with the Miller indices (hkl) will be transferred to the reciprocal lattice vector $\vec{G}_{hkl}$ in reciprocal space as defined by:

$$\vec{G}_{hkl} = h \cdot \vec{b}_1 + k \cdot \vec{b}_2 + l \cdot \vec{b}_3 \qquad \text{Eq.3.19}$$

This reciprocal lattice is formed by the terminal points of reciprocal vectors $\vec{b}_1$, $\vec{b}_2$ and $\vec{b}_3$ which related to the primitive vectors of crystal lattice $\vec{a}_1$, $\vec{a}_2$ and $\vec{a}_3$ by:

$$\vec{b}_i = 2 \cdot \pi \cdot \frac{\vec{a}_j \times \vec{a}_k}{\vec{a}_1 \cdot \left(\vec{a}_2 \times \vec{a}_3\right)} \qquad i, j, k \qquad cycl. \qquad \text{Eq.3.20}$$

At the end of the reciprocal lattice vector $\vec{G}_{hkl}$ is a reciprocal lattice point (hkl).

When the condition of diffraction by this plane (hkl) in Bragg's law is satisfied or that lattice exists on the plane (hkl), the reciprocal lattice vector $\vec{G}_{hkl}$ and the scattering vector ($\vec{Q}$) are equal, ($\vec{Q} = \vec{G}_{hkl}$) and

$$\vec{G}_{hkl} = \Delta\vec{k} = \vec{k}_s - \vec{k}_i \qquad \text{Eq.3.21}$$

This equation is called as **Laue equation**.

Finally, the real space distance (d_{hkl}) between each plane in atomic lattice is transferred to the reciprocal space distance ($d^*_{hkl} = \frac{2\pi}{d_{hkl}}$) related to the quantity of reciprocal lattice vector $\left|\vec{G}_{hkl}\right| = q$ as:

$$d^*_{hkl} = q = \frac{2\pi}{d_{hkl}} \qquad \text{Eq.3.22}$$

At the scattering angle of θ_B, Laue equation is corresponding to Bragg's law as this relationship:

$$q = 2 \cdot \frac{2\pi}{\lambda} \cdot \sin\theta_B \qquad \text{Eq.3.23}$$

Otherwise,

$$q = 2 \cdot \left|\vec{k}\right| \cdot \sin\theta_B \qquad \text{Eq.3.24}$$

In brief, the scattering plane (hkl) is transferred to represent as a reciprocal lattice point (hkl) and the incident and diffraction angles of the scattering geometry are transferred to be the reciprocal lattice vector perpendicular to the scattering plane.

The measurements to determine the structural properties of the crystalline materials are performed by the detailed analysis of a pattern of scattered x-ray intensity from the interaction with crystal atoms. With different measuring geometries of an incident x-ray beam, sample position and a detector, the different data of crystal properties are achieved to analyze. The measuring geometries are categorized into symmetrical and asymmetrical scattering geometries that depending on the angle between the sample surface and the reflecting plane or the interested plane (φ) as shown in *Fig.3.14* with definitions of all angles. For a case of symmetrical geometry, the reflecting plane is parallel to the sample surface, $\varphi = 0$ and $\omega_- = \omega_+ = \omega = \theta$, (+: means to high incidence and –: means to the low incidence). In case of asymmetrical geometry, the reflecting plane that interested to investigate is inclined from the sample surface $\varphi \neq 0$, $\omega \neq \theta$, $\omega_+ = \theta + \varphi$ and $\omega_- = \theta - \varphi$. These are commonly used to determine lattice parameters and the crystalline quality as tilts and twists of crystal materials by selecting the reflecting plane that interested to investigate.

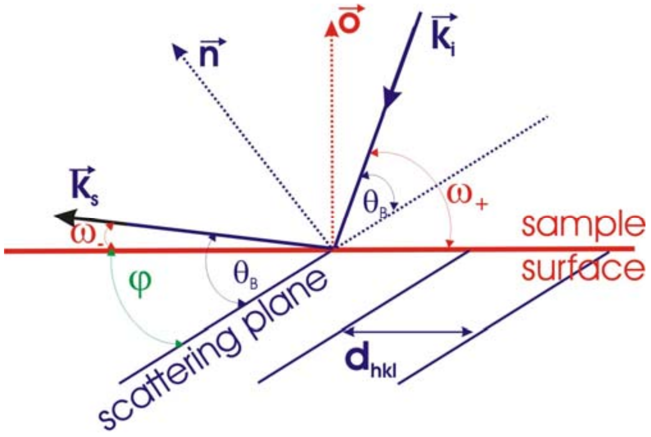

Figure 3.14 Schematic of the scattering geometry, k_i : incident wavevector, k_s: scattered wavevector, o: surface normal, n: normal on reflecting planes, θ_B: Bragg-angle, φ: angle between surface and reflecting plane after [Kros96].

To measure the intensity of symmetrical Bragg reflection ($\varphi = 0$, $\omega = \theta$), there are three main types of measuring scans as θ/2θ-scans, ω/2θ-scans and ω-scans. For θ/2θ-scans, the reflected x-rays are measured by the detector that rotating with the angel twice than that of the sample in the same direction around the diffractometer axis. As considered in reciprocal space, this motion of sample and detector relates to a change of $\vec{k}_s$ ($\vec{k}_i$ still points at the (000) of the reciprocal space) and the angle ω

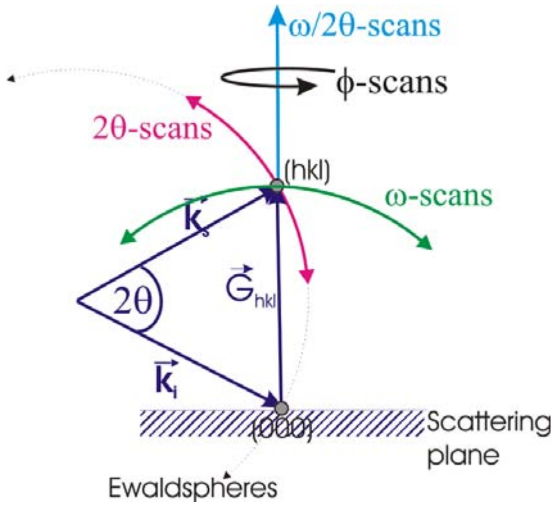

Figure 3.15 Schematic of the measuring geometry in reciprocal spaces after [Holy99, Reih08].

between the incident beam and the sample surface also changes during this motion as shown in *Fig.3.15*. In case of $\omega = \theta \pm \varphi$, the ω/2θ scan direction also runs radial from the (000) of the reciprocal space along $\vec{G}_{hkl}$. For the ω-scan, the detector is fixed in position at $2\theta_B$ and the sample is rotated involving to a change of ω along a transversal direction in reciprocal space as shown in *Fig.3.15*. By this ω-scans, information about the crystalline quality related to geometrical misorientations from the crystal growth direction is able to be detailed.

To characterize the crystalline quality of $Al_xGa_{1-x}N$, conventional high-resolution X-ray θ/2θ diffraction measurements and ω-scans around the (0002) $Al_xGa_{1-x}N$ Bragg reflection were performed to determine c-lattice parameter and tilts [A]. For a-lattice parameter and twist, grazing incidence in-plane diffraction (GIID) measurements of θ/2θ-scans and ω-scans around (10-10) $Al_xGa_{1-x}N$ reflections were applied [B]. As combine information from both measurements, Poisson's ratio of elastic properties and Vegard's law, information on composition of layers and residual in-plane strain are achieved to analyze. The full width at half maximum (FWHM) of the x-ray diffraction peaks in these measurements represents to the deviations of the lattice parameters and uniformity of the preferred orientation or misorientations in layers. Moreover, reciprocal space map (RSM) of the (0002) and (11-24) reflections [C] was performed to investigate strain state and mismatch of the $Al_xGa_{1-x}N$ layers and LT-AlN/HT-AlN superlattice buffer layers and to understand the role of LT-AlN/HT-AlN SLs to compensate the tensile strain in the subsequent $Al_xGa_{1-x}N$ layers.

A. Conventional HR-XRD of out-of-plane measurements

In this work, a Seifert XRD3003HR diffractometer was used to determine c-lattice parameter of $Al_xGa_{1-x}N$ and out-of-plane misorientations related to tilt of $Al_xGa_{1-x}N$ unit-column in layers by the θ/2θ-scans and ω-scans around the $Al_xGa_{1-x}N$ (0002) reflection, respectively as shown in *Fig.3.16*. By the measured 2θ position, d-space data or c-lattice constant were obtained by $c = 2 \cdot d_{(0002)}$. In GaN/$Al_xGa_{1-x}N$ multilayers and multi-quantumwells, the θ/2θ-scans of their (0002) reflections yield the interference fringes that interpret to their thickness and interface quality.

The Seifert XRD3003HR diffractometer consists of the x-ray tube with a copper anode emitting the $K_{\alpha 1}$ radiation of λ = 1.54056 °A and the $K_{\alpha 2}$ radiation of λ = 1.54444 °A, and the scintillation x-ray detector while it is necessary to mount a multilayer parabolic mirror or Bragg mirror and a monochromator of two Ge (220) monocrystals in front of the x-ray tube in order to achieve highly collimated parallel monochromatic X-ray beam of $\frac{\Delta\lambda}{\lambda} \approx 2.5 \times 10^{-5}$ and the fine angular resolution as

$\Delta\theta \approx 12''$ of beam divergence [Krost96, Reih08], and analyzer crystal in front of the detector as represented in *Fig.3.17*.

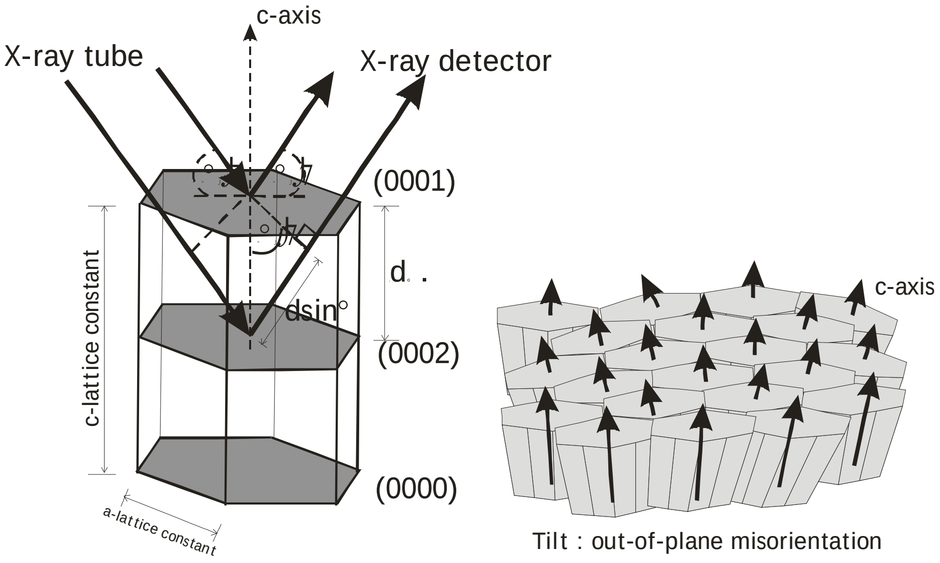

Figure 3.16 Schematic of incident and scattered x-ray beams of (0002) reflections (left) and tilts of crystals (right).

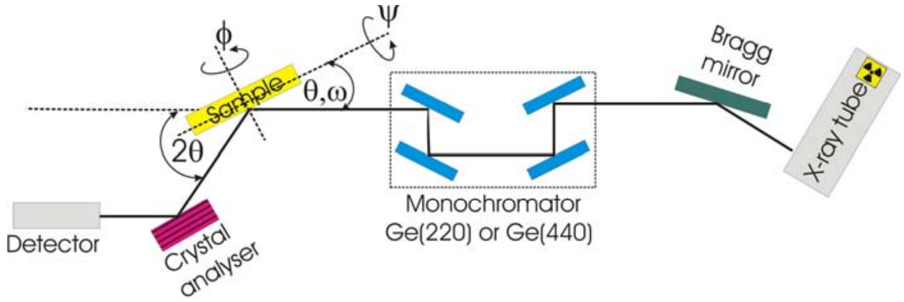

Figure 3.17 Schematic of the XRD 3003 HR diffractometer after [Kros96, Reih08].

B. Grazing incidence in-plane diffraction (GIID)

Grazing incidence in-plane diffraction (GIID) is a measuring technique of x-ray diffraction with a set-up of small grazing-incident angles for the incoming x-ray beam in order to study surfaces or thin layers of crystalline materials. With the small grazing-incident angles of the x-ray beam as shown in *Fig.3.18(above),* the penetration of x-rays is limited for a short distance in the order of nanometers. Therefore, the x-ray diffraction will be more sensitive with the surface layer or thin on-top layer. Below the critical angle (α_c) of the surface material, the x-rays are exponentially damped inside the materials. For most materials the critical angle is less than 0.3° to 0.4° [Reih08]. So, only

Bragg reflections of the surface structure are scattering sensitively. For more detailed information can be seen in [Kros96, Holy99].

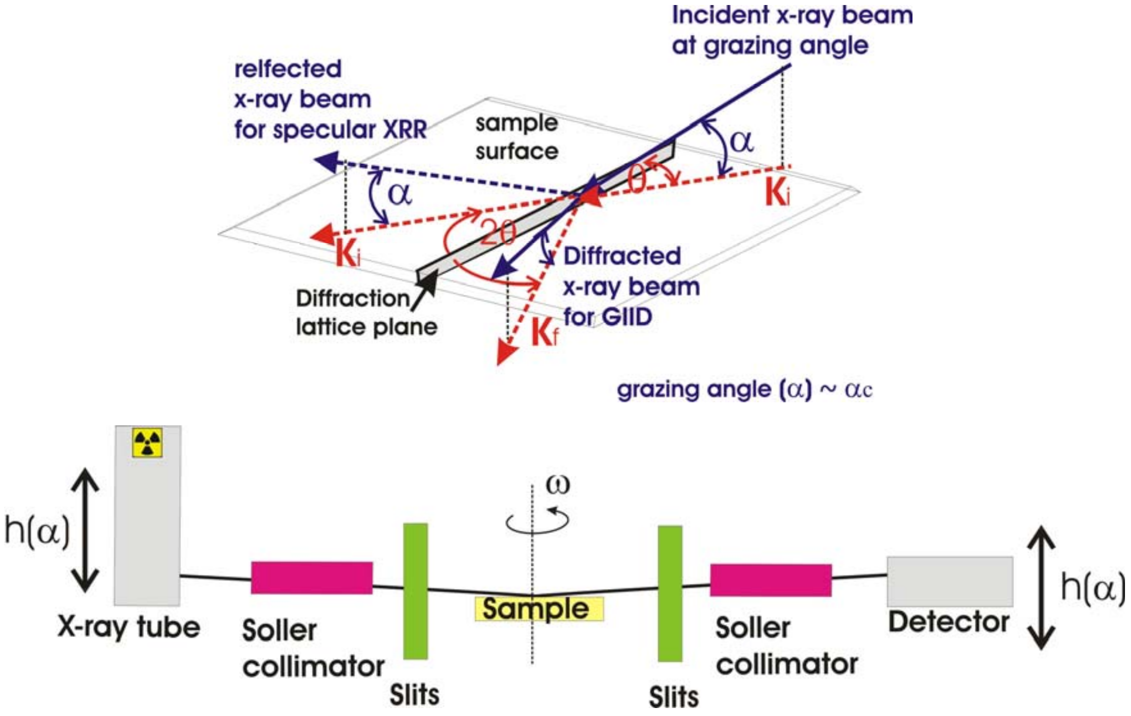

Figure 3.18 Schematic of GID geometry (above) and Seifert URD6 GID diffractometer (below) after [Krost96, Reih08].

For this work, a Seifert URD6 diffractometer is set up with a standing head on-down tube. Soller collimators made of parallel highly absorbing metal plates and slits, are placed in front of the x-ray tube and detector to parallelize the x-ray beam with a low axial divergence as depicted in *Fig.3.18(below).* As especially designed, the x-ray tube allows varying the incidence angle of X-ray (α) in order to change the penetration depth of x-rays into the epitaxial layers. The GIID measurements is applied to determine a-lattice parameter of $Al_xGa_{1-x}N$ and in-plane misorientations related to twist of $Al_xGa_{1-x}N$ unit-column in layers by the $\theta/2\theta$-scans and ω-scans around the $Al_xGa_{1-x}N$ (10-10) reflection, respectively as shown in *Fig.3.19*. With the measured 2θ position, the d-space data of is obtained and finally a-lattice constant obtained by $a = \frac{d_{(10-10)}}{\sin 60^\circ}$.

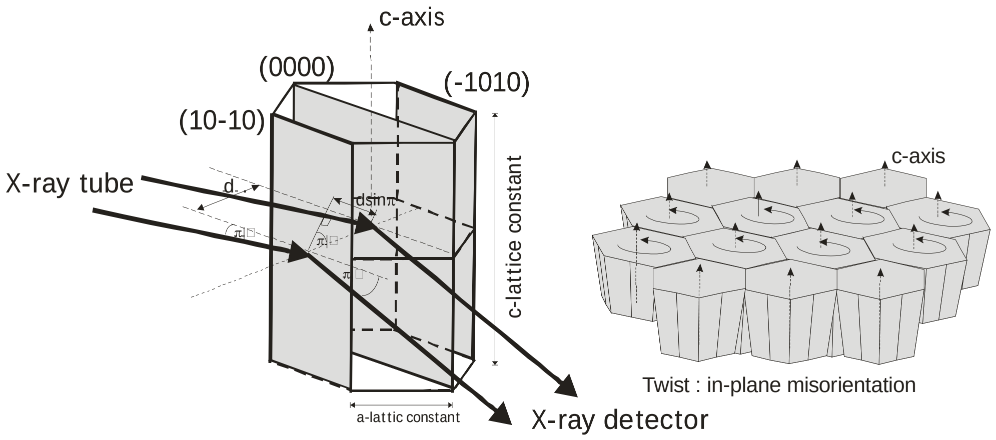

Figure 3.19 Schematic of incident and scattered x-ray beams of (10-10) reflections (left) and twists of crystals (right).

C. Reciprocal space map (RSM)

X-ray reciprocal space map (RSM) is frequently used to study and determine the structural properties of thin epitaxial films such as mismatch, strain state, relaxation, lattice constant and structural quality in particular pseudomorphic grown samples of high mismatched materials. Reciprocal space map is a two dimension measuring that combined 2θ-scans and ω-scans of HR-XRD measurements in the same one-time measurement.

Reciprocal space map is categorized into two measuring types that around symmetrical and asymmetrical reflections. Additional, shape and positions of reciprocal lattice points or the intensity contour plots are also able to reveal more information about mismatch, strain state, relaxation, mosaicity and composition etc. The horizontal and vertical positions of the lattice points yield information about the in-plane and out-of-plane lattice parameters, respectively and the arrangement of their positions involving to their lattice mismatch.

In particular, the RSM can be used to determine that the grown layers are fully strained or pseudomorphic, partially strained, or fully relaxed. The narrow width of the lattice point of the layer vertically aligned with that of the substrate means to a high quality pseudomorphic layer. The vertical elongation and interference fringes are due to the small finite layer thickness of superlattice or quantumwell structures. This contrasts to that of the fully relaxed layer representing a different in-plane lattice parameter from the substrate. For the broader lattice point means to a structurally less uniform layer or low quality with high misorientations. For more detailed information of reciprocal space map can be seen in [Krost96,Holy99,Piet04].

In this work, the RSM of the (0002) and (11-24) $Al_xGa_{1-x}N$ reflections was performed by using a Seifert URD6 diffractometer with a position sensitive detector (Braun) that consists of a Ge(220) crystal between two slits placed in front of the x- ray tube to achieve an parallel monochromatic beam for high resolution but still sufficient intensity for asymmetrical scans as shown in *Fig.3.20*. These measurements were performed to investigate the strain state and lattice parameters and mismatch of $Al_xGa_{1-x}N$ layers grown on LT-AlN/HT-AlN SL buffer layers and also the same study in GaN/$Al_xGa_{1-x}N$ multi-quantumwells.

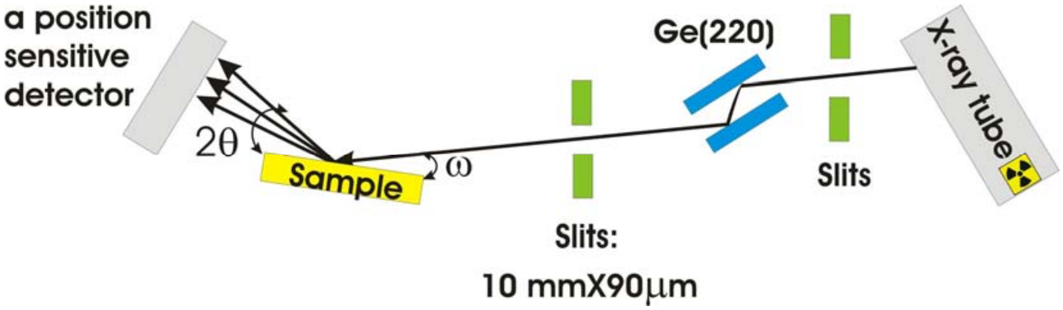

Figure 3.20 Schematic of a Seifert URD6 diffractometer with a position sensitive detector after [Reih08].

3.2.2 X-ray reflectivity (XRR)

X-ray reflectometry (XRR) is a surface-sensitive analytical technique to characterize material surfaces, thin films and multilayers for thickness determination between 2-500 nm with a high precision of about 1-3 Å and also for the determination of density and roughness. The basic principle of XRR measurement involves monitoring the intensity of the x-ray beam reflected by a flat-surface sample at grazing incident angles in the specular reflection where the condition of the reflected angle equal to the incident angle or the incident angle is always half of the angle of diffraction as depicted in *Fig.3.18(above).*

In multilayers, the reflections of the x-ray beam at the surface and interfaces depend on the different refractive indexes of the different layers as related to different electron densities. When the incident angles of the x-ray beam (θ) is below than a critical angle ($\theta \approx 0.3° - 0.4°$) for most layer materials or $\theta < \theta_c$, the total external reflections will occur. At above θ_c or $\theta > \theta_c$, the reflections from the different interfaces will interfere and this will represent the interference fringes. The period of the interference fringes and the fall in the intensity are related to the thickness and the roughness of the layers. Roughness will lead to diffuse scattering and result in a less intensity in the specularly reflected beam. When the interface is perfectly sharp and smooth, the reflected intensity will agree with a prediction by Fresnel law of reflectivity. The typical range of incident angle, θ, for these measurements is between 0 and 5.

For this work, XRR-measurements with a URD6 diffractometer with a rotating anode TXS x-ray tube of Bruker AXS are employed to investigate the interface quality and approximated thickness of GaN/AlGaN multi quantum wells. For more detailed information of X-ray reflectivity can be found in [Krost96, Holy99].

3.3 Microscopy for surface morphology and cross-sectional images

Nomarski microscopy is basically used to investigate surface morphology of samples. For more details in microstructure, roughness and dislocation propagation etc., scanning electron microscopy, atomic force microscopy and transmission electron microscopy are applied which are described conceptually here.

3.3.1 Nomarski microscopy

Differential interference contrast microscopy (DIC) also known as Nomarski microscopy or Nomarski interference contrast (NIC) is an optical contrast microscopy method. In this work, reflected Nomarski microscopy is employed to inspect the layer morphology, observe and locate cracks and defects on the surfaces immediately after growth. DIC works on the principle of interferometry of two polarized light beams which are laterally separated by a DIC prism and subsequently reflected from two different positions of the sample surface with different thickness to create bright-contrast areas of information about the surface morphology. The rays will experience different optical path lengths where the sample areas differ in thickness. This causes a change in phase of one ray related to the other. After reflection the two light rays are recombined in the same DIC prism leading to an interference pattern which is modulated by the surface topology. The schematic of DIC principle are shown in *Fig.3.21*. More detailed information of Nomarski DIC can be seen in reference [Murp01, Microweb].

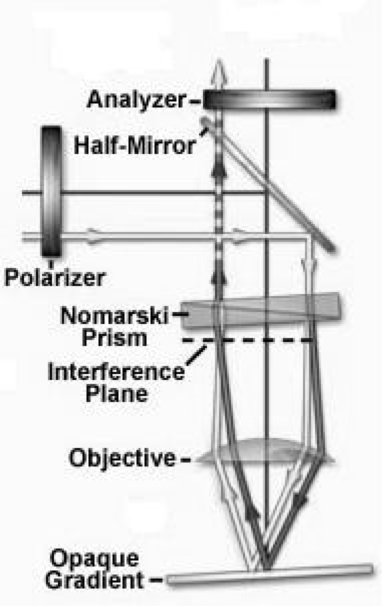

Figure 3.21 Schematic of reflected DIC microscopy [Microweb]

3.3.2 Field emission scanning electron microscopy

In a typical scanning electron microscopy (SEM) system, an image of a sample surface is formed from secondary electrons by bombarding the scanned sample with primary electrons emitted from a field emitter. By applying a voltage the emitted electrons pass though a set of electromagnetic lenses to the sample in a vacuum environment as shown in *Fig3.22*. The electron beam is focused by a series of electromagnetic lenses or condenser lenses in the electron column to a spot of 0.4 - 5 nm in diameter. By scanning coils in the final lens of the electron column, the beam scans in a raster pattern over a typically rectangular area of the sample surface.

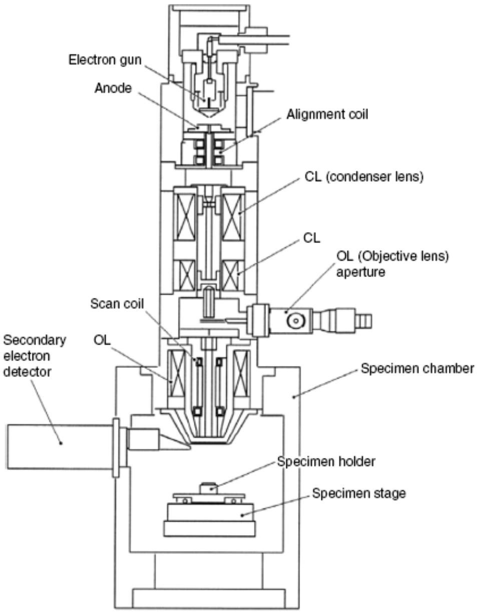

Figure 3.22 Schematic diagram of SEM [Zhou07].

When the primary electron beam interacts with atoms at the sample surface, the electrons loose energy by different processes as presented in *Fig.3.23*. The secondary electrons are the most common signal used to investigate the surface morphology.

Field-emission scanning electron microscopy (FESEM) provides enhanced resolution, and a clearer, less electrostatically distorted image as compared to conventional emitters, in particular for nonconductive samples of insulating materials. More detailed information can be seen in reference [Zhou07].

For this work a Hitachi S4800 FE-SEM is used to investigate the surface morphology and growth-step mechanism of AlN seed and buffer layers and $Al_xGa_{1-x}N$ layers and to approximate layer thickness and quality by cross-sectional images.

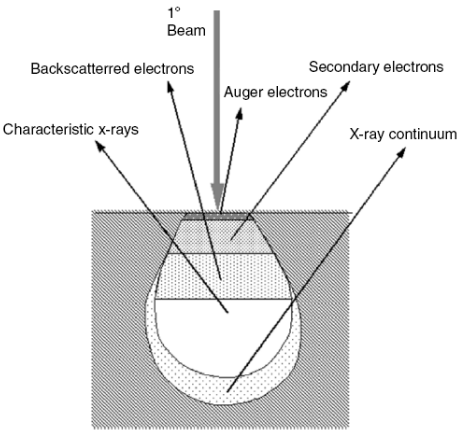

Figure 3.23 Illustration of several signals generated by the electron beam–specimen interaction in SEM [Zhou07]

3.3.3 Transmission electron microscopy

Transmission electron microscopy (TEM) is a method to form an image from the interaction of electrons transmitted through an ultra thin specimen (<1μm) [Willi09] with a significantly high resolution and a high magnification to examine fine detail and mainly to show microstructures inside the specimen. TEM is equipped with a tungsten filament or a lanthanum hexaboride (LaB_6) source for an emission source to emit electrons into the vacuum by connecting with a high voltage source (typically ~100-300 kV). The image is magnified and focused by several convex lenses of electromagnetic lenses which produced by electrons moving in a controlling magnetic field. The basic optical configuration of TEM consists of three main parts as the condenser lenses, the objective lenses, and the projector lenses as shown in *Fig.3.24*.

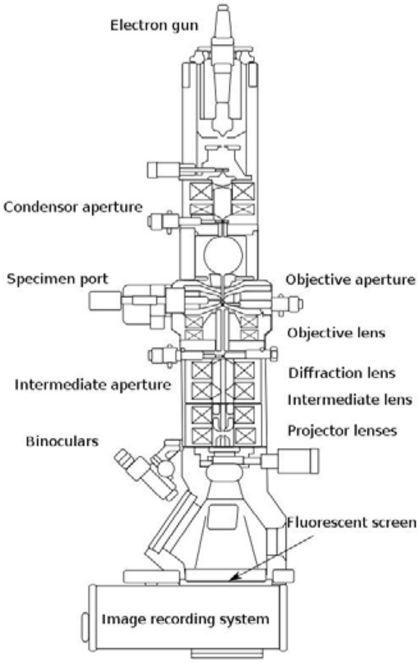

Figure 3.24 Schematic simple diagram of TEM [Wikiweb].

Based on the density of transmitted electrons and absorbed electrons, a projection image of the specimen is developed onto the imaging device such as a fluorescent screen or a CCD camera to produce bright contrast or gray-shades images. The density of electrons passed through the sample mainly depends on the composition or the local electron density of different material regions for example the regions of heavier metals will deflect electrons more. For diffraction contrast in the case of a crystalline sample, the electron beam undergoes Bragg scattering and this disperses electrons into discrete locations in the back focal plane. It can be applied to identify lattice defects in crystals, to determine the position of defects and the type of defect present by selecting the orientation of the sample. More detailed information can be found in reference [Fult08,Willi09].

3.3.4 Atomic force microscopy

Dominantly atomic force microscopy (AFM) is applied to analyze the surface morphology at the nanoscale with a high-resolution three-dimensional image of a scanning area typically around 1×1 to 150×150 μm^2. For this work, a Veeco Dimension 3000 is used to investigate the surface morphology of $Al_xGa_{1-x}N$ layers.

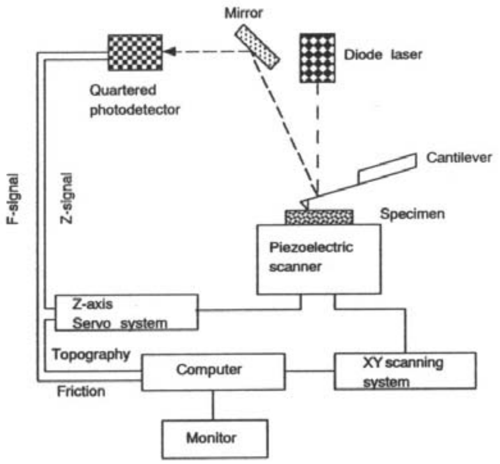

Figure 3.25 Schematic diagram of AFM [Khul08]

An image of the surface morphology is formed when the microscopic tip is dragged over the surface of the sample and forces between the tip and the sample lead to a deflection of the cantilever according to Hooke's law. Typically, the deflection is monitored by using a laser beam reflected off the back of the cantilever into a position sensitive detector or an array of photodiodes as depicted in *Fig.3.25*. The AFM is used in the operating modes of contact mode or tapping mode, which are conducted in air or liquid environments. To study the surface morphology, the samples are investigated using Tapping Mode AFM which consists of oscillating the cantilever nearly its resonance frequency of ~300 kHz and lightly tapping on the sample surface during the scanning. More details about AFM can be found in reference [Khul08, Kitt05]. The changes in the cantilever deflection or oscillation amplitude in the z direction are determined by differences in output voltages of the photodetector. The scanning motion is conducted by a piezoelectric tube scanner which scans the tip in a raster pattern onto the sample. A feedback loop maintains a constant oscillation amplitude by moving the scanner vertically at every x,y data point. By recording this movement continuously, a three dimensional map of the surface morphology is produced from which the root-mean-square roughness (rms) can be calculated.

3.4 Spectroscopy for optical properties

The optical properties were characterized by cathodoluminescence, photoluminescence and electroluminescence measurements which principles will be briefly explained in the next sections.

3.4.1 Cathodoluminescence spectroscopy

In this work, a JEOL JSM6400 SEM equipped with a LaB electron gun is applied for the cathodoluminescence measurements to investigate the optical quality of $Al_xGa_{1-x}N$ epilayers with and without doping and examine the efficiency of light emission or radiation recombination of electrons and holes in $Al_xGa_{1-x}N$/GaN multi quantum wells.

As mentioned before in section 3.3.2, cathodoluminescence is observed in both scanning electron microscopy and transmission electron microscopy when an electron beam generates carriers, e. g., a semiconductor, causing the material to emit light. The cathodoluminescence is collected by an optical system, in our case an elliptical mirror. The luminescence is transferred out of the microscope by a fiber optic and separated by a monochromator and then detected with a photomultiplier tube. By scanning the electron microscope's beam in an X-Y pattern and measuring the emitted luminescence at each point, a map of the optical measurements of the sample can be achieved.

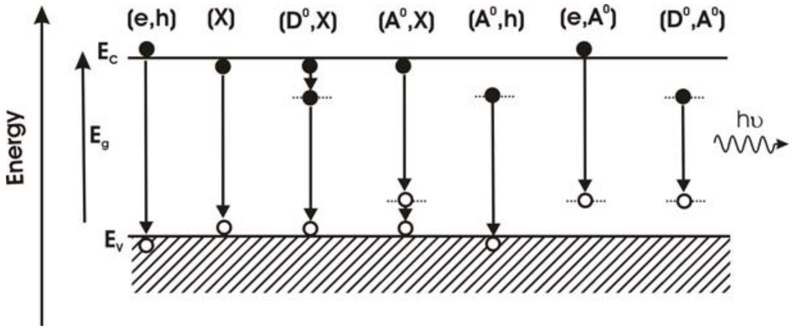

Figure 3.26 Radiative transitions in semiconductors after [Schö07]

Cathodoluminescence is produced from the efficient bombardment of an electron beam onto a semiconductor. Their electrons will be promoted to a higher level, e.g. from the valence band to the conduction band and leave holes behind. When an electron and a hole recombine, there are several possible ways to generate luminescence. Once the electrons are excited, they can fall directly to the hole and do not encounter any traps for the case of low trap or defect density known as intrinsic band to band (e,h) and free exciton (X) transitions. Otherwise, the electrons encounter the traps emitting other lower-energy luminescence. There are different types of optical transitions e.g. donor to acceptor transition (D^0,A^0), ED of the electron to the donor impurity, EA of the hole to the acceptor impurity, and (D^0,X), (A^0,X) of bound excitons to donor and accepter etc [Klin07,Yu05]. as depicted in *Fig.3.26*. The energy and FWHM of the luminescence depends on the kind of optical transition that corresponds with the quality of the materials and their optical properties. In general, the intensity of the cathodoluminescence is a function of the density of traps with respect to the purity and defect state of the semiconductor material. For more detailed information of the cathodoluminescence measurements refer to [Yaco90].

3.4.2 Photoluminescence spectroscopy

Photoluminescence (PL) spectroscopy is an important technique to measure the electronic structure, purity and crystalline quality of semiconductor materials. Photoluminescence spectroscopy is analogous to cathodoluminescence microscopy where atoms of a sample material are excited to a higher energy state and then return to a lower energy state or an equilibrium state by emitting that excess energy through a photon. The difference of these methods is that photoluminescence is excited by the impingement of a high-energy light beam typically with energies slightly higher than the luminescence energies observed in contrast to cathodoluminescence where the excitation energy is orders of magnitude higher than the luminescence energy. The energy of the emitted light relates to the difference in energy levels between the two electron states involved in the transition between the excited state and the equilibrium state. The return to equilibrium, also known as "recombination," can involve both radiative and nonradiative processes. The quantity or intensity of the emitted light is related to the relative contribution of the radiative process. Radiative transitions in semiconductors also involve localized defect levels with respect to nonradiative processes. The photoluminescence energy associated with these levels can be used to identify specific defects, and the amount of photoluminescence can be used to determine their density. Thus, material quality can be measured by quantifying the amount of radiative recombination. However the amount of photoluminescence and its dependence on the level of photo-excitation and temperature are directly related to the dominant recombination process because various excitation wavelengths allow for varying penetration depths into the material, and thus, varying levels of volume excitation. For more information of the photoluminescence measurements refer to [Ivch05].

In this work, a Helium-Cadmium laser of 25 mW generates light of which the UV line at 325.0 nm is selected by an interference filter. In the optical setup this light is focused onto a sample. After that, photoluminescence from the sample is passed through a grating monochromator and detected by a charge coupled device (CCD) camera. By He-Cd laser, radiation recombination of electrons and holes in $Al_{0.1}Ga_{0.9}N/GaN$ multi-quantum-well structure is also investigated by PL measurements. Additionally, a closed-cycle helium cryostat can be used to measure temperature dependent in the range from 10 to 300 K.

3.4.3 Electroluminescence spectroscopy

Electroluminescence (EL) is the generation of light by the recombination of electrically injected electrons and holes. The luminescence can be emitted by the passage of an electric current or the injection of charge through p-n junction materials and light emitting devices etc. In semiconductor electroluminescent devices such as light emitting diodes (LEDs), proper metallic contacts with the device-structure are required to provide the flow of electrons or holes. When applying a forward voltage to a p–n junction, formed by doping the materials with acceptors and donors, respectively, electrons flow through the materials from the n-type region into the p-type region and vice versa for holes. The electrons and the holes recombine radiatively. The emitted electroluminescence spectra can be detected by an optical detector to obtain an image of the distribution of radiative recombination for measuring the structural, optical and electrical characteristics of the devices. For more detailed information on electroluminescence spectroscopy refer to [Kita93]. In this work, p-type contacts of AlGaN-based LEDs are formed by oxidized Ni/Au contacts and contacted by bonding a wire to them; n-type contacts are formed using Al.

3.5 Electrical measurements

In this work the electrical properties of AlGaN-based LED samples were characterized by current-voltage and capacitance-voltage measurements. Their principles will be briefly explained here.

3.5.1 Current voltage characteristics

A current voltage characteristic or I–V curve of a PN junction-based semiconductor diode represents a relationship between the DC electric current through the diode and the corresponding DC voltage across its terminals. These I-V curves are used to determine basic parameters of the device and to model its behavior in an electrical circuit, referring to the standard symbols for current and voltage. According to Ohm's Law, the simplest I–V characteristic of a resistor exhibits a linear relationship between the applied voltage and the resulting electrical current as referring to a resistivity, except in this case environmental factors such as temperature or material characteristics of the resistor producing a non-

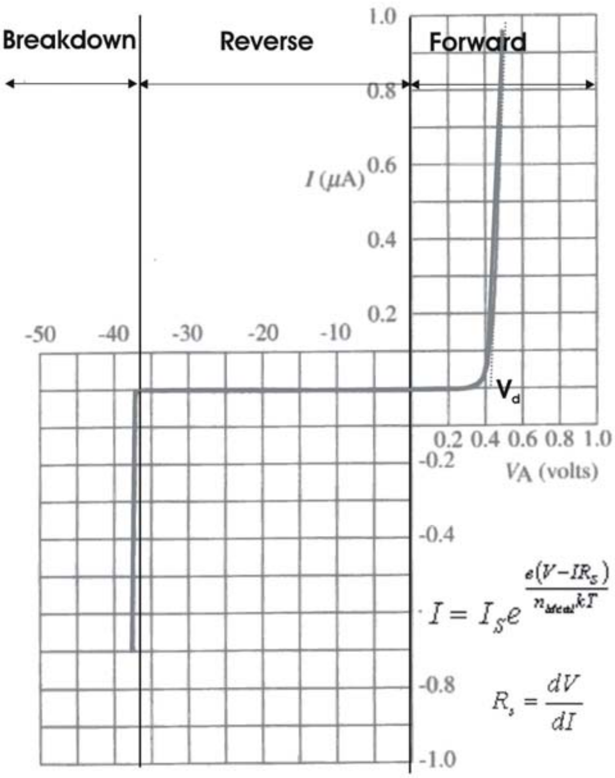

Figure 3.27 Measured I-V characteristic of Si pn junction diode at room temperature after [Pier96]

linear curve.

A diode's I–V characteristic can be classified into four operation regions as reverse breakdown, reverse, forward and forward voltage drop as shown in *Fig.3.27*. The region of reverse breakdown beyond the peak inverse voltage (PIV), the device is usually damaged permanently at very large reverse applied voltage. When the potential difference is increased above an arbitrarily defined "cut-in voltage" or "on-voltage" or "diode forward voltage drop (V_d)" in the forward region, the diode current becomes appreciable as a exponential function and the diode presents a very low resistance. In brief, to turn on the diode with a forward bias, the applied voltage developed across it is about its characterized voltage drop and then an external current can be passed through the diode. This value is different for other diode types depending on the bandgap [Schub03] of materials for example as low as 0.2 V for Schottky diodes, 0.6V to 0.7 V for a normal silicon diode, 1 V to 1.5 V for power diodes, 1.4 V for red-LEDs and more for blue LEDs where it is up to 4.0V. For more detailed information of the current–voltage characteristics refer to [Pier96, Schub03]. In this work, AlGaN-based LEDs are also characterized their electrical properties such as turn-on voltage by the I-V measurements.

3.5.2 Capacitance voltage measurements

Capacitance voltage measurement is a technique used to characterize electrical properties of semiconductor materials and devices. As applied to the epitaxially grown semiconductor materials, the C-V meter equipped with a mercury probe can measure the epitaxial layer as soon as it is unloaded from the reactor. The advantage of this technique is the ability of the mercury probe to easily form, non-destructive, contacts to planar materials without performing a time consuming metallization and photolithographic processing.

Two-dot concentric mercury probe formed a metal-semiconductor junction, a **Schottky barrier**, of well-defined area and backside contact that could be measured as easily as a conventional metallic contact to create a depletion region and may contain ionized donors and electrically active defects or traps. The depletion region with its ionized charges inside behaves like a parallel plate capacitor filled with a dielectric and varying plate distance: By varying the voltage applied to the junction, the depletion width possibly is varied. The dependence of the depletion width upon the applied voltage provides information on the semiconductor's internal characteristics, such as its doping profile and electrically active defect densities. The measurements generally are done at AC voltage.

The simplest application of C-V measurements is to monitor the type and concentration of dopants in the semiconductor materials. The capacitance is obtained by the change in charge with a corresponding change in applied voltage as calculated according to this expression:

$$C = \frac{dQ}{dV} \qquad \text{Eq.3.25}$$

In principle, when applying small voltage variations, charges are only added and removed at the edge of the depletion region analogous to the parallel plate capacitor. The junction capacitance in the depletion region across the PN junction simply depends on the dielectric constant, the area and the depletion layer width as calculated using this expression:

$$C_j = \frac{\varepsilon_S}{W} = \sqrt{\frac{q\varepsilon_S}{2(\phi_i - V_a)} \frac{N_a N_d}{N_a + N_d}} \qquad \text{Eq.3.26}$$

where W is the depletion layer width. C_j = the capacitance per unit area (F/m^2), q is the fundamental charge constant ($q = 1.6 \times 10^{-19}$ coulombs), ε_s is the electric semiconductor permittivity (F/m), ε is dielectric constant, ε_0 is the electric permittivity of free space (F/m), $\varepsilon_s = \varepsilon \cdot \varepsilon_0 = 8.9 \times 8.85 \times 10^{-12}$ F/m for GaN [Mork08],
$\varepsilon_s = \varepsilon \cdot \varepsilon_0 = 8.5 \times 8.85 \times 10^{-12}$ F/m for AlN [Mork08], V_a = the applied voltage (V), N_d = the doner density (per m^3), N_a = the acceptor density (per m^3), ϕ_i = built-in potential (V).

From Eq.5.10.2, the new expression of the capacitance squared, $\frac{1}{C^2}$, is obtained as

$$\frac{1}{C_j^2} = \frac{2}{q\varepsilon_S} \frac{N_a + N_d}{N_a N_d} (\phi_i - V_a) \qquad \text{Eq.3.27}$$

Thus, a plot of $\frac{1}{C_j^2}$ versus V_a yields a straight line or a linear dependence.

By the slope of the plot of $\frac{d\left(1/C_j^2 \right)}{dV_a}$ the carrier concentration profile is obtained for example the electron concentration or the donor density as N_d of n-type conductivity sample with positive applied voltage as followed this expression:

$$N_d = -\frac{2}{q\varepsilon_s}\left[\frac{1}{\frac{d\left(1/C_j^2\right)}{dV_a}}\right], \quad N_a >> N_d \qquad \text{Eq.3.28}$$

For N_a of p-type conductivity samples, the same measurements with negative applied voltage are performed.

Besides the C-V measurements provide the type and concentration, the corrresponding depth can be obtained at each voltage yielding a doping profile. In addition, the built-in voltage can be achieved at the intersection of the $\frac{1}{C_j^2}$ plotting at the horizontal axis. While the depth equals the depletion layer width which is obtained from this expression:

$$W = \frac{\varepsilon_S}{C_j} \qquad \text{Eq.3.29}$$

More information on C–V measurements can be found, e. g. in [Sze07, Cole08, Rose02, Pier96].

In this work C-V measurements are performed on samples of Si-doped AlGaN, Mg-doped AlGaN, Mg-doped AlGaN, and Mg-doped GaN/AlGaN multilayers to determine the electron or hole concentrations in the layers. This is performed by using a C-V meter equipped with a LEI 2017B mercury probe by evacuating the interface area of the mercury and the sample surface. This instrument monitors based on an equivalent circuit of the capacitance bridge by switching to a condenser for the capacity C_p by a parallel resistor R_p or to a condenser for the capacity C_s by a serial resistor R_s. The parallel resistivity refers to possible leak currents and the serial resistivity represents the conductive properties of the samples and contacts. In the ideal case, R_s is low ($R_S \rightarrow 0$) and R_p is very large ($R_S \rightarrow \infty$) [Schub03, Oley06].

Chapter 4
AlGaN growth

The first common requirement to develop electronic devices is a high-quality semiconductor material. Analogously, developing AlGaN-based LEDs on Si substrate firstly requires a high-quality AlGaN material with a low dislocation density and crack-free layers on the Si substrate. Due to their large differences in lattice mismatch and thermal expansion of the AlGaN layers and the Si substrate, efficient buffer layers reducing dislocations and compensating a thermally induced tensile strain are necessarily required to insert between them in order to improve the AlGaN quality. However, the first layer deposited on the Si substrate of a seeding or nucleation layer is also an important factor enabling to improve the AlGaN quality. Therefore, impacts of growth parameters of the AlN seeding layer on the $Al_{0.1}Ga_{0.9}N$ quality were investigated first. Next, growth parameters of LT-AlN/HT-AlN superlattice buffer layers were optimized. Their impacts on the $Al_{0.1}Ga_{0.9}N$ quality are presented and discussed in this chapter. Moreover, the quality of $Al_xGa_{1-x}N$ with $0.05 \leq x \leq 0.65$ grown on these optimized LT-AlN/HT-AlN SLs are revealed in the last section of this chapter.

4.1. Optimization of AlN seeding layer for high-quality $Al_xGa_{1-x}N$ growth

Due to the requirement of a seed or nucleation layer for MOVPE growth on heterosubstrates, the seed layer was optimized to enhance the buffer-layer quality. The efficient seed layer plays a role to reduce a misfit between a foreign substrate and an epilayer and to arrange for the next deposition with a good quality and uniform orientation [Bour98, Cont08, Dadg07, Dimi05, Jami05, Liu03, Ragh04].

With a systematic study of the impact of growth parameters as growth temperature, pressure, time and the V/III ratio of AlN-seed layer on the crystalline quality of $Al_{0.1}Ga_{0.9}N$/AlN/Si(111), it could be observed that the $Al_{0.1}Ga_{0.9}N$ quality strongly depends on the growth parameters of the AlN-seed layer. The on-top $Al_{0.1}Ga_{0.9}N$ layers were grown at 1145°C, 100 mbar, TMAl flow rate of 8.66 μmol/min, TMGa flow rate of 48.46 μmol/min, NH_3 flow rate of 31.25 mmol/min and V/III ratio of ~ 550 as standard growth parameters of ~250-nm-thick $Al_{0.1}Ga_{0.9}N$ for all samples. For standard reference growth parameters of the AlN-seed layer, AlN was grown at 1200°C, 100 mbar, for 8 minutes leading to a nominal thickness of ~12 nm with a V/III ratio of ~2600. To prevent the formation of Si_xN_y and amorphous growth of the seed layer, the pre-deposited layer was applied by the pre-flow of TMAl into the reactor before flowing NH_3 [Chen01, Dadg03a, Kwon02].

There are 4 series of $Al_{0.1}Ga_{0.9}N$/AlN samples with growth-parameter variations of the AlN layer i.e. the first series of growth temperature varied from 700 to 1200°C, the second series of growth time from 1 to 20 minutes related to the nominal thickness from ~1.5 to 30 nm, the third series of growth pressure from 70 to 200 mbar, and the last series of V/III ratio from ~1300 to ~6400 as summarized in *Table 4.1*. Schematic of $Al_{0.1}Ga_{0.9}N$/AlN samples with growth-parameter variations is shown in *Fig.4.1.1*.

Subsequently, the crystalline quality of $Al_{0.1}Ga_{0.9}N$ was characterized by HR-XRD measurements.

Table 4.1 variations of growth parameters of AlN seed layer in each series

Series	**Varied parameters of AlN seed layer**	**range**
1	Temperature (°C)	700-1200
2	Thickness (nm)	~1.5 - 30
3	Pressure (mbar)	70-200
4	V/III ratio	1300-6400

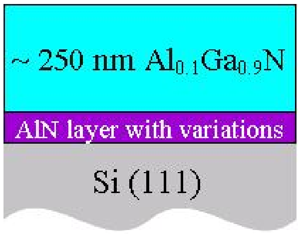

Figure 4.1.1 schematic of $Al_{0.1}Ga_{0.9}N$ on AlN seed layer with variations of growth parameters

4.1.1. The impact of growth temperature of the AlN-seed layer

In the first series, the growth temperature of the AlN-seed layer was varied from 700°C to 1200°C. In XRD measurements, the crystalline quality of the $Al_{0.1}Ga_{0.9}N$, represented by the FWHMs of θ/2θ-scans and ω-scans of the $Al_{0.1}Ga_{0.9}N$ (0002) and (10-10) reflections, was investigated. With an increasing growth temperature, the ω-FWHMs of the $Al_{0.1}Ga_{0.9}N$ (0002) reflections decrease from 2480 to 1220 arcsec and for the (10-10) reflections from 5110 to 2480 arcsec and the in-plane residual strain in the $Al_{0.1}Ga_{0.9}N$ layer also decreases from 0.17% to 0.10% as shown in *Fig.4.1.2*. It is indicated that by increasing the growth temperature, the $Al_{0.1}Ga_{0.9}N$ quality is continuously improved with lower ω-FWHMs of both reflections and lower residual strain. However, the temperature limitation of this machine is 1200°C for preventing the damage of quartz parts. So that, the growth temperature at 1200°C is the best growth temperature of the AlN layer for the high-quality $Al_{0.1}Ga_{0.9}N$ growth achievable on this system.

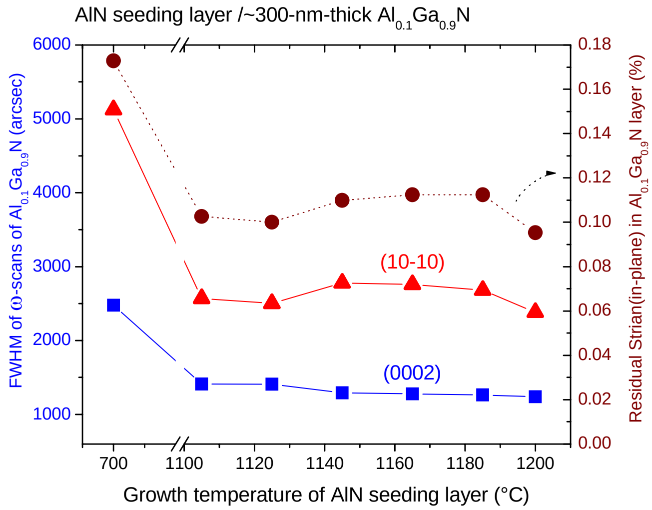

Figure 4.1.2 ω-FWHM of the $Al_{0.1}Ga_{0.9}N$ (0002) and (10-10) reflections and the in-plane residual strain in $Al_{0.1}Ga_{0.9}N$ layer as a function of growth temperature.

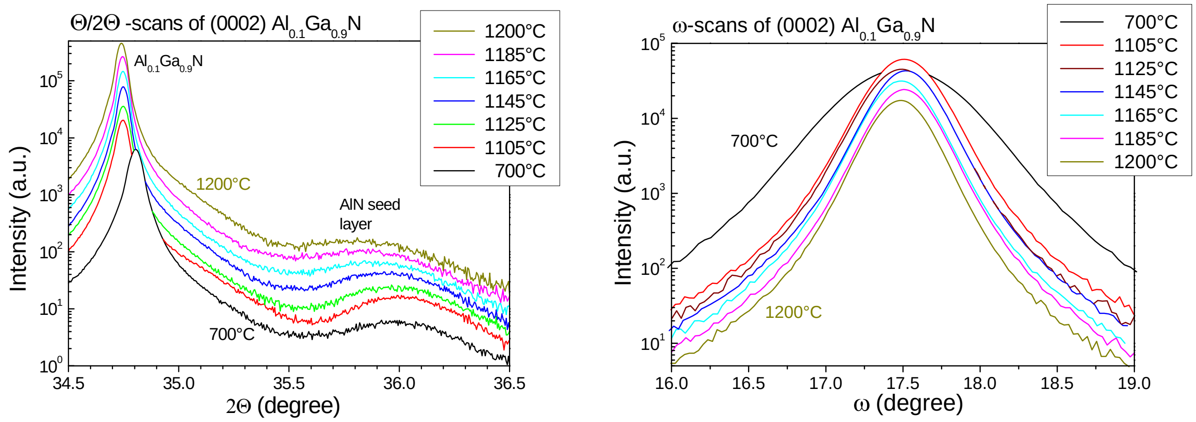

Figure 4.1.3 XRD θ/2θ-scans and ω-scans of the $Al_{0.1}Ga_{0.9}N$ (0002) reflections with various growth temperatures of the AlN-seed layer

In XRD θ/2θ-scans of the (0002) reflections, it can be observed that with an increasing growth temperature from 1105°C to 1200°C, the 2θ peaks of ~36.0° of AlN-seed layer are less distinguished and lower intensity as shown in *Fig.4.1.3 (left)*. This can be simply interpreted that AlN-seed layer grown at higher temperature in this range has a lower thickness or lower growth rate. The 2θ peak of LT-AlN at 700°C, is less pronounced than others but still more pronounced than that of 1200°C. It is possible that the thickness or growth rate of LT-AlN at 700°C is higher than that of HT-AlN at 1200°C. It also means to the AlN thickness of each sample in this series varied by the varied growth temperatures. So that, to precisely consider the optimized growth temperature of the AlN layer, it is necessary to take account of an identical thickness. In *Fig.4.1.3 (right)* of XRD ω-scans, it can be seen that $Al_{0.1}Ga_{0.9}N$ on the LT-AlN-seed layer is the worst crystalline quality with the broadest peak. As shown before in *Fig.4.1.2*, the crystalline quality of $Al_{0.1}Ga_{0.9}N$ on HT-AlN was better than on LT-AlN.

In AFM measurements, the surface morphology of the $Al_{0.1}Ga_{0.9}N$ on HT-AlN exhibits a very smoother surface, but higher pit density and bigger pit size than that of $Al_{0.1}Ga_{0.9}N$ on LT-AlN with a high roughness of 2.12 nm rms as shown in *Fig.4.1.4*. A reliable measurement of rms roughness of $Al_{0.1}Ga_{0.9}N$ on HT-AlN for this scan-area size can not be obtained due to a high disturbance by the pit features.

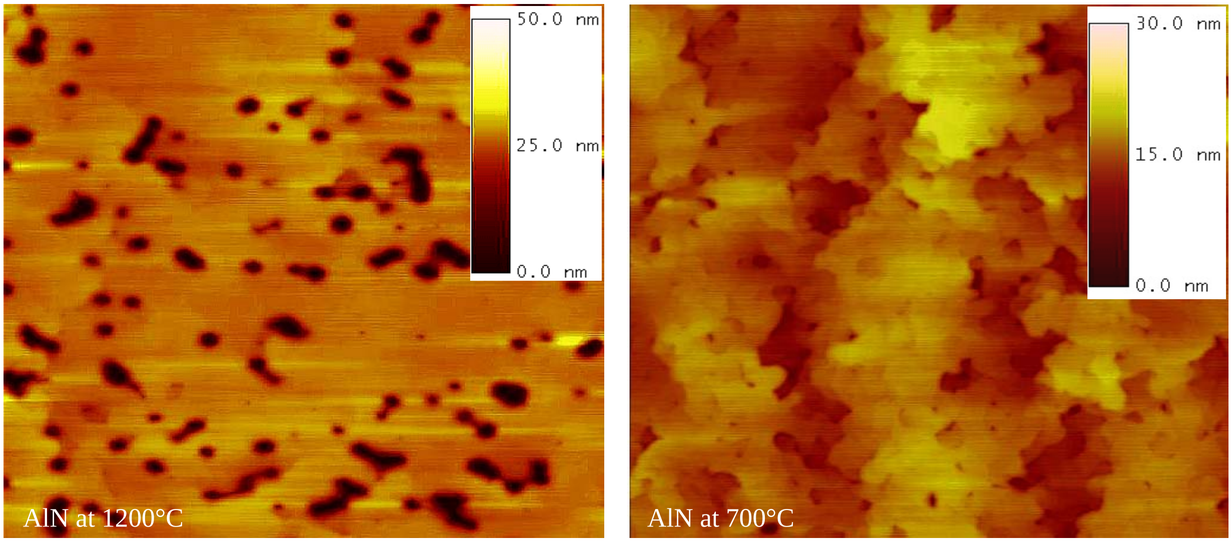

Figure 4.1.4 3×3 μm^2 AFM images show the different surface morphology of $Al_{0.1}Ga_{0.9}N$ on HT-AlN at 1200°C (left) with smoother surface but very higher big-pit density than that grown at 700°C (right)

In order to better understand their structures, two additional samples of thick HT-AlN and thick LT-AlN were grown for 3 hours. The XRD θ/2θ-scans of the (0002) reflections of the thick LT-AlN sample obviously pronounce the (10-10) and (10-11) reflections besides the 2θ peak of the (0002) reflections as shown in *Fig.4.1.5*. But there is only the 2θ peak of the (0002) reflection of the thick HT-AlN sample. This can be implied that the thick LT-AlN layer crystallizes with polycrystalline contributions. Additionally, their surface morphologies are revealed by FE-SEM images i.e. the HT-AlN surface morphology with a high density of pit defects and crystal platelets in different orientations of the LT-AlN as shown in *Fig.4.1.6*.

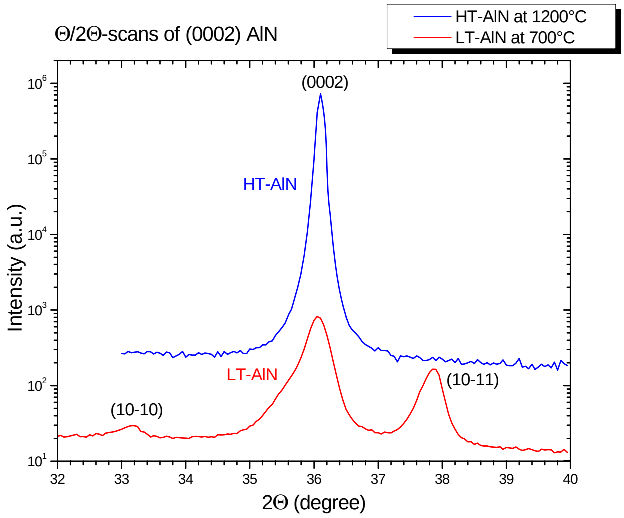

Figure 4.1.5 XRD θ/2θ–scans of the (0002) reflections of ~270-nm-thick HT-AlN at 1200°C and ~740-nm-thick LT-AlN at 700°C

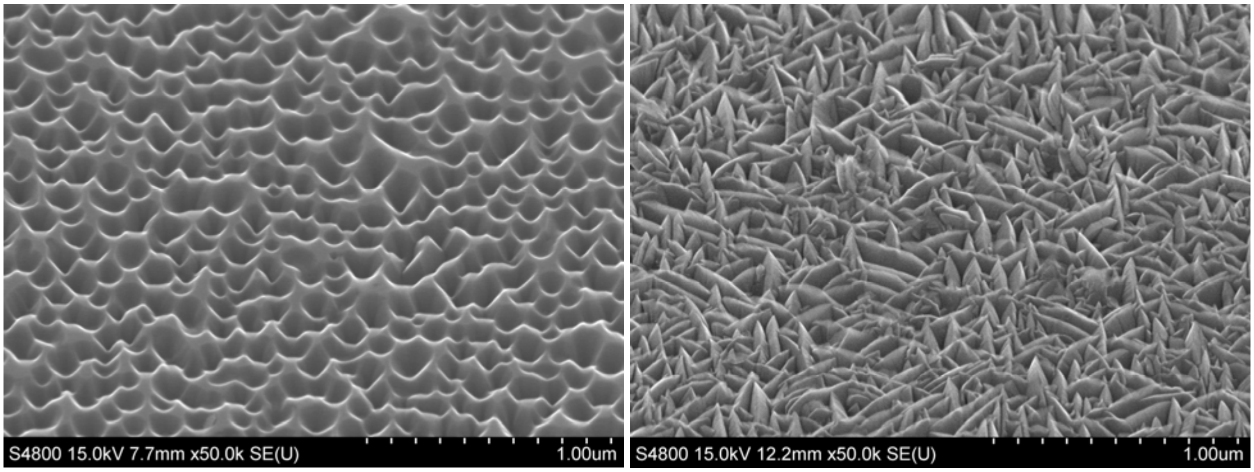

Figure 4.1.6 FE-REM images showing different surface morphologies of HT-AlN (left) and LT-AlN (right)

Furthermore in *Fig.4.1.7* cross-sectional TEM images exhibit the microstructure of HT-AlN with a high crystalline quality of uniform orientation and good arrangement. The big-size pits on the surface are ~120 nm in diameter and the depth ~100 nm. There are lots of pits on the surface. Some pit positions on the surface relate to threading dislocations originated from defects in the first HT-AlN layer above the Si substrate. On the other hand, lots of big-size pits are probably originated to relief grain-coalescence stresses in the high-quality layer [Ragh04, Ragh05, Reen08]. As shown in *Fig.4.1.8* of cross-sectional TEM images, LT-AlN consists of small crystal platelets with different orientations. The crystal platelets have a length of ~160 nm and a width of ~40 nm. There are lots of voids between the platelets as well as porous features. Then LT-AlN is grown with a lower stress or a higher relaxation than HT-AlN. In addition, their thicknesses are measured to yield the growth rates of HT-AlN of ~1.44 nm/min and LT-AlN of ~4.1 nm/min and also corresponded to the results of an optical interference technique (~1.5 and ~3.58 nm/min of HT-AlN and LT-AlN respectively).

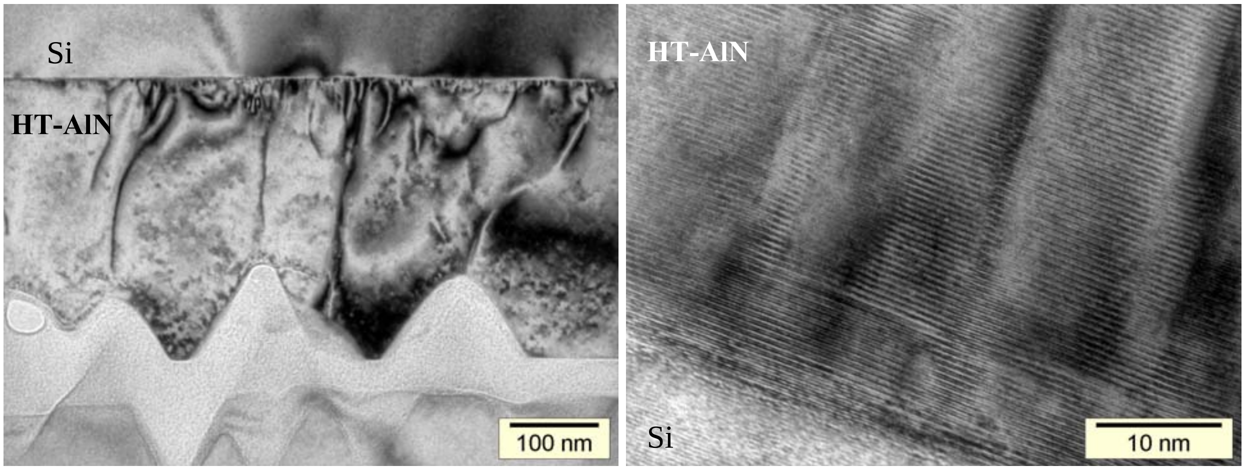

Figure 4.1.7 cross-sectional TEM images showing microstructures of HT-AlN/Si(111)

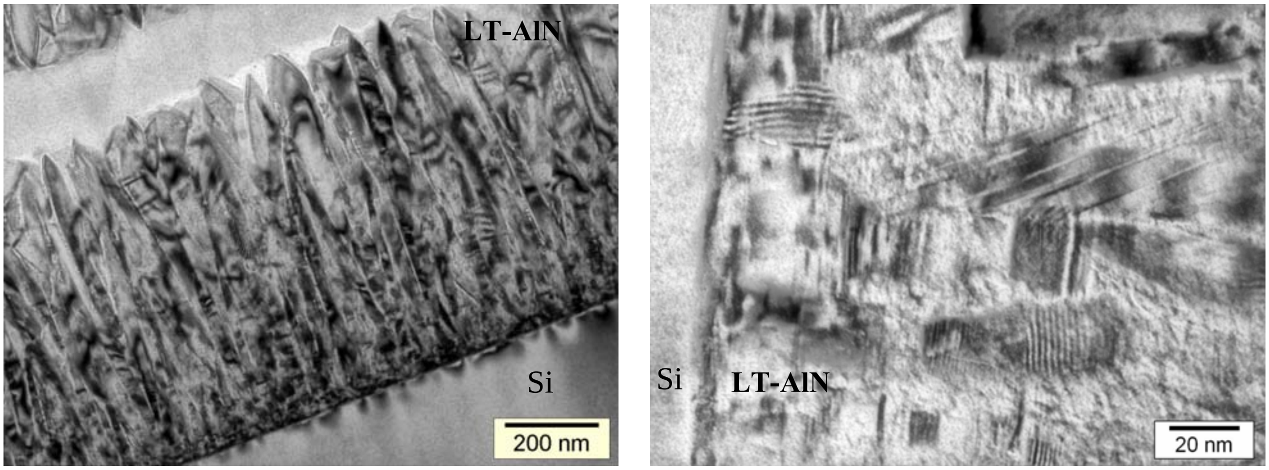

Figure 4.1.8 cross-sectional TEM images showing microstructures of LT-AlN/Si(111)

These results prove that HT-AlN grown at 1200°C has a higher crystalline quality and lower dislocation density but more big-size pits on the surface than LT-AlN at 700°C has. By increasing growth temperature, the surface diffusion length of Al-adatoms would be enhanced and then improves the AlN-layer quality [Brun08, Fuji06, Imur07, Loba08, Obha00]. Consequently, the subsequent $Al_{0.1}Ga_{0.9}N$ layers on the HT-AlN with fewer grain boundary dislocations are improved in their crystalline quality.

4.1.2. The impact of the AlN-seed layer thickness

For the series of growth time dependence, the HT-AlN seeding layer was grown for 1 to 20 minutes corresponding to a nominal thickness of ~1.5 to 30 nm. The nominal thicknesses of the AlN-seed layers are deduced from the growth rates as mentioned before. *Figure 4.1.9* shows that the ω-FWHM of the $Al_{0.1}Ga_{0.9}N$ (0002) reflections slightly decreases from 1370 to 1190 arcsec at the minimum around the AlN-layer thickness of ~6 nm, and for thicker than ~6 nm, it is almost constant about 1260 arcsec. Meanwhile the ω-FWHM of the (10-10) reflections steeply increases from 1580 to 2340 arcsec at the thickness of ~6 nm, after that it is almost constant. In brief, for the thinner AlN-seed layer than ~6 nm, tilts or out-plane misorientations of the $Al_{0.1}Ga_{0.9}N$ are decreased or improved but twists or in-plane misorientations are increased due to an increased coalescence of 3D-AlN islands as discussed in more detail in section 4.1.5. Simultaneously, the in-plane residual strain in the $Al_{0.1}Ga_{0.9}N$ layer continuously decreases from 0.13% to 0.08% and a significant improvement is achieved at a nominal thickness of ~6 nm or in a range of 5-10 nm by measuring of TEM. Taking into account all observations, the optimized thickness of the AlN-seed layer is about 5-10 nm for the best $Al_{0.1}Ga_{0.9}N$ layer quality.

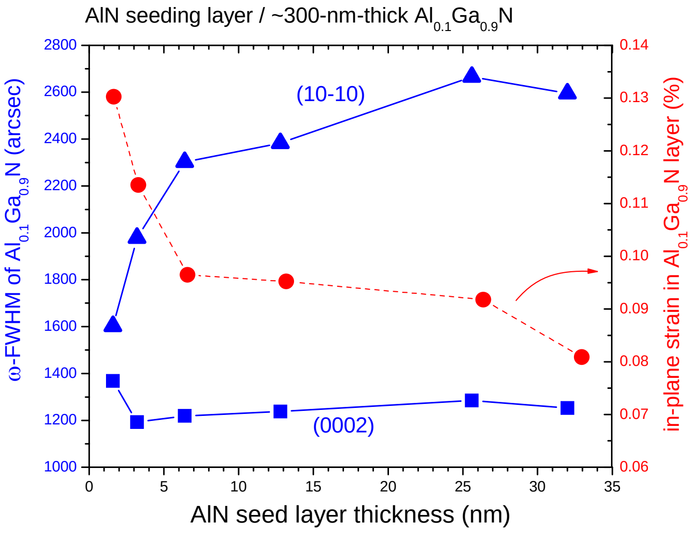

Figure 4.1.9 FWHM of XRD ω-scans of the $Al_{0.1}Ga_{0.9}N$ (0002) and (10-10) reflections and in-plane residual strain in $Al_{0.1}Ga_{0.9}N$ layer as a function of growth time of the AlN-seed layer.

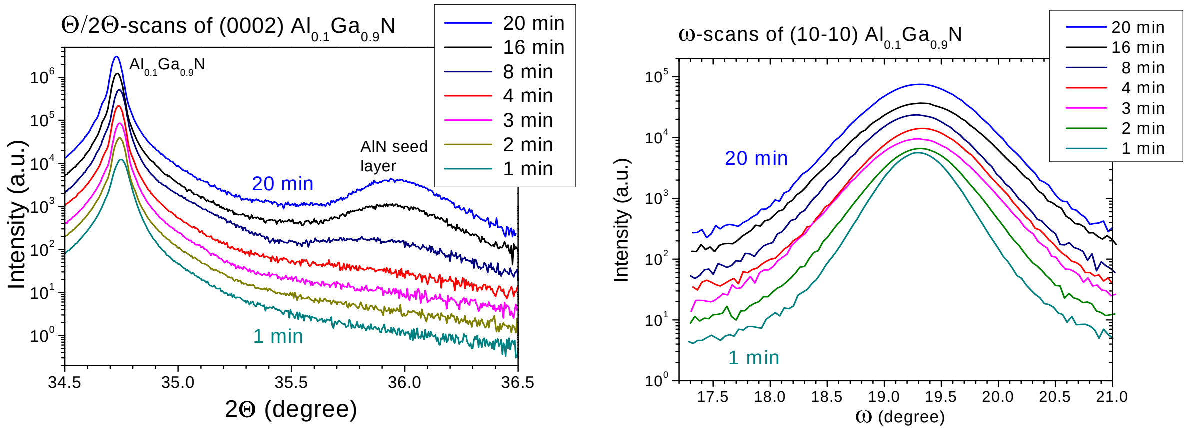

Figure 4.1.10 XRD θ/2θ-scans of the $Al_{0.1}Ga_{0.9}N$ *(0002) reflections and ω-scans of the* $Al_{0.1}Ga_{0.9}N$ *(10-10) reflections with various growth times or thicknesses of the AlN-seed layer*

As shown in *Fig.4.1.10 (left)*, the 2θ peak of the (0002) reflections of the AlN-seed layer is more distinguished and shows a higher intensity for a longer growth time due to the thicker AlN-layer. AFM measurements show a similar good-surface morphology of $Al_{0.1}Ga_{0.9}N$ layers on the AlN layer of ~ 3 nm (left) and ~24 nm (right) with growth steps, low pit density and low roughness of ~ 0.70 nm rms as shown in *Fig.4.1.11*.

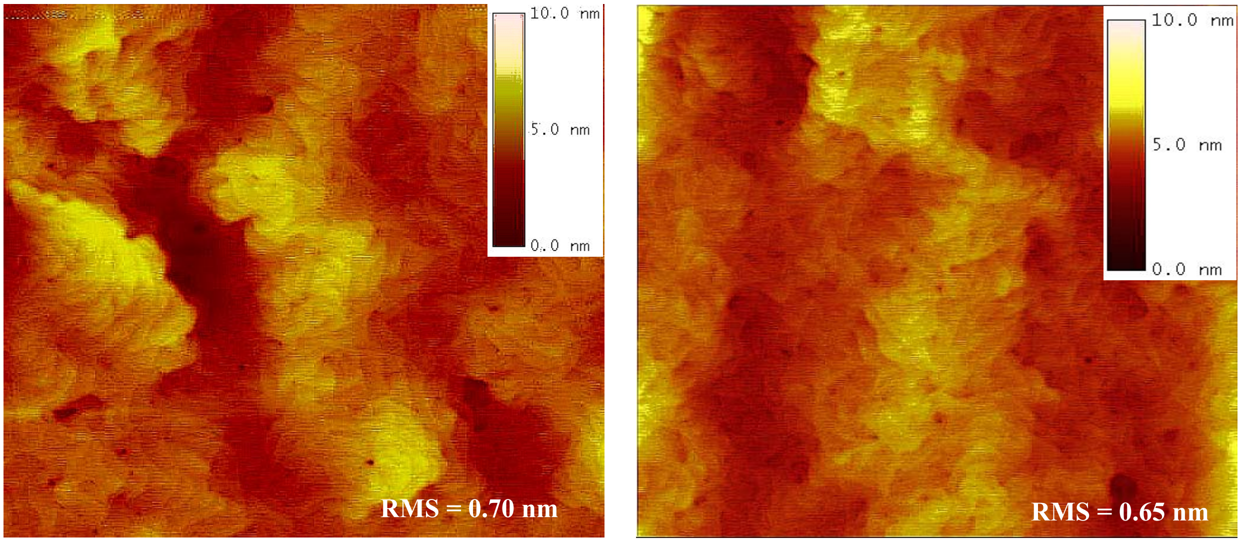

Figure 4.1.11 3×3 μm^2 *AFM images showing a similarly good surface morphologies of* $Al_{0.1}Ga_{0.9}N$ *layers on AlN layers of ~3 nm (left) and ~24 nm (right)*

4.1.3. The impact of growth pressure of the AlN-seed layer

To investigate the impact of growth pressure of the properties of the AlN-seed layer, the seed layer was grown within the pressure range from 70 to 200 mbar. The ω-FWHM of the $Al_{0.1}Ga_{0.9}N$(0002) reflections shows a minimum of 1330 arcsec at 100 mbar and for the (10-10) reflections except that of 70 mbar, the ω-FWHM has a minimum of 2050 arcsec at 150 mbar as shown in *Fig.4.1.12*. Overall the in-plane residual strain increases from 0.05% to 0.12% with increasing growth pressure.

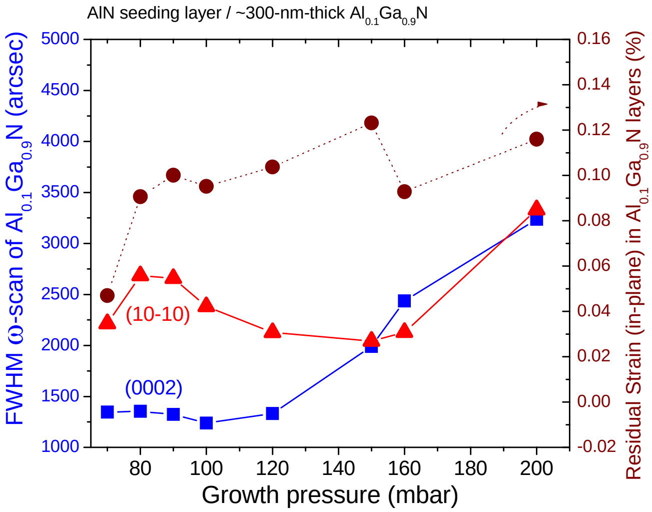

Figure 4.1.12 FWHM of XRD ω-scans of the $Al_{0.1}Ga_{0.9}N$ (0002) and (10-10) reflections and residual strain (in-plane) in $Al_{0.1}Ga_{0.9}N$ layers as a function of growth pressure of AlN-seed layer

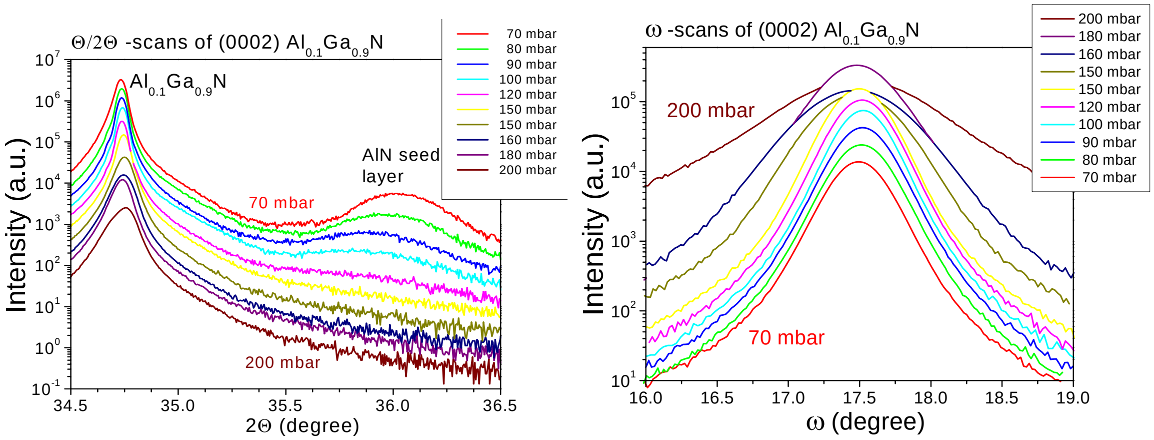

Figure 4.1.13 XRD θ/2θ-scans and ω-scans of the $Al_{0.1}Ga_{0.9}N$ (0002) reflections for various growth pressures of the AlN-seed layer

It can be observed that the 2θ peak of the (0002) reflections of the AlN-seed layer is less distinguished and has a lower intensity with a higher growth pressure which simply implies that it is thinner, as can be seen in *Fig.4.1.13 (left)*. It means that the AlN-seed-layer thickness is varied by growth pressure. As a reason, MOVPE growth of AlN or $Al_{0.1}Ga_{0.9}N$ at high pressures tends to promote gas phase pre-reactions between TMAl and NH_3 [Dadg06, Touz05], preventing Al incorporation and reducing the AlN growth rate, respectively [Crei02, Miho98]. Hence the growth of AlN at low pressures is preferred. As can be seen in *Fig.4.1.13 (right)*, the $Al_{0.1}Ga_{0.9}N$ grown at an AlN growth pressure of 200 mbar has the worst quality with the broadest ω-scan peak.

Actually, to precisely consider the optimized growth pressure of the AlN layer, it is necessary to take account of an identical thickness due to the impact of growth pressure on the AlN-seed-layer thickness. For this case, the best growth conditions of the AlN-seed layer for the good-quality $Al_{0.1}Ga_{0.9}N$ overlayer are obtained at pressures of 100-120 mbar.

4.1.4. The impact of V/III ratio of the AlN-seed layer

In the last series, when the NH_3 flow rate of the AlN-seed layer is increased from 11.16 to 55.80 mmol/min relating to V/III ratio from ~1300 to ~6400, the ω-FWHM of the $Al_{0.1}Ga_{0.9}N$(0002) reflections is almost constant about 1260 arcsec and for the (10-10) reflections, the FWHM continuously decreases from 2810 to 1980 arcsec as shown in *Fig.4.1.14*. The in-plane residual strain in $Al_{0.1}Ga_{0.9}N$ layers decreases from 0.11% to 0.05%. It shows that in this case the $Al_{0.1}Ga_{0.9}N$ quality is continuously improved with an increasing V/III ratio. This probably results from the effect of AlN-thickness variation. As can be seen in *Fig.4.1.15 (left)*, the 2θ peak of the (0002) reflections of the AlN-seed layer is less distinguished and shows a lower intensity with a higher V/III ratio indicating a thinner AlN-layer. The reason is that a high flow rate of NH_3 promotes gas phase reactions between TMAl and NH_3 and reduces the amount of TMAl which is available for AlN growth [Loba08, Dadg06]. To precisely consider the optimized V/III ratio of the AlN layer, it is necessary to take account of an identical thickness of the AlN layer.

Here $Al_{0.1}Ga_{0.9}N$ on the AlN seed layer grown with the highest V/III ratio of ~6400 is the best crystalline quality with the narrowest ω-scans of the (10-10) reflections as depicted in *Fig.4.1.15 (right).*

The best ω-FWHMs of ~250-nm-thick crack-free $Al_{0.1}Ga_{0.9}N$ grown on the optimized AlN-seed layer of each series are ~1260 and ~1980 arcsec for the (0002) and (10-10) reflections, respectively with a low roughness of ~0.7 nm rms for a 3x3 μm^2 scan area.

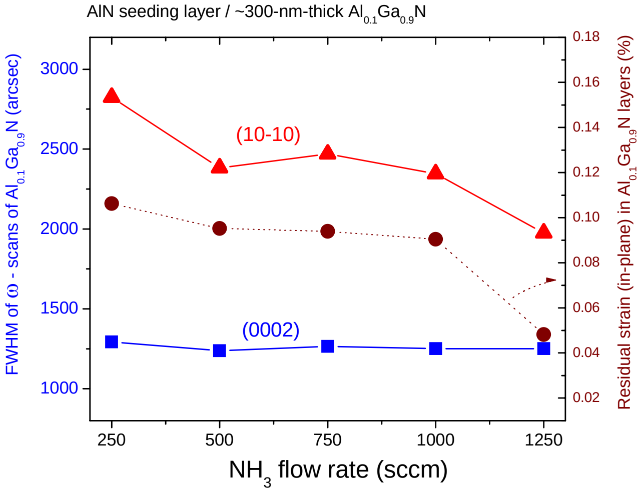

Figure 4.1.14 FWHM of XRD ω-scans of the $Al_{0.1}Ga_{0.9}N$ (0002) and (10-10) reflections and residual strain (in-plane) in $Al_{0.1}Ga_{0.9}N$ layer as a function of V/III ratios or NH_3 flow rates of AlN-seed layer.

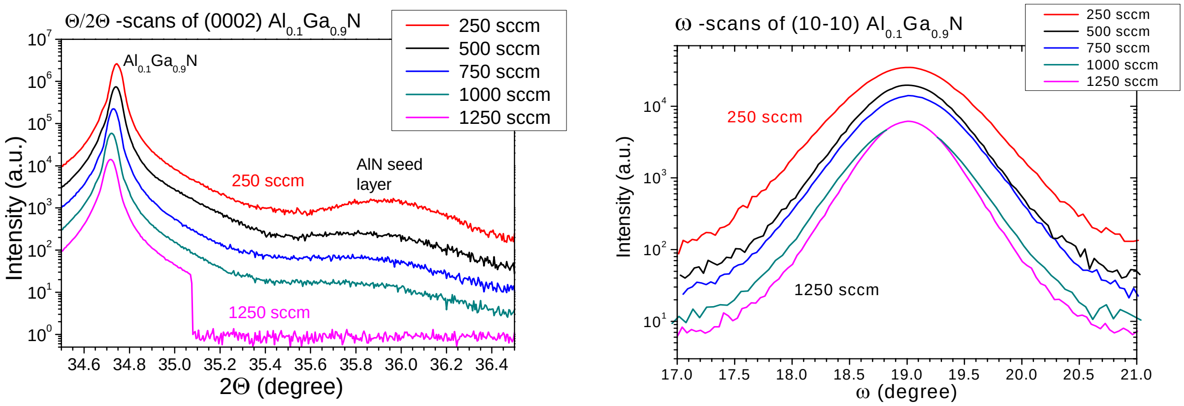

Figure 4.1.15 XRD θ/2θ-scans of the $Al_{0.1}Ga_{0.9}N$ (0002) reflections (left) and ω-scans of the $Al_{0.1}Ga_{0.9}N$ (10-10) reflections (right) grown with various V/III ratios or NH_3 flow rates of the AlN-seed layer

In all experiments variations of the AlN-layer thickness are observed and the subsequent $Al_{0.1}Ga_{0.9}N$ quality also strongly depends on the AlN-layer thickness. So that, to certainly optimize the growth parameters, the identical AlN-layer thickness necessarily would be controlled in each series. However, all results indicate that the AlN-layer thickness plays an important role to improve the $Al_{0.1}Ga_{0.9}N$ quality. Perhaps this relates to the coalescence of the AlN 3D-islands to provide the suitable AlN layer for the subsequent $Al_{0.1}Ga_{0.9}N$ layers. Therefore, the coalescence and growth mechanism of the AlN-seed layer were further investigated.

4.1.5. The impact of the gallium presence in the AlN-seed layer

In some experiments with and without baking the reactor before growing the next sample, it can be observed that the Ga remainder in the reactor walls can affect the quality of the next sample. Therefore experiments with Ga-flow variations in the AlN-seed layer were performed to investigate the influence of a Ga addition on the AlN-seed layer. There are 2 series of samples of only one layer of the AlN-seed layer on a Si(111) substrate with and without triethylgallium (TEGa) flow in the AlN layer. In each series, the growth time of the seed layers is varied from 1 to 8 minutes related to the nominal thickness of ~1.5 to ~12 nm. Afterwards, their surface morphology was observed by FE-SEM. Additional there are 2 samples of the pre-deposited layer of 10 second with and without TEGa. The sample structures are summarized in *table 4.2*. Schematic of Al(Ga)N samples with different thicknesses is shown in *Fig.4.1.16*.

Table 4.2 Al(Ga)N seed layers with different thicknesses

Series	Varied growth time (min)
1. Al(Ga)N with TEGa	10s TMAl+TMGa pre-flow and 0-8 min with NH_3 flow
2. AlN without TEGa	10s only TMAl pre-flow, and 0-8 min with NH_3 flow

Figure 4.1.16 schematic of Al(Ga)N seed layer with different thicknesses

Even though there are only the flows of TMAl with and without TEGa flow before the NH_3 flow for 10 s to pre-deposit Al and Ga adatoms on the hot Si(111) surface at 1200°C, it can be observed lots of unshaped islands in different sizes with a different bright contrast from the background or base surface as shown in *Fig.4.1.17.(a) and (d)*. It also shows that without the Ga flow, there are a fewer numbers of islands and they show a smaller size. All images are not in focus because the samples were charged by the electron beam due to the high resistance of the AlN material. In *Fig.4.1.18*, 3D-AFM measurements show that the sample surface is covered with a very thin AlN layer of very high roughness of ~4.4 nm rms and the different heights of the bigger-size islands and the base surface up to ~10 nm which relates to the brighter contrast areas of islands in FE-SEM images. Moreover, XRD θ/2θ-scans prove AlN being present in this layer by showing the 2θ peaks of the (0002) and (10-10) reflections of AlN with lattice constants in *Fig.4.1.19*, although this sample is grown only with TMAl for 10 minutes without NH_3. However, some EDX measurements of a sample with TMAl and TMGa could only detect Al and N but not Ga. Likely the amount of Ga is lower than the detection limit of this technique.

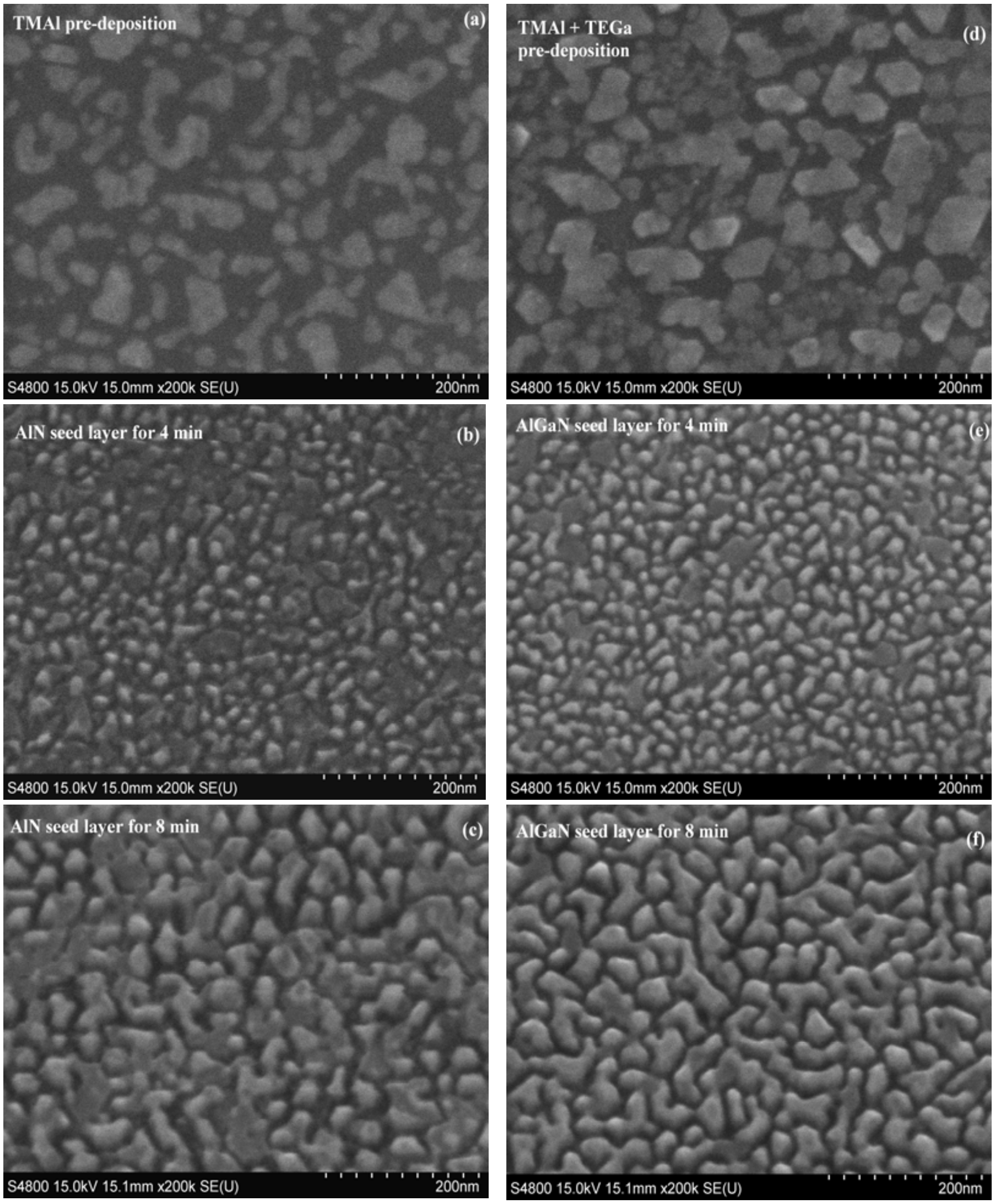

Figure 4.1.17 (a) – (f). FE-SEM images of the surface morphology of the AlN-seed layer (a-c) and the Al(Ga)N-seed layer (d-f)

As can be seen the surface morphology of the Al(Ga)N-seed layer with the Ga flow in *Fig.4.1.17 (e) and (f),* the Al(Ga)N seeds or islands are grown, distributed across the whole surface and coalesced with neighbouring islands to form larger islands. Also some different-contrast areas that probably originated in the pre-deposition layer can be observed. After 8 minutes of growth, an increasing numbers of Al(Ga)N islands coalesce to form larger islands. It is still a 3D-island growth, not a smooth surface of a 2D-layer growth. For the AlN-seed layer without the Ga flow in *Fig.4.1.17 (b) and (c)*, the growth mechanism of the AlN-seed layer is similar to that of the Al(Ga)N-seed layer. But the lateral growth rate or coalescence of the AlN-islands is lower or less pronounced than that of the Al(Ga)N. Moreover, the fewer numbers of AlN islands which scatter in size more and are more distant, leading to a lower number of coalesced islands than that of the Al(Ga)N-seed layer. Also more areas with different-contrast to the Al(Ga)N-seed layer are observed. It simply means that the Ga flow in the AlN-seed layer enables to promote the bigger AlN-islands, homogeneous distribution and faster coalescence. Thus the subsequent layers are improved with the better orientation.

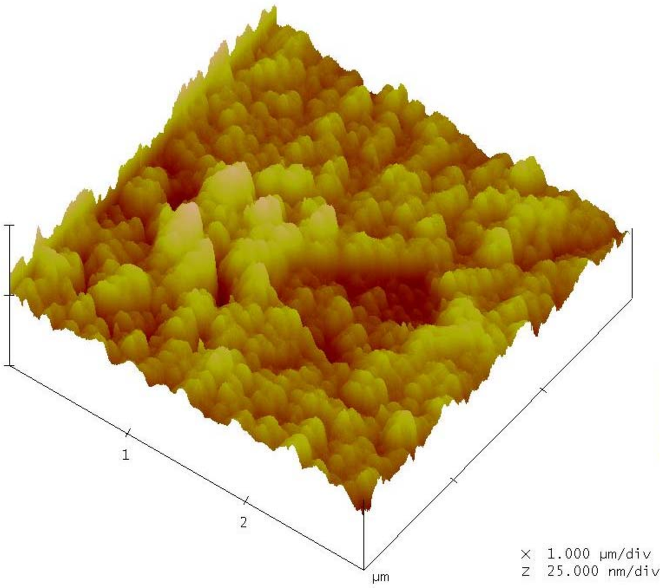

Figure 4.1.18 3D-AFM image showing the surface morphology of pre-deposition of TMAl and TMGa on Si(111) for 10 s without NH_3.

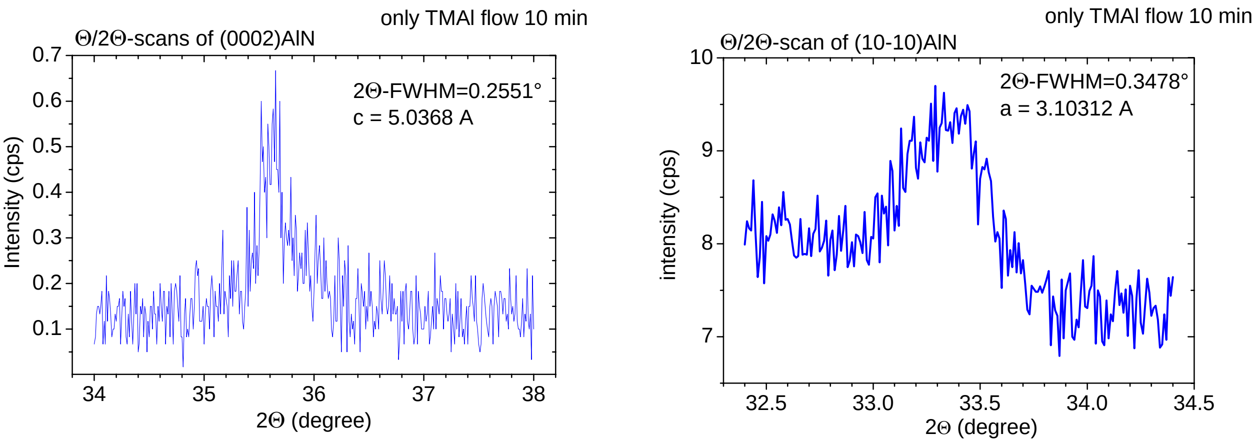

Figure 4.1.19 XRD $\theta/2\theta$*-scans showing the* 2θ *peaks of the AlN(0002) and (10-10) reflections of a 10 min TMAl pre-deposition layer*

With regard to XRD measurements in section 4.1.2, both ω-FWHMs of the $Al_{0.1}Ga_{0.9}N$ reflections are almost constant for a thicker AlN-layer thickness of 5-10 nm. For the thinner AlN layer, the ω-FWHM of the (0002) reflections representing tilt decreases but the ω-FWHM of the (10-10) reflections representing twist increases. Until the AlN-seed layers of about 5-10 nm, tilt and twist of the subsequent $Al_{0.1}Ga_{0.9}N$ layer are nearly constant. This means that the quality of the subsequent $Al_{0.1}Ga_{0.9}N$ layer depends on the thickness of AlN seed layers relating to their surface morphology of the AlN-seeds coalescence.

Furthermore, the AlN-seed layer with the Ga flow can improve the crystalline quality of subsequent $Al_{0.1}Ga_{0.9}N$ layers of the $Al_{0.1}Ga_{0.9}N$/AlN-SLs/AlN/Si(111) samples. With an increasing TEGa flow rate in the AlN-seed layer from 0 sccm to 60 sccm or 14.28 µmol/min, XRD measurements show that the ω-FWHMs of the $Al_{0.1}Ga_{0.9}N$ (0002) and (10-10) reflections are decreased until a minimum at the TEGa flow rate of 40 sccm whereas in-plane residual strain in the $Al_{0.1}Ga_{0.9}N$ layers is decreased continually as shown in *Fig.4.1.20 (left)*. With a too-high Ga-flow rate, the crystalline quality of $Al_{0.1}Ga_{0.9}N$ decreases again. So, it is indicated that optimized Ga presence in the AlN seed layer promoting the AlN-seed coalescence can improve the quality of the subsequent $Al_{0.1}Ga_{0.9}N$.

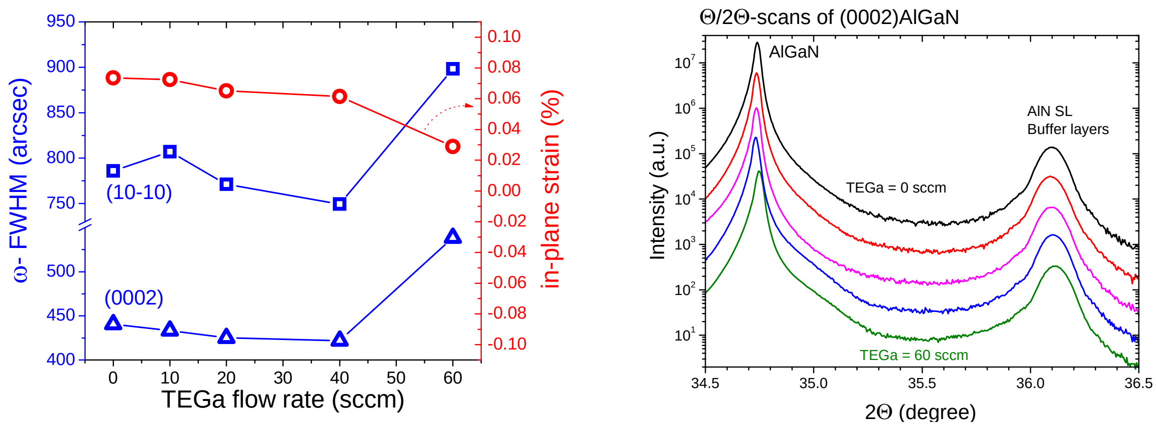

Figure 4.1.20 (left) ω-FWHMs of the $Al_{0.1}Ga_{0.9}N$ (0002) and (10-10) reflections and in-plane strain in $Al_{0.1}Ga_{0.9}N$ layer as a function of the TEGa flow rates in the AlN-seed layer (left) and $\theta/2\theta$-scans of the (0002) reflections of various TEGa flow rates (right).

In brief, an efficient AlN-seed layer to grow high-quality AlGaN requires that the AlN seeds are of a same suitable size and homogeneously distributed to provide suitable surface for the subsequent layer to deposit in the same orientation.

4.2 LT-AlN/HT-AlN superlattice buffer layers

As mentioned before, not only the AlN seeding layer but also the buffer layers play an important role to improve the crystalline quality of the $Al_xGa_{1-x}N$ overlayers. One promising approach to improve the $Al_xGa_{1-x}N$ quality is to introduce a set of superlattices as buffer layers such as a set of $Al_xGa_{1-x}N/Al_yGa_{1-y}N$ superlattices [Xi07c], a set of $Al_xGa_{1-x}N/AlN$ superlattice [Xi07c, Zhan02, Sun05, Wang02, Maye04], and a set of AlN/GaN superlattices [Niik07, Mura07] etc. Such periodic superlattice structures are able to reduce threading dislocations by bending them from the growth direction or forming annihilation loops or even terminating them [Felt01, Wu07, Mast06]. Moreover, superlattice structures are also useful for strain engineering to compensate the strain in the subsequent layers [Felt01, Mast06].

Therefore to improve the $Al_xGa_{1-x}N$ quality grown on Si substrates, the AlN-based superlattice structures of different growth temperature as low temperature AlN (LT-AlN) and high temperature (HT-AlN) layers are introduced as buffer layers. As discussed before in section 4.1.1, the HT-AlN layers have a higher crystalline quality but LT-AlN layers have a higher relaxation or lower strain in the layers. Therefore to insert thin LT-AlN layers periodically in between the HT-AlN layers as a pattern of superlattice structures might influence dislocation propagation due to a different strain of the AlN-layer stack at low temperature and then improve their crystalline quality. For this purpose, the $Al_{0.1}Ga_{0.9}N$ layers subsequently grown on LT-AlN/HT-AlN SL buffer layers were investigated for different SL growth conditions.

In this section, the impacts of growth parameters of LT-AlN/HT-AlN superlattice buffer layers on the $Al_{0.1}Ga_{0.9}N$ quality are presented and discussed. The quality of $Al_{0.1}Ga_{0.9}N$ on different thicknesses of LT-AlN/ HT-AlN SLs are detailed and discussed. The last presents a growth mechanism and microstructure of LT-AlN/HT-AlN SLs observed by FE-SEM measurements.

4.2.1. Optimization of growth parameters of LT-AlN/HT-AlN superlattices

To optimize the growth parameters of LT-AlN/HT-AlN SLs, firstly the optimized AlN seeding layer was grown on a Si (111) substrate, and then 5 periods of LT-AlN/HT-AlN SLs. Finally a ~250-nm-thick $Al_{0.1}Ga_{0.9}N$ layer was grown on top. As discussed before, AlN layers grown at higher growth temperature have a better crystalline quality. In order to obtain high-quality $Al_{0.1}Ga_{0.9}N$ overlayers, the HT-AlN layers were grown at the optimized growth temperature of the

AlN seeding layers of 1200°C. For the first series growth time or thickness of both AlN layers in the AlN-based SL stack were optimized, LT-AlN layers were grown at 950°C. The growth time of LT-AlN and HT-AlN layers were increased from 1 to 4 minutes. The next series is growth temperature of the LT-AlN layers varied from 600-950°C and the last for the number of AlN-based SL from 1-15 periods as summarized in *Table 4.3*. Schematic of $Al_{0.1}Ga_{0.9}N$/(LT-AlN/HT-AlN)SLs/AlN/Si samples with different growth parameters of AlN-SLs is shown in *Fig.4.2.1*.

Table 4.3 Variations of growth parameters of LT-AlN/HT-AlN SL buffer layers in each series

Series	**Varied parameters of LT-AlN/HT-AlN SL**	**range**
1	Time (min)	1-4
2	Temperature of LT-AlN (°C)	600 - 950
3	Number of SL (folds)	1-15

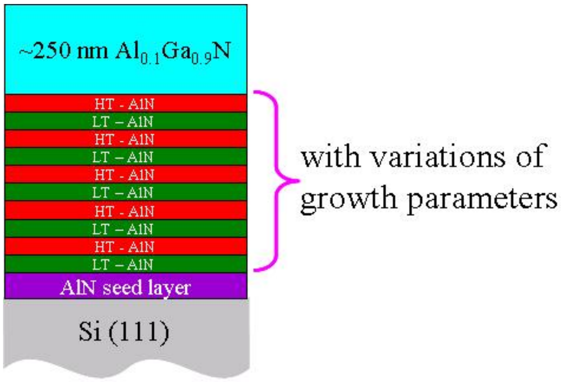

Figure 4.2.1 Schematic of $Al_{0.1}Ga_{0.9}N$ on LT-AlN/HT-AlN SLs with variations of growth parameters

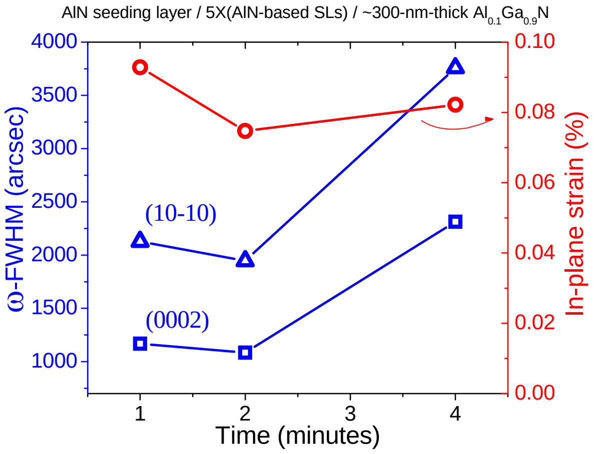

Fig.4.2.2 ω-FWHMs of both reflections and in-plane strain as a function of growth time

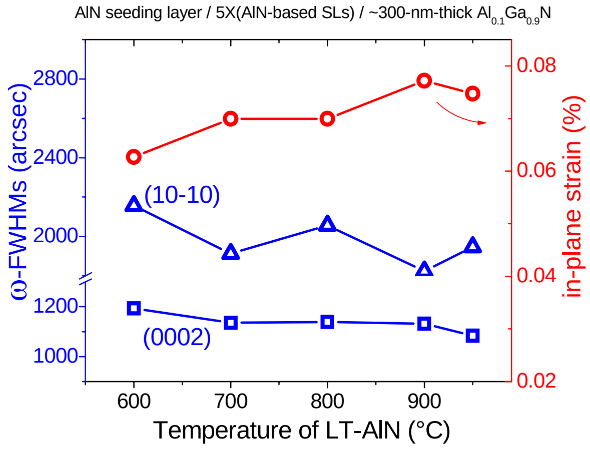

Fig.4.2.3 ω-FWHMs of both reflections and strain as a function of growth temperature

When the growth time of LT-AlN and HT-AlN layers are increased from 1 to 4 minutes, the best ω-FWHMs of 1080 and 1980 arcsec of the $Al_{0.1}Ga_{0.9}N$ (0002) and (10-10) reflections respectively are obtained at the growth time of 2 minutes of both AlN layers as shown in *Fig.4.2.2*. It relates to a thickness of LT-AlN of ~7 nm and HT-AlN of ~3 nm. The approximate thicknesses of

LT-AlN and HT-AlN layers or their growth rates are deduced from two samples of thick LT-AlN and HT-AlN layers at 700°C and 1200°C, respectively and their thicknesses are determined by TEM measurements and an optical interference technique i.e. the growth rates of 4.1 nm/min of LT-AlN and 1.5 nm/min of HT-AlN as shown in section 4.1.1.

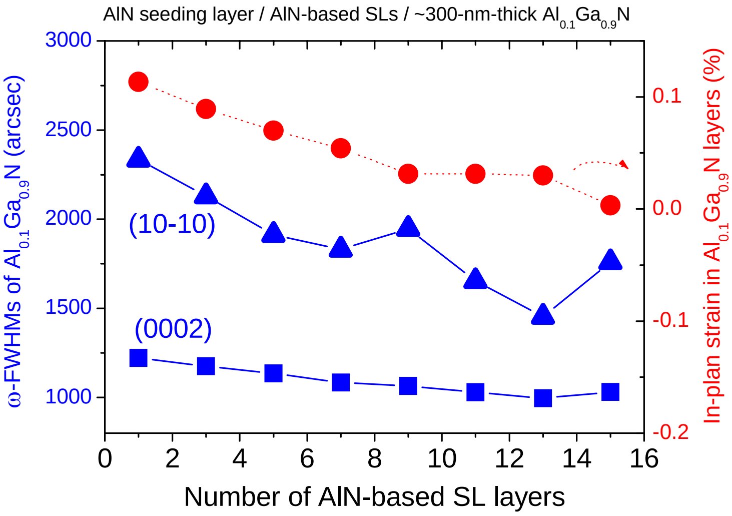

Figure 4.2.4 ω-FWHMs of the Al$_{0.1}$Ga$_{0.9}$N (0002) and (10-10) reflections and in-plane residual strain as a function of the number of SL

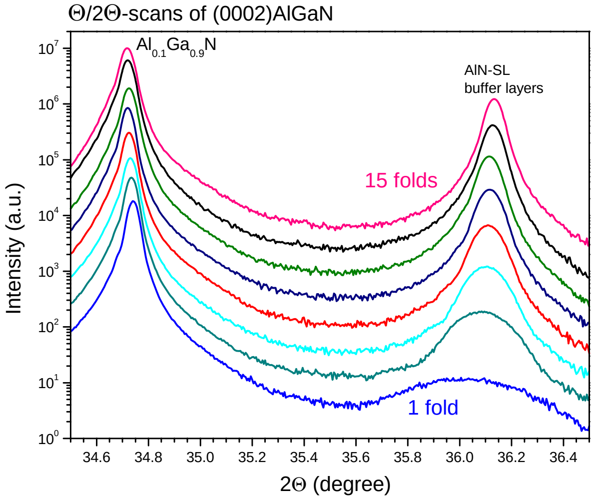

Figure 4.2.5 XRD $\theta/2\theta$-scans of the Al$_{0.1}$Ga$_{0.9}$N (0002) reflections with a variation of the number of SL

In the next series of optimization the growth temperature of the LT-AlN layers, ~7-nm-thick LT-AlN and ~3-nm-thick HT-AlN layers were investigated. The growth temperature of LT-AlN layers is varied from 600 to 950°C. In *Fig.4.2.3*, both ω-FWHMs of the $Al_{0.1}Ga_{0.9}N$ reflections tend to decrease but in-plane residual strain in the $Al_{0.1}Ga_{0.9}N$ layers tends to increase with an increasing growth temperature. By taking into account all parameters, the optimized growth temperature of LT-AlN layers is 700°C with the best ω-FWHMs of 1130 and 1910 arcsec of the $Al_{0.1}Ga_{0.9}N$ (0002) and (10-10) reflections, respectively.

A final optimization was performed for the number of AlN-based SL. When the period number is increased from 1 to 15, both ω-FWHMs of the $Al_{0.1}Ga_{0.9}N$ reflections and in-plan residual strain tend to decrease continuously. By taking into account the time necessary to grow them and the improvement, 13 periods can be regarded as an optimum number with the best ω-FWHMs of 1000 and 1450 arcsec of the (0002) and (10-10) reflections, respectively, as shown in *Fig.4.2.4*. In *Fig.4.2.5*, XRD θ/2θ-scans of the $Al_{0.1}Ga_{0.9}N$ (0002) reflections show more distinguished and narrower 2θ-position peaks of the AlN-SL buffer layers with an increasing number of the SL periods. It implies to the better-quality AlN-SL buffer layers.

In summary, the initially optimized growth parameters of the AlN-based SL buffer layers for high-quality $Al_{0.1}Ga_{0.9}N$ are 13 periods of LT-AlN layers grown at 700°C and HT-AlN layers at 1200°C.

4.2.2. Impact of LT-AlN and HT-AlN layers on AlN-based superlattices

In a further optimization the thicknesses of the LT-AlN and HT-AlN SL layers were varied individually. In *Fig.4.2.6*, the HT-AlN thickness was kept constant at ~3.0 nm, while the LT-AlN thickness was increased from ~3.6 to ~14.4 nm. Both ω-FWHMs and in-plane strain of ~450-nm-thick $Al_{0.1}Ga_{0.9}N$ tend to decrease with increasing LT-AlN thickness. But with a LT-AlN thickness of ~14.4 nm, $Al_{0.1}Ga_{0.9}N$ layers are cracked. Furthermore the HT-AlN thickness was kept constant of ~6.0 nm and the LT-AlN thickness was decreased from ~7.2 to ~3.6 nm. Both ω-FWHMs and in-plane strain of $Al_{0.1}Ga_{0.9}N$ tend to decrease and are below that of $Al_{0.1}Ga_{0.9}N$ with HT-AlN of ~3.0 nm. Thus, with an increasing thickness of the HT-AlN layers and a decreasing thickness of the LT-AlN layers, the crystalline quality of $Al_{0.1}Ga_{0.9}N$ is improved. Moreover, it is noticed that with a thinner HT-AlN of ~3 nm, in-plane strain in $Al_{0.1}Ga_{0.9}N$ layers is decreased when the LT-AlN thickness is increased but with a thicker HT-AlN of ~6 nm, in-plane strain is increased.

Thus a sample with thicker HT-AlN of ~7.5 nm and thinner LT-AlN of ~1.8 nm was grown. The $Al_{0.1}Ga_{0.9}N$ layer is improved with the best ω-FWHMs of 850 and 1370 arcsec of the (0002) and (10-10) reflections respectively. On the other hand, an absolutely different structured sample with thinner HT-AlN of ~1.5 nm and thicker LT-AlN of ~14.4 nm was grown. Here the $Al_{0.1}Ga_{0.9}N$ layers are cracked. These results prove that with an increasing HT-AlN thickness and a decreasing LT-AlN thickness simultaneously, the $Al_{0.1}Ga_{0.9}N$ quality, in particular, in-plane misorientation can be substantially improved.

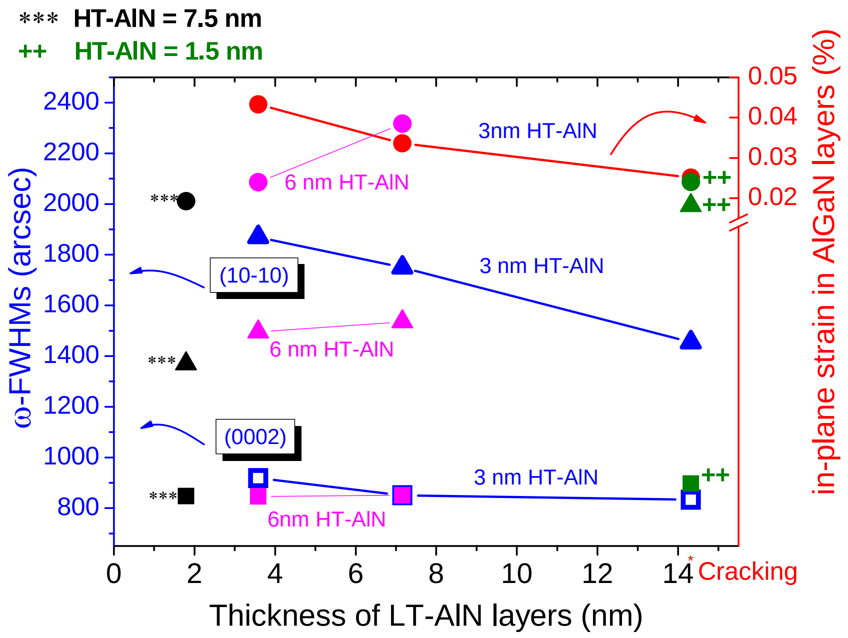

Figure 4.2.6 ω-FWHMs of the $Al_xGa_{1-x}N$ (0002) and (10-10) reflections and in-plane residual strain in $Al_xGa_{1-x}N$ layers as a function of LT-AlN thickness

Consequently, the next series of ~450-nm-thick $Al_{0.1}Ga_{0.9}N$ samples was grown with an increasing HT-AlN thickness up to ~10.5 nm and a decreasing LT-AlN thickness down to ~0.5 nm keeping the total thickness of the SL constantas shown in *Fig.4.2.7*. Additionally, one sample of $Al_{0.1}Ga_{0.9}N$ was grown on 4 periods of the SLs of ~7.2-nm-thick LT-AlN/~26.3-nm-thick HT-AlN and one other sample grown on ~126-nm-thick HT-AlN/~7.2-nm-thick LT-AlN buffer layers. In XRD measurements, the results show that the quality is improved continually with an increasing HT-AlN thickness and a decreasing the LT-AlN thickness. The best-quality ~450-nm-thick $Al_{0.1}Ga_{0.9}N$ on 13 periods of the SLs of ~10.5-nm-thick HT-AlN/~0.5-nm-thick LT-AlN is 700 and 840 arcsec of ω-FWHMs of the (0002) and (10-10) reflections, respectively. This is improved from the ω-FWHMs of 730 and 1500 arcsec of the (0002) and (10-10) reflections of the $Al_{0.1}Ga_{0.9}N$ on the SLs of ~3-nm-thick HT-AlN/~7.2-nm-thick LT-AlN.

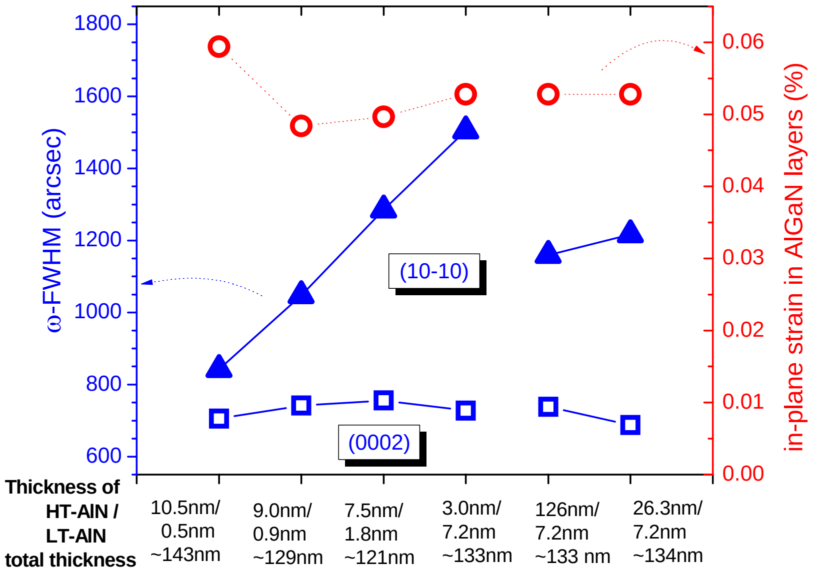

Figure 4.2.7 ω-FWHMs of the $Al_xGa_{1-x}N$ (0002) and (10-10) reflections and in-plane residual strain in $Al_xGa_{1-x}N$ layers with a variation of thicknesses of LT-AlN/HT-AlN SLs

In summary, the optimized growth parameters of the AlN-based SL buffer layers for high-quality $Al_{0.1}Ga_{0.9}N$ growth are 13 periods of ~0.5-nm-thick LT-AlN layers grown at 700°C and ~10.5-nm-thick HT-AlN layers at 1200°C.

4.2.3. Microstructure of LT- AlN/HT-AlN superlattice buffer layers

In order to better understand the growth mechanism of LT-AlN/HT-AlN SL buffer their surface morphology was investigated with FE-SEM measurements. Samples of LT-AlN/HT-AlN SLs without the $Al_{0.1}Ga_{0.9}N$ top layer were grown with an increasing number of SL periods as 2, 4, 8 and 13 periods. There was a comparison of two types of LT-AlN/HT-AlN SLs with different HT-AlN and LT-AlN thicknesses i.e. ~7 nm LT-AlN/~3 nm HT-AlN SLs and ~0.5 nm LT-AlN/~10.5 nm HT-AlN SLs.

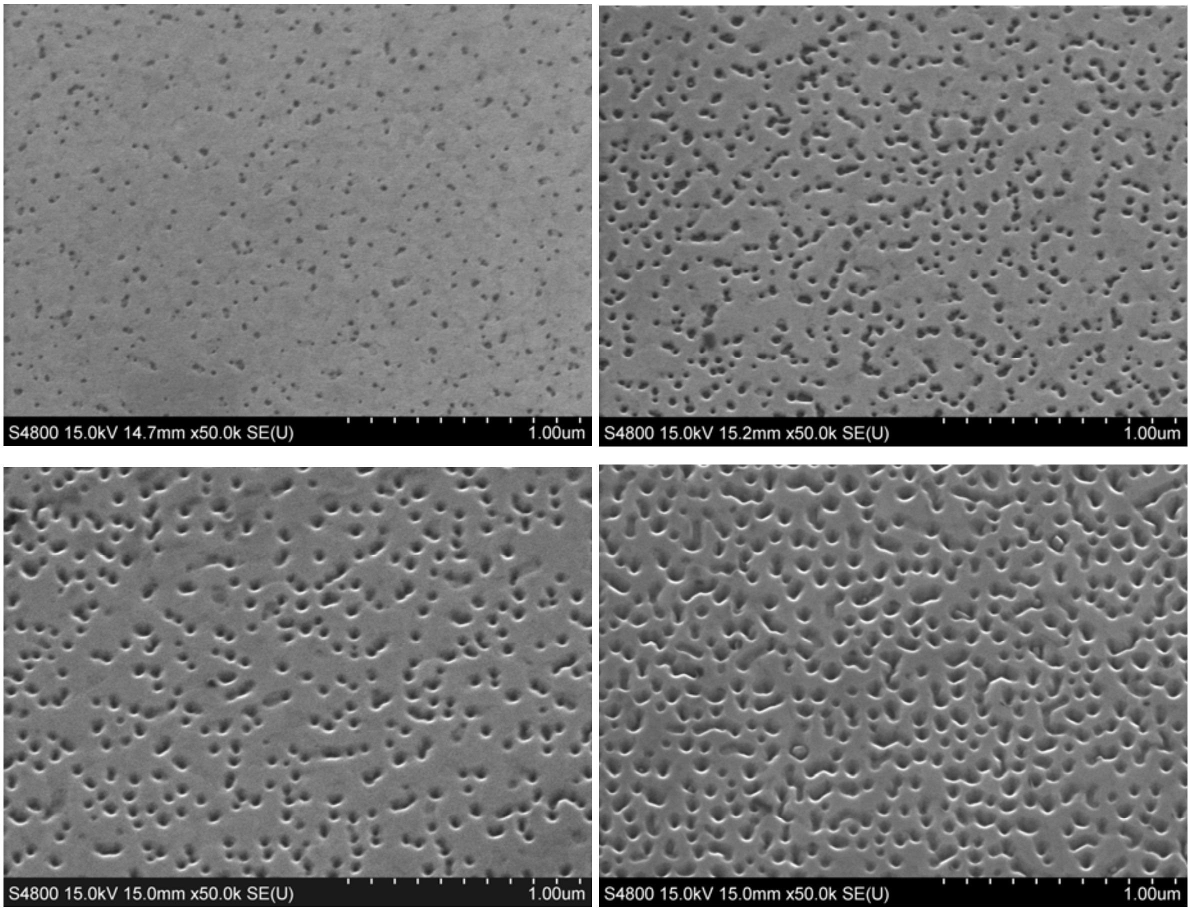

Figure 4.2.8 (a)-(d) FE-SEM images of the HT-AlN top layers of ~7 nm LT-AlN/~3 nm HT-AlN SLs with the number of SL periods of 2, 4, 8 and 13 periods, respectively

FE-SEM images in *Fig.4.2.8 (a)-(d)* reveal the surface morphology of the HT-AlN top layers of ~7 nm LT-AlN/~3 nm HT-AlN SLs with an increasing number of SL periods from 2 to 13 periods. It can be observed that even though the number of SL periods is increased, the pit density of all HT-AlN top layers are nearly identical and even increase a bit. However with a higher number of SL periods, the HT-AlN top layer surface appears smoother and the pit size tends to be bigger and deeper gradually until a number of 8 periods.

For the samples of superlattices of ~0.5 nm LT-AlN and ~10.5 nm HT-AlN SLs with an increasing number of SL periods from 8 to 13 periods, FE-SEM images show the surface morphology of the HT-AlN top layers with an obviously reduced pit-density. Also their surface appears smoother but the pit size is a bit bigger from approximate diameter of 33 nm to 54 nm as depicted in *Fig.4.2.9*.

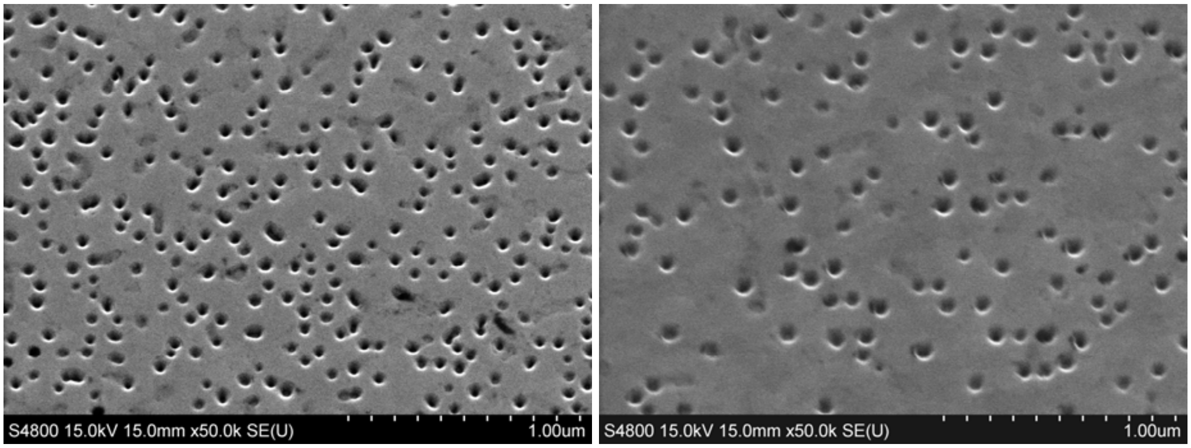

Figure 4.2.9 FE-SEM images of the HT-AlN top layers of ~0.5 nm LT-AlN/~10.5 nm HT-AlN SLs with the number of SL periods of 8 and 13 periods

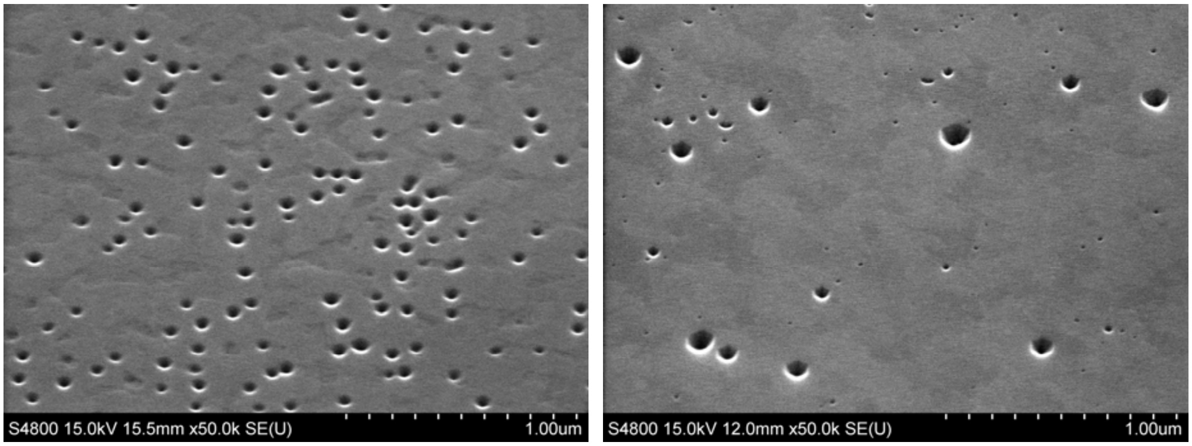

Figure 4.2.10 FE-SEM images of the HT-AlN top layer of SLs (left) and the $Al_{0.1}Ga_{0.9}N$ top layer on them (right)

However, the FE-SEM images of samples with the $Al_{0.1}Ga_{0.9}N$ top layers show that the subsequent $Al_{0.1}Ga_{0.9}N$ layers on 13 periods of both types of SLs have a smoother surface with a lower pit density as shown in *Fig.4.2.10*.

As mentioned before, the subsequent $Al_{0.1}Ga_{0.9}N$ layers on 13 periods of the SLs of ~0.5-nm-thick LT-AlN and ~10.5-nm-thick HT-AlN have a better crystalline quality, in particular, lower in-plane misorientations in XRD measurements than that on the SLs of ~7-nm-thick LT-AlN and ~3-nm-thick HT-AlN. Along with this the pit density is lower and the surface of the SLs of ~0.5-nm-thick LT-AlN and ~10.5-nm-thick HT-AlN is smoother. It is indicated that the optimized thicknesses of LT-AlN and HT-AlN layers by decreasing the thickness of LT-AlN, which tends to polycrystalline growth for thicker layers, and increasing the thickness of the HT-AlN layers could reduce the pit density and improve the AlN-SL quality and by this improve the quality of the subsequent $Al_{0.1}Ga_{0.9}N$ layers. However, LT-AlN layers are still required to improve the $Al_{0.1}Ga_{0.9}N$ quality: If $Al_{0.1}Ga_{0.9}N$ layers are grown on a ~130-nm-thick HT-AlN buffer layer solely; XRD measurements show a lower crystalline quality than on LT-AlN / HT-AlN SLs.

Cross-sectional TEM images can observe that the threading dislocations are rather annihilated at the interface between AlGaN and the AlN-SLs, the dislocation loops are preferentially formed in the first nanometers of the AlN-SL stack, and the recombination of dislocations happens in the AlN-SL and AlGaN layers as shown in *Fig.4.2.11*. The threading dislocation density of 8.4×10^{10} cm^{-2} in the SL stack was reduced to 1.8×10^{10} cm^{-2} in the layer. Besides, high resolution cross-sectional TEM images reveal the good-quality and abrupt interface of $Al_{0.1}Ga_{0.9}N$/AlN-based SLs with a sharp interface as shown in *Fig.4.2.12*. Surprisingly, it could not be observed a different microstructure for the LT-AlN and HT-AlN layers in the SL stack. This implies that these AlN-based superlattices are homogenous with the identical crystalline structure. It is also proven by XRD $\theta/2\theta$ measurements of the (0002) reflections that the fringe patterns of the multilayers could not be observed but with a sample of HT-$Al_{0.97}Ga_{0.03}N$/LT-AlN SLs, they could be observed as shown in *Fig.4.2.13*.

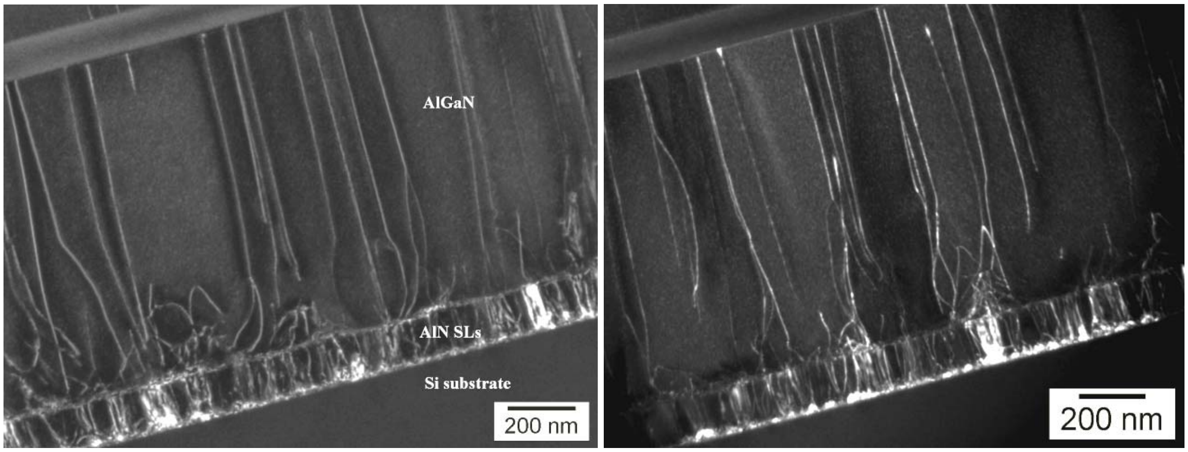

Figure 4.2.11 Cross-sectional TEM images of the sample of $Al_{0.1}Ga_{0.9}N$/AlN-based SLs showing the reduction of threading dislocations, dislocation loops and the combination of dislocations

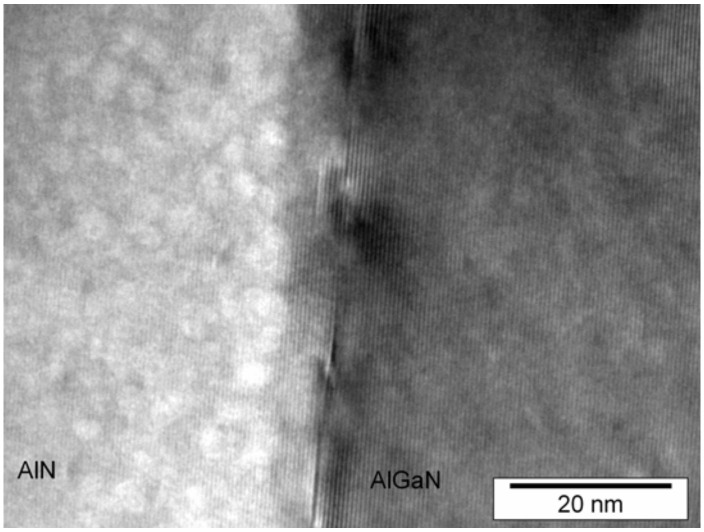

Figure 4.2.12 High resolution cross-sectional TEM images of the sample of $Al_{0.1}Ga_{0.9}N$*/AlN-based SLs showing the good-quality and abrupt interface with the sharp line*

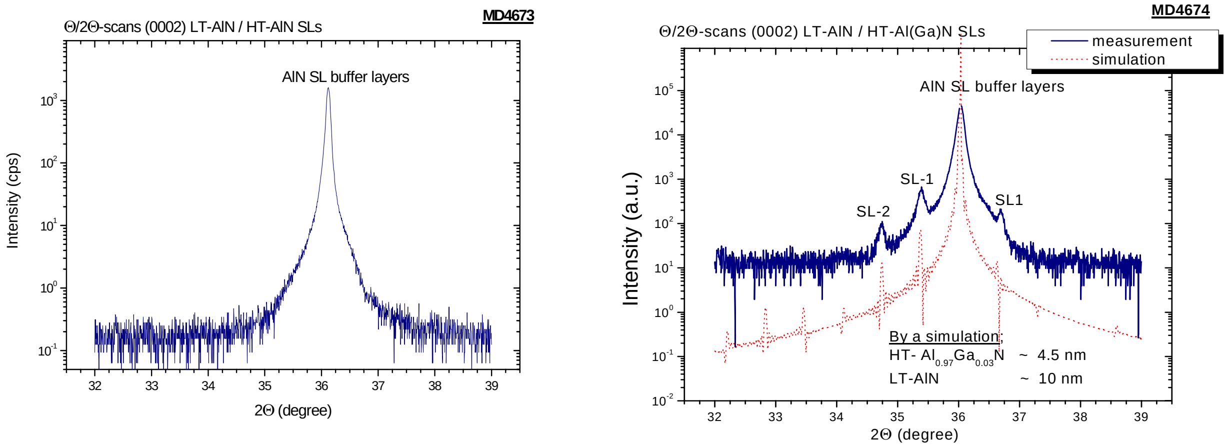

Figure 4.2.13 XRD $\theta/2\theta$ *measurements of the (0002) reflections of LT-AlN/HT-AlN SLs (left) and LT-AlN/HT-*$Al_{0.97}Ga_{0.03}N$ *SLs with the multilayer fringes (right)*

4.3. High-quality $Al_xGa_{1-x}N$ with Al contents ≤65%

As can be seen in *Fig.4.2.3.4* and *Fig.4.2.3.5*, the $Al_{0.1}Ga_{0.9}N$ grown on the optimized LT-AlN/HT-AlN superlattice buffer layers is of high crystalline quality and shows a reduced dislocation density in the AlGaN layer. To explore the growth of higher Al-content AlGaN layers, e. g., for deep UV emitters ~450-nm-thick $Al_xGa_{1-x}N$ with Al contents from x=0.05 to x=0.65 were grown on the optimized AlN-based seed and SL buffer layers consisting of ~10 nm AlN-seed layer at 1200°C and 13 periods of ~0.5 nm LT-AlN at 700°C and ~10.5 nm HT-AlN at 1200°C. Except the other standard growth parameters of 1145°C, 100 mbar and a V/III ratio of ~550, the TMGa molar flow rates of $Al_xGa_{1-x}N$ layers were decreased from 96.92 to 4.04 µmol/min in order to increase the Al contents. There are two additional samples of ~120-nm-thick $Al_{0.37}Ga_{0.63}N$ and ~65-nm-thick $Al_{0.65}Ga_{0.35}N$ to present their good crystalline qualities. A schematic of $Al_xGa_{1-x}N$ with Al contents ≤ 65% grown on (LT-AlN/HT-AlN)SLs/AlN/Si samples is shown in *Fig.4.3.1*.

In this section, MOVPE growth of these $Al_xGa_{1-x}N$ layers with Al contents ≤ 65% is discussed first and then their crystalline qualities. Their surface morphology and optical properties are also presented.

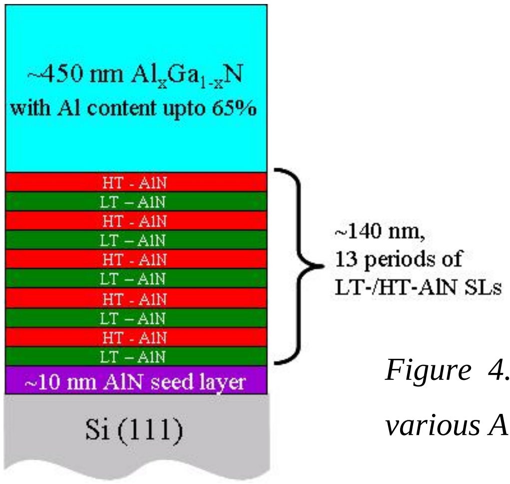

Figure 4.3.1 Schematic of ~450 nm $Al_xGa_{1-x}N$ with various Al contents on optimized LT-AlN/HT-AlN SLs.

4.3.1. MOVPE growth of $Al_xGa_{1-x}N$

With increasing of the Al contents, the $Al_xGa_{1-x}N$ growth rate decreases from 53.1 to 3.6 nm/min non-linearly but nearly proportionally to the total group-III (TMAl+TMGa) molar flow rate as shown in *Fig.4.3.2*. It should be noted that the efficiency of the group-III incorporation for all $Al_xGa_{1-x}N$ layers with these growth parameters is nearly constant.

In *Fig.4.3.3*, it shows the relationship of the Al contents of $Al_xGa_{1-x}N$ in solid phase and the ratios of $\frac{TMAl}{[TMAl+TMGa]}$ in gas phase. The Al contents of $Al_xGa_{1-x}N$ epilayers at the given ratio of $\frac{TMAl}{[TMAl+TMGa]}$ in gas phase slightly deviated from the linear dependence (y = x). This linear line means to the maximum incorporation efficiency of 100% to form $Al_xGa_{1-x}N$ in solid phase with a fraction by the same fraction of the precursors in gas phase. In this case of concave bowing, it could probably imply that the incorporation efficiency of TMAl to form $Al_xGa_{1-x}N$ epilayers of all compositions is slightly lower than that of TMGa.

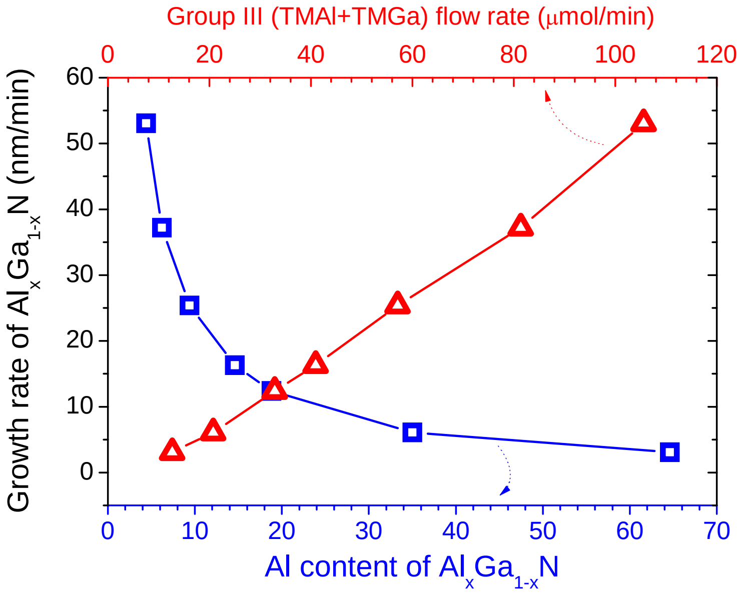

Figure 4.3.2 Growth rate of $Al_xGa_{1-x}N$ as a function of Al content shown in opened squares and as a function of Group III (TMAl+TMGa) flow rate shown in opened triangular

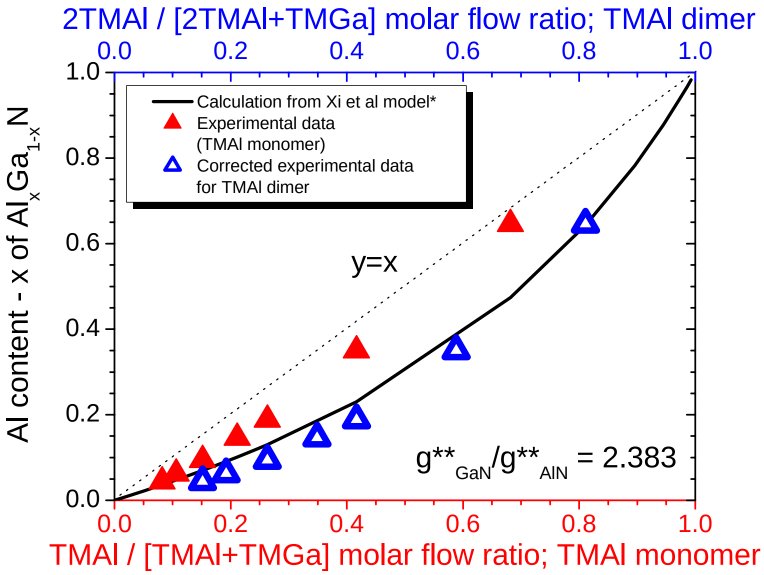

Figure 4.3.3 The relation of the Al contents of $Al_xGa_{1-x}N$ in solid phase and the ratios of $\frac{TMAl}{[TMAl+TMGa]}$ *in gas phase*

By a kinetic model of Xi et al as expressed in Eq.4.3.1-2 [Xi07a, Xi07b], it has be proposed to explain the bowing relationship between the Al fractions in solid phase and the TMAl molar flow ratios in gas phase within x=0-1 when keeping the total group-III flow rate constant by taking into account the molar growth rate ratio between GaN and AlN $\left(\frac{g_{GaN}^{**}}{g_{AlN}^{**}}\right)$. This model could classify the incorporation efficiency into 2 categories i.e. the positive deviation or convex bowing meaning to the lower Ga incorporation of $\left(\frac{g_{GaN}^{**}}{g_{AlN}^{**}}\right)<1$ and the negative deviation or concave bowing of the higher Ga incorporation of $\left(\frac{g_{GaN}^{**}}{g_{AlN}^{**}}\right)>1$ than the Al incorporation.

$$g = g^{**}\Phi_M \qquad \text{………...Eq.4.3.1}$$

$$x = \frac{g_{AlN}}{g_{AlN}+g_{GaN}} = \frac{g_{AlN}^{**}\Phi_{M,Al}}{g_{AlN}^{**}\Phi_{M,Al}+g_{GaN}^{**}\Phi_{M,Ga}} \qquad \text{………...Eq.4.3.2}$$

where g = the growth rate of an epitaxial layer in solid phase (nm/min)

g^{**} = the molar growth rate at unit molar flow rate in gas phase (nm/μmol)

Φ_M = the molar flow rate in gas phase (μmol/min)

x = the Al-mole fraction or Al content of an epitaxial layer in solid phase

For our case, the approximated growth rates of pure GaN and AlN are determined from additional experiments to be 20 nm/min at the molar flow rate of 48.46 μmol/min and 1.5 nm/min at the molar flow rate of 8.66 μmol/min, respectively and the molar growth rate ratio of GaN and AlN $\left(\frac{g_{GaN}^{**}}{g_{AlN}^{**}}\right)$ of 2.383. With regard to the predominately dimeric nature of TMAl precursor under equilibrium condition of the bubbler of MOVPE system [Miho98], the $\frac{TMAl}{[TMAl+TMGa]}$ ratios were corrected to the ratios of $\frac{2TMAl}{[2TMAl+TMGa]}$. Following this model to simulate the relationship for our case, the calculated relationship as shown by a black line and the corrected experimental results as shown in the blue open triangle are in good agreement as for the case of the negative deviation or concave bowing of $\left(\frac{g^{**}_{GaN}}{g^{**}_{AlN}}\right) > 1$. It implies that for the growth parameters the Al incorporation efficiency to form $Al_xGa_{1-x}N$ layers is lower than that of Ga with the ratio of $\left(\frac{g^{**}_{GaN}}{g^{**}_{AlN}}\right) = 2.383$.

4.3.2. Crystalline quality of $Al_xGa_{1-x}N$

The $Al_xGa_{1-x}N$ crystalline quality was characterized by high-resolution XRD measurements, the ω-FWHMs of the $Al_xGa_{1-x}N$ (0002) reflections fluctuate around 700 arcsec for ~0.05 < x < ~0.10 and with increasing Al content it continually increases to 1060 arcsec. The minimum ω-FWHM of the (10-10) reflection is 1020 arcsec at x = 0.10 as shown in *Fig.4.3.2.1*. Even though the XRD results show that the best crystalline quality of $Al_xGa_{1-x}N$ grown on the optimized AlN-based buffer layers is $Al_{0.1}Ga_{0.9}N$, the $Al_xGa_{1-x}N$ with both lower and higher Al contents than x = 0.10 are still of good quality within the small deviation observed.

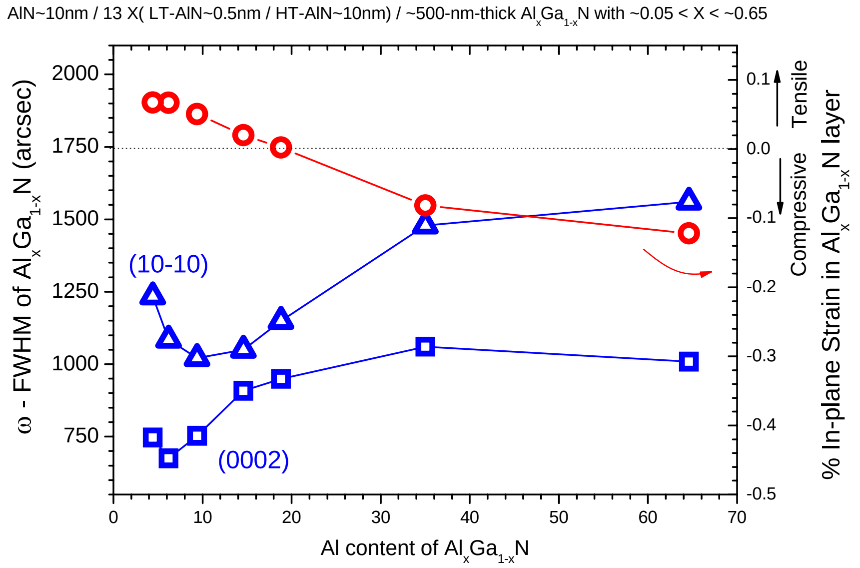

Figure 4.3.4 The ω-FWHMs of the ~450-nm-thick $Al_xGa_{1-x}N$ (0002) and (10-10) reflections and in-plane strain as a function of Al contents

As can be seen in *Fig.4.3.4*, with a higher Al content the in-plane strain in $Al_xGa_{1-x}N$ layers continuously decreases from 0.067% to -0.122%. Here the in-plane lattice constant of the AlGaN layer in comparison to the AlN-SL buffer layer is lower, thus the compressive stress induced on the AlGaN layer can be expected to be reduced with increasing Al content. However, for Al contents higher than x=0.20, the in-plane stress becomes compressive although the still present tensile component from cooling. This result can be understood by a low degree of relaxation when the high Al-content layers are grown on AlN buffer, resulting in a high compressive stress which overcompensates tensile stress from cooling and will be discussed in more detail later in this chapter. In XRD θ/2θ scans of the (0002) reflections shoulder peaks of the high Al-content $Al_{0.20}Ga_{0.80}N$ and $Al_{0.37}Ga_{0.63}N$ samples as depicted in *Fig.4.3.5* can be observed. This is probably related to the presence of differently strained or relaxed states in these layers.

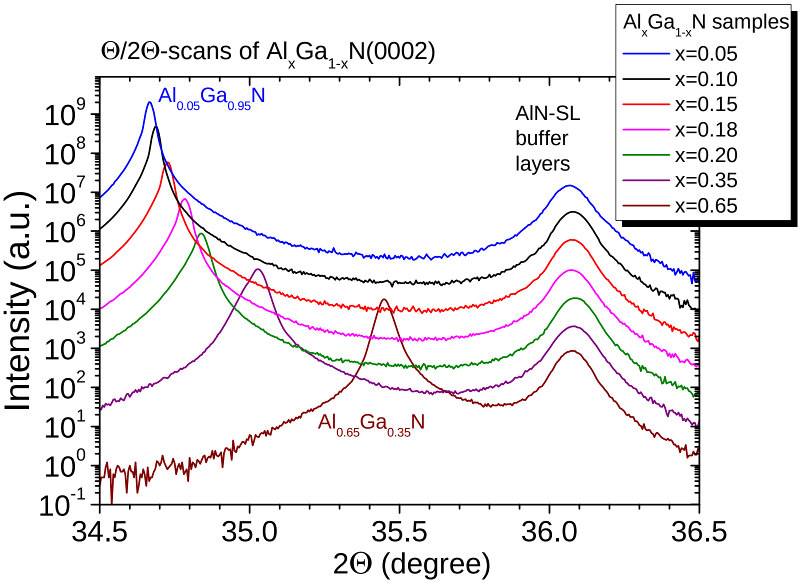

Figure 4.3.5 XRD θ/2θ scans of the (0002) reflections of $Al_xGa_{1-x}N$ with various Al contents

Furthermore, for the samples of ~120-nm-thick $Al_{0.37}Ga_{0.63}N$ and ~65-nm-thick $Al_{0.65}Ga_{0.35}N$ grown on these optimized AlN SL buffer layers, their finite thickness fringes are obviously observed in XRD θ/2θ-scans of the $Al_xGa_{1-x}N$ (0002) reflection as shown in *Fig.4.3.6* and *Fig.4.3.7*, respectively. This indicates an excellent surface and interface quality of the $Al_xGa_{1-x}N$ layers with high Al contents of 0.37 and 0.65. Additionally, the simulations of $Al_{0.37}Ga_{0.63}N$ and $Al_{0.65}Ga_{0.35}N$ yield their thicknesses of 120 and 63 nm that well agree with ~130 and ~65 nm by in-situ optical interference measurements, respectively.

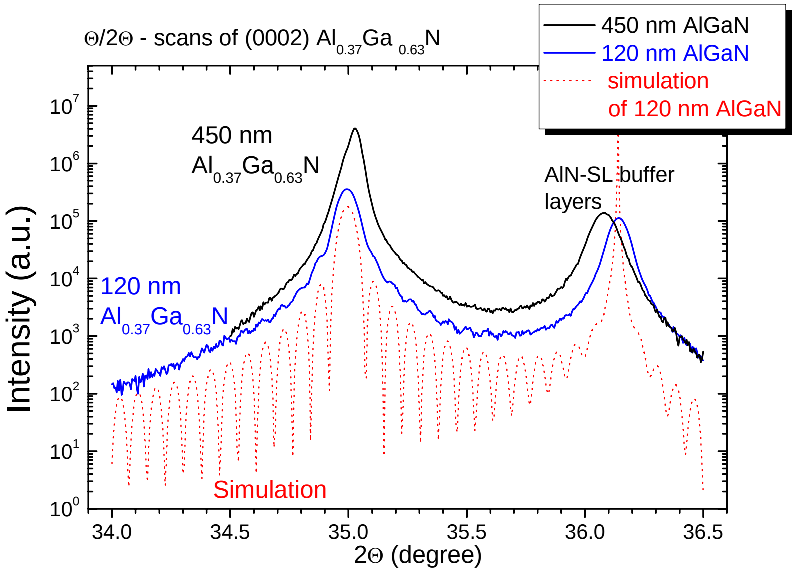

Figure 4.3.6 XRD θ/2θ-scans and simulations of ~120-nm-thick $Al_{0.37}Ga_{0.63}N(0002)$ reflections showing their finite thickness fringes

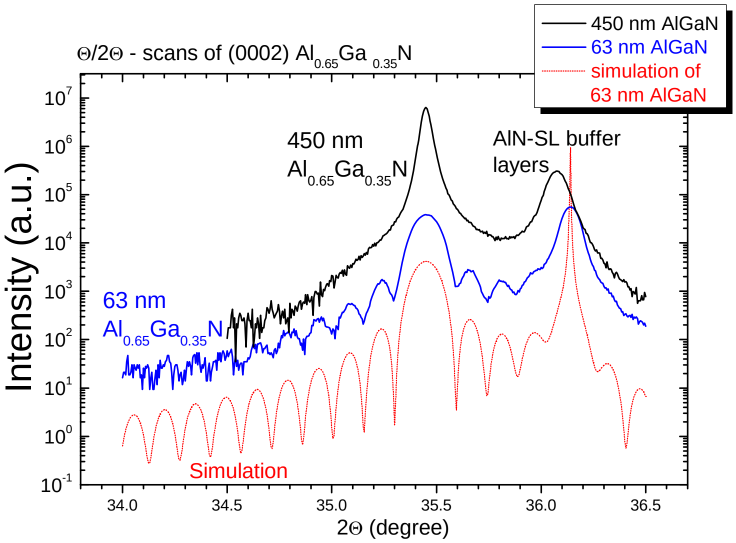

Figure 4.3.7 XRD θ/2θ-scans and simulations of ~65-nm-thick $Al_{0.65}Ga_{0.35}N(0002)$ reflections showing their finite thickness fringes

In order to investigate the crystalline quality and the strain states of the optimized LT-AlN/HT-AlN SL buffer layers in more detail, reciprocal space mapping (RSM) measurements of the (0002) and (11-24) reflections were performed by using a Seifert URD6 diffractometer with a position sensitive detector. These samples of ~450 nm $Al_xGa_{1-x}N$ with various Al fractions from x=0.05 to x=0.65 on the optimized AlN SLs were characterized.

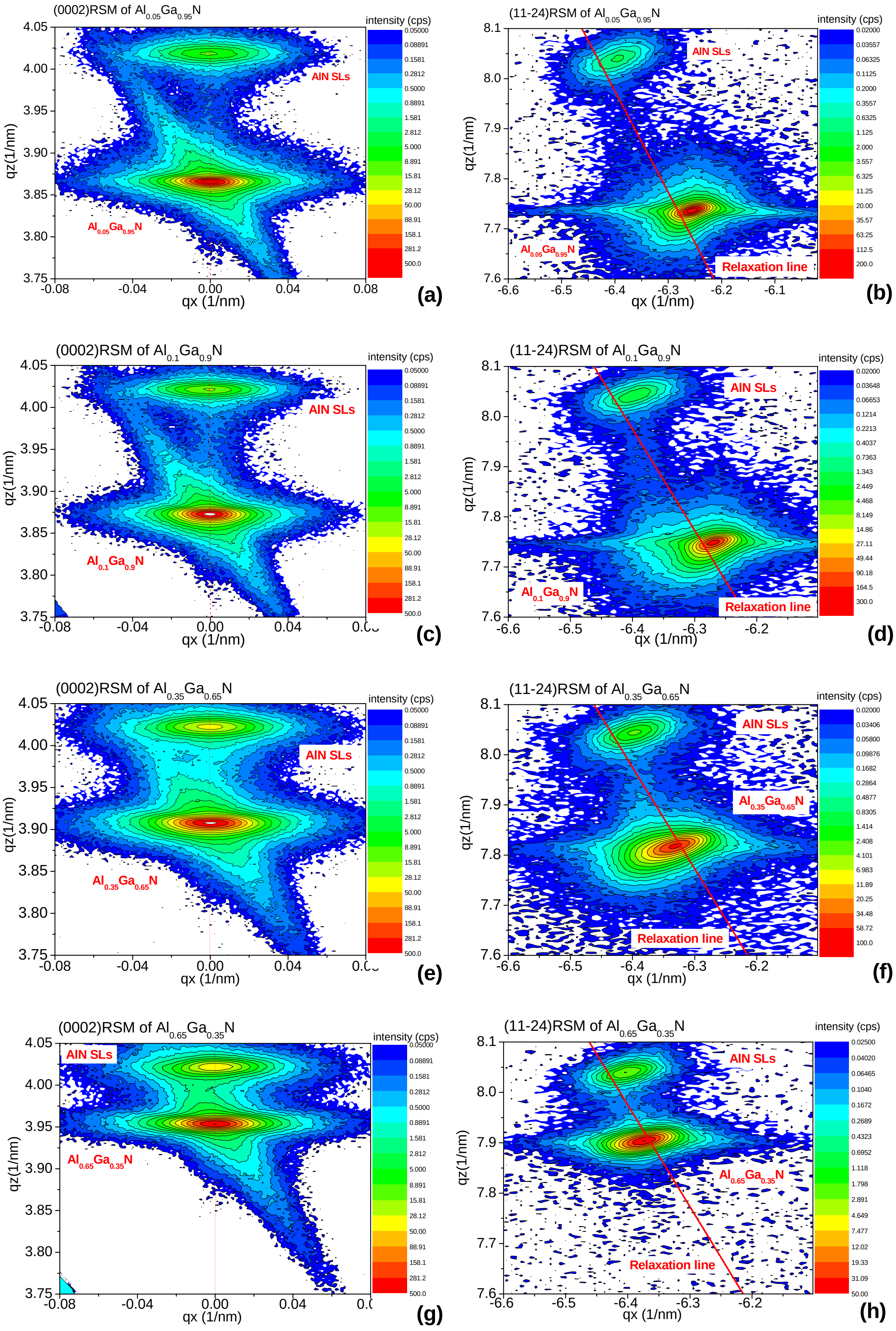

Figure 4.3.8 (a)-(h) Symmetric and asymmetric RSM of the (0002) and (11-24) reflections of $Al_xGa_{1-x}N$ on the optimized AlN-based superlattices

As shown in *Fig.4.3.8 (a), (c), (e), and (g)*, the all symmetry RSM measurements of the $Al_xGa_{1-x}N$(0002) reflections show that the maximum position of the $Al_xGa_{1-x}N$ (0002) reflections aligns to that of AlN-based superlattices for all samples. This results from the same arrangement in their c directions. The maximum position of $Al_xGa_{1-x}N$ with higher Al contents obviously moves closer to the peaks of AlN SLs due to their smaller lattice constants. Broader intensity distribution of the AlN superlattices means to more tilts than that of the $Al_xGa_{1-x}N$ layers.

Simultaneously, the asymmetry RSM measurements of the (11-24) reflections reveal that the maximum position of the $Al_xGa_{1-x}N$ layers does not align to that of the AlN-based superlattices with respect to the different arrangement in their in-plane directions and moved closer to the peaks of the AlN SLs due to their smaller lattice constants as revealed in *Fig.4.3.8 (b), (d), (f), and (h)*. This indicates that the $Al_xGa_{1-x}N$ layers grown on the AlN superlattices are not pseudomorphically grown and the mismatch strain is lower with higher Al contents.

Furthermore these RSM measurements yield more information on the a- and c-lattice constants of all $Al_xGa_{1-x}N$ and AlN SLs. As can be observed in *Fig.4.3.9*, both lattice constants of $Al_xGa_{1-x}N$ considerably decrease when the Al content of $Al_xGa_{1-x}N$ increases. The c-lattice constant of AlN-SLs tends to increase and the a-lattice constant decreases. As followed Poisson's ratio, this would respect to a lower tensile strain in AlN-SLs.

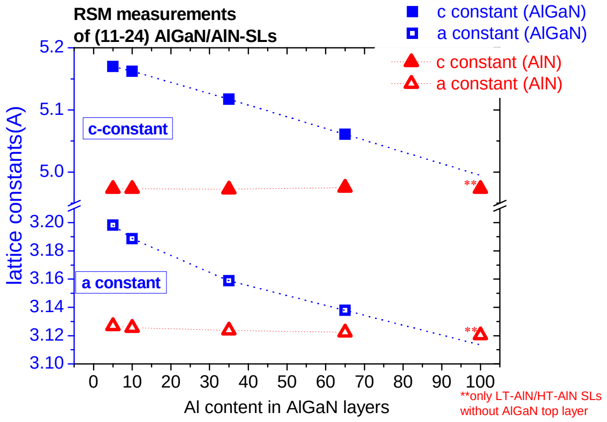

Figure 4.3.9 The a- and c- lattice constants of $Al_xGa_{1-x}N$ and AlN SLs as a function of Al contents

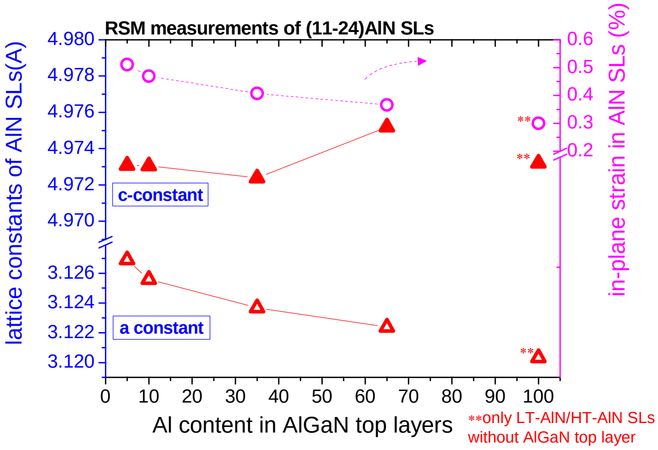

Figure 4.3.10 Lattice constants and residual strain of AlN SLs as a function of Al contents

The reduced in-plane residual strain in AlN-SLs layers relates to the higher Al content of the $Al_xGa_{1-x}N$ or the smaller lattice mismatch between the $Al_xGa_{1-x}N$ and AlN-SLs due to smaller lattice constants of the $Al_xGa_{1-x}N$ with higher Al contents as shown in *Fig.4.3.10*. As a consequence, the residual strain in the $Al_xGa_{1-x}N$ layers is continually reduced until it becomes compressive with Al contents higher than x = ~0.25 as revealed in *Fig.4.3.11*. This result slightly deviates from the results by the conventional XRD and GIID measurements for the compressive strain in $Al_xGa_{1-x}N$ with x > ~0.2 in *Fig.4.3.4*.

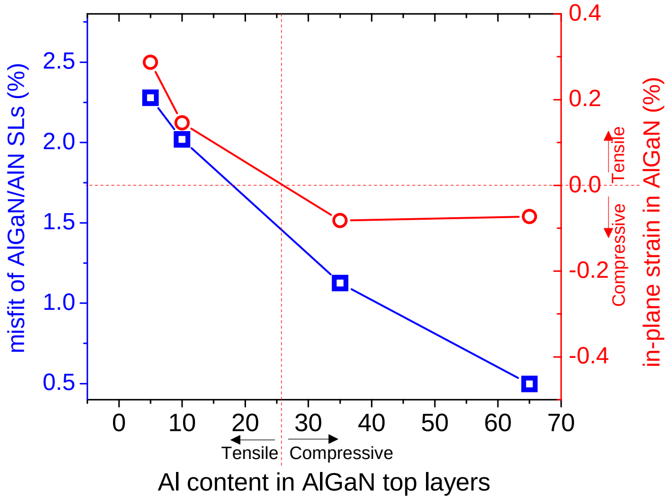

Figure 4.3.11 Misfit of $Al_xGa_{1-x}N$/AlN SLs and in-plane strain in AlGaN as a function of Al contents

All these results show that both $Al_xGa_{1-x}N$ and AlN-SL layers are strained against each other. The AlN-SL layers can induce compressive strain in the $Al_xGa_{1-x}N$ layers and the $Al_xGa_{1-x}N$ layers induced tensile strain in the AlN-SL layers. With a high Al content, the $Al_xGa_{1-x}N$ layers are grown on the AlN-based superlattices not a full relaxation but with the partial compressive strain and during growing time it is probably compressive strain. About the strain engineering by these AlN-SLs, see more details in Chapter 5.

4.3.3. Surface morphology of $Al_xGa_{1-x}N$

The surface morphology of all ~450 nm $Al_xGa_{1-x}N$ layers is crack-free. As observed by Nomarski optical microscopy shown in *Fig.4.3.12*, the surface of the $Al_xGa_{1-x}N$ with a higher Al content appears rougher due to a smaller grain size. As investigated in more detail by AFM measurements, the $Al_xGa_{1-x}N$ with a higher Al content obviously exhibits a smaller grain size, a smaller growth-step width, a higher roughness, and a higher pit density as shown in *Fig.4.3.13 (a) – (d)*. By counting, the pit density on the $Al_{0.05}Ga_{0.95}N$ surface is estimated to about 4.8×10^7 cm^{-2} and 3.8×10^8 cm^{-2} on the $Al_{0.65}Ga_{0.35}N$ surface including nanoparticle density of 2.4×10^9 cm^{-2}. By the 5×5 µm²-scan area, it is clarified that the surface roughness of the $Al_xGa_{1-x}N$ with a higher Al content is higher e.g. the surface roughness 0.703 nm rms of $Al_{0.05}Ga_{0.95}N$, 1.917 nm rms of $Al_{0.10}Ga_{0.90}N$, and 2.318 nm rms of $Al_{0.65}Ga_{0.35}N$.

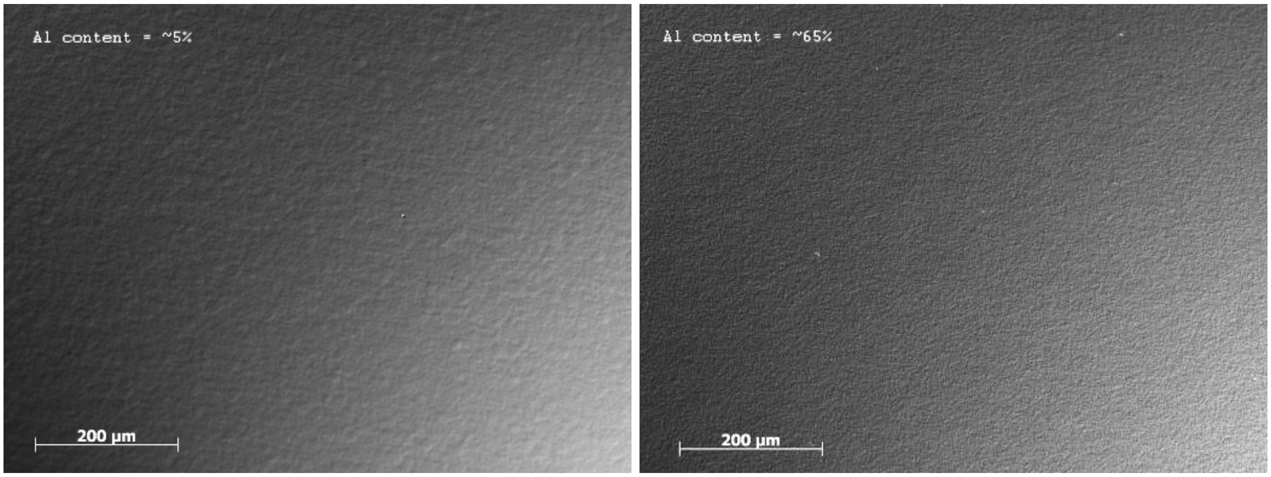

Figure 4.3.12 Optical micrograph of $Al_{0.05}Ga_{0.95}N$ surface (left) and $Al_{0.65}Ga_{0.35}N$ surface (right), showing smaller grain size with higher Al content

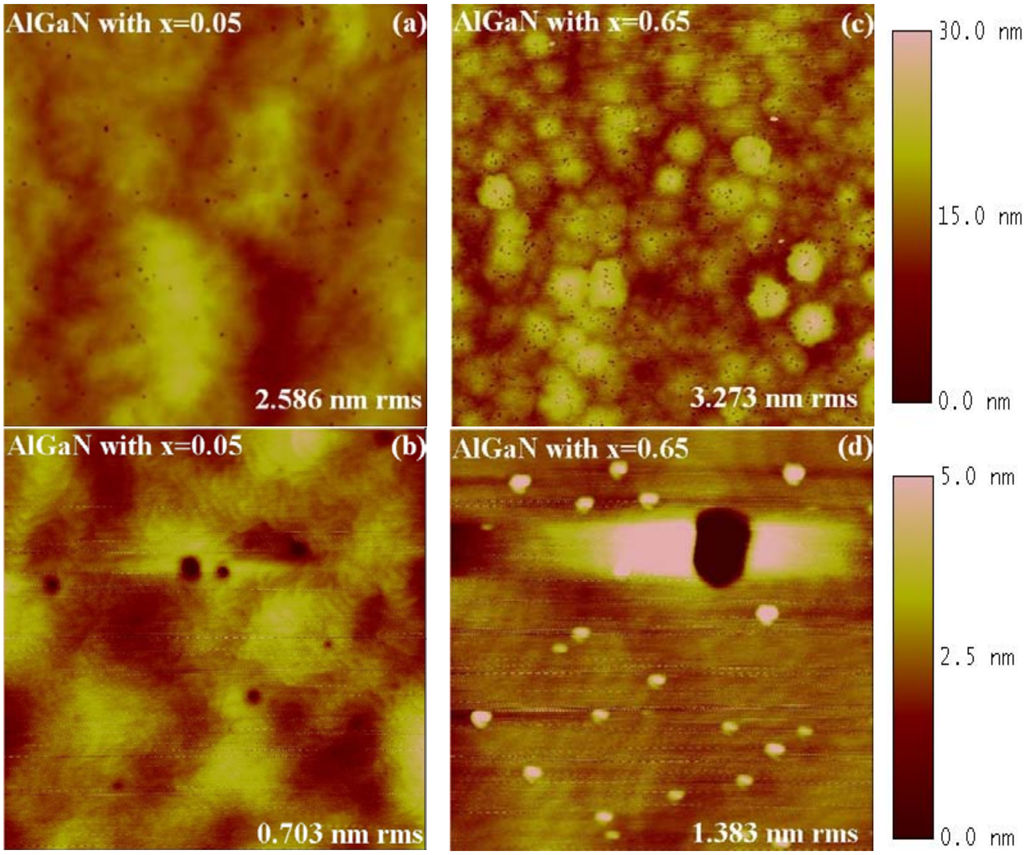

Figure 4.3.13 AFM images of $Al_{0.05}Ga_{0.95}N$ of 20×20 μm^2 scans (a) and 5×5 μm^2 scans (b) and images of $Al_{0.65}Ga_{0.35}N$ of 20×20 μm^2 scans (c) and 1×1 μm^2 scans (d).

As grown on the optimized AlN-seed and LT-AlN/HT-AlN superlattice buffer layers, the ~450-nm-thick $Al_xGa_{1-x}N$ with Al content up to x=0.65 are achieved with a good crystalline quality and good surface morphology without cracking. To further develop the AlGaN-based UV optoelectronic devices, the optical properties of $Al_xGa_{1-x}N$ layers were investigated by cathodoluminescence (CL) measurements.

4.3.4. Optical properties of $Al_xGa_{1-x}N$

$Al_{0.1}Ga_{0.9}N$ and $Al_{0.65}Ga_{0.35}N$ layers were investigated by CL measurements. *Fig.4.3.14* show near-bandgap luminescence peaks in the UV region i.e. 3.746 and 5.399 eV corresponding to 330 and 240 nm of $Al_{0.1}Ga_{0.9}N$ and $Al_{0.65}Ga_{0.35}N$, respectively. In addition, the linewidth or FWHM of the near-bandgap emission peak of $Al_{0.1}Ga_{0.9}N$ is narrow with 72 meV and a very high emission intensity compared with the weak yellow luminescence indicating a very good optical quality of the $Al_{0.1}Ga_{0.9}N$ layer. For $Al_{0.65}Ga_{0.35}N$, the linewidth of the near-bandgap emission peak is broader with 217 meV due to alloy broadening with increasing Al content. The inhomogeneity of Al contents in $Al_{0.65}Ga_{0.35}N$ layers is observed in CL wavelength mapping as shown in *Figure 4.3.15.* One can see a fluctuation of the dominating peak wavelength from 251 to 249.5 nm. Still a high emission intensity compared with the very weak yellow luminescence is observed also indicating a good optical quality of the $Al_{0.65}Ga_{0.35}N$ layer.

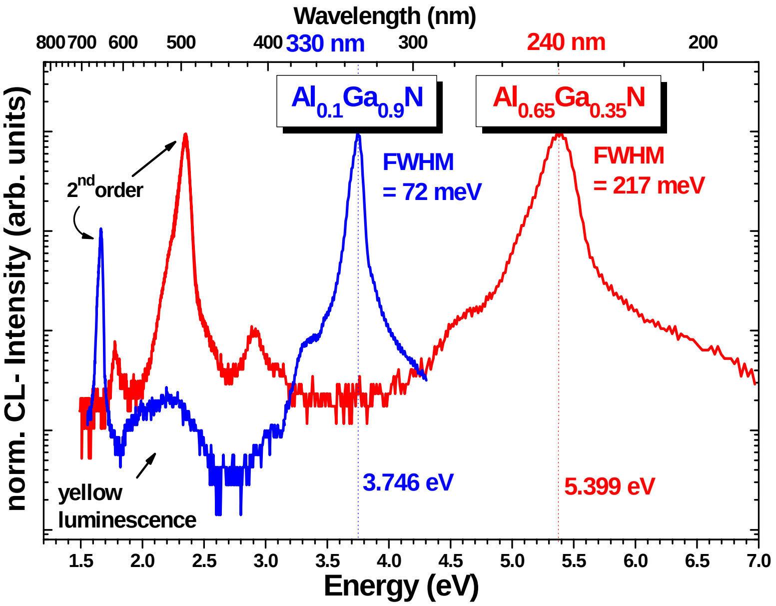

Figure 4.3.14 The CL measurements showing the near-bandgap peaks of $Al_{0.10}Ga_{0.90}N$ and $Al_{0.65}Ga_{0.35}N$

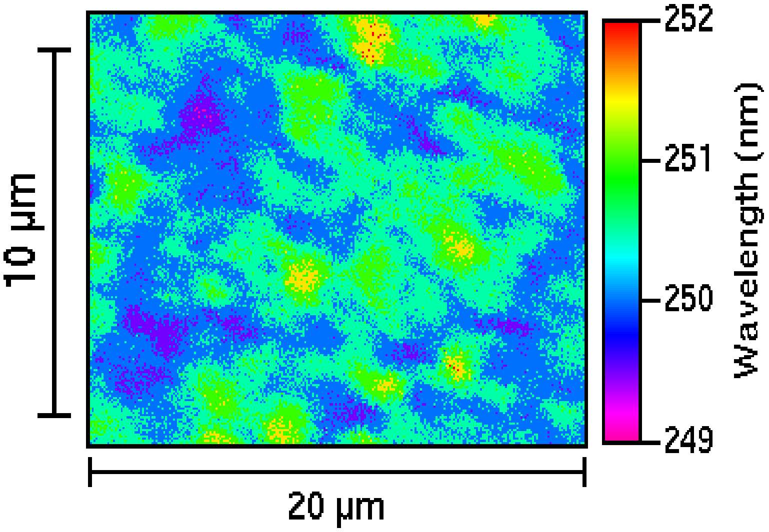

Figure 4.3.15 CL wavelength mapping of the $Al_{0.65}Ga_{0.35}N$ *sample visualizing the alloy fluctuation at the surface.*

In summary, by reducing the dislocation density and controlling strain in the layers by introducing optimized LT-AlN/HT-AlN superlattices as buffer layers, crack-free $Al_xGa_{1-x}N$ layers with Al fraction up to x=0.65 and a high crystalline and optical quality are achieved on Si (111) substrates. The optimized AlN-based seeding and superlattice buffer layers are efficient to improve the $Al_xGa_{1-x}N$ layer qualities to develop AlGaN-based UV optoelectronic devices on silicon substrates.

Chapter 5

Strain Engineering

To grow heteroepitaxial $Al_xGa_{1-x}N$ layers on a foreign Si(111) substrate, there are two huge obstacles i.e. the large lattice mismatch of 19% between AlN and Si(111) and 16.9% between GaN and Si(111) [Dadg02, Kros02] and the large different thermal expansion coefficients of 6.8×10^{-6} K^{-1} of AlN [Figg09] and 6.0×10^{-6} K^{-1} of GaN [Rode05] as compared to 3.9×10^{-6} K^{-1} of Si [Mazu09] at 1000K. These problems of stresses and strains in $Al_xGa_{1-x}N$ epilayers originate many causes to reduce the crystalline quality and cracking after cooling down. In order to overcome these problems, the efficient buffer layers not only improve the crystalline quality that characterized by ex-situ HRXRD measurements but also induce compressively strained $Al_xGa_{1-x}N$ epilayers to compensate the thermal-mismatch tensile strain of the Si substrate during cooling down. Therefore the strain engineering of growing epilayers is necessary to determine by in-situ curvature measurements of optical interferences. In this chapter, the strain engineering of $Al_{0.1}Ga_{0.9}N$ layers by AlN-based SL buffer layers and LT-AlN interlayers are presented and discussed in their influences.

5.1. Strain engineering by AlN-based SL buffer layers

As mentioned in 4.2.2, when the growth time or thickness of LT-AlN of superlattice buffer layers was decreased and the HT-AlN thickness increased simultaneously until LT-AlN of ~0.5 nm and HT-AlN of ~10.5 nm in nominal thickness approximated by their growth rates, the best crystalline quality of $Al_{0.1}Ga_{0.9}N$ was obtained and in-plane residual tensile strain in $Al_{0.1}Ga_{0.9}N$ layers tended to be reduced. Besides ex-situ measurements of XRD techniques, the stresses in layers during growth were observed by in-situ curvature measurements to evaluate the impact of LT-AlN and HT-AlN to induce tensile or compressive stresses in growing epilayers.

In this section, the strain engineering of growing $Al_{0.1}Ga_{0.9}N$ layers by different LT-AlN/HT-AlN SLs are revealed and discussed first. Next, the strain engineering by optimized LT-AlN/HT-AlN SLs of ~1 μm $Al_{0.1}Ga_{0.9}N$ layers and the last the strain engineering by an inserting LT-AlN interlayer between the $Al_{0.1}Ga_{0.9}N$ layers thicker than ~1 μm are presented and discussed.

First, two samples of $Al_{0.1}Ga_{0.9}N$ layers were grown on different LT-AlN/HT-AlN SLs. Sample A was ~450 nm $Al_{0.1}Ga_{0.9}N$ layers on the ~230 nm superlattice buffer layers of thicker LT-AlN layers of ~16 nm for 4 minutes and thinner HT-AlN layers of ~1.5 nm for 1 minute and sample

B was the ~130 nm SLs of thinner LT-AlN layers of ~4 nm for 1 minute and thicker HT-AlN layers of ~6 nm for 4 minutes. Their structures were summarized in *Table 5.1*.

Table 5.1 two samples of $Al_{0.1}Ga_{0.9}N$ on LT-AlN/HT-AlN SLs with different thicknesses

Sample	**Sample structure**
A	~450 nm $Al_{0.1}Ga_{0.9}N$/ 13×(~16 nm LT-AlN/~1.5 nm HT-AlN) SLs/ ~10 nm AlN/Si
B	~450 nm $Al_{0.1}Ga_{0.9}N$/ 13×(~4 nm LT-AlN/~6 nm HT-AlN) SLs/ ~10 nm AlN/Si

The curvature measurements during AlN-SL growth show that there are tensile stresses in both growing epilayers with a higher increasing tendency of sample A than that of sample B until after the AlN-SL growth by the tensile stresses in layers of +5.16 and +4.52 GPa, respectively. During $Al_{0.1}Ga_{0.9}N$ growth, the curvature measurements show that there are compressive stresses in both growing epilayers with a stronger compressive stress in layers of sample B than that of sample A with reducing tensile stresses in layers of +0.12 and +0.47 GPa after the $Al_{0.1}Ga_{0.9}N$ growth, respectively as presented in *Fig.5.1.1*. The approximated stresses in each layer are determined by the well-known Stoney's formula in case for $h_f << h_s$ as explained in section 3.3.

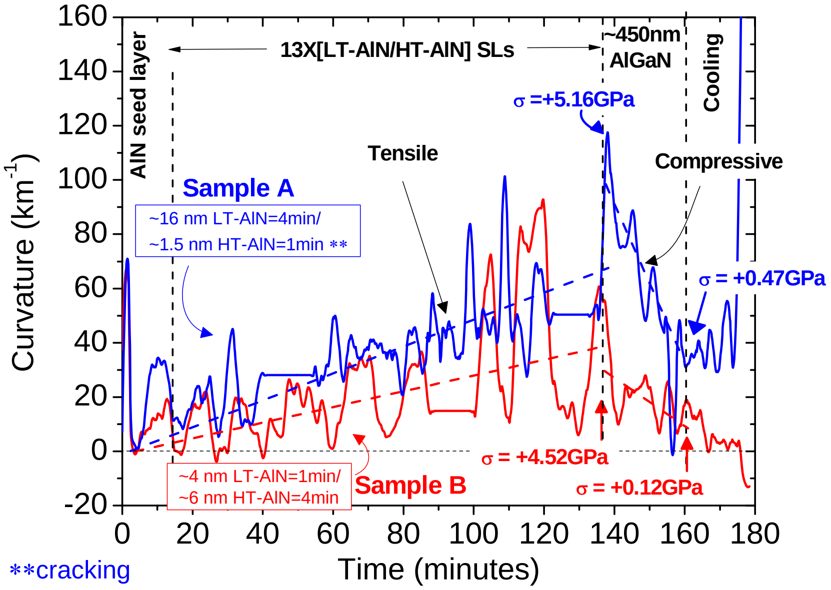

Figure 5.1.1. In situ curvature measurements of 2 samples of ~450 nm $Al_{0.1}Ga_{0.9}N$ on the different thickness of LT-AlN/HT-AlN SL buffer layers

This can be indicated that both AlN-SL structures enable to induce some compressive stresses in $Al_{0.1}Ga_{0.9}N$ layers by the smaller lattice constants of AlN. The stress difference ($\Delta\sigma$) in growing epilayers after AlN-SLs and $Al_{0.1}Ga_{0.9}N$ growths of sample A of 4.69 GPa is slightly larger than that of sample B of 4.40 GPa. The $Al_{0.1}Ga_{0.9}N$ layers on the thicker LT-AlN/thinner HT-AlN SLs of sample A were cracking after cooling because there were still high tensile stresses in these layers before cooling and then leading to an inadequate compensation the thermal-mismatch tensile stresses of Si substrate during cooling. This cracking probably results from the higher tensile stresses in the thicker LT-AlN layers of AlN SLs. The crystalline qualities of the $Al_{0.1}Ga_{0.9}N$ overlayers of both samples are good in a small difference by XRD measurements as shown in *Fig.4.2.2.1*. This probably results from both $Al_{0.1}Ga_{0.9}N$ grown on the higher-quality HT-AlN layer of SLs and perhaps the LT-AlN layers of a reasonable thickness could recrystallize to improve their quality during a ramping and stabilizing growth temperature for the subsequent HT-AlN growth. Meanwhile the high quality of HT-AlN layers lead to fewer threading dislocations and the very-thin LT-AlN could reduce the thermally induced tensile stresses in HT-AlN layers as same as the principle of strain engineering by an inserting of LT-AlN interlayer into the thick GaN or $Al_xGa_{1-x}N$ growth [Aman98, Dadg00, Bläs02, Reih03]. As a consequence, the HT-AlN buffer layers with more relaxation and higher quality were obtained.

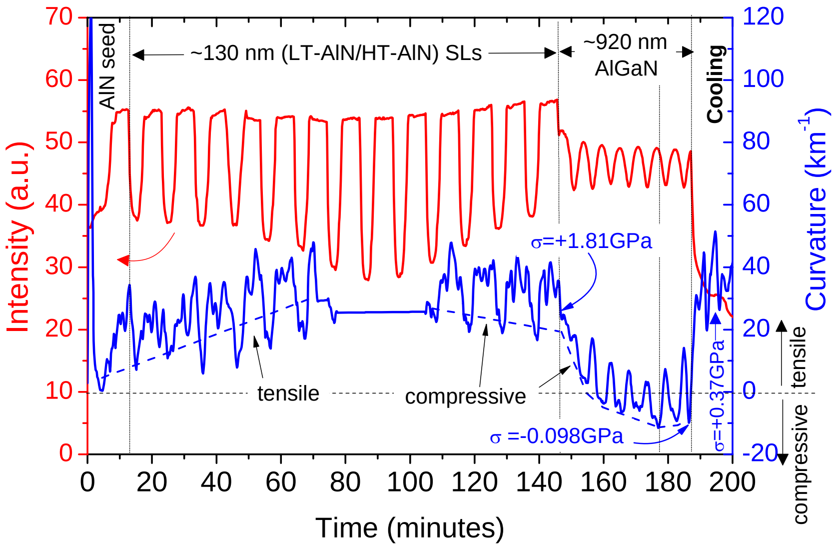

Figure 5.1.2. In situ curvature measurement and reflective intensity of ~920 nm $Al_{0.1}Ga_{0.9}N$ / ~130 nm LT-AlN/HT-AlN SL buffer layers showing the compressive stress in $Al_{0.1}Ga_{0.9}N$ layers

For in situ curvature measurements of the sample of thicker ~920 nm crack-free $Al_{0.1}Ga_{0.9}N$ on the improved ~130 nm LT-AlN/HT-AlN SL buffer layers as can be seen in *Fig.5.1.2,* the optical reflectivity was observed the oscillations of optical interferences of two laser beams obviously. It could be implied to the good and smooth surface morphology of these epilayers.

Meanwhile, the curvature measurements of the first few periods of AlN-SL growth presented that there are tensile stresses in growing epilayers and compressive stresses in during growth of the last few periods until after this SL growth by the tensile stress of +1.81 GPa. Around the middle of SL growth the reflectivity could be not detected because of the destructive interference at that related thickness. Moreover, it could be observed that the fluctuations of curvatures and reflectivity corresponded with the fluctuations of growth temperature of AlN layers i.e. by decreasing the growth temperature of LT-AlN the curvatures were also decreasing and with an increasing growth temperature of HT-AlN the curvatures were also increasing due to the thermally induced tensile stress in layers. At the end of the AlN-SL growth, there was a nearly balance of all stresses with nearly flat curvatures indicating to the nearly relaxed state of the AlN-SL growth. This proves that the optimized LT-AlN layers could be able to reduce the thermal stresses or strains in AlN-SL layers. For the $Al_{0.1}Ga_{0.9}N$ growth, there were continuously compressive stresses in growing epilayers until the $Al_{0.1}Ga_{0.9}N$ thickness of ~690 nm with the maximum compressive stress of -0.111 GPa and when the $Al_{0.1}Ga_{0.9}N$ layers were grown in thicker, the curvatures were slightly increased until after the growth of ~920 nm $Al_{0.1}Ga_{0.9}N$ layers by a compressive stress of -0.098 GPa. This result indicates to the $Al_{0.1}Ga_{0.9}N$ growth in thicker than ~690 nm with increased tensile stresses in layers. Therefore the strain engineering of LT-AlN interlayer is required to compensate these induced tensile stresses as detailed in topic 5.2. Although the curvature measurements show a tensile stress of +0.37GPa in the $Al_{0.1}Ga_{0.9}N$ layers after cooling down, there was no cracking in layers. It means to the sufficient strain compensation in the $Al_{0.1}Ga_{0.9}N$ layers by such these LT-AlN/HT-AlN SL buffer layers. Additionally the in-plane residual tensile strain in these $Al_{0.10}Ga_{0.90}N$ layers is a small value of 0.083% by XRD measurements.

When the sample of ~1.4 μm $Al_{0.10}Ga_{0.90}N$ was grown on ~140 nm LT-AlN/HT-AlN SL buffer layers with an inserting LT-AlN interlayer, the in situ curvature and reflectivity measurements analogously presented that there were continuously compressive stresses in $Al_{0.10}Ga_{0.90}N$ layers of -0.26 GPa before inserting LT-AlN interlayer, -0.58 GPa after the growth and +0.11 GPa after cooling down as shown in *Fig.5.1.3*. There was no cracking in layers indicating to the efficient strain compensation in the $Al_{0.1}Ga_{0.9}N$ layers thicker than 1 μm by inserting the AlN interlayers. Additionally the in-plane residual tensile strain in these $Al_{0.10}Ga_{0.90}N$ layers is a smaller value of 0.054%.

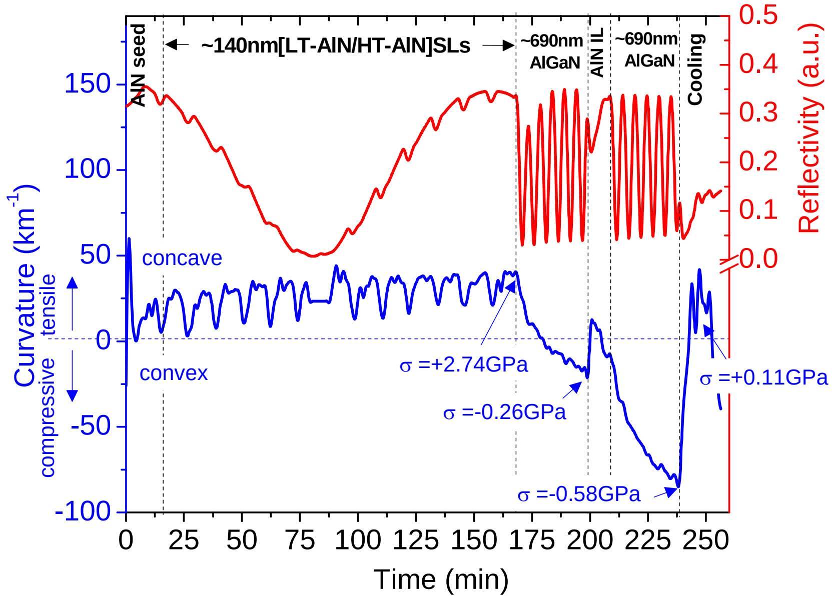

Figure 5.1.3. In situ curvature measurement and reflective intensity of ~1.4 µm $Al_{0.10}Ga_{0.90}N$ / ~140 nm LT-AlN/HT-AlN SL buffer layers showing the compressive stress in $Al_{0.10}Ga_{0.90}N$ layers

5.2. Strain engineering by AlN interlayers

In general, the maximum thickness of crack-free epilayers grown on Si substrate is about 1 µm without inserting interlayers [Kros02, Ragh05a]. As mentioned above and can seen in *Fig.5.1.2*, after the epilayers are grown thicker than the critical thickness of the maximum induced compressive strain in $Al_{0.10}Ga_{0.90}N$ layers by the optimized buffer layers the compressive stress in epilayers turns to be tensile stress continuously by the thermal-mismatch induced tensile strain of the Si substrate until cracking occurs during cool down. Therefore the AlN interlayers play a role to induce the compressive strain in the subsequent $Al_{0.10}Ga_{0.90}N$ layers further and not reduce the $Al_{0.10}Ga_{0.90}N$ quality.

In this section, optimization of LT-AlN interlayers by varying growth temperature for thick, crack-free $Al_{0.1}Ga_{0.9}N$ growth is presented and discussed in their impacts on the $Al_{0.1}Ga_{0.9}N$ quality. Additionally, two samples of different AlN-IL structures of two sets of LT-AlN and HT-AlN with their different thicknesses are revealed and discussed.

The samples of ~690nm $Al_{0.1}Ga_{0.9}N$ / LT-AlN IL / ~690nm $Al_{0.1}Ga_{0.9}N$ / AlN SLs / Si(111) with a variation of AlN-IL growth temperature from 630°C to 900°C were grown. In-situ curvature measurements of all samples present that there are compressive stresses in both parts of $Al_{0.1}Ga_{0.9}N$ layers induced by the optimized AlN superlattices and LT-AlN interlayers as depicted in *Fig.5.2.1*. Due to a difference in original bowing of Si substrates, the efficiency of LT-AlN interlayers to induce compressive stresses in $Al_{0.1}Ga_{0.9}N$ layers are determined by a difference of stresses ($\Delta\sigma$) in growing epilayers after AlN-IL growth and AlGaN growth and the largest stress difference of 0.49 GPa was obtained by LT-AlN IL at 700°C as shown in *Fig.5.2.2* and *Table 5.2*. It can be observed that the stress difference tends to be decreased with a higher AlN-IL growth temperature than 700°C due to an increase in thermally induced tensile stress and tensile grain coalescence stresses of smoother epilayers. By Nomarski optical microscopy, the surface morphologies of all $Al_{0.1}Ga_{0.9}N$ samples after cooling down appear as smooth crack-free surface. With a higher AlN-IL growth temperature, the $Al_{0.1}Ga_{0.9}N$ surface tends to be smoother for example the surface of $Al_{0.1}Ga_{0.9}N$ on AlN-IL of 700°C appears rougher than that of 900°C as revealed in *Fig.5.2.3*.

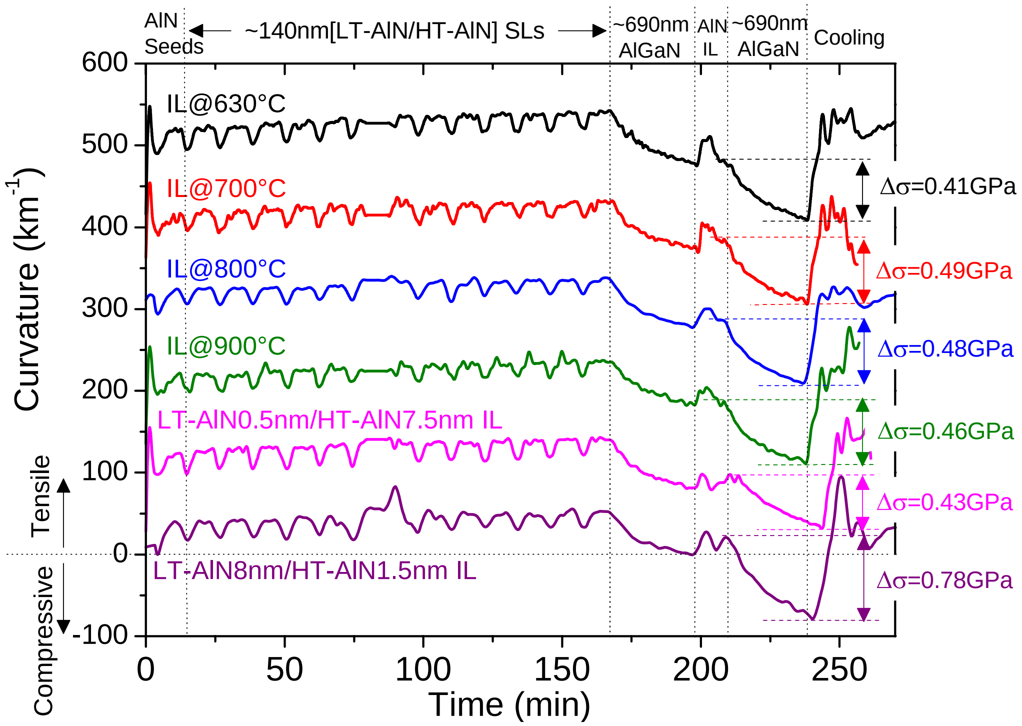

Figure 5.2.1. In situ curvature measurement of ~1.4 μm $Al_{0.1}Ga_{0.9}N$ on ~140 nm LT-AlN/HT-AlN SL buffer layers showing the compressive strain in $Al_{0.1}Ga_{0.9}N$ layers

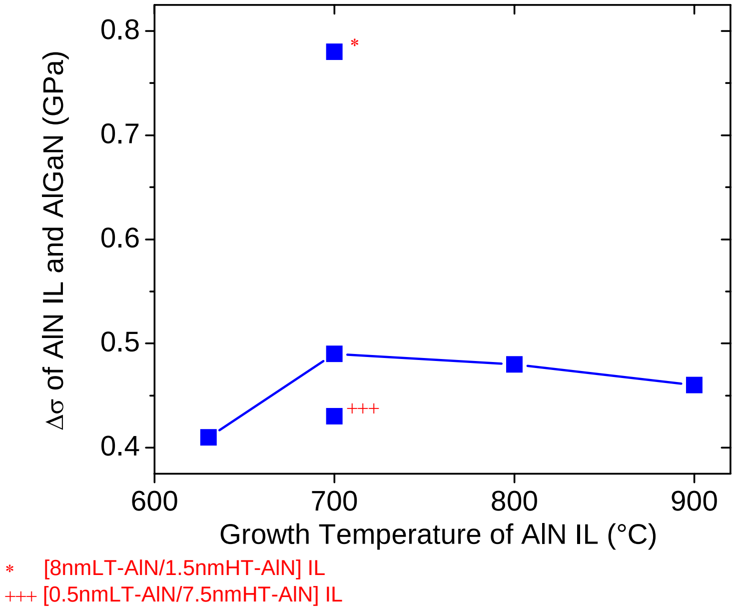

Figure 5.2.2. $\Delta\sigma$ in growing layers after AlN-IL growth and $Al_{0.1}Ga_{0.9}N$ AlGaN growth as a function of growth temperature of AlN IL

Table 5.2. Stress energy in the growing epilayers on Si(111) substrate

AlN interlayer structure	**Stress energy in the growing layers (σ, GPa)**					
	after AlN-SL growth	**after AlN-IL growth**	**after AlGaN growth**	**after cooling down**	**Δσ of IL and AlGaN**	**Δσ of AlGaN and Cooling**
at 630°C	3.21	-0.14	-0.55	0.26	0.41	0.81
at 700°C	2.74	-0.09	-0.58	0.11	0.49	0.69
at 800°C	2.58	-0.09	-0.57	0.17	0.48	0.74
at 900°C	2.67	-0.11	-0.57	0.18	0.46	0.75
[0.5nm LT-AlN at 700°C / 7.5nm HT-AlN at 1200°C]	2.66	-0.02	-0.45	0.18	0.43	0.63
[8.0nm LT-AlN at 700°C / 1.5nm HT-AlN at 1200°C]	3.19	0.25	-0.53	0.15	0.78	0.68

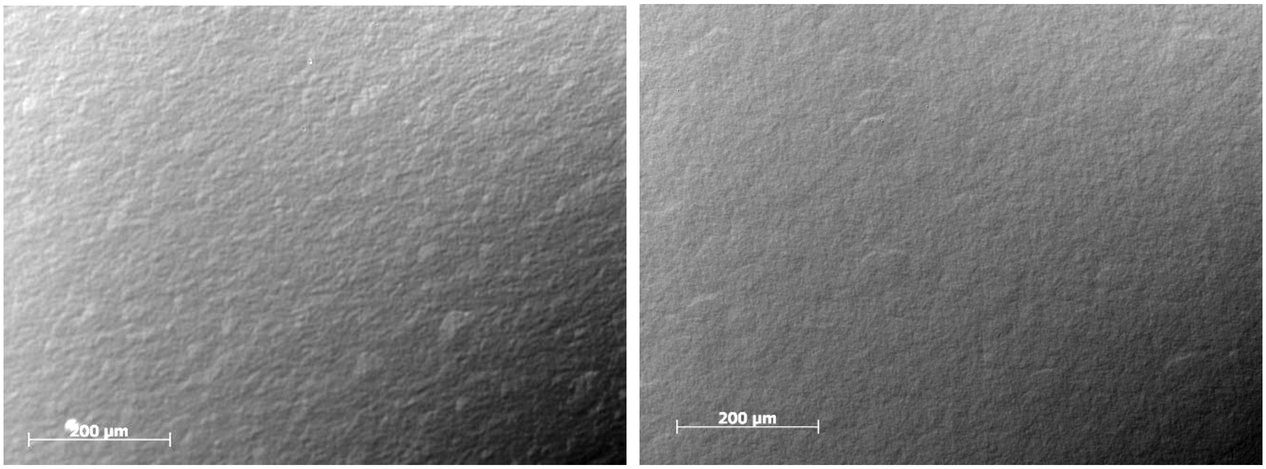

Figure 5.2.3. Optical microscopy showing the surface morphologies of $Al_{0.1}Ga_{0.9}N$ on AlN IL grown at 700°C (left) and 900°C (right)

XRD θ/2θ-scans of the (0002)$Al_{0.1}Ga_{0.9}N$ reflections show that the splitting of the $Al_{0.1}Ga_{0.9}N$ 2θ-peaks are less distinguished with a higher AlN-IL growth temperatures until 900°C it could not be observed as shown in *Fig.5.2.4* and *Fig.5.2.5*. It can be implied that the splitting peaks correspond with different strain or relaxation states in $Al_{0.1}Ga_{0.9}N$ layers before and after inserting LT-AlN interlayers. Since in-plane residual strains in $Al_{0.1}Ga_{0.9}N$ layers on a higher AlN-IL growth temperature decrease continually until 900°C the strain turns to increase as shown in *Fig.5.2.6*. Simultaneously, ω-FWHMs of the (0002) and (10-10) $Al_{0.1}Ga_{0.9}N$ reflections announce that the crystalline qualities of $Al_{0.1}Ga_{0.9}N$ layers grown on AlN-IL of 700°C and 800°C are lower than that of 630°C and 900°C as shown in *Fig.5.2.7*. This means that $Al_{0.1}Ga_{0.9}N$ layers grown on AlN interlayers of 700°C and 800°C are more relaxation but lower quality than that of 630°C and 900°C. This probably results from a lower crystalline quality and more relaxation in layers with a lower growth temperature.

For a- and c-lattice constants of $Al_{0.1}Ga_{0.9}N$ as revealed in *Fig.5.2.6*, there is a smaller deviation of both lattice constants in the same direction i.e. when increasing AlN-IL growth temperature both lattice constants decreases continually until 900°C they turn to increase. This can mainly result from the Al-content fluctuation in $Al_{0.1}Ga_{0.9}N$ layers.

In summary, all AlN interlayers with growth temperature of 630-900°C can compensate tensile mismatch strains in $Al_{0.1}Ga_{0.9}N$ layers after cooling down and with an increasing growth temperature the tensile strains and their crystalline quality tend to be increasing. To compromise between the strain engineering and the quality, the optimized growth temperature of AlN interlayers was 700-800°C.

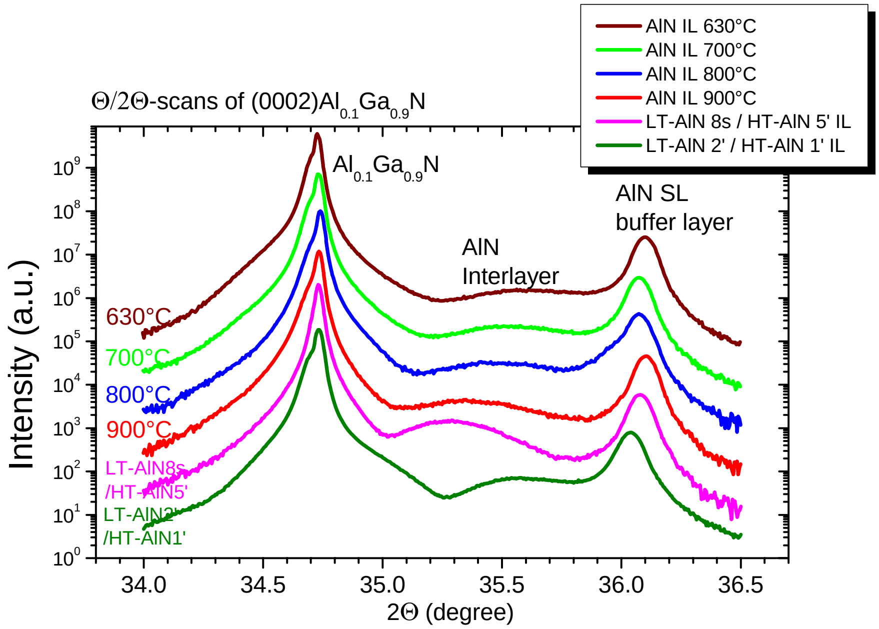

AlN seed layer/ AlN SL buffer layer / $Al_{0.1}Ga_{0.9}N$ (~700nm) / AlN InterLayer / $Al_{0.1}Ga_{0.9}N$(~700 nm)

Figure 5.2.4. XRD θ/2θ-scans of the $Al_{0.1}Ga_{0.9}N(0002)$ reflection with a variation of AlN-IL growth temperature

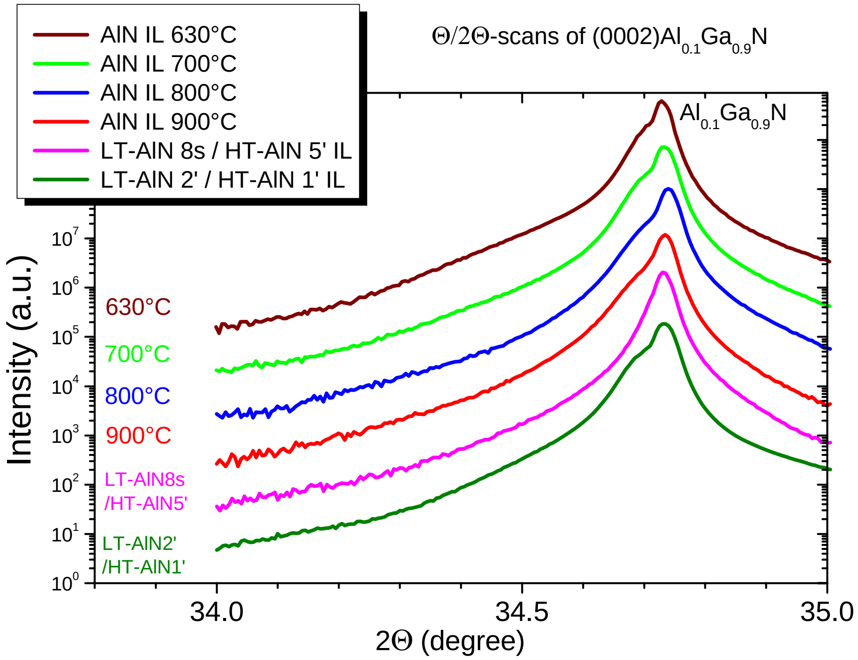

Figure 5.2.5. XRD θ/2θ-scans of the $Al_{0.1}Ga_{0.9}N(0002)$ reflection showing the splitting $Al_{0.1}Ga_{0.9}N$ 2θ-peak of different strain states with a variation of AlN-IL growth temperature

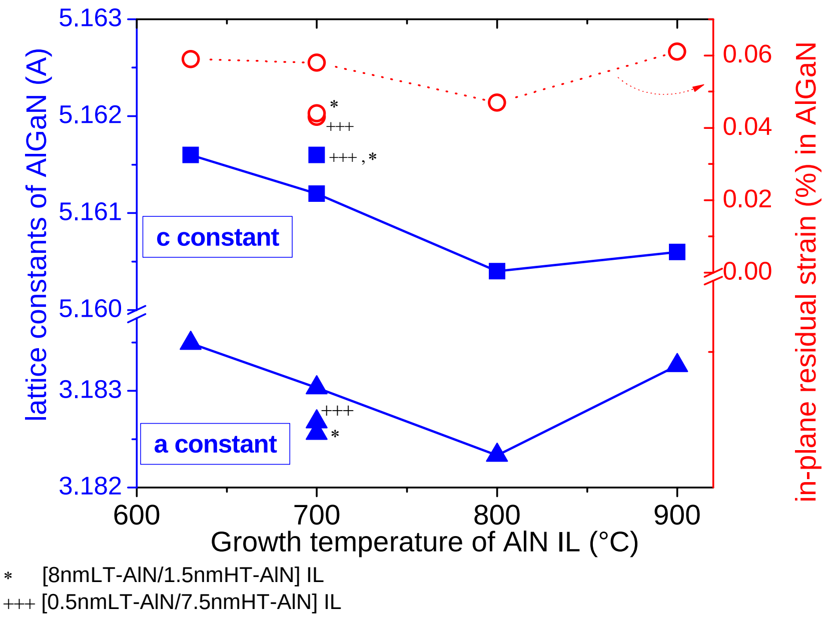

Figure 5.2.6. a- and c- lattice constants and in-plane residual strain of $Al_{0.1}Ga_{0.9}N$ *layers as a function of AlN-IL growth temperature*

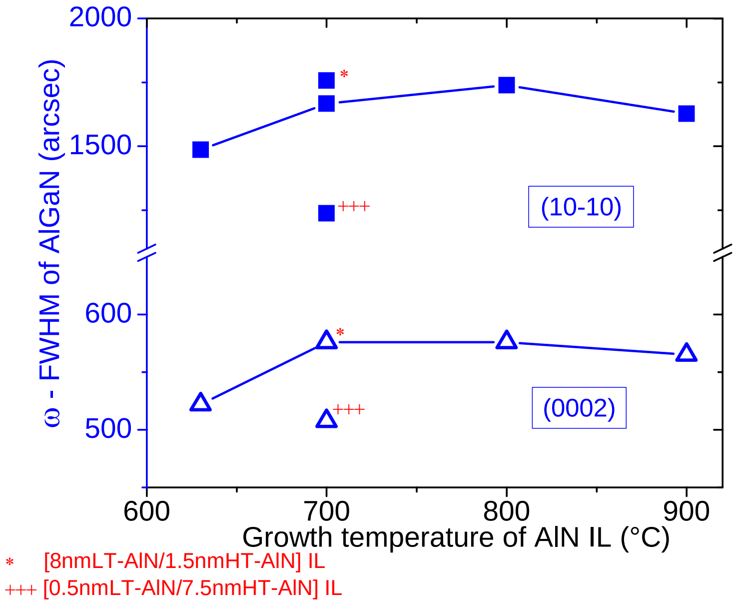

Figure 5.2.7. ω-FWHMs of the $Al_{0.1}Ga_{0.9}N$*(0002) and (10-10) reflections as a function of AlN-IL growth temperature*

Furthermore, there are 2 additional samples of different AlN-IL structures of 2 sets of LT-AlN 700°C and HT-AlN 1200°C with their different thicknesses. By the set of interlayers of a thin HT-AlN of 1.5 nm and a thick LT-AlN of 8 nm, the curvature measurements show the largest stress difference of 0.78 GPa and almost the smallest stress difference of 0.43 GPa by the set of interlayers of a thick HT-AlN of 7.5 nm and a thin LT-AlN of 0.5 nm as shown in *Fig.5.2.2.* and *Table 5.2*. These results can prove that the LT-AlN layers play a role to induce compressive strain in $Al_{0.1}Ga_{0.9}N$ layers more than the HT-AlN layers do. On the other hand, XRD measurements present that the crystalline quality of $Al_{0.1}Ga_{0.9}N$ layers on the set of thin LT-AlN/thick HT-AlN interlayers is improved to the best quality and the worst $Al_{0.1}Ga_{0.9}N$ quality of the set of thick LT-AlN/thin HT-AlN interlayers as shown in *Fig.5.2.7*. Even though the splitting $Al_{0.1}Ga_{0.9}N$ 2θ-peak of the set of thick HT-AlN/thin LT-AlN interlayers can be not observed as depicted in *Fig.5.2.4* and *Fig.5.2.5*, the in-plane residual strain in $Al_{0.1}Ga_{0.9}N$ layers is the lowest due to the smallest a-lattice constant and the largest c-lattice constant as shown in *Fig.5.2.6*. This can be implied that HT-AlN plays a role to improve the $Al_{0.1}Ga_{0.9}N$ quality due to its higher crystalline quality.

In brief, there are the different roles of LT-AlN and HT-AlN layers. The LT-AlN interlayers with a lower crystalline quality and more relaxation can induce a stronger compressive strain in $Al_{0.1}Ga_{0.9}N$ layers but lead to a worse $Al_{0.1}Ga_{0.9}N$ quality. It clarifies that the best strain engineering and the best quality can not be obtained simultaneously. Therefore, it will be possible that one of approaches to achieve the 2 aims is to use the set of interlayers of HT-AlN and LT-AlN with their optimized thicknesses.

Chapter 6
AlGaN-based LED growth

In principle, there are 3 important factors to obtain an efficient LED i.e. high-quality material-based layers, good carrier confinements of QW structure and high carrier injections requiring highly n- and p-type doped layers. After crack-free, high-quality and thick $Al_{0.1}Ga_{0.9}N$ layers were achieved, further investigations were performed to obtain high n- and p-type conductivities and an optimized QW structure. For these AlGaN-based UV LEDs, n-type $Al_{0.1}Ga_{0.9}N$ layers were achieved by Si doping, p-type layers were achieved by $GaN/Al_{0.1}Ga_{0.9}N$ multilayers doped with Mg and the active region of the LED is grown as $GaN/Al_{0.1}Ga_{0.9}N$ multiquantum wells to emit UV light.

In this chapter, optimization of Si and Mg doping in the $Al_{0.1}Ga_{0.9}N$ layers for n- and p-type conductivities are discussed first and then optimization of the $GaN/Al_{0.1}Ga_{0.9}N$ MQW structure. Characterization of the AlGaN-based UV LEDs is presented in the last section.

6.1. Optimization of doping in AlGaN

The high conductivities of n- and p-type regions depend on donor and acceptor activation efficiencies. For Si donors in GaN layers they are almost 100% but for Mg acceptors with their high activation energies about only 1% are typically activated with a decreasing activation for increasing Al-concentration in AlGaN as discussed in section 2.5.3.

6.1.1. n-type conductivity of Si-doped $Al_{0.1}Ga_{0.9}N$

In MOVPE grown materials there are typically some unintentional impurities which can act as compensation centres such as carbon (C), hydrogen (H) and oxygen (O) [Resh05, Wrig02]. In addition to compensation by impurities, intrinsic defects as well as dislocations can partially compensate donors and acceptors and thus prevent an efficient doping of the material [Jone99]. Especially this increases in $Al_xGa_{1-x}N$ layers with a higher Al content [Stam98, McCl98]. Therefore a high conductivity of n-type $Al_xGa_{1-x}N$ layers with $x \geq 0.4$ is not easy to be achieved (see in section 2.5.3).

For this work, $Al_{0.1}Ga_{0.9}N$:Si samples were grown on LT-AlN/HT-AlN SL buffer layers as described in chapter 4.2.1 by standard growth parameters and SiH_4 for Si doping in $Al_{0.1}Ga_{0.9}N$ layers to investigate n-type conductivity.

Capacitance-voltage (C-V) measurements show that the electron concentration (n) in ~450-nm-thick $Al_{0.1}Ga_{0.9}N$:Si layers with a constant Si-doping flow of 0.25 sccm or 2.232 nmol/min is enhanced from 4.9×10^{17} to 5.3×10^{17} cm^{-3} when the number of AlN-SL periods increases from 9 to 11 periods as depicted in *Fig.6.1.1.(left) and (right).* This shows that improving $Al_{0.1}Ga_{0.9}N$ crystalline quality by an increasing number of AlN-SL periods as shown in *Fig.6.1.2* reduces compensation centers in agreement with the results discussed in chapter 4.2.1.

Moreover, additional ~450-nm-thick $Al_{0.1}Ga_{0.9}N$:Si sample grown on improved 13 periods of AlN-SL buffer layer has higher electron density of 6.1×10^{17} cm^{-3} due to higher crystalline quality.

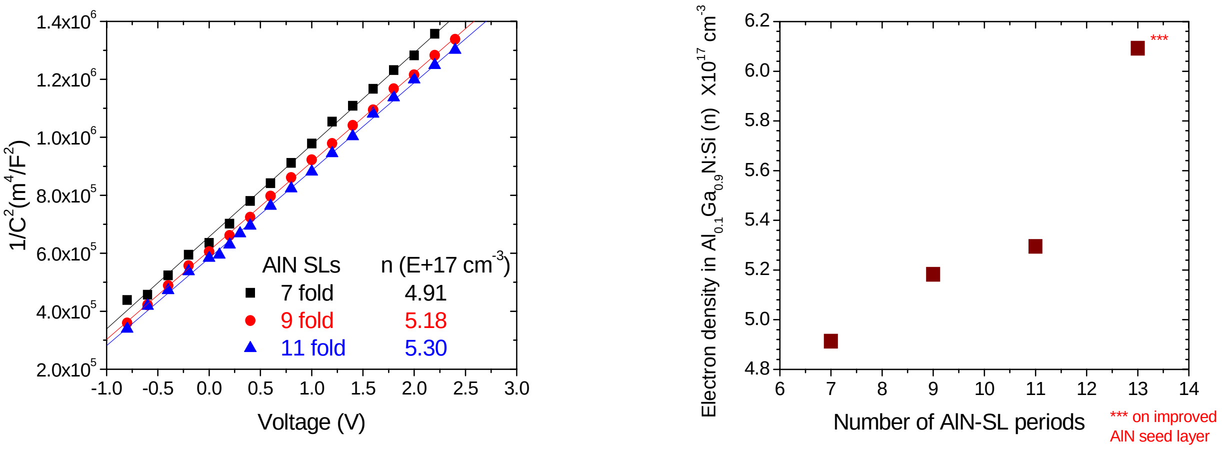

Figure 6.1.1 C-V measurements of $Al_{0.1}Ga_{0.9}N$:Si layers on AlN SLs with varied number of SL periods (left) and the electron density in layers as a function of the number of AlN-SL periods (right)

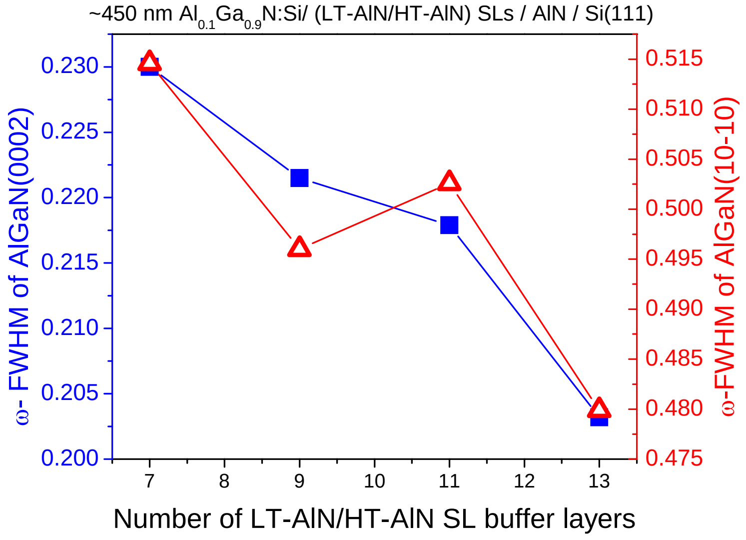

Figure 6.1.2 Decreasing ω-FWHMs of (0002) and (10-10) reflections of $Al_{0.1}Ga_{0.9}N$:Si as a function of the number of AlN-SL periods

Subsequently, $Al_{0.1}Ga_{0.9}N$:Si samples were grown on 13 periods of AlN-SL buffer layers with a variation of the Si flow rate from 0.05 to 0.5 sccm or 0.446 to 4.464 nmol/min and one additional sample with a Si flow rate of 2 sccm or 17.857 nmol/min grown on a further improved AlN buffer layer. With an increasing Si flow rate, the electron concentration of $Al_{0.1}Ga_{0.9}N$:Si layers by C-V measurements increases from 3.7×10^{16} to 2.0×10^{18} cm^{-3} and the additional sample with a Si flow rate of 2 sccm yields a maximum electron density of 2.6×10^{18} cm^{-3} as depicted in *Fig.6.1.3* and *Fig.6.1.4*.

The results in *Fig.6.1.4* show a linear relationship of electron density and Si flow rate in a range from 0.05 – 0.5 sccm. From the data one can predict a compensating acceptor density in the $Al_{0.1}Ga_{0.9}N$ layers of ~2.7×10^{17} cm^{-3}. However, the electron density of the sample with a Si flow rate of 2 sccm only slightly increases from 2.0×10^{18} to 2.6×10^{18} cm^{-3} compared to the sample with 0.5 sccm.

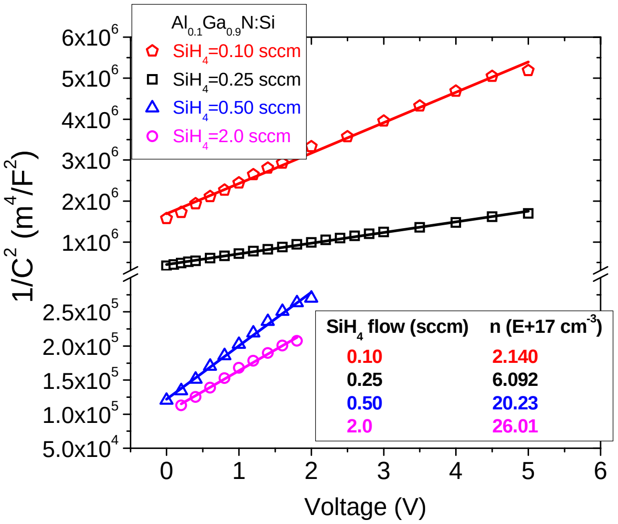

SiH_4 flow (sccm)	n (E+17 cm^{-3})
0.10	2.140
0.25	6.092
0.50	20.23
2.0	26.01

Figure 6.1.3 C-V measurements of $Al_{0.1}Ga_{0.9}N$:Si layers showing an increasing electron density with higher SiH_4 flow rate

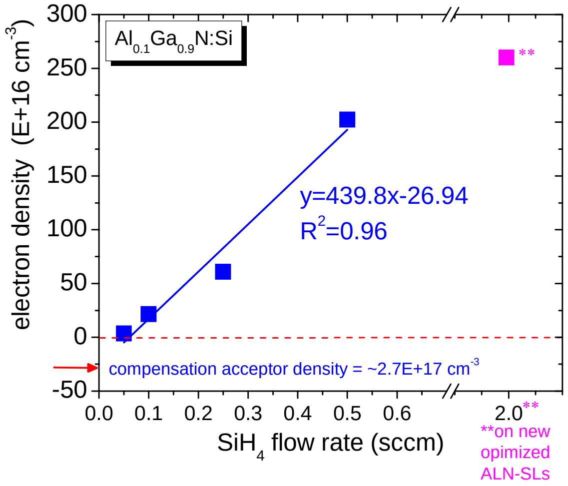

Figure 6.1.4 Electron density of $Al_{0.1}Ga_{0.9}N$:Si layers as a function of SiH_4 flow rate

In additional in-situ curvature measurements during MOVPE growth of the $Al_{0.1}Ga_{0.9}N$:Si layers. it is observed that with a higher Si flow rate of 1 sccm or 8.929 nmol/min, the $Al_{0.1}Ga_{0.9}N$:Si epilayers are stronger tensely stressed than that of lower Si flow rates of 0.1 and 0.5 sccm or 0.893 and 4.464 nmol/min, respectively in *Fig.6.1.5*. As discussed by Dadgar et al. [Dadg07] and Romanov and Speck [Roma03], higher Si doping in GaN epilayers induces stronger tensile stress due to edge dislocation climb which is likely also the case here in the $Al_{0.1}Ga_{0.9}N$ layers.

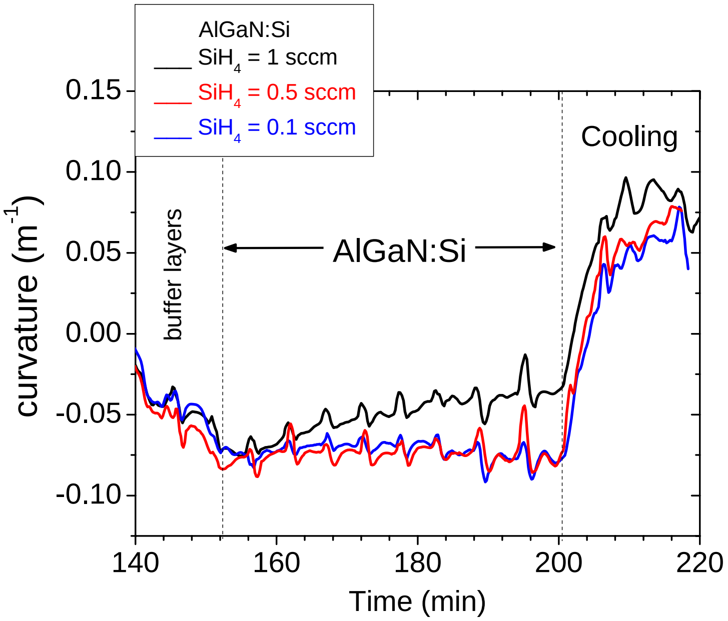

Figure 6.1.5 In situ curvature measurements of $Al_{0.1}Ga_{0.9}N$*:Si with varying* SiH_4 *flow rate*

In HR-XRD and GID measurements, lattice constants, in-plane residual strain and ω-FWHMs around the (0002) and (10-10) reflections of $Al_{0.1}Ga_{0.9}N$:Si layers are obtained as presented in *Fig.6.1.6* and *Fig.6.1.7*. As compared to lattice constants of undoped samples, the c-lattice constant of the Si-doped sample grown with 2 sccm is smaller with a larger a-lattice constant and also higher in-plane tensile strain than that of an undoped sample. These results confirm that Si doping in $Al_{0.1}Ga_{0.9}N$ layers leads to an increased tensile strain in these layers. By varying the Si flow rate in the range from 0.1 to 0.5 sccm, both lattice constants and tensile strain are nearly constant.

In *Fig.6.1.7*, the $Al_{0.1}Ga_{0.9}N$:Si crystalline quality is represented by ω-FWHMs of the (0002) and (10-10) reflections of $Al_{0.1}Ga_{0.9}N$:Si layers with a variation of the Si flow rate. In a range from 0.1 to 0.5 sccm, both ω-FWHMs are nearly constant. As compared to undoped $Al_{0.1}Ga_{0.9}N$, for the Si-doped $Al_{0.1}Ga_{0.9}N$ with a Si flow rate of 2 sccm, both ω-FWHMs of the (0002) and (10-10) reflections increase from 0.17° to 0.26° or 610 to 940 arcsec and from 0.20° to 0.28° or 720 to 1010 arcsec, respectively. This indicates a low impact of Si doping in the $Al_{0.1}Ga_{0.9}N$ layers on the crystalline quality and tensile strain at low doping concentrations. But for a high Si flow rate of 2 sccm the $Al_{0.1}Ga_{0.9}N$ crystalline quality degrades and tensile strain increases probably by Si atoms leading to a more defective growth as the incorporation of point defects or an enhanced 3D growth mode.

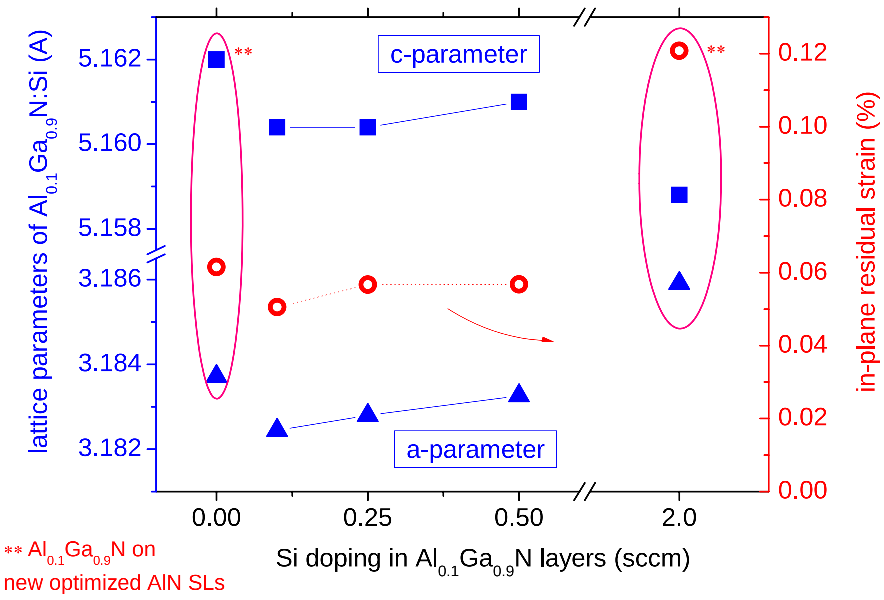

Figure 6.1.6 lattice constants and in-plane residual strain in $Al_{0.1}Ga_{0.9}N$:Si layers as a function of the SiH_4 flow rate (sccm)

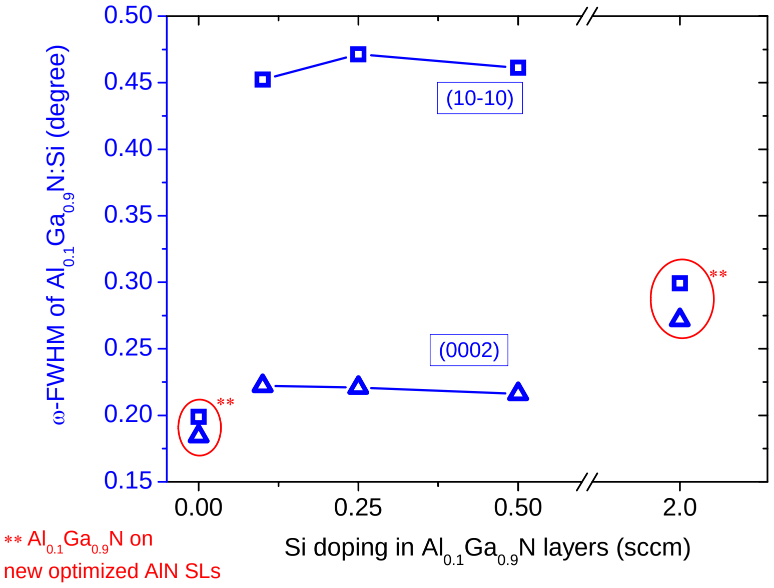

Figure 6.1.7 ω-FWHMs of $Al_{0.1}Ga_{0.9}N$:Si (0002) and (10-10) reflections as a function of SiH_4 flow rate (sccm)

In *Fig.6.1.8*, 10×10 μm^2 AFM measurements exhibit the surface morphologies of undoped $Al_{0.1}Ga_{0.9}N$ *(left)* and $Al_{0.1}Ga_{0.9}N$:Si *(right)* with a SiH_4 flow rate of 2 sccm or 17.857 nmol/min. Si doping results in a smaller grain size and a rougher surface (a increasing roughness from 11.66 nm rms to 25.28 nm rms). These $Al_{0.1}Ga_{0.9}N$ samples nevertheless show a crack-free surface as evaluated by Nomarski microscopy.

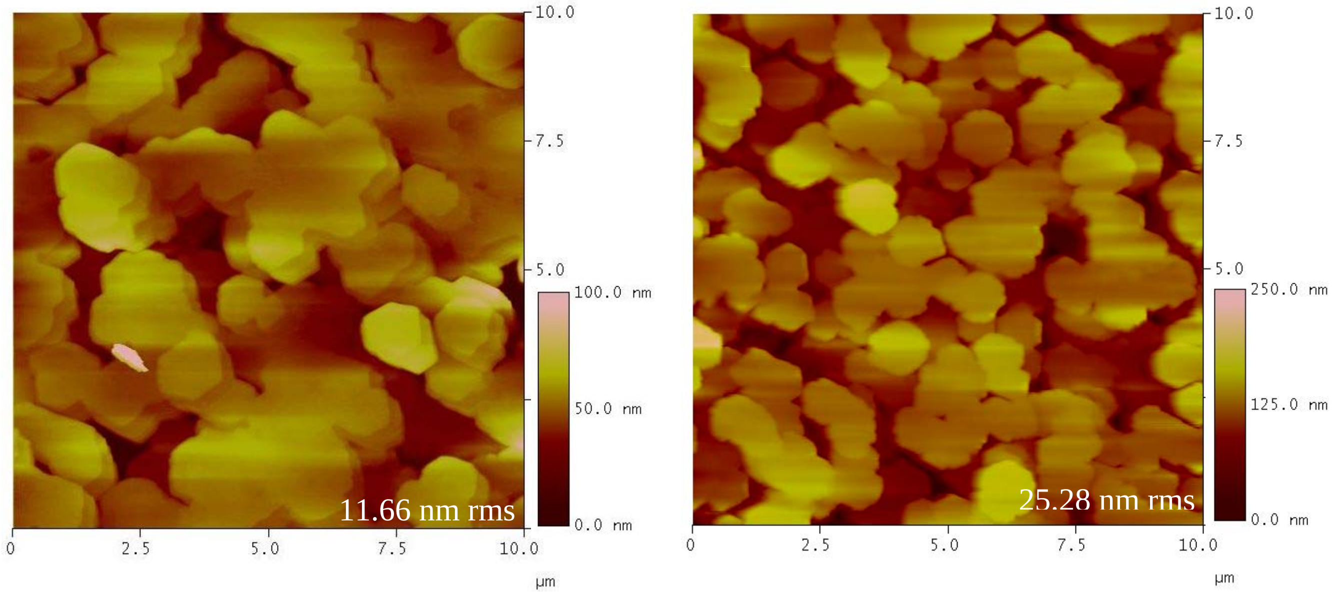

Figure 6.1.8 AFM images showing the surface morphologies of undoped $Al_{0.1}Ga_{0.9}N$ (left) and $Al_{0.1}Ga_{0.9}N$:Si with a smaller gain size and rougher surface (right)

In summary, the Si doping efficiency in $Al_{0.1}Ga_{0.9}N$ layers depends on the $Al_{0.1}Ga_{0.9}N$ quality and high Si flow rates can reduce the $Al_{0.1}Ga_{0.9}N$ quality and increase in-plane tensile strain in the layers.

6.1.2. p-type conductivity

Even though in group-III nitride semiconductors p-type conductivity is difficult to achieve by Mg doping due to a high activation energy and a too low Mg solubility to compensate for the low activation as described in chapter 2.5.3. GaN:Mg layers could be achieved with a hole density of mid 10^{17} cm^{-3} [Kauf00] up to ~10^{18} cm^{-3} [Bayr08, Nagam08]: On Si substrates values for GaN:Mg of 5×10^{17} cm^{-3} [Dadgar] and 8×10^{17} cm^{-3} [Wu07b] are achieved. In $Al_{0.2}Ga_{0.8}N$:Mg a hole density of ~10^{17} cm^{-3} [Yao08, Nagam09] and for $Al_{0.32}Ga_{0.78}N$:Mg of 2×10^{18} cm^{-3} [Obat04] can be achieved whereas no report on that of AlGaN:Mg on Si substrates exists. Here, the growth parameters of $Al_{0.1}Ga_{0.9}N$:Mg layers on Si substrates were investigated to obtain p-type conductivity which could not be achieved by a simple doping approach. While the p-type conductivity of GaN:Mg layers was obtained it could be used to achieve p-type conductivity of Mg-doped GaN/$Al_{0.1}Ga_{0.9}N$ multilayers for AlGaN-based UV LEDs.

6.1.2.1 Mg-doped AlGaN

To determine an approximately suitable Mg concentration the impact of the Mg-doping flow rate on $Al_{0.1}Ga_{0.9}N$:Mg layers was investigated by growing ~1.5 µm $Al_{0.1}Ga_{0.9}N$:Mg samples with one inserted LT-AlN interlayer on undoped $Al_{0.1}Ga_{0.9}N$ / AlN seed layer / Si(111). Cp_2Mg was used for Mg doping and the Mg flow rate was varied from 60 and 120 sccm or 0.153 and 0.307 µmol/min, respectively.

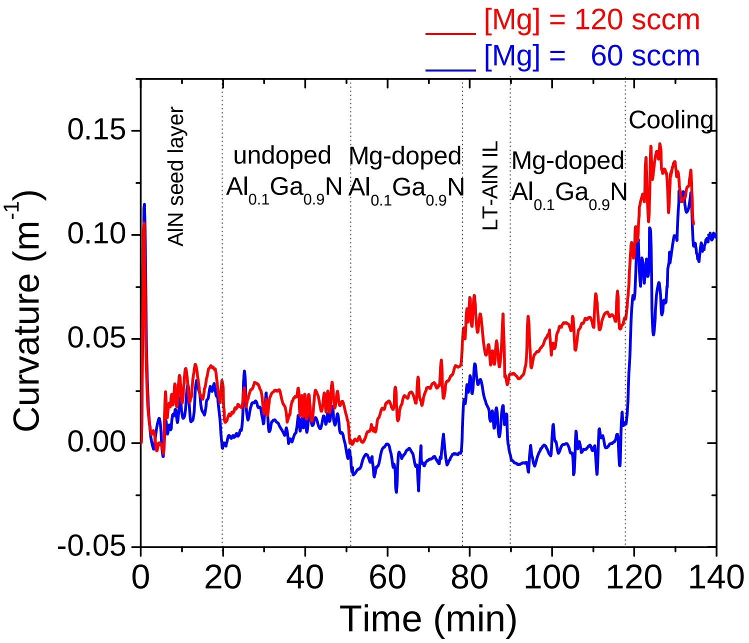

Figure 6.1.9 In situ curvature measurements of $Al_xGa_{1-x}N$:Mg at different Mg-flow-rate

In *Fig.6.1.9*, in situ curvature measurements show that with a higher Mg flow rate, a stronger tensile stress is induced in the $Al_xGa_{1-x}N$:Mg layer. After cooling, the high tensile strains cause a high number of cracks in the layers. Moreover non-optimized growth condition also leads to a lot of defects such as hillocks as shown in *Fig.6.1.10.*

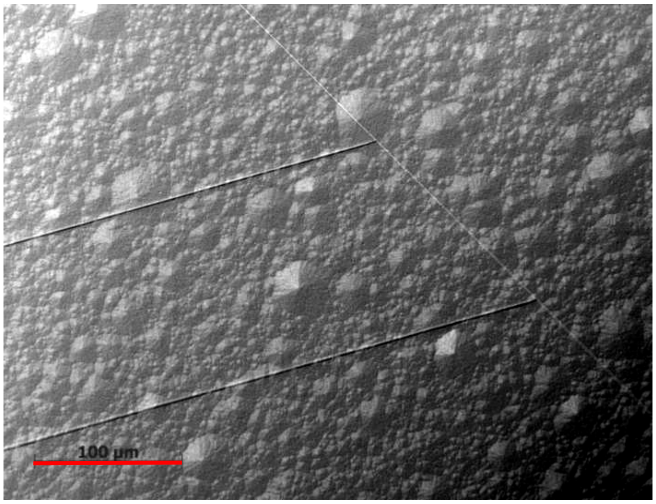

Figure 6.1.10 Nomarski microscope image showing surface morphology of unoptimized $Al_xGa_{1-x}N$:Mg with a high density of differently-sized hillocks and cracks

Capacitance-Voltage (C-V) measurements of some non-optimized $Al_{0.1}Ga_{0.9}N$:Mg samples show n-type conductivity which reduces with an increasing Mg flow rate. This indicates a high density of unintentional donors in the layers.

To optimize the growth parameters of the $Al_{0.1}Ga_{0.9}N$:Mg layers, samples of ~350 nm $Al_xGa_{1-x}N$:Mg with a constant Mg flow rate of 240 sccm or 0.614 µmol/min grown on ~100 nm undoped $Al_{0.1}Ga_{0.9}N$ / ~140 nm optimized LT-AlN/HT-AlN superlattice buffer layers / ~10 nm HT-AlN seeding layer were grown on Si(111) substrates as depicted in *Fig.6.1.11*. As varied from standard growth parameters of $Al_{0.1}Ga_{0.9}N$ layers, the growth temperature of Mg-doped $Al_{0.1}Ga_{0.9}N$ was reduced by 100°C to 1045°C and the flow rates of TMGa and TMAl were reduced by a half to 6 and 10 sccm or 24.23 and 4.33 µmol/min, respectively. There are 5 samples of $Al_{0.1}Ga_{0.9}N$:Mg with different growth parameters as summarized in table 6.1.

Table 6.1 $Al_{0.1}Ga_{0.9}N$:Mg samples with a varia
of growth parameters

Sample	**Varied parameters of $Al_{0.1}Ga_{0.9}N$:Mg**	
	Growth Temp (°C)	Flow rate of TMG, TMA (sccm)
U1	1145	12, 20
U2	1045	6, 10
D1	1045	6, 10
D2	1145	6, 10
D3	1045	12, 20

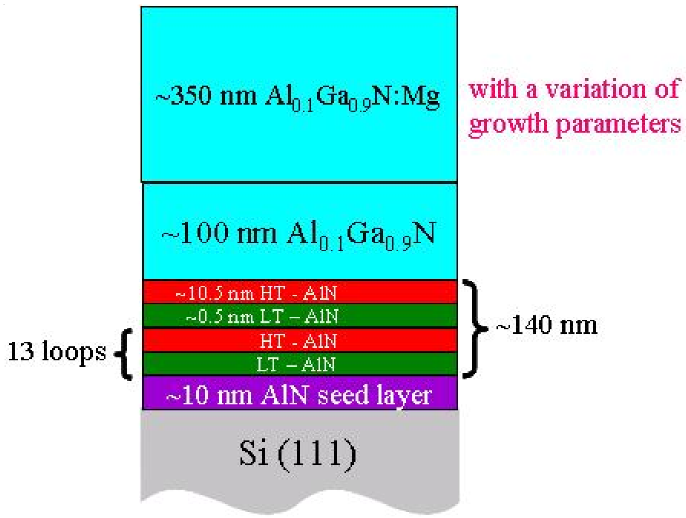

Figure 6.1.11 Schematic of Mg-doped $Al_{0.1}Ga_{0.9}N$ samples with a variation of growth parameters

By in situ measurements during growth, there is no big difference in the growth rates of $Al_xGa_{1-x}N$:Mg epilayer for the growth temperatures of 1045°C and 1145°C by using the same low group-III flow rate (sample D1 and D2). For the variation of the group-III flow rate, the growth rate reduces nearly proportional to the group-III flow rate i.e. the growth rate reduces by a half to ~13-15 nm/min from ~ 23-26 nm/min of the standard growth rate. As grown at 1045°C, compressive stresses induced in $Al_xGa_{1-x}N$:Mg layers during growth by the identical AlN-SL buffer layers are obviously stronger than that for 1145°C as shown in *Fig.6.1.12*. This indicates that Mg doping in $Al_xGa_{1-x}N$ grown at lower temperatures of 1045°C induces a lower tensile stress in the layers than that for the higher standard temperature of 1145°C. Probably Mg at 1045°C could be more soluble or incorporate with $Al_xGa_{1-x}N$ than at 1145°C.

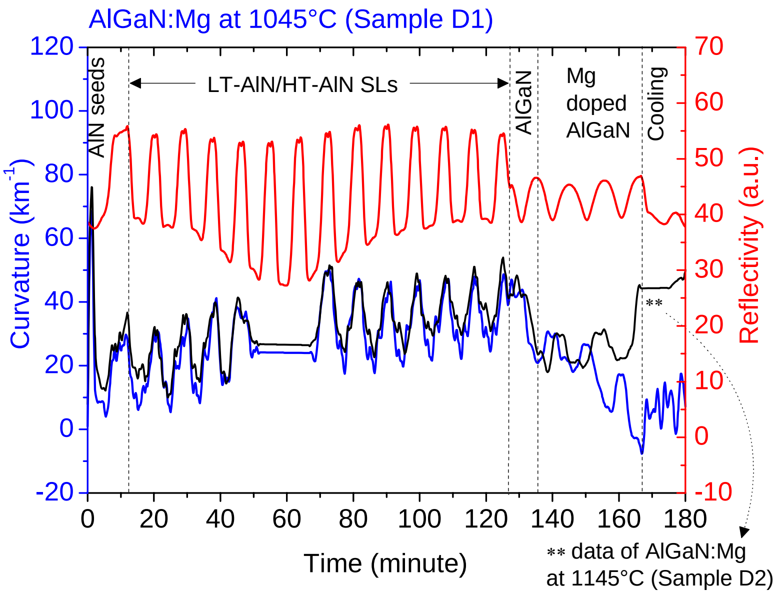

Figure 6.1.12 In situ curvature measurements (blue) and 632-nm optical reflectivity of $Al_xGa_{1-x}N$:Mg at 1045°C (red) as compared with the curvature measurements of $Al_xGa_{1-x}N$:Mg at 1145°C (black).

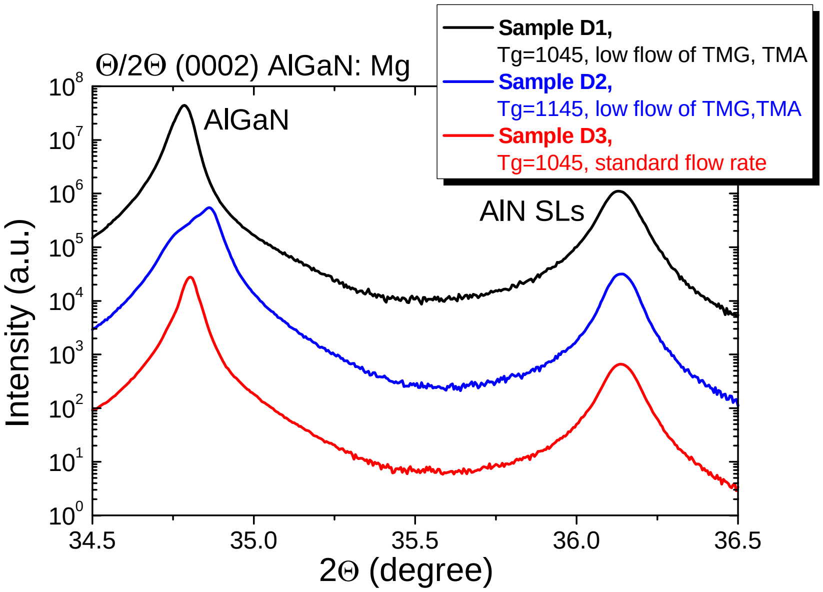

Figure 6.1.13 XRD θ/2θ-scans of the $Al_xGa_{1-x}N$:Mg (0002) reflections with a variation of growth parameters

In *Fig.6.1.13*, XRD θ/2θ-measurements of $Al_xGa_{1-x}N$:Mg(0002) reflections show a shoulder peak of different Al contents of the $Al_xGa_{1-x}N$:Mg layers grown at 1145°C with a lower group-III flow compared to undoped $Al_xGa_{1-x}N$ buffer layers.

Furthermore, lattice constants, in-plane tensile residual strain, ω-FWHMs of the (0002) and (10-10) reflections and Al contents of $Al_xGa_{1-x}N$:Mg epilayers with a variation of growth parameters are determined and shown in *Fig.6.1.14* and in *Fig.6.1.15,* respectively.

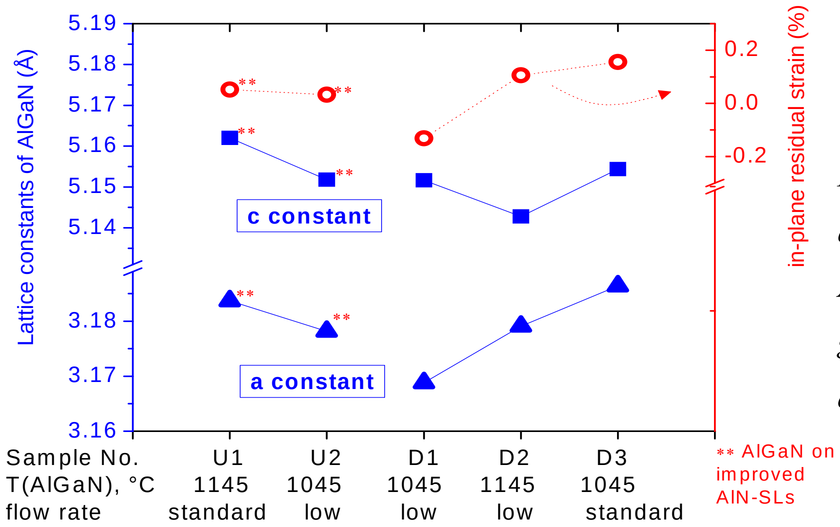

Figure 6.1.14 Lattice constants and in-plane residual strain of $Al_xGa_{1-x}N$:Mg with a variation of growth parameters as determined by XRD

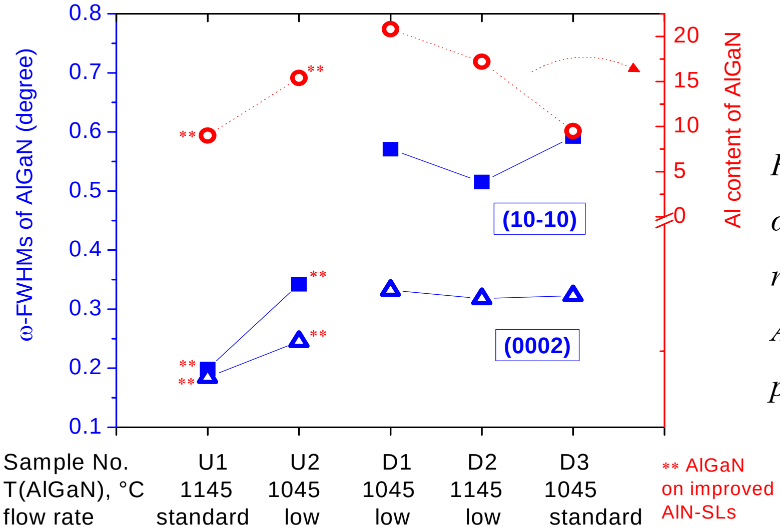

Figure 6.1.15 FWHMs of the XRD ω-scans of (0002) and (10-10) reflections and Al contents of $Al_xGa_{1-x}N$:Mg with varying growth parameters as determined by XRD

For undoped $Al_xGa_{1-x}N$ samples, when both growth temperature and group-III flow rate of sample U2 are reduced from that of sample U1, both lattice constants decrease corresponding to an increasing Al content from x = ~ 0.9 to ~0.15. Also in-plane strain is reduced. While the ω-FWHMs of the (0002) and (10-10) reflections increase due to a lower crystalline quality with an increase in Al content. It can be concluded that with a lower growth temperature and a lower group-III flow rate, the efficiency of Al-incorporation and in-plane strain in $Al_xGa_{1-x}N$ layers are improved and the crystalline quality of $Al_xGa_{1-x}N$ degrades with higher Al content.

For Mg-doped $Al_xGa_{1-x}N$ samples, with a low group-III flow rate, the growth temperature dependence was investigated by decreasing the growth temperature from 1145°C (sample D2) to 1045°C (sample D1). The results show that $Al_xGa_{1-x}N$ grown at 1045°C (sample D1) exhibits larger c-lattice and smaller a-lattice constants and a reduced in-plane tensile strain as compared to the sample grown at higher temperature. From the viewpoint of strain engineering a lower temperature seems more appropriate for Mg doping in $Al_xGa_{1-x}N$ even though it leads to a lower crystalline quality due to a higher Al-incorporation.

Further $Al_xGa_{1-x}N$:Mg layers, sample D1 and D3, were grown at the same temperature of 1045°C. The results show that $Al_xGa_{1-x}N$ grown at a lower flow rate (sample D1) has a reduced in-plane strain and an increased Al-composition. It is indicated that a lower group-III flow rate is more appropriate for Mg doping in $Al_xGa_{1-x}N$ at a lower temperature of 1045°C.

It can be observed that the Al content of $Al_xGa_{1-x}N$ of samples U1 and D3 are nearly the same at the same group-III flow rate even for a difference in growth temperature and at presence of Mg doping. Thus the efficiency of Al-incorporation in $Al_xGa_{1-x}N$ depends stronger on the group-III flow rate than on the growth temperature.

In *Fig.6.1.16*, cathodoluminescence (CL) measurements of $Al_xGa_{1-x}N$:Mg at 1045°C of sample D1 grown with a lower group-III flow rate and sample D3 grown with a higher flow rate show that both intensity and energy of the near-bandgap luminescence peak are situated at ~3.728 eV and ~3.6845 eV, respectively which originates in a higher Al content in agreement with XRD results. At higher growth rate (sample D3), yellow luminescence is more dominant than for a lower growth rate indicating a higher defect density. This also confirms that $Al_xGa_{1-x}N$:Mg grown at 1045°C with a low group-III flow rate has a better quality and lower defect density in the layer compared to a higher group-III flow rate. In addition, with respect to the DAP luminescence or blue luminescence one additional luminescence around 3.2627 eV is observed in Mg doped $Al_xGa_{1-x}N$ [Kauf99, Naka09].

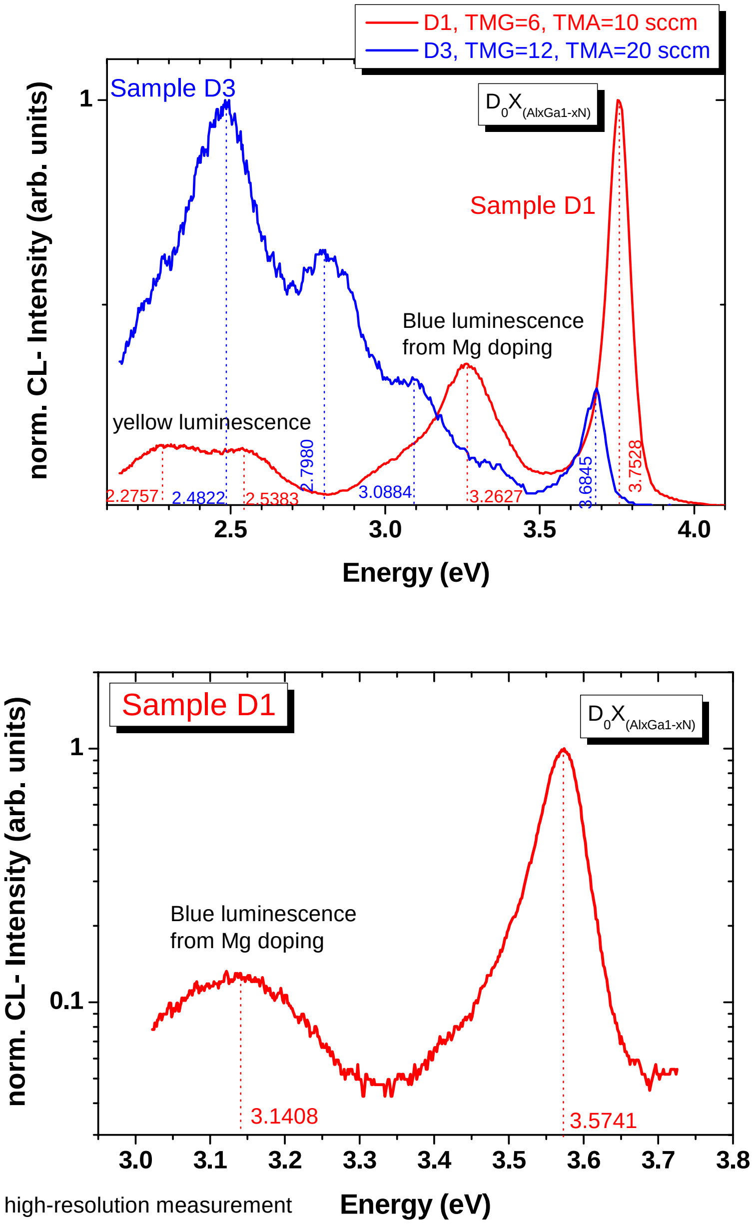

Figure 6.1.16 CL measurements of $Al_xGa_{1-x}N$:Mg with group-III-flow-rate difference (above) high-resolution- measurement of the band-edge region (below)

Nomarski microscopy exhibits a smooth and crack-free surface morphology for undoped $Al_{0.1}Ga_{0.9}N$ and the improved $Al_{0.1}Ga_{0.9}N$:Mg appears with a smaller grain size and few cracks. In *Fig.6.1.17*, 20×20 μm^2 AFM images also show a smaller grain size, a more difference in grain size, a better lateral coalescence but a few plateau area of $Al_{0.1}Ga_{0.9}N$:Mg *(right)* as compared with undoped $Al_{0.1}Ga_{0.9}N$ *(left)*. For 20×20 μm^2 scan area, a roughness of $Al_{0.1}Ga_{0.9}N$:Mg of 7.40 nm rms is lower than 9.27 nm rms of undoped $Al_{0.1}Ga_{0.9}N$. But a roughness of 10×10 μm^2 scan area of 5.11

nm rms of $Al_{0.1}Ga_{0.9}N$:Mg is higher than 2.43 nm rms of undoped $Al_{0.1}Ga_{0.9}N$. This shows a smoother surface morphology but more dominant in 3D growth of undoped $Al_{0.1}Ga_{0.9}N$.

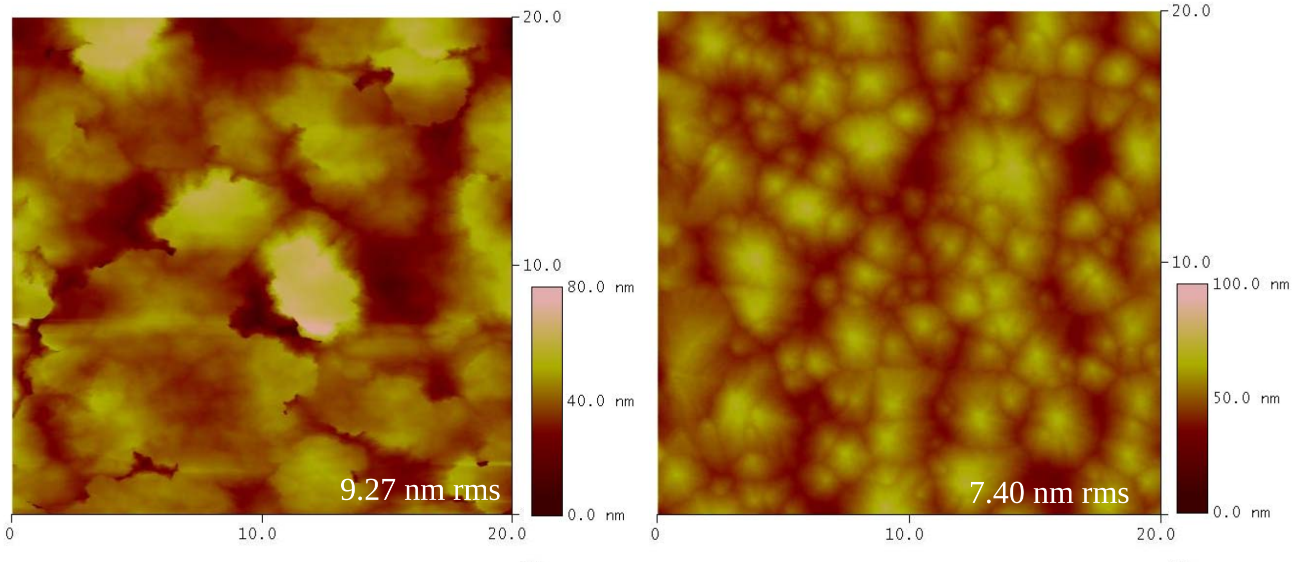

Figure 6.1.17 20×20 μm^2 AFM measurements showing the surface morphology of undoped $Al_{0.1}Ga_{0.9}N$ (left) as compared with improved $Al_xGa_{1-x}N$:Mg (right)

For their electrical properties as determined by C-V measurements, all $Al_xGa_{1-x}N$:Mg samples show no conductivity and high resistivity

In summary, all results presented show that a lower growth temperature of 1045°C and a lower group-III flow rate of 6 sccm for TMGa and 10 sccm for TMAl are more appropriate for Mg doping in $Al_xGa_{1-x}N$ layers achieving a lower defect density, even though p-type conductivity in $Al_xGa_{1-x}N$:Mg layers could not be determined.

6.1.2.2 Mg-doped GaN

As discussed in chapter 6.1.2.1, a lower growth temperature and lower group-III flow rate are beneficial to dope Mg in $Al_{0.1}Ga_{0.9}N$. Analogously the Mg-doping efficiency of GaN depends on growth parameters such as growth temperature, Mg flow rate and group-III flow rate etc. For this investigation, the TMGa flow rate of GaN:Mg was kept constant at a low flow rate of 6 sccm. The GaN:Mg samples were ~400-nm-thick GaN:Mg layers grown on ~250 nm GaN / ~460 nm $Al_{0.1}Ga_{0.9}N$ / 13 periods of AlN-based superlattices / HT-AlN seeding layer / Si(111) as depicted in

Fig. 6.1.18. Cp_2Mg flow rate was constant at 120 sccm or 0.307 μmol/min and the Cp_2Mg bubbler was maintained at a temperature of 25°C.

To optimize the p-type conductivity the growth temperature was varied from 900°C to 1100°C in the first series and the Mg flow rate was varied from 60 to 180 sccm or 0.153 to 0.460 μmol/min in the second series as shown in *table 6.2*.

Table 6.2 GaN:Mg samples with a variation of growth parameters

Series	**Varied parameters of GaN:Mg**	**range**
A	Temperature (°C)	900 - 1100
B	Mg flow rate (sccm)	60 - 180

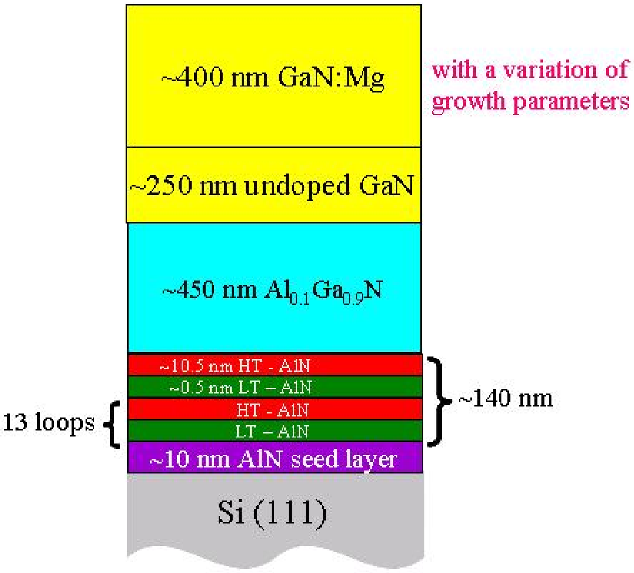

Figure 6.1.18 Schematic of GaN:Mg samples with a variation of growth parameters

A. impact of growth temperature

In *Fig.6.1.19* θ/2θ-XRD measurements of (0002) and (10-10) reflections of GaN:Mg samples with different growth temperatures, the 2θ peaks of GaN are easily distinguished from that of the $Al_{0.1}Ga_{0.9}N$ buffer layers for the (0002) reflections. It is also observed that there are some differences in the 2θ positions of the GaN(10-10) reflections. This originates from a difference in thermally induced tensile strain with a variation of growth temperatures.

With an increased growth temperature of the GaN:Mg layers, except that of 1050°C, their a-lattice constants tend to increase and the c-lattice constants slightly decrease and with it in-plane residual strain increases, as shown in *Fig.6.1.20*. These results correspond to a higher thermally induced tensile stress with higher growth temperature. The repetition of a sample, however, with an inferior crystalline quality shows the impact of the crystalline quality on strain as the c-lattice constant is smaller and the a-lattice constant larger and with it in-plane strain is significantly higher than for the other sample (*Fig.6.1.20 and Fig.6.1.21*).

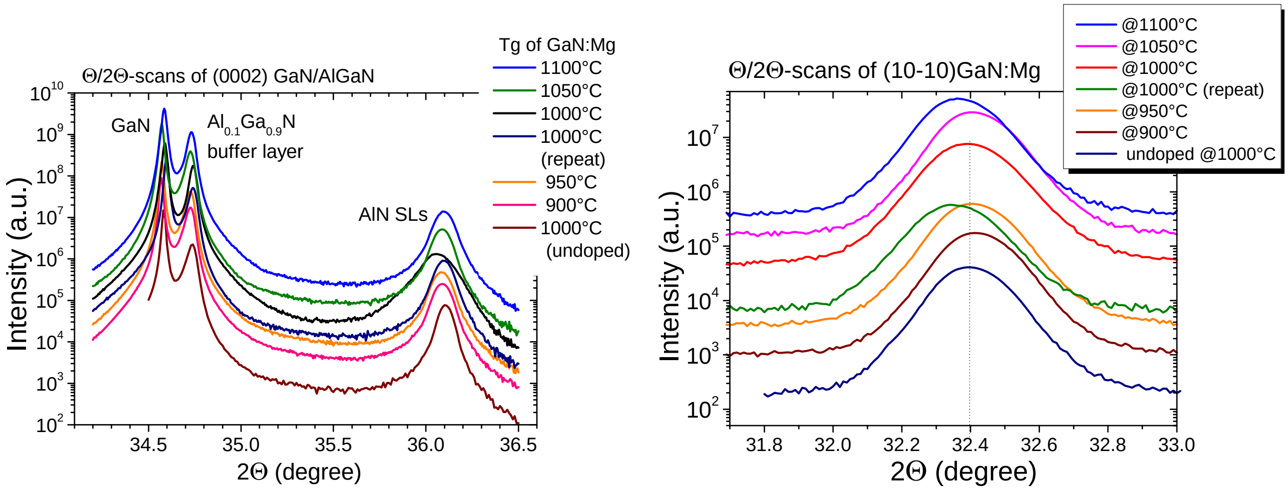

Figure 6.1.19 XRD $\theta/2\theta$-scans of the GaN:Mg (0002) (left) and (10-10) reflections (right) with a variation of growth temperatures

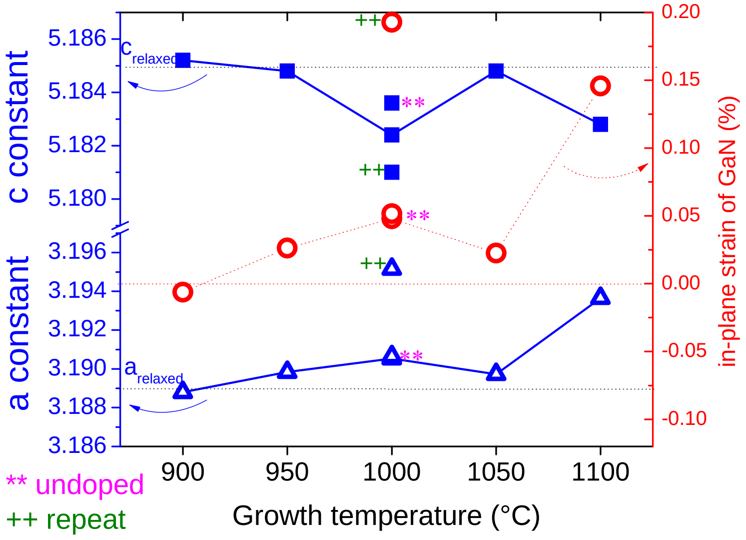

Figure 6.1.20 Lattice constants and in-plane residual strain of GaN:Mg with variation of growth temperatures

For the crystalline quality of GaN:Mg as revealed in *Fig.6.1.21*, with an increase in GaN:Mg layers growth temperature, the ω-FWHM of the GaN(0002) reflections is nearly constant around 0.15° and also that of AlN-SL buffer layers is nearly constant around 0.43° as implied by the constant crystalline quality of the AlN-SLs buffer layers. But the ω-FWHMs of GaN(10-10) reflections tend to increase from 0.21° to 0.41°, except that of the layer grown at 1050°C. It can be concluded that with an increasing growth temperature, twist or in-plane misorientation of the GaN:Mg layers increases. Even the undoped GaN quality is typically improved with a higher growth temperature. As compared to undoped GaN, the crystalline quality of undoped GaN is higher with lower ω-FWHMs than that of GaN:Mg. It implies that these Mg-doping parameters can cause a reduction of the GaN crystalline quality and a stronger effect with a higher growth temperature.

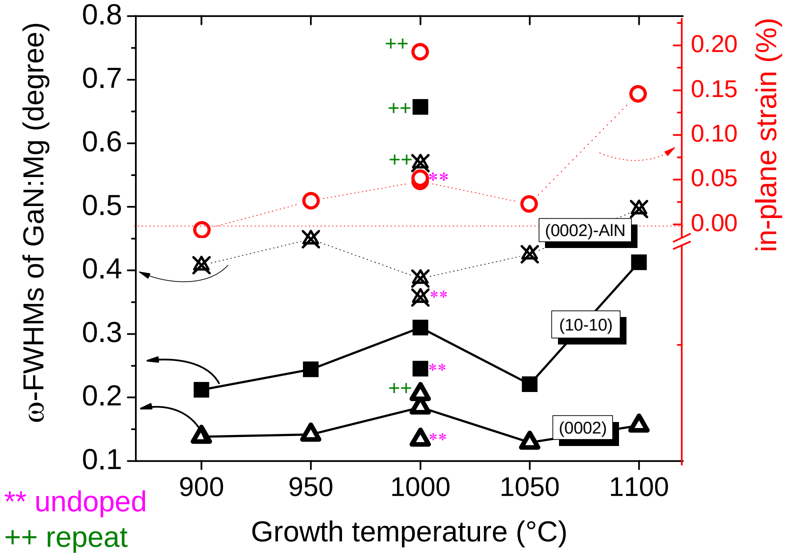

Figure 6.1.21 ω-FWHMs of the GaN:Mg (0002) and (10-10) reflections and in-plane residual strain with variation of growth temperatures

The hole concentrations were determined by C-V measurements without a thermal annealing of the GaN:Mg samples before measurement. With a variation of the GaN:Mg growth temperature, a p-type conductivity or hole concentration of ~4E+16 cm^{-3} is obtained at a growth temperature of 950°C and 1000°C as presented in *Fig.6.1.22*. At lower and higher temperatures than this, there are no conductivities of GaN:Mg grown at 900°C with a higher quality and GaN:Mg at 1100°C with a lower quality. This indicates that the hole density or Mg activation in the GaN layers do not strongly depend on the GaN quality as improved for higher growth temperatures but strongly on the growth temperature. For a repetition of the sample grown at 1000°C, which yields a worse but still reasonable crystalline quality, the hole density is enhanced to ~ 6E+16 cm^{-3} and ~ 8E+16 cm^{-3} (not show here). This is most likely due to an enhanced Mg incorporation from memory effects in the MOVPE reactor.

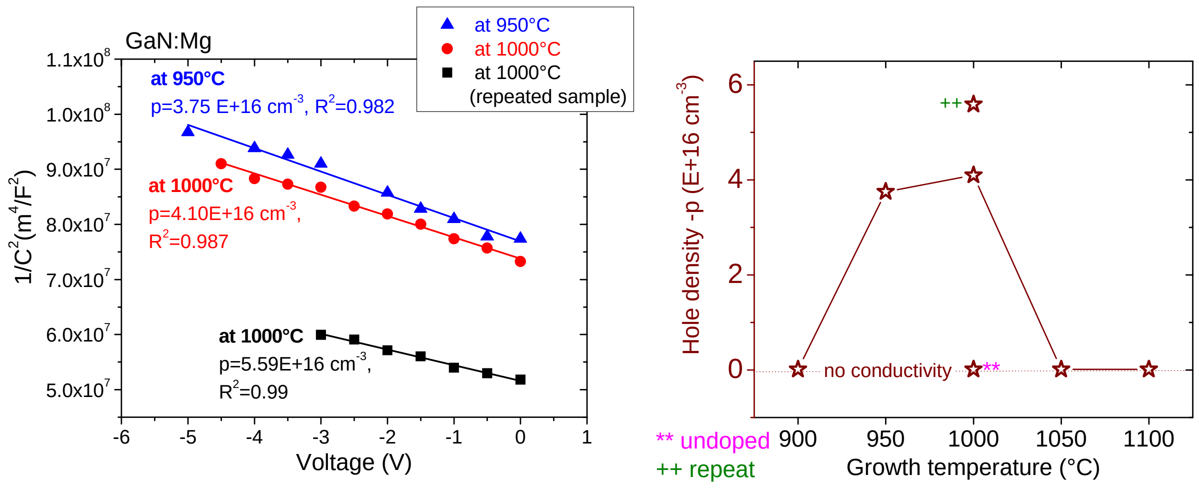

Figure 6.1.22 C-V measurements (left) and hole density of GaN:Mg layers as a function of growth temperature(right)

The hole concentration, lattice constants, ω-FWHMs and in-plane residual strain of GaN:Mg layers with a variation of growth temperature are depicted in *table 6.3*. No significant relationship between these parameters is found.

Table 6.3 Hole density, lattice parameters, ω-FWHMs and residual strain of GaN:Mg layers as a function of Mg flow rate and as compared with ω-FWHMs of AlN-SL buffer layers

Sample of GaN:Mg	Temp (°C)	Hole density (E+16 cm^{-3})	Lattice parameters (Å)		ω-FWHMs (degree)		strain (%)	ω-FWHM (0002) of AlN SLs (degree)
			a	c	(10-10)	(0002)		
T1	900	-	3.1888	5.1852	0.212	0.138	-0.006	0.408
T2	950	3.75	3.1898	5.1848	0.244	0.142	0.026	0.449
T3	1000	4.10	3.1905	5.1824	0.310	0.185	0.048	0.387
T4	1050	-	3.1897	5.1848	0.221	0.129	0.023	0.425
T5	1100	-	3.1936	5.1828	0.413	0.156	0.146	0.497
T6(~T3)	1000	5.59	3.1906	5.1836	0.245	0.134	0.052	0.357

As observed by Nomarski microscopy, the surface morphologies of all GaN:Mg samples in this series are crack-free. In *Fig.6.1.23*, AFM measurements show different surface morphologies of undoped GaN *(a,b)* and GaN:Mg *(c,d)*. For undoped GaN, the surface morphology is very smooth with a roughness of 0.77 nm rms of a 10×10 μm^2 image with obviously visible growth steps *(a)* and 6.615 nm rms of a 100×100 μm^2 image *(b)*. For GaN:Mg, the surface morphology is rougher, more porous, smaller grain size and more differently-sized grains with a roughness of 2.75 nm rms and 10.85 nm rms of 10×10 μm^2 and 100×100 μm^2 images *(c,d),* respectively. This confirms that with Mg doping the GaN crystalline quality is interior.

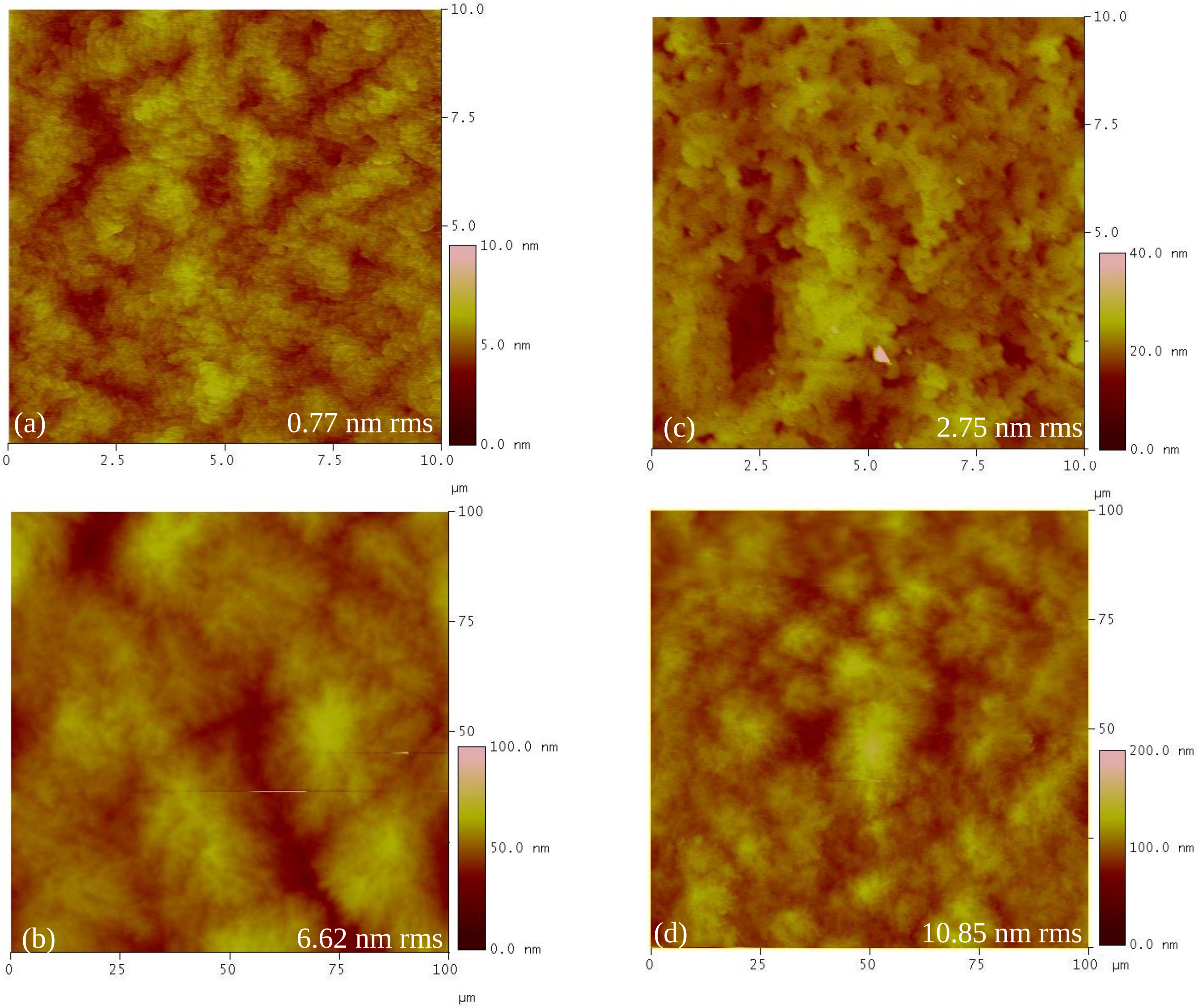

Figure 6.1.23 10×10 μm^2 and 100×100 μm^2 AFM measurements showing surface morphology of undoped GaN (a,b) as compared with that of GaN:Mg of Mg flow rate of 120 sccm at 1000°C (c,d), respectively

With increasing growth temperature, the surface morphology of GaN:Mg layers grown at 1100°C exhibits a larger grain size and a very smoother surface than that of GaN:Mg at 900°C as exhibited in *Fig.6.1.24(right) and (left)*, respectively. For 100×100 μm^2 scan area, a roughness of

GaN:Mg at 1100°C of 4.157 nm rms is much lower than 20.45 nm rms of GaN:Mg at 900°C and 10.85 nm rms of GaN:Mg at 1000°C unlikely a lower crystalline quality with a higher temperature by XRD measurements as discussed above.

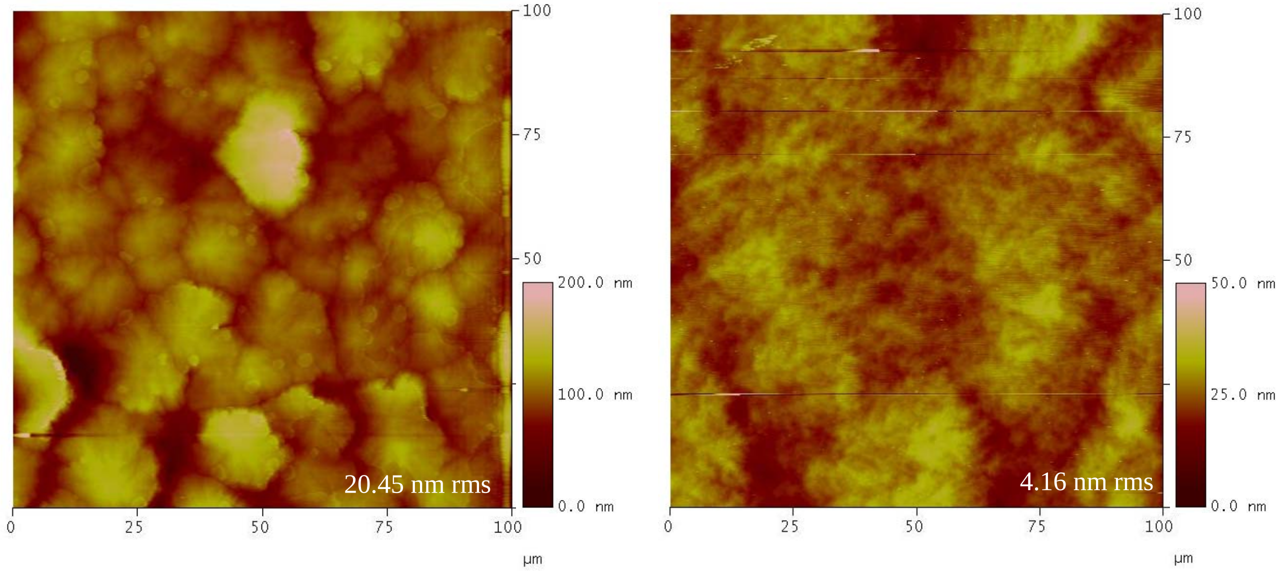

Figure 6.1.24 100×100 μm AFM measurements showing surface morphology of GaN:Mg at 900°C (left) as compared with GaN:Mg at 1100°C (right)

However, it can be concluded from all results that the optimized growth temperature for Mg doping in GaN is 1000°C. This probably relates to optimized temperature for Mg-incorporation or solubility in GaN layers due to a poor material quality with, e.g., much C and other point defects, thus self compensation for too low growth temperature and a low Mg incorporation for too high temperature.

B. impact of Mg flow rate

To optimize the Mg flow rate of GaN:Mg, the Mg flow rate was varied from 60 to 180 sccm corresponding to 0.153 to 0.307 μmol/min. Samples were ~400-nm-thick GaN:Mg layers grown at 1000°C on ~250 nm undoped GaN / ~460 nm $Al_{0.1}Ga_{0.9}N$ / 13 periods of AlN-based superlattices / HT-AlN seeding layer / Si(111).

$\theta/2\theta$-XRD measurements of GaN(0002) and (10-10) reflections presented in *Fig.6.1.25* show that the 2θ peak of GaN can be well distinguished from that of the $Al_{0.1}Ga_{0.9}N$ buffer layers. It can be observed that there are some differences in the 2θ positions of both reflections of GaN due to a difference in strain state.

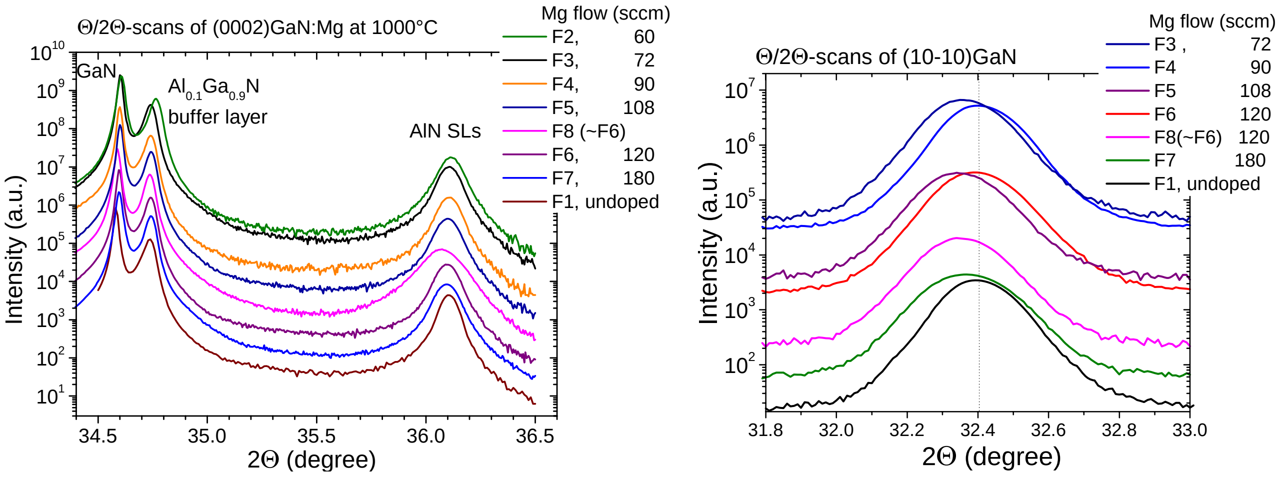

Figure 6.1.25 XRD θ/2θ-scans of the GaN:Mg (0002) and (10-10) reflections (left and right) with a variation of Mg flow rate

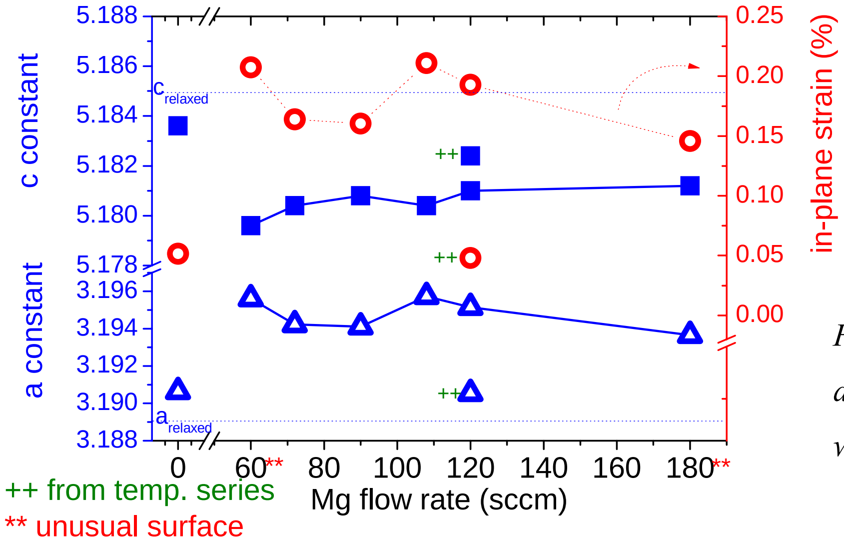

Figure 6.1.26 Lattice constants and in-plane strain of GaN:Mg with a variation of Mg flow rate

For this series of Mg flow rate dependence, the crystalline qualities of all Mg-doped samples are unsatisfied and worse than that of the temperature-series because these samples were grown on a worse quality of AlN-SL buffer layers with higher ω-FWHMs of AlN-SL(0002) reflections as depicted in *Fig.6.1.27*. The ω-FWHMs of the AlN-SLs are nearly constant around 0.56° and the ω-FWHM of GaN (0002) nearly constant around 0.21° and ω-FWHMs of GaN(10-10) around 0.6° with small fluctuations whereas an identical sample from the temperature-series had ω-FWHM of AlN-SL(0002) of 0.38°, ω-FWHM of GaN(0002) of 0.18° and ω-FWHM of GaN(10-10) of 0.3°.

Also in-plane strain of all samples is around 0.16% higher than that of the temperature-series of 0.05%.

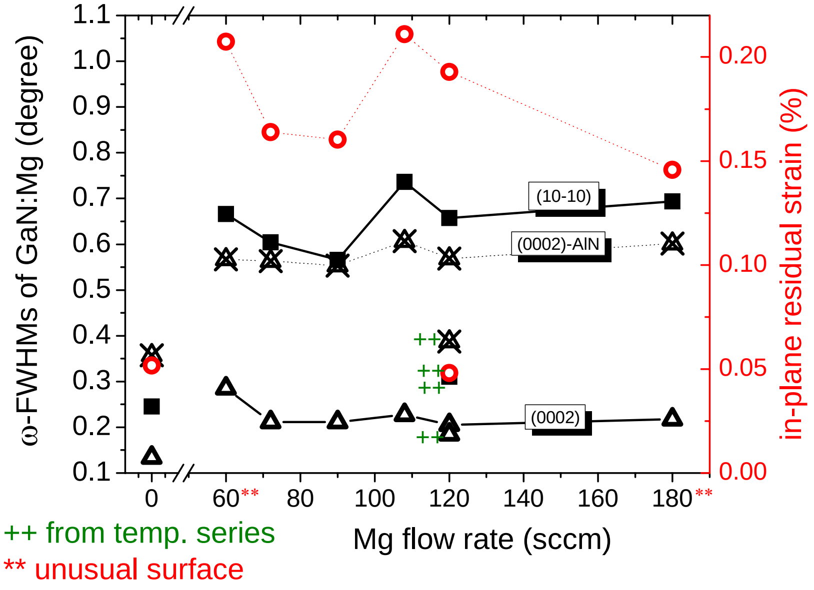

Figure 6.1.27 ω-FWHMs of the GaN:Mg (0002) and (10-10) reflections and in-plane residual strain with a variation of Mg flow rate

All GaN:Mg samples in this series were grown at 1000°C and they yield p-type conductivity as determined by C-V measurements and presented in *Fig.6.1.28 (left)*. With increasing Mg flow rate from 60 to 180 sccm the hole concentrations of the GaN:Mg layers except that for 72 sccm tend to slightly increase in a small range from 5.0E+16 to 5.8E+16 cm^{-3} as presented in *Fig.6.1.28 (right)*.

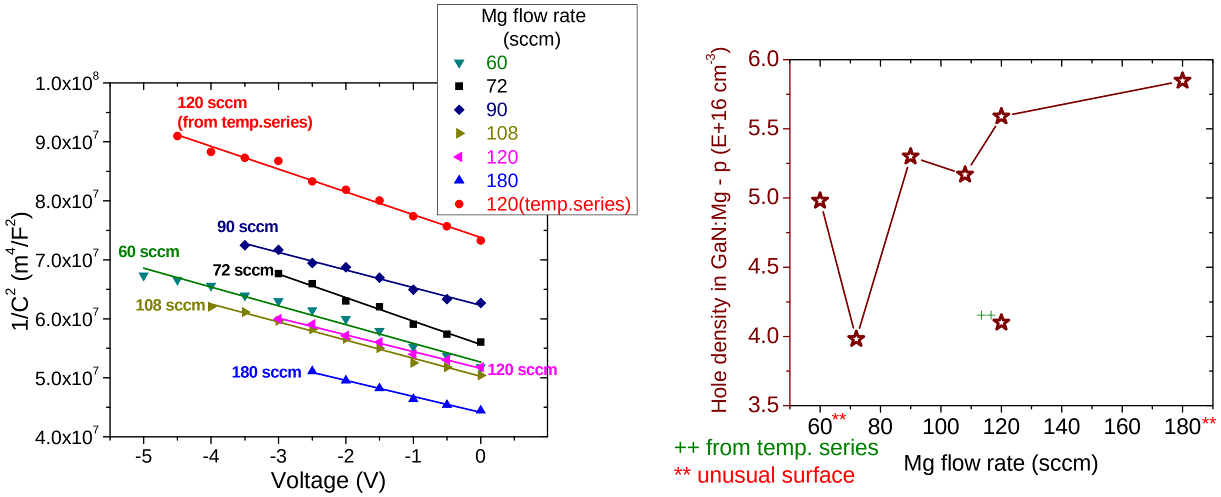

Figure 6.1.28 C-V measurements (left) and hole density of GaN:Mg layers as a function of Mg flow rate (right)

Due to the unusual surface of the GaN:Mg samples grown with a Mg precursor flow of 60 and 180 sccm with some large white areas around the sample edges, if even the results of these samples would be ignored, the best results in a range from 72 to 120 sccm still shows an increased hole density with increasing Mg flow rate. Although a strong influence of the Mg flow rate on the hole density of GaN:Mg could not be observed due to an unsatisfying GaN crystalline quality in this series, it could be concluded that the hole density continuously increases with an increasing Mg flow rate in a range from 72 to 120 sccm.

The influence of deposits in the reactor on the GaN quality and on the hole density might be very strong. Therefore, the hole concentration of these GaN:Mg layers is slightly varied or almost constant around 5E+16 cm^{-3}.

The hole concentration of the GaN:Mg layers with a variation of the Mg flow rate and their lattice constants, ω-FWHMs and in-plane residual strain are determined and depicted in *table 6.4*.

Table 6.4 Hole density, lattice parameters, ω-FWHMs and residual strain of GaN:Mg layers as a function of Mg flow rate and as compared with ω-FWHMs of AlN-SL buffer layers

Sample of GaN:Mg	Mg flow rate		Hole density (E+16 cm^{-3})	Lattice parameters (Å)		ω-FWHMs (degree)		strain (%)	ω-FWHM (0002) of AlN-SLs (degree)
	(sccm)	(μmol/min)		a	c	(10-10)	(0002)		
F1	0	0	--	3.1906	5.1836	0.245	0.134	0.05	0.357
F2	60	0.153	4.98	3.1956	5.1796	0.666	0.285	0.21	0.567
F3	72	0.184	3.98	3.1942	5.1804	0.604	0.212	0.16	0.563
F4	90	0.230	5.30	3.1941	5.1808	0.566	0.211	0.16	0.553
F5	108	0.276	5.17	3.1957	5.1804	0.736	0.227	0.21	0.607
F6	120	0.307	5.59	3.1952	5.1810	0.657	0.206	0.19	0.569
F7	180	0.460	5.85	3.1936	5.1812	0.694	0.217	0.14	0.602
F8 (~F6)	120	0.307	4.10	3.1905	5.1824	0.310	0.185	0.05	0.387

It is observed that the results of all measured parameters are nearly constant and no relationship exists between them and the doping concentration. This likely originates in an unsatisfied GaN crystalline quality leading to a limited efficiency of Mg doping and a nearly constant hole concentration in GaN:Mg layers around 5E+16 cm^{-3}. As observed by Nomarski microscopy, the surface morphologies of all GaN:Mg samples in this series are crack-free and no big difference.

Although an optimized Mg flow rate has not yet been obtained, by taking into account all parameters and conductivity of all samples in this series, the appropriate Mg flow rate to p-dope GaN at 1000°C is about 120 sccm or 0.307 μmol/min.

6.1.2.3 Mg-doped (GaN/$Al_{0.1}Ga_{0.9}N$) superlattices

To develop AlGaN-based UV LEDs, p-type AlGaN layers are necessarily required as well as n-type AlGaN and active layers with efficient radiative carrier recombination. The growth parameters of GaN:Mg and $Al_{0.1}Ga_{0.9}N$:Mg were investigated as discussed before in section 6.1.2.1 and 6.1.2.2. Only GaN:Mg layers were achieved with p-type conductivity and $Al_{0.1}Ga_{0.9}N$:Mg layers showed no p-type behaviour which could be also attributed to the higher acceptor activation energy with increasing Al composition. Even though GaN is generally avoided in combination with UV optoelectronic devices due to its light absorption for wavelengths below ~ 360 nm [Khan05,Nish03], to apply Mg-doped GaN/AlGaN multilayers for p-type regions is the most promising approach to obtain p-type conductivity with AlGaN layers. The structure of GaN/AlGaN multilayers is able to reduce the acceptor activation energy in AlGaN layers and enhance the sheet hole concentration accumulated at interfaces due to the strong piezoelectric field of the strained GaN/AlGaN heterostructure as discussed in chapter 2.2.3 and 2.5.3.

By using optimized growth parameters of GaN and $Al_{0.1}Ga_{0.9}N$ layers as low flow rates of 6 sccm of TMGa and 10 sccm of TMAl at low growth temperatures of 1000°C and a Mg flow rate of 120 sccm (0.307 μmol/min), the samples grown with 20 periods of Mg-doped GaN/$Al_{0.1}Ga_{0.9}N$ SLs with a total thickness of ~400 nm were grown on ~460 nm undoped $Al_{0.1}Ga_{0.9}N$ / 13 periods of AlN-based superlattices / HT-AlN seeding layer / Si(111) as presented in *Fig.6.1.29*. The thicknesses of GaN and $Al_{0.1}Ga_{0.9}N$ are ~10 nm for each layer.

To investigate the optimized Mg-doped regions of the GaN/$Al_{0.1}Ga_{0.9}N$ SLs, there are 4 types of different Mg-doped regions i.e. uniform Mg doping in both layers (sample SL3), Mg doping only in the GaN layers (sample SL5), in the second half of each GaN layer and the first part half of each $Al_{0.1}Ga_{0.9}N$ layer only (sample SL4), and for only the first half of each GaN layer and the second half of each $Al_{0.1}Ga_{0.9}N$ layer (sample SL6) along the growth direction. In addition, an undoped sample (sample SL1), uniform Mg-doped sample at 950°C (sample SL2) and the reproduced samples of sample SL3 and SL4 (sample SL7 and SL8, respectively) were grown to characterize their crystalline qualities and electrical properties. Different Mg-doping parameters of all samples are summarized in *table 6.5*.

Table 6.5 Mg-doped (GaN/Al$_{0.1}$Ga$_{0.9}$N) SLs with a variation of growth parameters

Sample	**Diff. Mg-doped regions of GaN/Al$_{0.1}$Ga$_{0.9}$N SLs**			
	GaN		**Al$_{0.1}$Ga$_{0.9}$N**	
	1st half	**2nd half**	**1st half**	**2nd half**
SL1	u	u	u	u
SL2 (T$_g$ =950°C)	+	+	+	+
SL3	+	+	+	+
SL4	+	u	u	+
SL5	+	+	u	u
SL6	u	+	+	u
SL7 (repeat of SL3)	+	+	+	+
SL8 (repeat of SL4)	u	+	+	u

Note u = undoped, + = with Mg doping

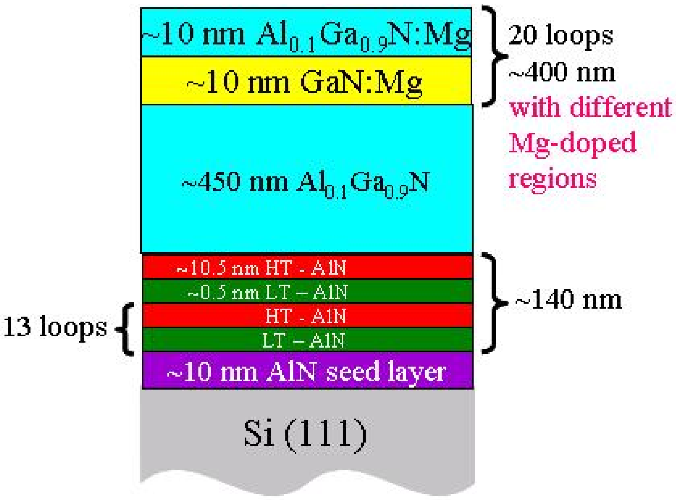

Figure 6.1.29 Schematic of Mg-doped (GaN/Al$_{0.1}$Ga$_{0.9}$N) SLs with different Mg-doped regions

In XRD measurements in *Fig.6.1.30*, θ/2θ-scans of GaN/Al$_{0.1}$Ga$_{0.9}$N (0002) reflections show only slightly differing crystallographic properties for the different types of Mg-doped regions i.e. distinguished interference fringes of GaN/Al$_{0.1}$Ga$_{0.9}$N SLs and broader in high-order peaks, except sample SL6 and SL8 with very broad fringes. This is in agreement with their higher ω-FWHMs of the AlN-SL (0002) and GaN/Al$_{0.1}$Ga$_{0.9}$N-SL (10-10) reflections of sample SL6 and SL8 than that of the other samples as depicted in *Fig.6.1.31*. All of this result from the relatively low quality of the AlN-SL buffer layers of these samples leading to a low quality of the GaN/Al$_{0.1}$Ga$_{0.9}$N SLs. With a comparable quality of the AlN-SL buffer layers of sample SL3, SL4 and SL5 in *Fig.6.1.31*, a fluctuation of the ω-FWHMs of GaN/$Al_{0.1}Ga_{0.9}N$-SL (10-10) reflections is larger than that of the (0002) reflections and it also shows a variation of the in-plane residual strain indicating a variation of in-plane misorientation or twist. It is concluded that the quality of GaN/$Al_{0.1}Ga_{0.9}N$ SLs with a uniform Mg doping is better than that of other samples with partial doping which is leading to a higher in-plane residual strain as shown in *Fig.6.1.32*.

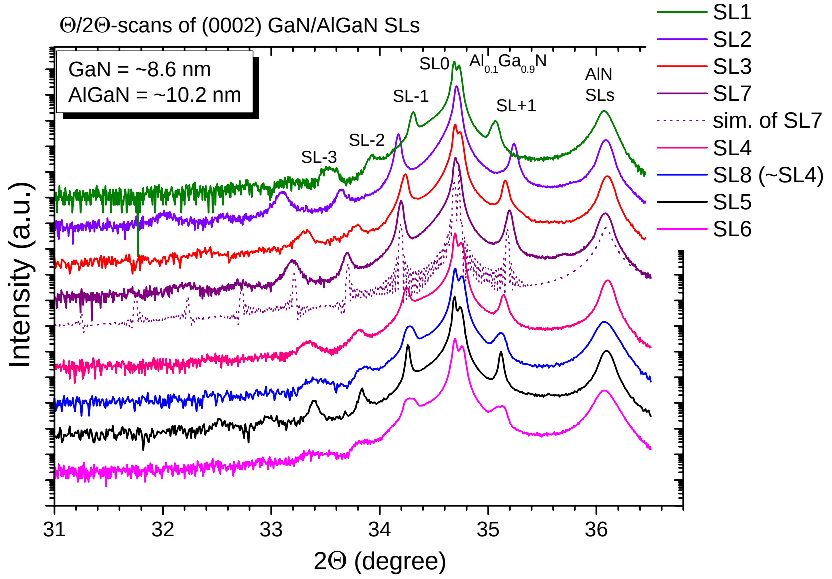

Figure 6.1.30 XRD θ/2θ-scans of the GaN/$Al_{0.1}Ga_{0.9}N$ (0002) reflections with a variation of Mg-doping regions

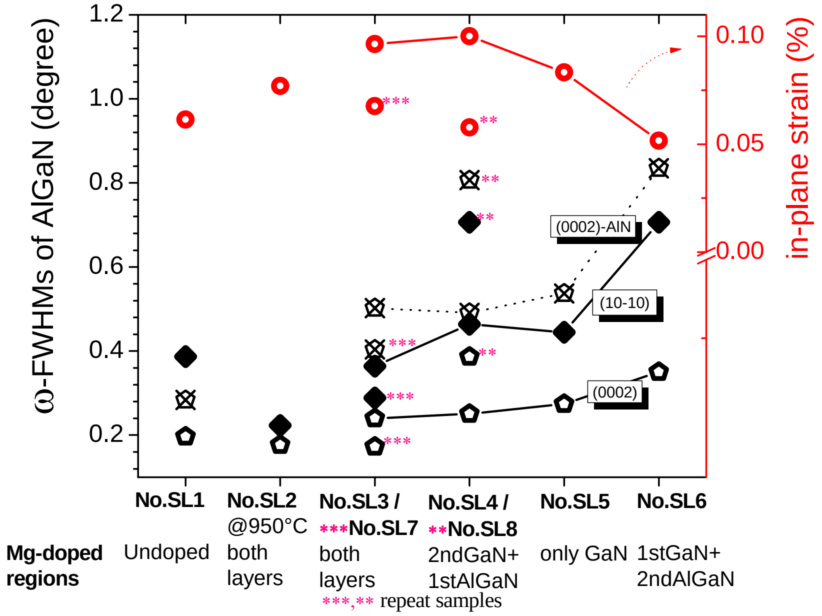

Figure 6.1.31 ω-FWHMs of the (0002) and (10-10) reflections and in-plane residual strain of GaN/$Al_{0.1}Ga_{0.9}N$ SLs with a variation of Mg-doping regions

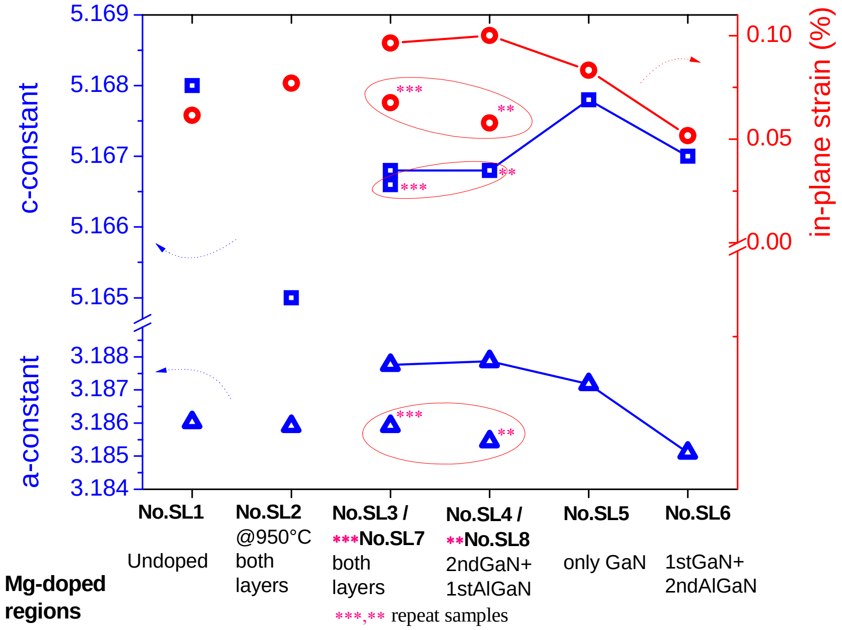

Figure 6.1.32 Lattice constants and in-plane residual strain of GaN/Al$_{0.1}$Ga$_{0.9}$N SLs with a variation of Mg-doping regions

As compared to the crystalline quality of Mg-doped GaN/Al$_{0.1}$Ga$_{0.9}$N SLs, the crystalline quality of undoped GaN/Al$_{0.1}$Ga$_{0.9}$N SLs (sample SL1) on the better-quality AlN-SLs is slightly lower than that of uniform Mg-doped samples (sample SL3 and SL7) with a slightly higher ω-FWHMs in *Fig.6.1.31*.

Nomarski microscopy exhibits crack-free surface morphologies of uniform Mg-doped and undoped GaN/AlGaN samples and no big difference. The 100×100 μm^2 AFM measurements present an increasing roughness of uniform Mg-doped GaN/AlGaN SLs of 8.86 nm rms from 5.26 nm rms of undoped samples in *Fig.6.1.33 (right) and (lef),* respectively. There is a slightly differently-sized grains and a slightly better lateral coalescence of the sample with an Mg doping. In 10×10 μm^2 scan area, the roughness of the Mg-doped SLs of 1.29 nm rms is slightly smoother than 1.36 nm rms of the undoped sample. As compared to the undoped Al$_{0.1}$Ga$_{0.9}$N surface morphology of 2.43 nm rms in *section 6.1.2.1* this surface of undoped AlGaN top-layers of the SLs is smoother with a bigger grain size (these all AlGaN layers are grown by identical growth parameters). The evaluated Al compositions of the AlGaN top-layers of these GaN/AlGaN SLs are in average ~0.065 showing a pseudomorphic SL structure. Moreover, the estimated thicknesses of the layers by simulating the XRD spectra are ~8.6 nm and ~10.2 nm for GaN and Al$_{0.1}$Ga$_{0.9}$N, respectively.

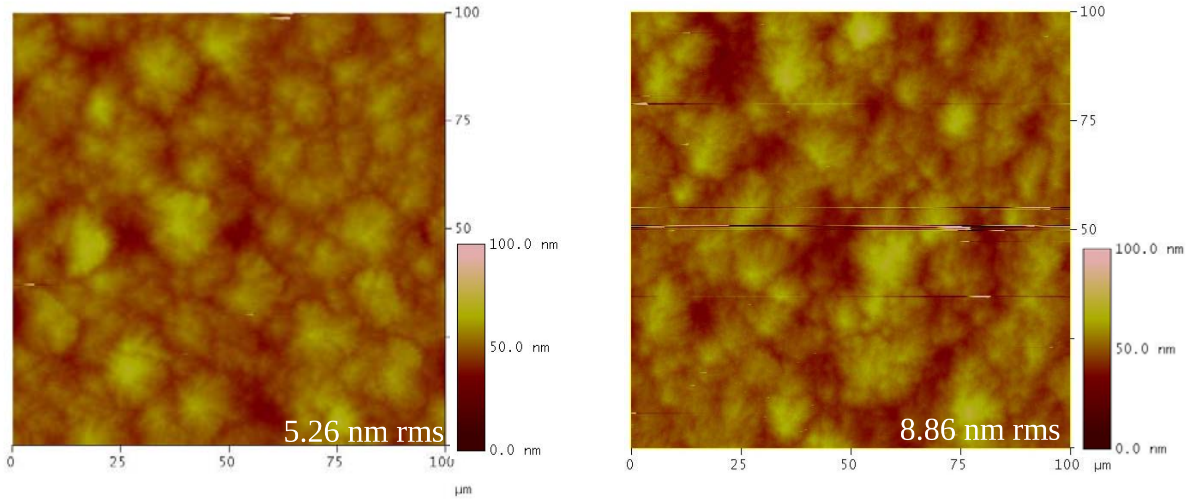

Figure 6.1.33 100×100 μm^2 AFM images showing the surface morphology of undoped GaN/$Al_{0.1}Ga_{0.9}N$ SLs (left) as compared with that of Mg-doped SLs (right)

In *Fig.6.1.34 and Table 6.6*, C-V measurements of GaN/$Al_{0.1}Ga_{0.9}N$ SLs show that with a variation of the Mg-doped regions in GaN/$Al_{0.1}Ga_{0.9}N$ SLs, a variation of the p-type conductivity can be observed. Mg-doped GaN/$Al_{0.1}Ga_{0.9}N$ SLs grown at 950°C (sample SL2) yields lower p-type conductivity than that of all others at 1000°C. Therefore the appropriate temperature to dope Mg in GaN and $Al_{0.1}Ga_{0.9}N$ layers is 1000°C.

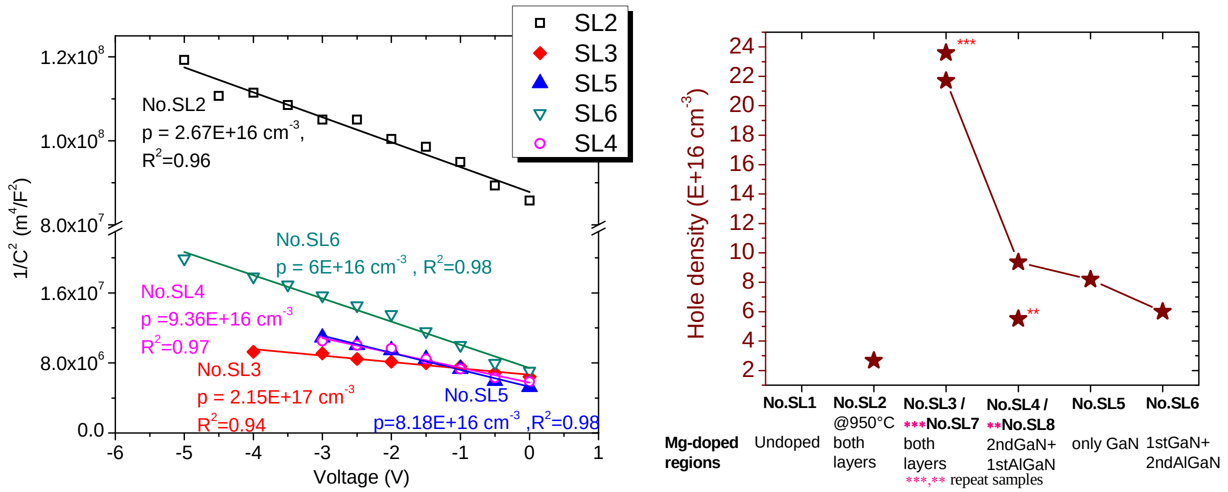

Figure 6.1.34 C-V measurements (left) and hole density of GaN/$Al_{0.1}Ga_{0.9}N$ SLs with a variation of Mg-doping regions (right)

Sample SL3 and a reproduced uniformly doped sample (sample SL7) present the highest p-type conductivity of ~2.4E+17 cm^{-3} whereas other samples with Mg doping in only some part of the SL result in a reduced p-type conductivity by a factor of two or above. Thus one reason is not only the impact of the GaN/$Al_{0.1}Ga_{0.9}N$ SL quality with differently doped regions but also the higher Mg concentration in the uniformly doped GaN/$Al_{0.1}Ga_{0.9}N$ SLs compared to that with only partial Mg doping. Unlikely Kozodoy et al. [Kozo99] and Waldron et al. [Wald01] presented that modulation-Mg-doping in only some regions such as the interface regions of GaN/AlGaN multilayers or only AlGaN layers is able to improve the hole concentration, mobility and resistivity compared to uniform Mg doping.

Additionally this GaN/$Al_{0.1}Ga_{0.9}N$ superlattice structure with uniform Mg doping shows a free-hole enhancement about one order from ~5.6E+16 cm^{-3} of bulk GaN:Mg layers (sample F6) to 2.4E+17 cm^{-3} of the superlattice structure (sample SL7) as depicted in *Fig.6.1.35*.

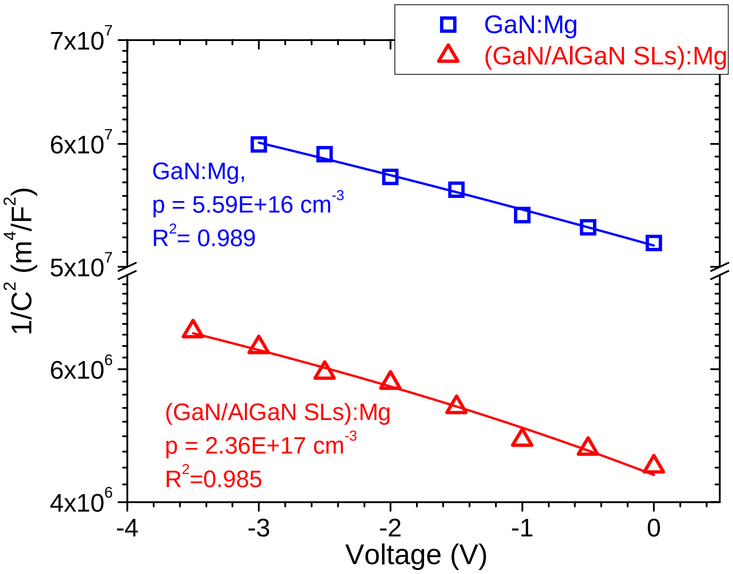

Figure 6.1.35 C-V measurements showing p-type conductivity of Mg-doped (GaN/$Al_{0.1}Ga_{0.9}N$) SL sample as compared with that of a GaN:Mg sample

The hole concentration of Mg-doped GaN/$Al_{0.1}Ga_{0.9}N$ multilayers with a variation of the Mg doping regions and their lattice constants, in-plane residual strain and ω-FWHMs are depicted in *table 6.6*.

For samples SL3, SL4 and SL5, with a comparable quality of the AlN-SL buffer layers, it could be observed that Mg doping in some parts of the GaN / AlGaN SLs leads to a lower GaN / AlGaN SL quality and lower hole concentration than uniform doping. In the case of reproduced samples, the quality of sample SL7 with uniform doping is better than that of sample SL3 but their hole concentrations show no difference.

With decreasing hole concentration tensile strain decreases, consequently Mg doping induces tensile strain. This decreases strain of samples with doping in some parts of the SLs is confirmed by smaller a-lattice and larger c-lattice constants than for uniform doping. Analogously, sample SL2 of 950°C with a better quality shows lower tensile strain and a lower hole concentration. As discussed before, a hole enhancement by using GaN/$Al_{0.1}Ga_{0.9}N$ superlattice structures results from a strong piezoelectric field within the strained GaN/$Al_{0.1}Ga_{0.9}N$ heterostructure.

Table 6.6 Hole density, lattice parameters, ω-FWHMs and residual strain of Mg-doped (GaN/$Al_{0.1}Ga_{0.9}N$) SLs with a variation of Mg-doped regions

Sample	Mg-doped regions	Hole density (E+16 cm^{-3})	Lattice parameters (Å)		ω-FWHMs (degree)		Al content	Strain (%)	ω–FWHM (0002) of AlN SLs (degree)
			a	c	(10-10)	(0002)			
SL1	undoped	-	3.1860	5.1680	0.387	0.197	6.4	0.061	0.284
SL2	Tg = 950°C	2.67	3.1859	5.1650	0.223	0.177	7.2	0.077	--
SL3	both layers	21.70	3.1878	5.1668	0.364	0.240	5.6	0.096	0.502
SL4	2ndGaN + 1stAlGaN	9.36	3.1879	5.1668	0.464	0.251	5.6	0.100	0.491
SL5	GaN only	8.18	3.1872	5.1678	0.444	0.274	5.8	0.083	0.537
SL6	1stGaN + 2ndAlGaN	6.00	3.1851	5.1670	0.707	0.351	7.2	0.052	0.835
SL7	~ SL3	23.60	3.1859	5.1666	0.289	0.173	6.8	0.068	0.404
SL8	~ SL4	5.51	3.1854	5.1668	0.706	0.386	7.0	0.058	0.807

In summary, p-type conductivity with a hole concentration of ~2.4E+17 cm^{-3} was obtained by using uniformly Mg-doped GaN/$Al_{0.1}Ga_{0.9}N$ multilayers.

6.2. Optimization of GaN/$Al_{0.1}Ga_{0.9}N$ multi-quantumwells

After n-type $Al_{0.1}Ga_{0.9}N$ and p-type GaN/$Al_{0.1}Ga_{0.9}N$ multilayers were obtained successfully, the light emitting region was investigated to develop AlGaN-based UV LEDs. In principle, the light-emission efficiency of a QW depends on many factors e.g. a QW-material quality, well width, barrier width, and band-offset ($\Delta E_C, \Delta E_V$) of well and barrier etc. To confine electrons and holes for an efficient radiative recombination, it is required that the well thickness has approximately the dimension of the free-exciton.

6.2.1. Crystallography of GaN/$Al_{0.1}Ga_{0.9}N$ multi-quantumwells

For this work, 5 periods of ~3-nm-thick GaN/~10-nm-thick $Al_{0.1}Ga_{0.9}N$ multi-quantum wells with $\Delta E_C =\sim 0.110eV$ and $\Delta E_V =\sim 0.071eV$ at room temperature as estimated theoretically by expressions in [Hang01] were designed to achieve near UV-luminescence at about 340-350 nm corresponding to about 3.54-3.64 eV. High-resolution XRD measurements were applied to determine the nominal thickness and crystallography of the GaN/$Al_{0.1}Ga_{0.9}N$ MQW samples. The 5 periods of GaN/$Al_{0.1}Ga_{0.9}N$ MQWs were grown on ~1.8-µm-thick $Al_{0.1}Ga_{0.9}N$:Si with inserting LT-AlN interlayer by 3 times / AlN-SL buffer layers / AlN seed layers / Si(111) substrate as presented in *Fig.6.2.1*. The GaN and $Al_{0.1}Ga_{0.9}N$ layers were grown with standard growth parameters as described in *chapter 6.1.2*.

In order to gain a higher probability to confine electrons in the MQW region, the $Al_{0.1}Ga_{0.9}N$:Si buffer layers were grown with a slightly (0.01-0.02) higher Al composition than the $Al_{0.1}Ga_{0.9}N$ barrier. The first series was grown with an $Al_xGa_{1-x}N$ composition around [Al] = 0.09 and the $Al_xGa_{1-x}N$ buffer layers around [Al] = 0.10. For the second series, the $Al_xGa_{1-x}N$ barrier has an Al composition around 0.10 and the $Al_xGa_{1-x}N$ buffer layers around 0.11.

The MQWs were grown on the $Al_{0.1}Ga_{0.9}N$:Si buffer layers. But a high Si flow rate for the $Al_{0.1}Ga_{0.9}N$ layers to obtain a high electron concentration can reduce the $Al_{0.1}Ga_{0.9}N$ quality as discussed in *chapter 6.1.1*. For the first series of Si optimization of the ~1.8-µm-thick $Al_{0.1}Ga_{0.9}N$:Si layers on the MQW quality, the Si flow rate was varied from 2 to 1, 0.5, and 0.25 sccm (from 17.857 to 2.232 nmol/min) in the first $Al_{0.1}Ga_{0.9}N$ layers to the forth $Al_{0.1}Ga_{0.9}N$ layers that separated by LT-AlN interlayers whereas the MQW growth parameters were kept constant. There are two other samples with a Si flow rate of 2 sccm for all $Al_{0.1}Ga_{0.9}N$ layers and one with a flow of 2 sccm of the first $Al_{0.1}Ga_{0.9}N$ layers only and 0.25 sccm for the others. With a variation of the growth time of the GaN well and $Al_{0.09}Ga_{0.91}N$ barriers, there are additional samples with various well- and barrier- thicknesses. The parameters of the MQW samples which are varied are summarized in *table 6.7*.

Table 6.7 Ga N/AlGaN MQW samples with various growth parameters

Sample		**SiH$_4$ in each part of *n*-AlGaN (sccm)**	**MQW thicknesses (nm)**	
			GaN	AlGaN
Series 1	A	2/0.25/0.25/0.25	2.4	3.3
	B	2/ 1/ 0.5/ 0.25	2.1	2.9
	C		2.2	8.3
Series 2	D	2/ 1/ 0.5/ 0.25	2.2	~6
	E		4.4	

Note series 1, Al content of 0.09 and 0.10 for $Al_xGa_{1-x}N$ barrier and buffer layers, respectively
series 2, Al content of 0.10 and 0.11 for $Al_xGa_{1-x}N$ barrier and buffer layers, respectively

Figure 6.2.1 GaN/$Al_{0.1}Ga_{0.9}N$ MQW samples with various growth parameters

In *Fig.6.2.2*, HR-XRD θ/2θ-scans of the GaN/$Al_{0.1}Ga_{0.9}N$ (0002) reflections show that for all samples distinguished interference fringes and finite thickness fringes are observed indicating smooth surfaces and interfaces of the GaN/$Al_{0.1}Ga_{0.9}N$ MQW structures.

Sample A of the $Al_{0.1}Ga_{0.9}N$:Si buffer layers with a Si flow rate of 0.25 sccm reduced from 2 sccm of the first $Al_{0.1}Ga_{0.9}N$:Si layers only shows a better crystalline quality with more slightly distinguished fringes as compared with sample B of the $Al_{0.1}Ga_{0.9}N$:Si layers with a Si flow rate of

0.25 sccm reduced in sequence from 0.5, 1, and 2 sccm of the first $Al_{0.1}Ga_{0.9}N$:Si layers. To enhance the electron density of n-type $Al_{0.1}Ga_{0.9}N$ layers, the sample-B structure is better suited. Additionally there is one sample with a Si flow rate of 2 sccm for all $Al_{0.1}Ga_{0.9}N$ layers leading to a few cracks in the layers (not shown here). This indicates that the quality of the MQWs is certainly influenced from the quality of the $Al_{0.1}Ga_{0.9}N$:Si buffer layers with a high Si flow rate resulting in a lower $Al_{0.1}Ga_{0.9}N$ quality. To achieve an appropriate thickness of the $Al_xGa_{1-x}N$ barrier of about 10 nm, sample C is grown by increasing the barrier growth time by a factor of two which led to a sample with ~2.2 nm GaN/~8.3 nm $Al_{0.09}Ga_{0.91}N$ MQWs without a significant reduction in quality.

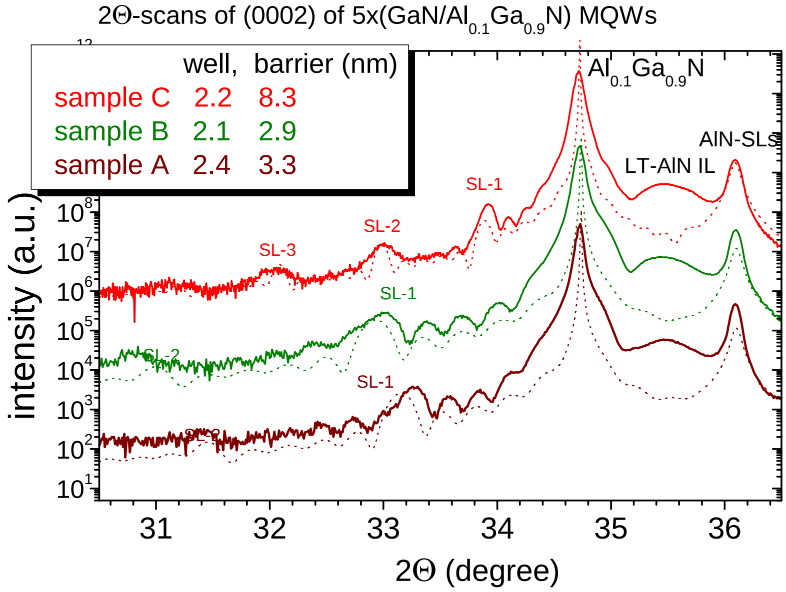

Figure 6.2.2 XRD θ/2θ-scans of the GaN/$Al_{0.1}Ga_{0.9}N$ (0002) reflections with different MQW thicknesses

In *Fig.6.2.3*, it can be seen that the quality of these GaN/$Al_{0.09}Ga_{0.91}N$ MQW structures on the AlN-SL buffer layers with a quality fluctuation are nearly stable as represented by nearly constant ω-FWHMs of (0002) and (10-10) reflections around 0.20°or 720 arcsec and 0.55° or 1980 arcsec, respectively. Sample A shows a higher in-plane residual strain whereas those of sample B and C are nearly constant. Therefore further MQW samples were grown on the $Al_xGa_{1-x}N$:Si layers with Si flow rate of 0.25 sccm reduced in sequence from 0.5, 1, and 2 sccm of the first AlGaN layer.

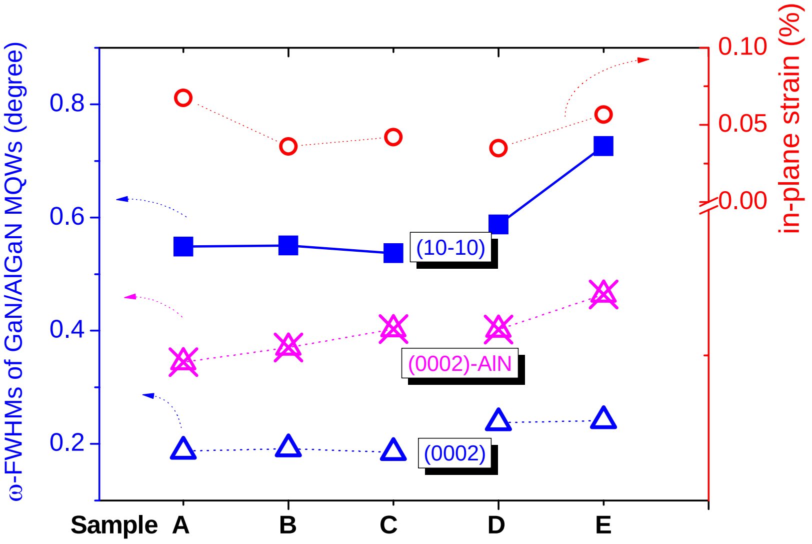

Figure 6.2.3 ω-FWHMs of the GaN/Al$_{0.1}$Ga$_{0.9}$N (0002)and (10-10) reflections and in-plane strain with different MQW structures

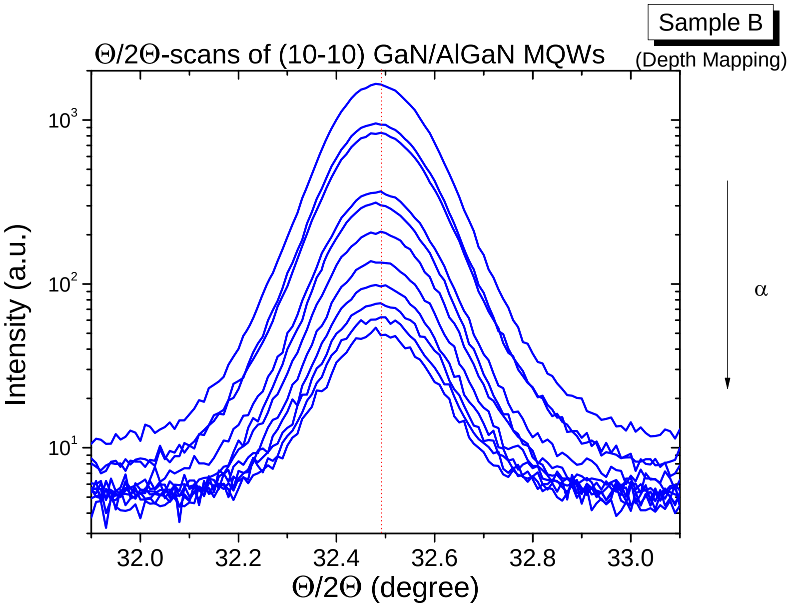

Figure 6.2.4 Depth mapping of GIID measurements of the GaN/Al$_{0.1}$Ga$_{0.9}$N (10-10) reflections

Depth sensitive GIID measurements of sample B show an identical 2θ-position of the GaN/Al$_{0.09}$Ga$_{0.91}$N MQWs and prove that the layers were grown pseudomorphically (*Fig. 6.2.4*).

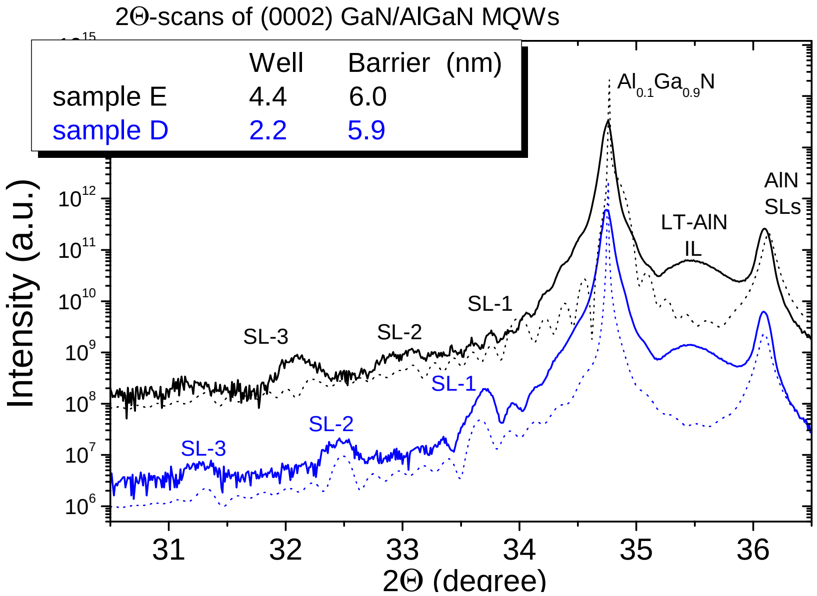

Figure 6.2.5 XRD θ/2θ-scans of the GaN/Al$_{0.1}$Ga$_{0.9}$N (0002) reflections with different MQW thicknesses

Next for the second series of the main Al$_x$Ga$_{1-x}$N:Si buffer layers with a slightly higher Al composition around 0.11, two samples were grown with a variation of the GaN-well thickness. As shown in *Fig.6.2.5* of HR-XRD θ/2θ-scans of the GaN/Al$_{0.1}$Ga$_{0.9}$N (0002) reflections, sample D with ~2.2 nm GaN / ~5.9 nm Al$_{0.1}$Ga$_{0.9}$N MQWs and sample E with ~4.4 nm GaN / ~6 nm Al$_{0.1}$Ga$_{0.9}$N MQWs show interference fringes and their finite thickness fringes indicating a good MQW quality.

Sample E with a thicker GaN well shows a lower quality with an increased ω-FWHM (10-10) reflection of 0.73° from 0.59° and also an increased in-plane strain of 0.06% from 0.03% when compared to sample D whereas the ω-FWHM of the (0002) reflection is constant around 0.24° or 870 arcsec as revealed in *Fig.6.2.3*. To some part this might originate in a lower AlN-SL quality of sample E.

A MQW series of 3 samples with different MQW-structures i.e. ~1.8 nm GaN/~7.6 nm Al$_{0.1}$Ga$_{0.9}$N, ~3.4 nm GaN/~10 nm Al$_{0.1}$Ga$_{0.9}$N, and ~14.2 nm GaN/~10 nm MQWs for sample W1, W2 and W3, respectively was grown on optimized AlGaN:Si buffer layers as presented in *Fig. 6.2.6* and in *table 6.8.*

Table 6.8 Ga N/AlGaN MQW samples with various thicknesses

Sample	**MQW thichness (nm)**	
	GaN	AlGaN
W1	~1.8	~7.6
W2	~3.4	~10
W3	~14.2	~10

Figure 6.2.6 GaN/$Al_{0.1}Ga_{0.9}N$ MQW samples with various thicknesses

In XRD θ/2θ-scans of the GaN/$Al_{0.1}Ga_{0.9}N$ (0002) reflections as shown in *Fig.6.2.7*, all samples show distinguished interference fringes and finite thickness fringes in high order indicating a good-quality of the surfaces and interfaces of these GaN/$Al_{0.1}Ga_{0.9}N$ MQW structures.

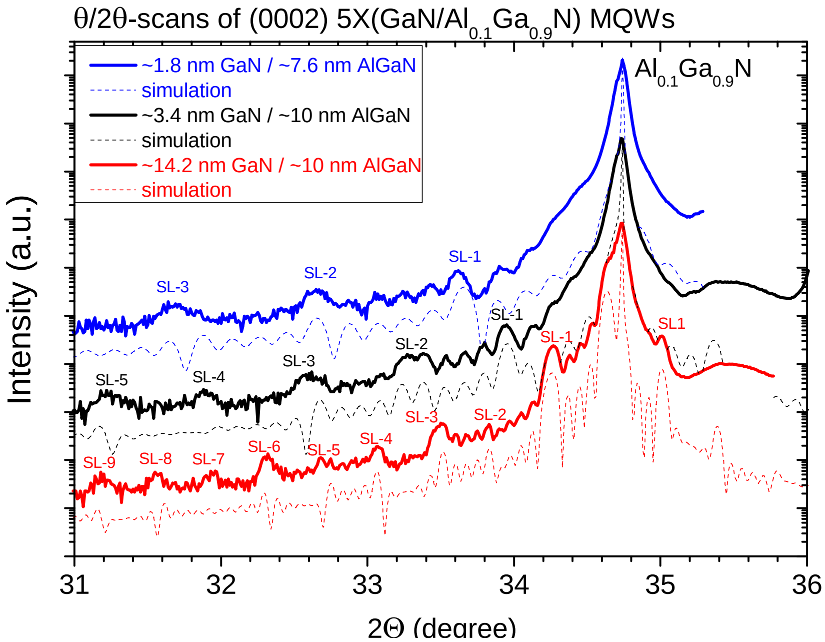

Figure 6.2.7 XRD θ/2θ-scans of the GaN/$Al_{0.1}Ga_{0.9}N$ (0002) reflections with a variation of MQW thicknesses

6.2.2. Optical quality of GaN/$Al_{0.1}Ga_{0.9}N$ multi-quantumwells

The optical qualities of these GaN/$Al_{0.1}Ga_{0.9}N$ MQW samples were characterized by photoluminescence (PL) and cross-sectional cathodoluminescence (CL) measurements. Using a He-Cd laser, PL measurements were performed at room temperature and at 10 K. Both show near UV luminescence at ~350 nm of the ~1.8 nm GaN/~7.6 nm $Al_{0.1}Ga_{0.9}N$ MQW, at ~360 nm of the ~3.4 nm GaN/~10 nm $Al_{0.1}Ga_{0.9}N$ MQW and no UV luminescence of the ~14.2 nm GaN well sample. An intense DAP luminescence (green luminescence for this case) related to group-III defects at ~540 nm or ~2.3 eV is observable in all samples as shown in *Fig.6.2.8 and Fig.6.2.9*.

It can be observed that with a narrow GaN well of 1.8 nm and a narrow $Al_{0.1}Ga_{0.9}N$ barrier of ~7.6 nm a higher luminescence energy was achieved likely due to a reduction of QCSE and higher energy of the carriers in the well but a four times lower UV-luminescence intensity compared to the ~3.4 nm GaN-well sample. The results imply a low efficiency to confine electrons and holes to efficiently recombination radiatively which worsens with a thin GaN-well and $Al_{0.1}Ga_{0.9}N$-barrier.

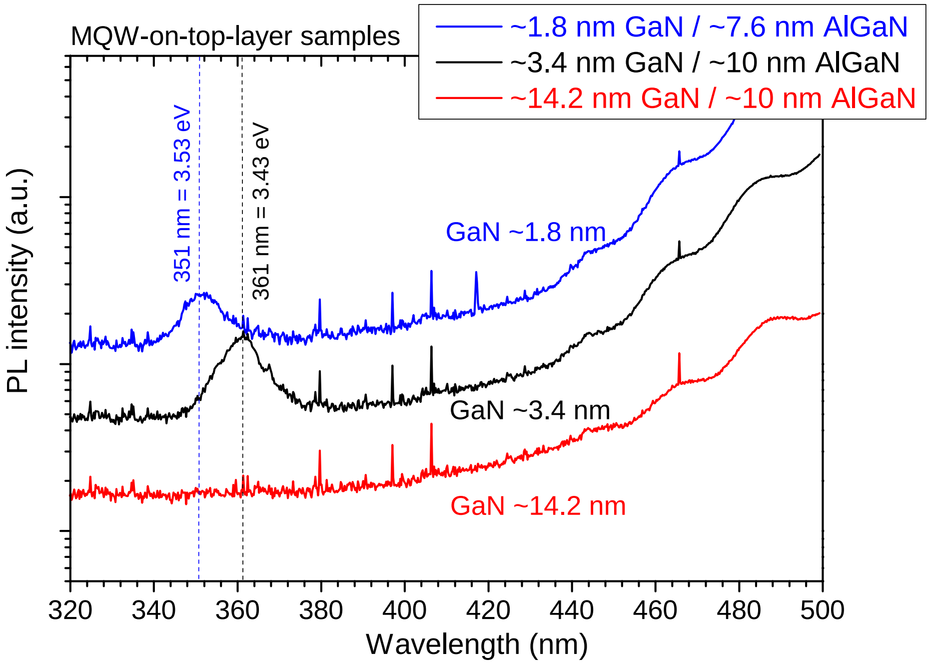

Figure 6.2.8 PL measurements on GaN/ $Al_{0.1}Ga_{0.9}N$ MQW structures at room temperature showing near UV-luminescence at 351 and 361 nm

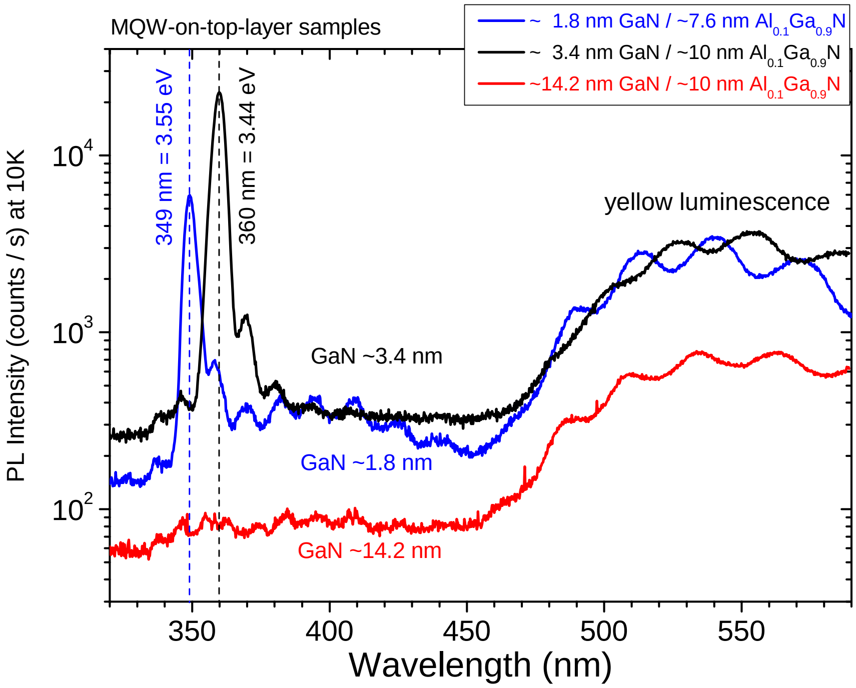

Figure 6.2.9 PL measurements on GaN/ $Al_{0.1}Ga_{0.9}N$ MQW structures at 10K showing near UV-luminescence at 349 and 360 nm

As shown in *Fig.6.2.10*, cross-sectional cathodoluminescence (CL) measurements of the ~1.8 nm GaN/~7.6 nm $Al_{0.1}Ga_{0.9}N$ MQW show that in the upper part the sample material is charged (distorted optical data) by the electron beam due to a high resistivity compared to the other sample regions. However it is indicated that the lower part of the $Al_{0.1}Ga_{0.9}N$:Si layers has a good optical quality and a dominant near-bandgap luminescence peak at ~340 nm without a DAP-luminescence peak. The upper part of the GaN/$Al_{0.1}Ga_{0.9}N$ MQW shows 2 UV-luminescence peaks at ~340 and ~350 nm related to $Al_{0.1}Ga_{0.9}N$-barrier and GaN-QW luminescence, respectively and an intense DAP-luminescence. When compared to PL measurements, both measurements are in good agreement. This is also the case for the other MQW samples as shown in Fig.A1 and A2 in appendix. They demonstrate that the UV-luminescence and DAP-luminescence both originate in the QW region. For the case of intense DAP- and low UV-luminescence of these GaN/$Al_{0.1}Ga_{0.9}N$ MQW structures, there are 2 possible processes which reduce the probability of radiative recombination i.e. an enhanced density of local defects or impurities in the materials and/or tunneling effects due to a too-thin $Al_{0.1}Ga_{0.9}N$ barrier. As seen in Fig.A1 in the appendix, additional MQW samples of the thick $Al_{0.1}Ga_{0.9}N$ barrier of ~20 nm yields an intense UV-luminescence and very low DAP-luminescence.

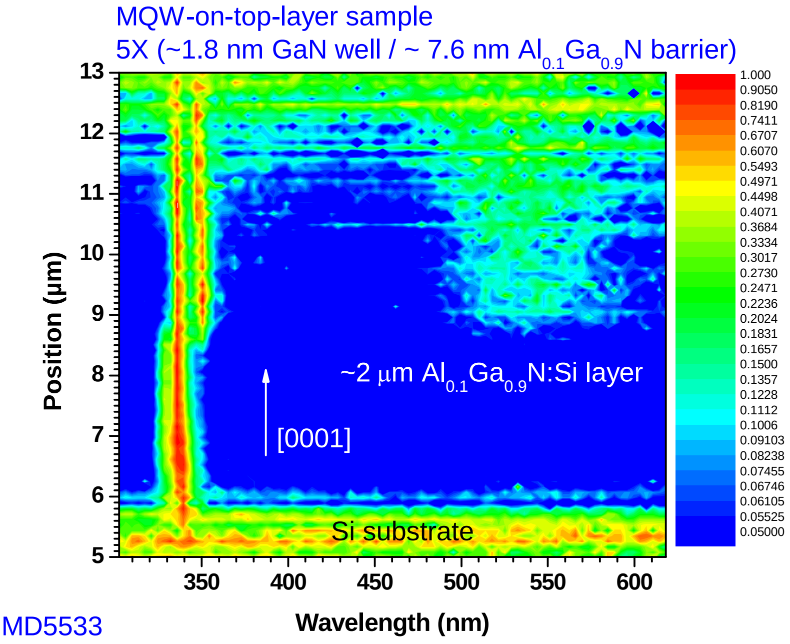

Figure 6.2.10 Cross-sectional CL measurements at 5K showing near UV-luminescence at ~340 and ~350 nm of ~1.8 nm GaN/~7.6 nm $Al_{0.1}Ga_{0.9}N$ MQW structures

The ~3 nm GaN/~10 nm $Al_{0.1}Ga_{0.9}N$ MQW structure with a good crystallography yields a low UV-luminescence and an intense DAP-luminescence due to a low efficiency of carrier confinements for effective radiative recombination.

6.3. Characterization of AlGaN-based UV LEDs

Full structures of AlGaN-based UV LED samples were grown which consist of 5 periods of ~100 nm Mg-doped GaN/$Al_{0.1}Ga_{0.9}N$ SLs with a ~20 nm GaN:Mg cap-layer for p-contacting followed by a 5 period GaN/$Al_{0.1}Ga_{0.9}N$ MQW grown on top of a ~1.8 µm thick $Al_{0.1}Ga_{0.9}N$:Si layer including ~10 nm thick LT-AlN:Si interlayers on a ~140 nm thick AlN-based superlattice buffer layer and a ~10 nm HT-AlN seeding layer on Si(111) as revealed in *Fig.6.3.1*.

With a growth-parameter variation of the GaN/AlGaN MQW, there are 3 samples to characterize the electrical and optical properties by current-voltage (I-V) and electroluminescence (EL) measurements: one sample with ~1.8 nm GaN/~10 nm $Al_{0.1}Ga_{0.9}N$ MQW (sample L1), one with ~3.4 nm GaN/~10 nm $Al_{0.1}Ga_{0.9}N$ MQW (sample L2) and one with ~3.4 nm GaN/~10 nm $Al_{0.15}Ga_{0.85}N$ MQW (sample L3) as summarized in *table 6.9*.

Table 6.9 AlGaN-based LED samples with various QW thicknesses

Sample	**QW thickness (nm)**	
	GaN	$Al_xGa_{1-x}N$
L1	1.8	~10, [Al]=0.1
L2	3.4	~10, [Al]=0.1
L3	3.4	~10, [Al]=0.12

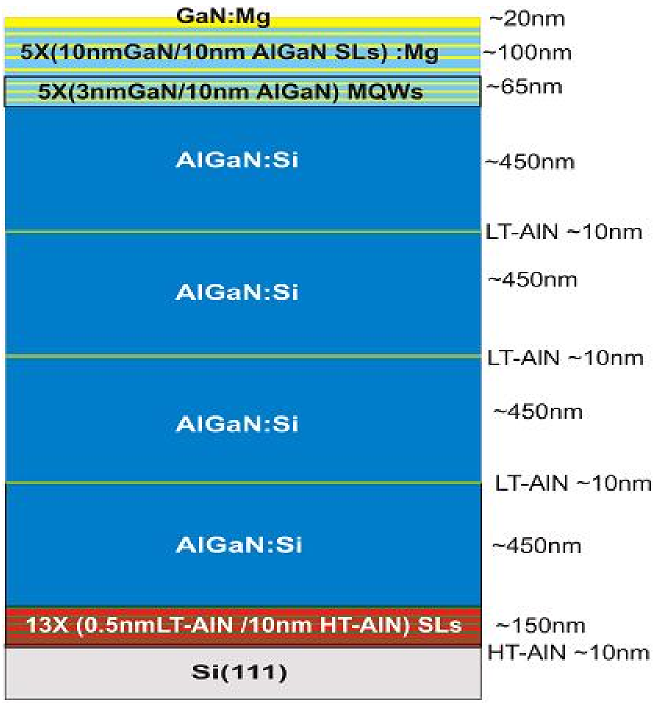

Figure 6.3.1 Scheme of the full structure for AlGaN-based UV LED samples on Si(111)

Nomarski microscopy shows a crack-free surface morphology for all samples (*Fig.6.3.2*). Moreover, in situ curvature measurements of these samples exhibit that compressive stress is induced during growth in the $Al_{0.1}Ga_{0.9}N$ layers by the AlN-SL buffer layer and the LT-AlN interlayers. This compressive stress is sufficient to compensate thermally induced tensile stress after cooling as represented in *Fig.6.3.3* leading to the crack-free surface morphology of this LED structure.

In order to more accurately investigate the thickness, material properties and dislocation propagation, cross-sectional TEM measurements were performed. It shows different contrast structures of each layer and a decreasing dislocation density with increasing thickness in *Fig.6.3.4*. Besides a major reduction in dislocation density within the AlN-based SLs, a continuously decreasing dislocation density in the $Al_{0.1}Ga_{0.9}N$:Si buffer layers from 3.0×10^{14} to 0.6×10^{14} cm^{-2}, can be observed. In *Fig.6.3.5*, the detailed TEM image obviously exhibits 5 periods of (~3.5 nm GaN/~7.2 nm $Al_{0.1}Ga_{0.9}N$) MQWs, 5 periods of Mg-doped (~8.4 nm GaN/~8.2 nm $Al_{0.1}Ga_{0.9}N$) SLs and ~18.3 nm GaN:Mg cap layer.

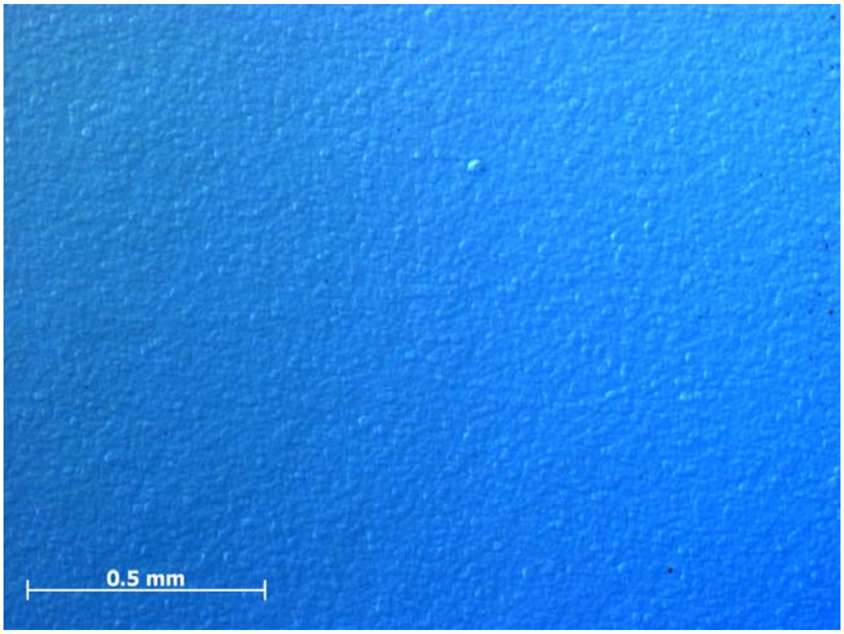

Figure 6.3.2. Nomarski microscopy image showing crack-free surface morphology of AlGaN-based LED sample on Si(111)

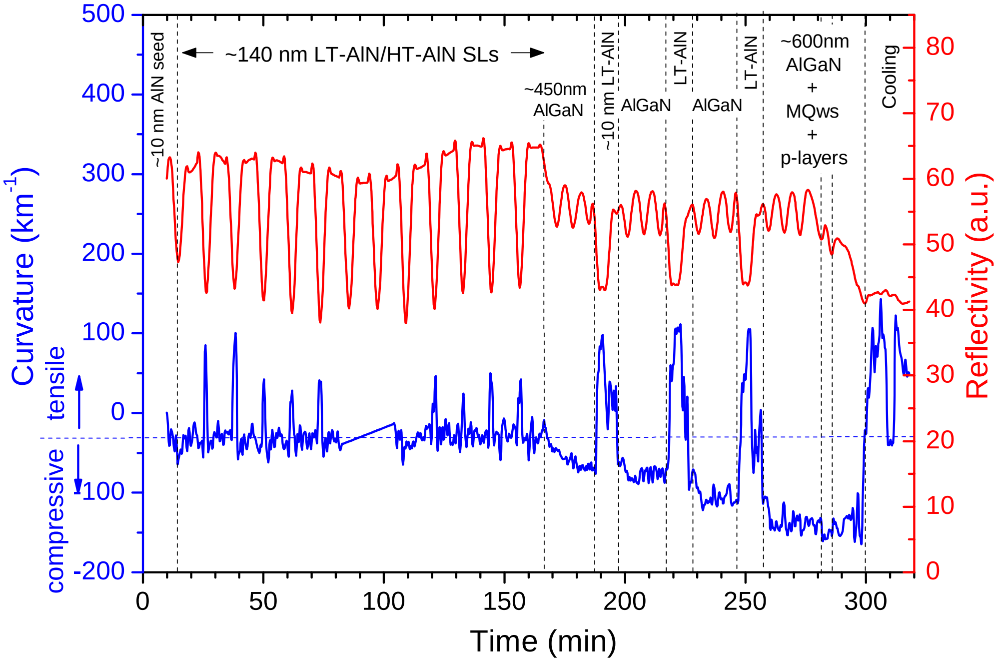

Figure 6.3.3 In situ curvature measurements of AlGaN-based LED sample on Si(111)

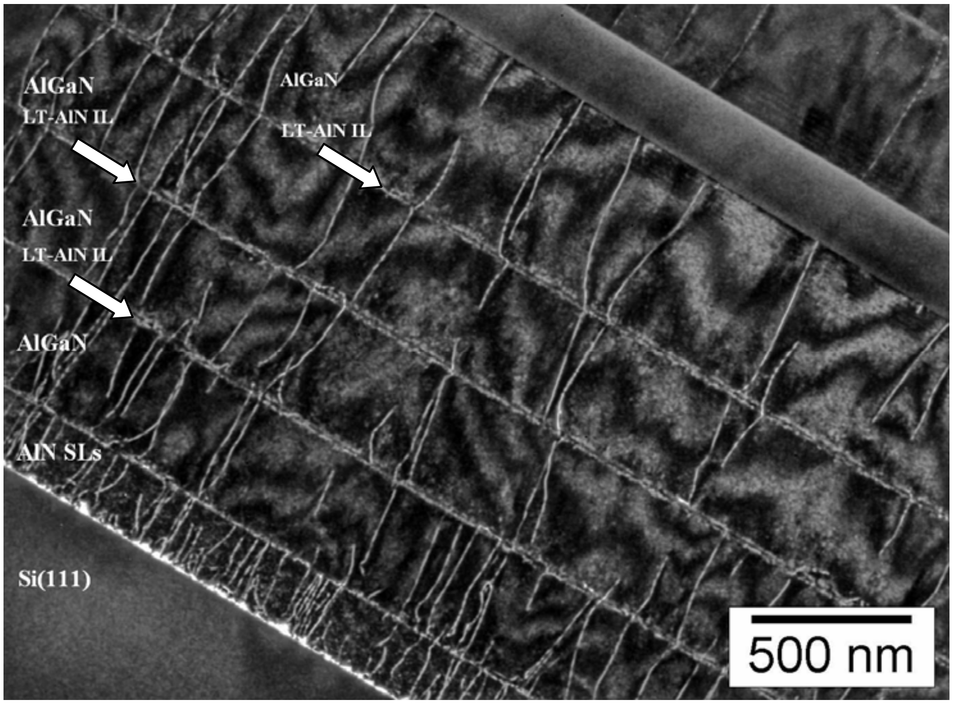

Figure 6.3.4. Cross-sectional TEM image of AlGaN-based UV LED sample on Si(111)

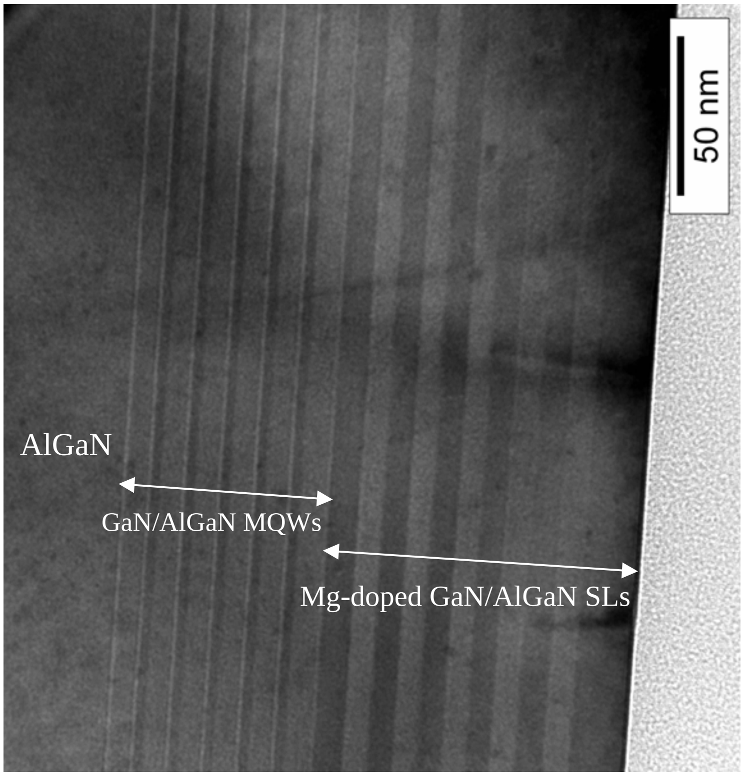

Figure 6.3.5 Cross-sectional TEM image showing obviously different contrast structures of GaN and $Al_{0.1}Ga_{0.9}N$ layers of GaN/$Al_{0.1}Ga_{0.9}N$ MQWs and Mg-doped GaN/$Al_{0.1}Ga_{0.9}N$ SLs

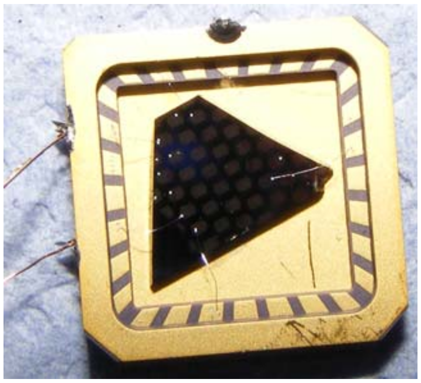

Figure 6.3.6 AlGaN-based LED structure on Si(111) with metal contacts in the ship carrier

In order to characterize the electrical properties of the LED samples L1, L2, and L3, p-type metal contacts of ~20 nm Ni/~20 nm Au were evaporated on top and alloyed. N-type Al contacts were evaporated on the Si substrate. The whole sample was glued with Ag adhesive into a chip carrier as shown in *Fig.6.3.6*.

Current-voltage (I-V) measurements were performed to characterize the LED samples as exhibited in *Fig.6.3.7*. All LEDs represent a forward-diode characteristic with turn-on voltages in the range of 2.6 - 3.1 V and a high series-resistance in the range of 550 - 990 Ω at 20 mA. Sample L1 of ~1.8 nm GaN/~10 nm $Al_{0.1}Ga_{0.9}N$ MQW structure shows a better I-V characteristic with a steeper plot and a lower resistivity of 550 Ω than others but a bit lower turn-on voltage. Main reason for the high series resistance is the undoped AlN SL buffer. Sample L3 of ~3.4 nm GaN/~10 nm $Al_{0.12}Ga_{0.88}N$ MQW structure on $Al_{0.15}Ga_{0.85}N$:Si buffer layers shows the worst characteristic with the highest series resistance of 990 Ω due to a lower material quality of the $Al_{0.12}Ga_{0.88}N$ barrier and n-type $Al_{0.15}Ga_{0.85}N$ buffer layers with higher Al composition. More details on some of the electrical properties of these LED structures can be found in reference [Günt09].

The optical properties of these LED samples were characterized at room temperature by electroluminescence (EL) microscopy on the top side at 4-6 V and 1 mA as revealed in *Fig.6.3.8*. The dominant luminescence of all LED samples is green luminescence and it is also observed a low intensity near UV-luminescence at about 360 nm. Sample L2 with thicker GaN wells of ~3.4 nm shows a bit higher intensity and lower emission energy than sample L1 with thinner GaN wells of ~1.8 nm in good agreement with PL measurements of the same MQW structures. However with higher Al composition of sample L3 a near UV-luminescence with a high intensity of the green luminescence can be observed. This low UV-luminescence intensity results from a low efficiency to confine carriers within the QW structure, absorption of some UV-light by the GaN top layers and probably an electrons overflow through the QW region to the p-type region which can be reduced with AlGaN blocking layers between the QW and the p-type region.

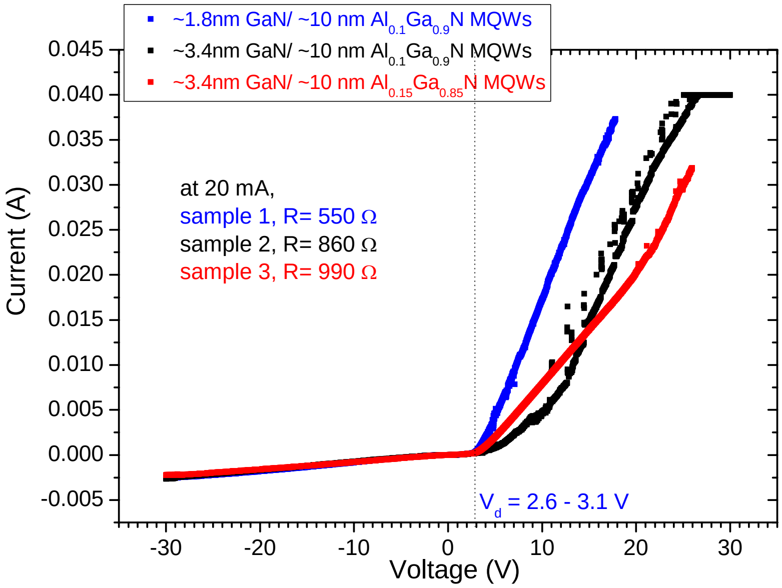

All LEDs with the same n-type and p-type structures

Figure 6.3.7 I-V measurements of AlGaN-based UV LED samples on Si(111)

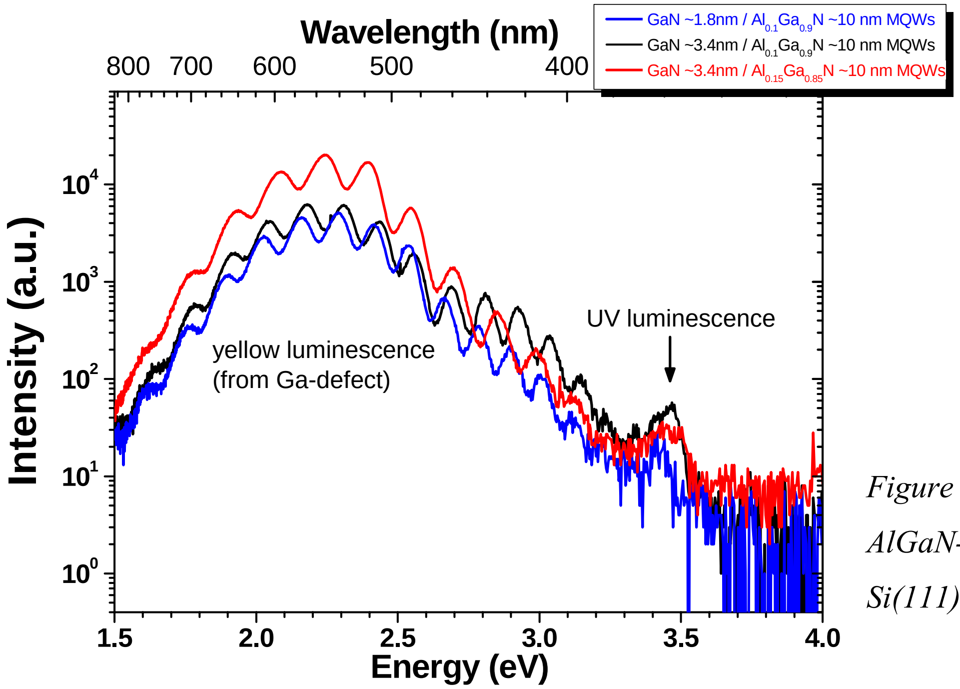

Figure 6.3.8 EL measurements of AlGaN-based UV LED samples on Si(111)

In summary, the first crack-free AlGaN-based UV LED on Si(111) substrate with a turn-on voltage about 3 V was achieved. It yields a low efficiency of UV-luminescence and higher intense green luminescence due to inefficient MQW structure. For the use in LED applications, these LED structure are required to be improved especially the MQW structure and an injection barrier should be introduced.

Chapter 7

Summary

In this work, the MOVPE growth of AlGaN-based UV-LEDs on Si(111) substrates was investigated and the first crack-free AlGaN-based UV-LEDs on Si(111) substrates were successfully demonstrated with an emission wavelength at ~350 nm. This could be achievable due to high-quality AlGaN materials, high injected carrier concentrations and radiative recombination in quantumwells.

High-quality $Al_xGa_{1-x}N$ layers with $0.05 \le x \le 0.65$ on Si substrate were achieved by using high-quality AlN seeding layer at high growth temperature and inserting novel LT-AlN/HT-AlN superlattices as buffer layers. These superlattice buffer layers not only reduce the dislocation density and improve the quality of AlGaN but also help compensating thermally induced tensile strain in AlGaN layers after cooling from growth temperature. Mechanisms to reduce the dislocation density in the AlN-based SLs and AlGaN layers such as bending dislocation propagation from the growth direction, forming dislocation loops, combining and terminating dislocations were observed by cross-sectional TEM measurements. The dislocation density was reduced from 8.4×10^{10} cm^{-2} in the AlN-SLs to 1.8×10^{10} cm^{-2} in the $Al_{0.1}Ga_{0.9}N$ layers. During MOVPE growth, compressive stresses in $Al_xGa_{1-x}N$ layers were induced by these LT-AlN/HT-AlN superlattice buffer layers to efficiently compensate a thermally tensile strain after cooling down leading to crack-free ~450-nm-thick $Al_xGa_{1-x}N$ layers and upto ~1-μm-thick $Al_{0.1}Ga_{0.9}N$ layers without an inserting LT-AlN interlayer. As grown on these LT-AlN/HT-AlN superlattice buffer layers, tensile residual strain in these $Al_xGa_{1-x}N$ layers continuously reduced with a higher Al composition and turned to be compressive for [Al]> 0.2. $Al_xGa_{1-x}N$ layers with $0.05 \le x \le 0.65$ exhibited smooth surfaces with visible growth steps, low pit densities and roughness for 5×5 μm^2-scan area in the range of 0.7 – 2.3 nm rms by AFM measurements.

The best crystalline quality of $Al_{0.1}Ga_{0.9}N$ was obtained with the best ω-FWHMs of the (0002) and (10-10) reflections of ~750 and ~1020 arcsec, respectively and this $Al_{0.1}Ga_{0.9}N$ had a good optical quality with a narrow linewidth and very high intensity of a near-bandgap emission at 3.746 eV or 330 nm. Meanwhile the near-bandgap emission of $Al_{0.65}Ga_{0.35}N$ was at 5.399 eV or 240 nm with a low yellow luminescence intensity.

Crack-free $Al_xGa_{1-x}N$ layers with $0.05 \le x \le 0.65$ were achieved on the Si substrates with good crystalline and optical qualities by growing on such these optimized AlN-based superlattice buffer and seed layers.

MOVPE growth of crack-free $Al_{0.1}Ga_{0.9}N$ layers thicker than 1µm on Si substrate was successful by inserting LT-AlN interlayers in between the $Al_{0.1}Ga_{0.9}N$ layers inducing compressive stress in the subsequently grown $Al_{0.1}Ga_{0.9}N$ layers to compensate thermally induced tensile strain from the different thermal expansion of Si substrate resulting in crack-free layers even in excess of ~2 µm after cooling.

One important factor to develop UV-LEDs, is a high carrier concentrations in AlGaN layers. The maximum electron concentration of 2.6×10^{18} cm^{-3} was achieved in *n*-type $Al_{0.1}Ga_{0.9}N$:Si layers. In case of p-type conductivity, Mg-doped GaN/$Al_{0.1}Ga_{0.9}N$ superlattices yielded a hole concentration of up to 2.4×10^{17} cm^{-3}.

GaN/$Al_{0.1}Ga_{0.9}N$ MQWs with a good crystalline interfaces quality, as proven by XRD measurements with well visible interference fringes and finite thickness fringes and TEM cross-sectional measurements, were applied for active layers emitting a UV-luminescence at ~360 nm in PL measurements at room temperature.

As a full LED structure on Si(111) substrate, AlGaN-based UV-LEDs consisted of thick $Al_{0.1}Ga_{0.9}N$:Si layers on LT-AlN/HT-AlN SL buffer layers and an active layer of GaN/$Al_{0.1}Ga_{0.9}N$ MQWs as followed by Mg-doped (GaN/$Al_{0.1}Ga_{0.9}N$) superlattices and GaN:Mg cap layers. This crack-free LED yielded a ~350 nm UV luminescence in electroluminescence measurements at room temperature. As characterized by I-V measurements, the turn-on voltage is in a range of 2.6 - 3.1 V.

Outlook

For shorter wavelength UV emitters, $Al_xGa_{1-x}N$ with higher Al composition is required. To achieve a higher crystalline quality of such layers, the thicknesses and number of LT-AlN/HT-AlN SL buffer layers are required to be optimized for each composition of $Al_xGa_{1-x}N$ as well as the growth parameters of the $Al_xGa_{1-x}N$ layers.

Further improvements which are advantageous for better performance are:

- To enhance the activation efficiency of Si-doping by improving the $Al_xGa_{1-x}N$:Si growth parameters and using short-period superlattices for higher Al concentrations.

- To enhance the activation efficiency of Mg-doping and for other shorter wavelength devices in GaN/AlGaN superlattices, further optimization and higher AlGaN/AlGaN superlattices need to be optimized.

For better carrier confinement in the MQW system, the Al composition of $Al_xGa_{1-x}N$ barrier layers is proposed to be increased. Also the addition of In-segregation might promote a higher efficiency of radiative recombination. To avoid electron overshoot and recombination within the p-type layer, an $Al_xGa_{1-x}N$:Mg electron blocking layer of higher Al concentration than the $Al_xGa_{1-x}N$ buffer should be inserted.

For an enhancement of light extraction and improving performance, a thin-film LED, p-side down mounted onto a carrier, and subsequent Si removal are required.

List of Figures

List of Tables

* * *

Bibliography

A

[AdEnweb] www.advanced-energy.com

[Acar08], S. Acar, S.B. Lisesivdin, M. Kasap, S. Özcelik, and E. Özbay, *"Determination of two-dimensional electron and hole gas carriers in AlGaN/GaN/AlN heterostructures grown by Metal Organic Chemical Vapor Deposition"*, Thin Solid Films **516**, 2041 (2008).

[Adiv01a] V. Adivarahan, G. Simin, G. Tamulaitis, R. Srinivasan, J. Yang, M.A. Khan, M.S. Shur and R. Gaska, *''Indium–silicon co-doping of high-aluminum-content AlGaN for solar blind photodetectors''*, Appl. Phys. Lett. **79** (12), 1903 (2001).

[Adiv01b] V. Adivarahan, A. Chitnis, J.P. Zhang, M. Shatalov, J.W. Yang, G. Simin, M.A. Khan, R. Gaska and M.S. Shur, *''Ultraviolet light-emitting diodes at 340 nm using quaternary AlInGaN multiple quantum wells''*, Appl. Phys. Lett. **79**, 4240 (2001).

[Adiv04] V. Adivarahan, W.H. Sun, M. Shatalov, S. Wu, H.P. Maruska, and M.A. Khan, *''250 nm AlGaN light-emitting diodes''*, Appl. Phys. Lett. **85** (12), 2175 (2004).

[Adiv05] V. Adivarahan, J. Yang, A. Koudymov, G. Simin, and M.A. Khan, *"Stable CW Operation of Field-Plated GaN-AlGaN MOSHFETs at 19 W/mm"*, IEEE ELECTRON DEVICE LETTERS **26** (8), 535 (2005).

[Adiv09] V. Adivarahan, A. Heidari, B. Zhang, Q. Fareed, S. Hwang, M. Islam, and M.A. Khan, *''280nm Deep Ultraviolet Light Emitting Diode Lamp with an AlGaN Multiple Quantum Well Active Region''*, Appl. Phys. Express **2**, 102101 (2009).

[Akas92] I. Akasaki, H. Amano, K. Itoh, N. Koide, and K. Manabe, *"GaN-based UV/blue light emitting devices''*, Inst. Phys. Conf. Ser., **129**, 851 (1992).

[Akzoweb] www.akzonobel.com

[AlTa08] T.M. Al Tahtamouni, A. Sedhain, J.Y. Lin, and H.X. Jiang, *''Si-doped high Al-content AlGaN epilayers with improved quality and conductivity using indium as a surfactant''*, Appl. Phys. Lett. **92**, 092105 (2008).

[Aman89] H. Amano, M. Kito, K. Hiramatsu and I. Akasaki, *"P-Type Conduction in Mg-Doped GaN Treated with Low-Energy Electron Beam Irradiation (LEEBI)"*, Jpn. J. Appl. Phys. **28**, L2112 (1989).

[Aman98] H. Amano, M. Iwaya, T. Kashima, M. Katsuragawa, I. Akasaki, J. Han, S. Hearne, J.A. Floro, E. Chason and J. Figiel, *"Stress and Defect Control in GaN Using Low Temperature Interlayers"*, Jpn. J. Appl. Phys. **37**, L1540 (1998).

[Amba98] O. Ambacher, *''Growth and applications of Group III-nitrides''*, J. Phys. D: Appl. Phys. **31**, 2653 (1998).

[Amba99] O. Ambacher, R. Dimitrov, M. Stutzmann, B. E. Foutz, M. J. Murphy, J. A. Smart, J. R. Shealy, N. G. Weimann, K. Chu, M. Chumbes, B. Green, A. J. Sierakowski, W. J. Schaff, and L. F. Eastman, *"Role of Spontaneous and Piezoelectric Polarization Induced Effects in Group-III Nitride Based Heterostructures and Devices"*, Phys. Stat. Sol. B **216**, 381 (1999).

[Amba02] O. Ambacher, J. Majewski, C. Miskys, A. Link, M. Hermann, M. Eickhoff, M. Stutzmann, F. Bernardini, V. Fiorentini, V. Tilak, B. Schaff and L. F. Eastman, *"Pyroelectric properties of Al(In)GaN/GaN hetero- and quantum well structures"*, J. Phys.: Condens. Matter **14**, 3399 (2002).

[Arul05] S. Arulkumaran, T. Egawa, S. Matsui, and H. Ishikawa,*"Enhancement of breakdown voltage by AlN buffer layer thickness in AlGaN/GaN high-electron-mobility transistors on 4 in. diameter silicon"*, Appl. Phys. Lett. **86**, 123503 (2005).

[Auth01] A. Authier, *"Dynamical Theory of X-Ray Diffraction"*, Oxford University Press, Oxford (2001).

B

[Bayr08] C. Bayram, J. L. Pau, R. McClintock, and M. Razeghi, *"Performance enhancement of GaN ultraviolet avalanche photodiodes with p-type δ-doping",* Appl. Phys. Lett. **92**, 241103 (2008).

[Beau97] B. Beaumont, S. Haffouz, P. Gibart M. Leroux, Ph. Lorenzini, E. Calleja, and E. Muñoz, *"Violet GaN based light emitting diodes fabricated by metal organics vapour phase epitaxy"*, Materials Science and Engineering B **50**, 296 (1997).

[Bern97] F. Bernardini, V. Fiorentini, and D. Vanderbilt, *"Spontaneous polarization and piezoelectric constants of III-V nitrides"*, Phys. Rev. B **56**, R10024 (1997).

[Bile05] Y. Bilenko, A. Lunev, X. Hu, J. Deng, T.M. Katona, J. Zhang, R. Gaska, M.S. Shur, W. Sun, V. Adivarahan, M. Shatalov and M.A. Khan, *''10 Milliwatt Pulse Operation of 265nm AlGaN Light Emitting Diodes''*, Jpn. J. Appl. Phys. **44** (3), L98 (2005).

[Bläs02] J. Bläsing, A. Reiher, A. Dadgar, A. Diez, and A. Krost , *"The origin of stress reduction by low-temperature AlN interlayers"*, Appl. Phy. Lett. **81** (15), 2722 (2002).

[Bori05] B. Borisov, V. Kuryatkov, Y. Kudryavtsev, R. Asomoza, S. Nikishin, D.Y. Song, M. Holtz, and H. Temkin, *''Si-doped* $Al_xGa_{1-x}N$ *(* $0.56 \le x \le 1$*) layers grown by molecular beam epitaxy with ammonia''*, Appl. Phys. Lett. **87**, 132106 (2005).

[Bour98] A. Bourret, A. Barski, J. L. Rouviere, G. Renaud, and A. Barbier, *"Growth of aluminum nitride on (111) silicon: Microstructure and interface structure"*, J. Appl. Phys. 83 (4), 2003 (1998)

[Brun08] F. Brunner, H. Protzmann, M. Heuken, A. Knauer, M. Weyers, and M. Kneiss, *"High-temperature growth of AlN in a production scale 11x2" MOVPE reactor"*, Phys. Stat. Sol. C **5** (6), 1799 (2008).

[Bush04] A.R. Bushroa, C. Jacob, H. Saijo, S. Nishino, "Lateral epitaxial overgrowth and reduction in defect density of 3C-SiC on patterned Si substrates", J. Cryst. Growth **271**, 200 (2004).

C

[Cantu03] P. Cantu, S. Keller, U.K. Mishra, and S.P. DenBaars, *"Metalorganic chemical vapor deposition of highly conductive* $Al_{0.65}Ga_{0.35}N$ *films"*, Appl. Phy. Lett. 82 (21), 3683 (2003).

[Chan01] S.J. Chang, Y.K. Su, T.L. Tsai, C.Y. Chang, C.L. Chiang, C.S. Chang, T.P. Chen, and K.H. Huang, *"Acceptor activation of Mg-doped GaN by microwave treatment"*, Appl. Phys. Lett. **78** (3), 312 (2001)

[Chemweb] www.chemicalbook.com

[CHChen96] C.H. Chen, H. Liu, D. Steigerwald, W. Imler, C.P. Kuo, M.G. Craford, M. Ludowise, S. Lester and, J. Amano, *"A Study of Parasitic Reactions Between NH 3 and TMGa or TMAI"*, J. Electron. Mater. **25**, 1004 (1996).

[Chen96] G.D. Chen, M. Smith, J.Y. Lin, H.X. Jiang, S.H. Wei, M.A. Khan, and C.J. Sun, *''Fundamental optical transitions in GaN''*, Appl. Phys. Lett. **68** (20), 2784 (1996).

[Chen01] P. Chen, R. Zhang, Z.M. Zhao, D.J. Xi, B. Shen, Z.Z. Chen, Y.G. Zhou, S.Y. Xie, W.F. Lu, and Y.D. Zheng, *"Growth of high quality GaN layers with AlN buffer on Si(111) substrates"*, J. Cryst. Growth **225**, 150 (2001).

[Cheng01] Y.C. Cheng, C.C. Liao, S.W. Feng, C.C. Yang, Y.S. Lin, K.J. Ma, C.C. Chou, C.M. Lee and J.I. Chyi, *"Laser-Induced Activation of p-Type GaN with the Second Harmonics of a Nd:YAG Laser"* , Jpn. J. Appl. Phys. 40, 2143 (2001).

[Chen07] K. Cheng, M. Leys, J. Derluyn, S. Degroote, D.P. Xiao, A. Lorenz, S. Boeykens, M. Germain, and G. Borghs, *"AlGaN/GaN HEMT grown on large size silicon substrates by MOVPE capped with in-situ deposited* Si_3N_4*"*, J. Cryst. Growth **298**, 822 (2007).

[Choi00] S.C. Choi, J.H. Kim, J.Y. Choi, K.J. Lee, K.Y. Lim, and G.M. Yang, *"Al concentration control of epitaxial AlGaN alloys and interface control of GaN/AlGaN quantum well structures"*, J. Appl. Phys. **87**, 172 (2000).

[Chua06] X. Chuanbing, J. Fengyi, F. Wenqing, W. Li, L. Hechu and M. Chunnan, *''Different properties of GaN-based LED grown on Si(111) and transferred onto new substrate''*, Science in China: Series E Technological Sciences **49** (3), 313 (2006).

[Clam06] J. Y. Clames, Ch. Giesen, T. Meyer, and M. Heuken, *"MOCVD of InGaN-based light emitting structures on silicon substrates with strain optimized buffer layers using long Al pre-deposition"*, Phys. Stat. Sol. C **3** (6), 2191 (2006).

[Cole08] C.C. Coleman, *"Modern Physics for semiconductor science"*, Wiley-VCH, Weinheim (2008).

[Cont02] O. Contreras, F.A. Ponce, J. Christen, A. Dadgar and A. Krost, *''Dislocation annihilation by silicon delta-doping in GaN epitaxy on Si''*, Appl. Phys. Lett. **81**(25), 4712 (2002).

[Cont08] O.E. Contreras, F. Ruiz-Zepeda, A. Dadgar, A. Krost, and F.A. Ponce, *"Atomic Arrangement at the AlN/Si(110) Interface"*, Appl. Phys. Express 1, 061104 (2008).

[Cord05] Y. Cordier, F. Semond, M. Hugues, F. Natali, P. Lorenzini, H. Haas, S. Chenot, M. Laügt, O. Tottereau, P. Vennegues, and J. Massies, *"AlGaN/GaN/AlGaN DH-HEMTs grown by MBE on Si(111)"*, J. Cryst. Growth **278**, 393 (2005).

[Crab01] R**.**H**.** Crabtree**,** *"The organometallic chemistry of the transition metals"*, 3rd Edition, Wiley-Interscience Publication, New York (2001)

[Crei02] J. R. Creighton, *"Vapor Pressures of the Adducts Formed during AlGaN Organometallic Vapor-Phase Epitaxy"*, J. Electronic materials **31** (12), 1337 (2002).

[Crei04] J.R. Creighton, G.T. Wang, W.G. Breiland, and M.E. Coltrin, *"Nature of the parasitic chemistry during AlGaInN OMVPE"*, J. Cryst. Growth **261**, 204 (2004).

D

[Dabr00] J. Dabrowski and H. J. Müssig, *"Silicon Surfaces and Formation of Interfaces"* , World Scientific Publishing, Singapore (2000)

[Dadgar] A. Dadgar, private communication

[Dadg00] A. Dadgar, J. Bläsing, A. Diez, A. Alam, M. Heuken and A. Krost, *"Metalorganic Chemical Vapor Phase Epitaxy of Crack-Free GaN on Si (111) Exceeding 1 µm in Thickness"*, Jpn. J. Appl. Phys. **39** (11B), L1185 (2000).

[Dadg01] A. Dadgar, J. Christen, T. Riemann, S. Richter, J. Bläsing, A. Diez, A. Krost, A. Alam, and M. Heuken, *‘‘Bright blue electroluminescence from an InGaN/GaN multiquantum-well diode on Si(111): Impact of an AlGaN/GaN multilayer’’,* Appl. Phys. Lett. **78** (15), 2211 (2001).

[Dadg02] A. Dadgar, M. Poschenrieder, O. Contreras, J. Christen, K. Fehse, J. Bläsing, A. Diez, F. Schulze, T. Riemann, F. A. Ponce, and A. Krost, *‘‘Bright, Crack-Free InGaN/GaN Light Emitters on Si(111)’’*, phys. stat. sol. (a) **192**, (2), 308 (2002).

[Dadg02v] A. Dadgar and A Krost, *“MOVPE growth of GaN on Si”*, Vacuum Science and Technology: Nitrides as seen by the technology (2002).

[Dadg03a] A. Dadgar, M. Poschenrieder, J. Bläsing, O. Contreras, F. Bertram, T. Riemann, A. Reiher, M. Kunze, I. Daumiller, A. Krtschil, A. Diez, A. Kaluz, A. Modlich, M. Kamp, J. Christen, F.A. Ponce, E. Kohn, and A. Krost, *‘‘MOVPE growth of GaN on Si(111) substrates’’*, J. Cryst. Growth **248**, 556 (2003).

[Dad03b] A. Dadgar, A. Strittmatter, J. Bläsing, M. Poschenrieder, O. Contreras, P. Veit, T. Riemann, F. Bertram, A. Reiher, A. Krtschil, A. Diez, T. Hempel, T. Finger, A. Kasic, M. Schubert, D. Bimberg, F. A. Ponce, J. Christen, and A. Krost, *“Metalorganic chemical vapor phase epitaxy of gallium-nitride on silicon”*, Phys. Stat. Sol. (c) **0** (6), 1583 (2003).

[Dadg03c] A. Dadgar, M. Poschenrieder, A. Reiher, J. Bläsing, J. Christen, A. Krtschil, T. Finger, T. Hempel, A. Diez, and A. Krost, *“Reduction of stress at the initial stages of GaN growth on Si(111)”*, Appl. Phys. Lett. **82** (1), 28 (2003).

[Dadg06] A. Dadgar, A. Krost, J. Christen, B. Bastek, F. Bertram, A. Krtschil, T. Hempel, J. Bläsing, U. Haboeck, and A. Hoffmann, *“MOVPE growth of high-quality AlN”*, J. Cryst. Growth **297**, 306 (2006).

[Dadg07a] A. Dadgar, P. Veit, F. Schulze, J. Bläsing, A. Krtschil, H. Witte, A. Diez, T. Hempel, J. Christen, R. Clos, and A. Krost, *“MOVPE growth of GaN on Si – Substrates and strain”*, Thin Solid Films 515, 4356 (2007).

[Dadg07b] A Dadgar, F Schulze, M Wienecke, A Gadanecz, J Bläsing, P Veit, T Hempel, A Diez, , J Christen and A Krost, *“Epitaxy of GaN on silicon-impact of symmetry and surface reconstruction”*, New J. Phys. **9**, 389 (2007).

[Dami08] B. Damilano, F. Natali, J. Brault, T. Huault, D. Lefebvre, R. Tauk, E. Frayssinet, J. C. Moreno, Y. Cordier, F. Semond, S. Chenot, and J. Massies, *‘‘Blue (Ga,In)N/GaN Light Emitting Diodes on Si(110) Substrate’’*, Appl. Phys. Express, **1**, 121101(2008).

[Dasg03] P. K. Dasguptu, I. Y. Eom, K. J. Morris and L. Jianzhong, *‘‘Light emitting diode-based detectors: Absorbance, fluorescence and spectroelectrochemical measurements in a planar flow-through cell’’*, Anal. Chim. Acta, 500, 337 (2003).

[Dimi05] G. P. Dimitrakopulos, 1, A. M. Sanchez, Ph. Komninou, Th. Kehagias, Th. Karakostas, G. Nouet, and P. Ruterana, *“Interfacial steps, dislocations, and inversion domain boundaries in the GaN/AlN/Si (0001)/(111) epitaxial system”*, phys. stat. sol. (b) 242 (8), 1617 (2005).

E

[Egaw02a] T. Egawa, B. Zhang, N. Nishikawa, H. Ishikawa, T. Jimbo, and M. Umeno, *“InGaN multiple-quantum-well green light-emitting diodes on Si grown by metalorganic chemical vapor deposition’’,* J. Appl. Phys., **91** (1), 528 (2002).

[Egaw02b] T. Egawa, T. Moku, H. Ishikawa, K. Ohtsuka and T. Jimbo, *‘‘Improved Characteristics of Blue and Green InGaN-Based Light-Emitting Diodes on Si Grown by Metalorganic Chemical Vapor Deposition’’*, Jpn. J. Appl. Phys. Part 2, **41** (6B), L 663 (2002).

[Egaw05] T. Egawa, B. Zhang, and H. Ishikawa, *‘‘High Performance of InGaN LEDs on (111) Silicon Substrates Grown by MOCVD’’*, IEEE Electron Device Lett. **26**, 169 (2005).

[Etzk01] E. V. Etzkorn and D. R. Clarke, *“Cracking of GaN films”*, J. Appl. Phys., **89**, (2), 1025 (2001).

F

[Felt01] E. Feltin, S. Dalmasso, P. de Mierry, B. Beaumont, H. Lahrèche, A. Bouillé, H. Haas, M. Leroux and P. Gibart, *‘‘Green InGaN Light-Emitting Diodes Grown on Silicon (111) by Metalorganic Vapor Phase Epitaxy’’*, Jpn. J. Appl. Phys., **40,** L738 (2001).

[Fieg07] M. Fiegera, M. Eickelkampa, L. R. Koshrooa, Y. Dikmea, A. Noculaka, H. Kalischa, M. Heukena,b, R.H. Jansena, and A. Vescana “MOVPE, processing and characterization of AlGaN/GaN HEMTs with different Al concentrations on silicon substrates”, J. Cryst. Growth, **298**, 843 (2007)

[Figg09] S. Figge, H. Kröncke, D. Hommel, and B. M. Epelbaum, *“Temperature dependence of the thermal expansion of AlN”*, Appl. Phys. Lett., **94**, 101915 (2009)

[Folls98] D. M. Follstaedt, J. Han, P. Provencio and J. G. Fleming, *“Microstructure of GaN grown on (111)Si by MOCVD”*, MRS Internet J. Nitride Semicond. Res. 4S1, 63.27 (1999).

[Freu03] L.B. Freund and S. Suresh, *‘‘Thin film materials: stress, defect formation and surface evolution’’*, Cambridge University Press, Cambridge (2003)

[Fuji06] N. Fujimoto, T. Kitano, G. Narita, N. Okada, K. Balakrishnan, M. Iwaya, S. Kamiyama, H. Amano, I. Akasaki, K. Shimono, T. Noro, T. Takagi, and A. Bandoh, *"Growth of high-quality AlN at high growth rate by high temperature MOVPE"*, Phys. Stat. Sol. C **3** (6), 1617 (2006).

[Fuji08a] S. Fujikawa, T. Takano, Y. Kondo, and H. Hirayama, *''Realization of 340-nm-Band High-Output-Power (>7mW) InAlGaN Quantum Well Ultraviolet Light-Emitting Diode with p-Type InAlGaN''*, Jpn. J. Appl. Phys. 47, 2941 (2008).

[Fuji08b] S. Fujikawa, T. Takano, Y. Kondo, and H. Hirayama, *''340 nm-band high-power InAlGaN quantum well ultraviolet light-emitting diode using p-type InAlGaN layers''*, Phys. Stat. Sol. (c), **5**, 2280 (2008).

[Fult08] B. Fultz and J. Howe, *"Transmission Electron Microscopy and Diffractometry of Materials"*, 3rd Edition, Springer, Berlin, Heidelberg (2008).

G

[Gelh03] O. Gelhausen, H. N. Klein, M. R. Phillips, and E. M. Goldys, *''Low-energy electron-beam irradiation and yellow luminescence in activated Mg-doped GaN''*, Appl. Phys. Lett., **83**, 3293 (2003).

[Goep00] I. D. Goepfert, E. F. Schubert, A. Osinsky, P. E. Norris, and N. N. Faleev, *"Experimental and theoretical study of acceptor activation and transport properties in p-type $Al_xGa_{1-x}N$/GaN superlattices"*, J. Appl. Phys., **88** (4), 2030 (2000)

[Götz96a] W. Götz, N.M. Johnson, J. Walker, D.P. Bour, and R.A. Street, *"Activation of acceptors in Mg-doped GaN grown by metalorganic chemical vapor deposition"*, Appl. Phys. Lett. **68** (5), 661 (1996)

[Götz96b] W. Götz, N. M. Johnson, C. Chen, H. Liu, C. Kuo, and W. Imler, *"Activation energies of Si donors in GaN"*, Appl. Phys. Lett. **68** (22), 3144 (1996).

[Grun91] M. Grundmann, A. Krost and D. Bimberg, *''Low-temperature metalorganic chemical vapor deposition of InP on Si(001)''*, Appl. Phys. Lett. **58**, 284 (1991)

[Guha98a] S. Guha and N. A. Bojarczuk, *''Ultraviolet and violet GaN light emitting diodes on silicon''*, Appl. Phys. Lett., **72** (4), 415 (1998).

[Guha98b] S. Guha and N. A. Bojarczuk, *''Multicolored light emitters on silicon substrates''***,** Appl. Phys. Lett., 73 (11), 1494 (1998).

[Günt09] K.-M. Günther, Diplomarbeit, Uni. Magdeburg (2009).

H

[Hack94] P. Hacke, A. Maekawa, N. Koide, K. Hiramatsu, and N. Sawaki, *"Characterization of the Shallow and Deep Levels in Si Doped GaN Grown by Metal-Organic Vapor Phase Epitaxy"*, Jpn. J. Appl. Phys. **33**, 6443 (1994).

[Hack01] S. Hackenbuchner, J.A. Majewski, G. Zandler, and P. Vogl, *"Polarization induced 2D hole gas in GaN/AlGaN Heterostructures"*, J. Cryst. Growth **230** , 607 (2001).

[Han98] J. Han, M. H. Crawford, R. J. Shul, J. J. Figiel, M. Banas, L. Zhang, Y. K. Song, H. Zhou, and A. V. Nurmikko, *''AlGaN/GaN quantum well ultraviolet light emitting diodes''*, Appl. Phys. Lett., **73** (12), 1688 (1998).

[Han03] B. Han, J. M. Gregie, and B. W. Wessels, *''Blue emission band in compensated GaN:Mg codoped with Si''***,** PHYS. REV.B, **68**, 045205 (2003).

[Hang01] D. R. Hang, C. H. Chen, Y. F. Chen, H. X. Jiang and J. Y. Lin, *"*$Al_xGa_{1-x}N$*/GaN band offsets determined by deep-level emission"*, J. Appl. Phys., 90 (4), 1887 (2001).

[Hara01] K. Harafuji, *"Transport of Gas-Phase Species Stored in Stagnant Volumes under a GaN Metalorganic Vapor Phase Epitaxy Horizontal Reactor"*, Jpn. J. Appl. Phys. Part 1, **40** (11), 6263 (2001)

[Heik03] S. Heikman, S. Keller, D. S. Green, S. P. DenBaars, and U. K. Mishra , *''High conductivity modulation doped AlGaN/GaN multiple channel heterostructures''***,** J. Appl. Phys., **94** (8), 5321 (2003).

[Herm04] M. A. Herman, W. Richter, and H. Sitter, *"Epitaxy: Physical Principles and Technical Implementation"*, Springer-Verlag, Berlin, Heidelberg (2004).

[Hira04] H. Hirayama, K. Akita, T. Kyono, T. Nakamura, and K. Ishibashi, *''High-Efficiency 352nm Quaternary InAlGaN-Based Ultraviolet Light-Emitting Diodes Grown on GaN Substrates''*, Jpn. J. Appl. Phys. 43, L1241 (2004).

[Hira05] H. Hirayama, *''Quaternary InAlGaN-based high-efficiency ultraviolet light-emitting diodes''*, J. Appl. Phys., **97**, 091101 (2005).

[Hira08] H. Hirayama, T. Yatabe, N. Noguchi, and N. Kamata,*''222–282 nm AlGaN and InAlGaN-based deep-UV LEDs fabricated on high-quality AlN on sapphire''*, Phys. Stat. Sol. (c), **5**, 2283 (2008).

[Hira09] H. Hirayama, S. Fujikawa, N Noguchi, J Norimatsu, T Takano, K. Tsubaki, and N Kamata,*''222–282 nm AlGaN and InAlGaN-based deep-UV LEDs fabricated on high-quality AlN on sapphire''*, Phys. Status Solidi A 206 (6), 1176 (2009).

[Hirak05] A. Hirako, K. Kusakabe and K. Ohkawa, *"Modeling of Reaction Pathways of GaN Growth by Metalorganic Vapor-Phase Epitaxy Using TMGa/NH_3/H_2 System: A Computational Fluid Dynamics Simulation Study"*, Jpn. J. Appl. Phys., **44** (2), 874 (2005)

[Holy99] V.Holy, U.Pietsch, and T. Baumbach, *''High-resolution x-ray scattering from thin films and multilayers''*, Springer-Verlag, Berlin, Heidelberg (1996)

[Hsu07] Y. P. Hsu, S. J. Chang, W. S. Chen, J. K. Sheu, J. P. Chu, and C. T. Kuo, *''Crack-Free High-Brightness InGaN/GaN LEDs on Si(111) with Initial AlGaN Buffer and Two LT-Al Interlayers''*, *J. Electochem. Soc.*, **154** (3), H191-H193, (2007)

[Hull00] B. A. Hull, S. E. Mohney, H. S. Venugopalan, and J. C. Ramer, *''Influence of oxygen on the activation of p-type GaN''*, Appl. Phys. Lett., **76**, 2271 (2000).

I

[Ibac03] H. Ibach and H. Lüth, *''Solid-state physics: an introduction to principles of materials science''*, 3rd edition, Springer-Verlag, Berlin, Heidelberg, New York (2003)

[Iida04] K. Iida, T. Kawashima, A. Miyazaki, H. Kasugai, S. Mishima, A. Honshio, Y. Miyake, M. Iwaya, S. Kamiyama, H. Amano, and I. Akasaki, *''350.9 nm UV Laser Diode Grown on Low-Dislocation-Density AlGaN''*, Jpn. J. Appl. Phys., **43** (4A), L499 (2004).

[Iman98] S. Imanaga and H. Kawai, *"One-dimensional simulation of charge control in a novel AlN/GaN insulated gate heterostructure field effect transistor with modulation doping"*, J. Cryst. Growtth, **189/190**, 742 (1998).

[Imur07] M. Imura, K. Nakano, N. Fujimoto, N. Okada, K. Balakrishnan, M. Iwaya, S. Kamiyama, H. Amano, I. Akasaki, T. Noro, T. Takagi, and A. Bandoh, *"Dislocations in AlN Epilayers Grown on Sapphire Substrate by High-Temperature Metal-Organic Vapor Phase Epitaxy"*, Jpn. J. Appl. Phys. **46**, 1458 (2007).

[Ishi08] H. Ishikawa, T. Jimbo, and T. Egawa,*''GaInN light emitting diodes with AlInN/GaN distributed Bragg reflector on Si''*, phys. stat. sol. (c) **5**, (6), 2086 (2008).

[Itan93] M. Itano, F. Kern, M. Miyashita, and T. Ohmi, *"Particle Removal from Silicon Wafer Surface in Wet Cleaning Process"*, IEEE Transactions on Semicond. Manufact. 6, 258 (1993)

[Ivch05] E. L. Ivchenko, *"Optical Spectroscopy of Semiconductor Nanostructures"*, Alpha Science International, Ltd, Harrow, UK, (2005)

[Ive05] T. Ive, O. Brandt, H. Kostial, K. J. Friedland, L. Däweritz, and K. H. Ploog, *"Controlled n-type doping of AlN:Si films grown on 6H-SiC(0001) by plasma-assisted molecular beam epitaxy"*, Appl. Phys. Lett. **86**, 024106 (2005).

J

[Jami05] M. Jamil, J. R. Grandusky, V. Jindal, F. Shahedipour-Sandvika, S. Guha and M. Arif, *"Development of strain reduced GaN on Si (111) by substrate engineering"*, Appl. Phys. Lett. **87**, 082103 (2005).

[Jang02] S. H. Jang, S. J. Lee, I. S. Seo, H. K. Ahn, O. Y. Lee, J. Y. Leem, and C. R. Lee, *"Characteristics of GaN/Si(1 1 1) epitaxy grown using $Al_{0.1}Ga_{0.9}N/AlN$ composite nucleation layers having different thicknesses of AlN"*, J. Cryst. Growth, **241**, 289 (2002).

[Jang03] S. H. Jang and C. R. Lee, *''High-quality GaN/Si(111) epitaxial layers grown with various $Al_{0.3}Ga_{0.7}N/GaN$ superlattices as intermediate layer by MOCVD''*, J. Crys. Growth, 253, 64 (2003).

[Jin04] R.Q. Jin, J.P. Liu, J.C. Zhang, and H. Yang, *"Growth of crack-free AlGaN film on thin AlN interlayer by MOCVD"*, J. Cryst. Growth, **268**, 35 (2004).

[John04] J. W. Johnson, E. L. Piner, A. Vescan, R. Therrien, P. Rajagopal, J. C. Roberts, J. D. Brown, S. Singhal, and K. J. Linthicum, *"12 W/mm AlGaN–GaN HFETs on Silicon Substrates"*, IEEE ELECTRON DEVICE LETTERS, **25** (7), 459 (2004).

[Jone99] R. Jones, J. Elsner, M. Haugk, R. Gutierrez, Th. Frauenheim, M. I. Heggie, S. Öberg, and P. R. Briddon, *"Interaction of Oxygen with Threading Dislocations in GaN"*, Phys. Stat. Sol. (a) **171**, 167 (1999).

K

[Kalu03] N.E. Kaluza, *''MOVPE growth and characterization of AlxGa1-xN/GaN Heterostructures for HEMT application''*, Dissertation, RWTH Aachen (2003).

[Kauf99] U. Kaufmann, M. Kunzer, H. Obloh, M. Maier, Ch. Manz, A. Ramakrishnan, and B. Santic, *"Origin of defect-related photoluminescence bands in doped and nominally undoped GaN"*, Phys. Rev. B **59** (8), 5561 (1999).

[Kauf00] U. Kaufmann, P. Schlotter, H. Obloh, K. Ko¨hler, and M. Maier, *"Hole conductivity and compensation in epitaxial GaN:Mg layers"*, Phys. Rev. B **62** (16), 10867 (2000).

[Kawa98] H. Kawai, M. Hara, F. Nakamura, T. Asatsuma, T. Kobayashi, and S. Imanaga, *"An AlN/GaN insulated gate heterostructure field effect transistor with regrown n-GaN source and drain contact"*, J. Cryst. Growth, **189/190**, 738 (1998)

[Kell03] S. Keller and S. DenBaars, *''Metalorganic chemical vapor deposition of group III nitrides: a discussion of critical issues''*, J. Crystal Growth **248**, 479 (2003).

[Khan93] M. A. Khan, J. N. Kuznia, D. T. Olson, T. George and W. T. Pike, *‘‘GaN/AlN digital alloy short-period superlattices by switched atomic layer metalorganic chemical vapor deposition’’*, Appl. Phys. Lett. **63**, 3470 (1993).

[Khan01] M. Asif Khan, V. Adivarahan, J. P. Zhang, C. Chen, E. Kuokstis, A. Chitnis, M. Shatalov, J. W. Yang and G. Simin, *‘‘Stripe Geometry Ultraviolet Light Emitting Diodes at 305 Nanometers Using Quaternary AlInGaN Multiple QuantumWells’’*, Jpn. J. Appl. Phys. Pt. 2, **40** (12A), L 1308 (2001).

[Khan05] - M. A. Khan, M. Shatalov, H. P. Maruska, H. M. Wang and E. Kuokstis,*‘‘III–Nitride UV Devices’’*, Jpn. J. Appl. Phys., **44**, (10), 7191 (2005).

[Khul08] K. C. Khulbe, C. Y. Feng and T. Matsuura, *“Synthetic Polymeric Membranes Characterization by Atomic Force Microscopy”*, Springer, Berlin, Heidelberg (2008)

[Kim00] K. S. Kim, M. S. Han, G. M. Yang, C. J. Youn, H. J. Lee, H. K. Cho ,and
J. Y. Lee, *‘‘Codoping characteristics of Zn with Mg in GaN’’*, Appl. Phys. Lett., 77, 1123 (2000).

[Kim03] K. H. Kim, J. Li, S. X. Jin, J. Y. Lin, and H. X. Jiang, *‘‘III-nitride ultraviolet light-emitting diodes with delta doping’’***,** Appl. Phys. Lett., **83** (3), 566 (2003).

[Kino00] A. Kinoshita, H. Hirayama, M. Ainoya, Y. Aoyagi, and A. Hirata, ‘‘Room-temperature operation at 333 nm of $Al_{0.03}Ga_{0.97}N/Al_{0.25}Ga_{0.75}N$ quantum-well light-emitting diodes with Mg-doped superlattice layers’’, Appl. Phys. Lett., **77**, 175 (2000).

[Kips02] G. Kipshidze, V. Kuryatkov, B. Borisov, Y. Kudryavtsev, R. Asomoza, S. Nikishin and H. Temkin, ‘‘*Mg and O codoping in p-type GaN and $Al_xGa_{1-x}N$ (0<x<0.08)*’’, Appl. Phys. Lett., **80** (16), 2910 (2002).

[Kips03] G. Kipshidze, V. Kuryatkov, K. Zhu, B. Borisov, M. Holtz, S. Nikishin and H. Temkin, *‘‘AlN/AlGaInN superlattice light-emitting diodes at 280 nm’’*, J. Appl. Phys., **93** (3),1363 (2003)

[Kita93] A.H. Kitai, *“Solid state luminescence: theory, materials and devices”*, Chapman & Hall, London (1993)

[Kitt05] C. Kittle, *“Introduction to Solid State Physics”*, 8th edition, John Wiley & Sons, Inc., New Jersey (2005)

[Klin07] C.F. Klingshirn, *“Semiconductor Optics”* , 3rd Edition, Springer-Verlag, Berlin, Heidelberg (2007)

[Klug74] H. P. Klug and L. E. Alexander, *“X-ray diffraction procedures for polycrystalline and amorphous materials”*, Wiley, New York, (1974) [Knei06] M. Kneissl, Z. Yang, M. Teepe, C. Knollenberg, N. M. Johnson, A. Usikov, and V. Dmitriev, *“Ultraviolet InAlGaN Light Emitting Diodes Grown on Hydride Vapor Phase Epitaxy AlGaN/Sapphire Templates”*, Jpn. J. Appl. Phys. 45 (2006) 3905.

[Koid99] Y. Koide, T. Maeda, T. Kawakami, S. Fujita, T. Uemura, N. Shibata, and M. Murakami, *‘‘Effects of Annealing in an Oxygen Ambient on Electrical Properties of Ohmic Contacts to p-Type GaN’’*, J. Electron. Mater., **28**, 341(1999).

[Kond04] A. V. Kondratyev, R. A. Talalaev, W. V. Lundin, A. V. Sakharov, A. V. Tsatul’nikov, E. E. Zavarin, A. V. Fomin, and D. S. Sizov, *“Aluminum incorporation control in AlGaN MOVPE: experimental and modeling study”*, J. Cryst. Growth, **272**, 420 (2004)

[Koro01] R. Y. Korotkov, J. M. Gregie, and B. W. Wessels,*‘‘Electrical properties of p-type GaN:Mg codoped with oxygen’’,* Appl. Phys. Lett., **78**, 222 (2001).

[Kozo99a] P. Kozodoy, M. Hansen, S. P. DenBaars, and U. K. Mishra, *“Enhanced Mg doping efficiency in Al0.2Ga0.8N/GaN superlattices”*, Appl. Phys. Lett., **74**, (24), 3681 (1999).

[Kozo99b] P. Kozodoy, Y. P. Smorchkova, M. Hansen, H. Xing, S. P. DenBaars, and U. K. Mishra A. W. Saxler, R. Perrin, and W. C. Mitchel**,** *“Polarization-enhanced Mg doping of AlGaN/GaN superlattices”*, Appl. Phys. Lett., **75** (16), 2444 (1999)

[Kozo00] P. Kozodoy, H. Xing, S. P. DenBaars, U. K. Mishra, A. Saxler, R. Perrin, S. Elhamri, and W. C. Mitchel, *‘‘Heavy doping effects in Mg-doped GaN’’*, J. Appl. Phys., **87**, 1832 (2000).

[Kros96] A. Krost, G. Bauer, and J. Woitok, *‘‘High resolution x-ray diffraction’’ in ‘‘Optical characterization of epitaxial semiconductor layers’’*, Springer-Verlag, Berlin, Heidelberg (1996).

[Kros02a] A. Krost and A. Dadgar, “*GaN-based devices on Si”,* Phys. Stat. Sol. (a), **194**, 361 (2002).

[Kros02b] A. Krost and A. Dadgar, *“GaN-based optoelectronics on silicon substrates”,* Materials Science and Engineering **B93**, 77 (2002).

[Kros04] A. Krost, A. Dadgar, J. Bläsing, A. Diez, T. Hempel, S. Petzhold, J. Christen and R. Clos, *“Evolution of stress in GaN heteroepitaxy on AlN/Si(111): From hydrostatic compressive strain to biaxial tensile”,* Appl. Phys. Lett. **85**, 3441 (2004).

[Kuku08] S.A. Kukushkin, A.V. Osipov, V.N. Bessolov, B.K. Medvedev, V.K. Nevolin, and K.A. Tcarik, *‘‘Substrates for epitaxy of gallium nitrides: new materials and techniques’’*, Rev. Adv. Mater. Sci., **17**, 1 (2008).

[Kuo02] C. H. Kuo, S. J. Chang, Y. K. Su, L. W. Wu, J. K. Sheu, C. H. Chen, and G. C. Chi, *‘‘Low Temperature Activation of Mg-Doped GaN in O2 Ambient’’*, Jpn. J. Appl. Phys., **41**, 112 (2002).

[Kwon02] M. K. Kwon, Y. H. Jeong, E. H. Shin, J. W. Yang, K. Y. Lim, J. I. Roh and K. S. Nahm, *"Effect of an Al Pre-seeded AlN Buffer on GaN Films Grown on Si(111) Substrates by Using SiC Intermediate Layers"*, J. Korean Physical Society **41** (6), 880 (2002).

L

[Lahr00] H. Lahreche, P. Vennegues, O. Tottereau, M. Laügt, P. Lorenzini, M. Leroux, B. Beaumont, and P. Gibart, *"Optimisation of AlN and GaN growth by metalorganic vapour-phase epitaxy (MOVPE) on Si(111)"*, J. Cryst. Growth **217**, 13 (2000).

[Latweb1] www.ledmagazine.com, *"Lattice Power demonstrates high-power InGaN LEDs grown on silicon"*.

[Latweb2] www.latticepower.com, *"Data sheet of Latticepower blue chip"*.

[Li02] J. Li, T.N. Oder, M. L. Nakarmi, J. Y. Lin, and H. X. Jiang, *''Optical and electrical properties of Mg-doped p-type* $Al_xGa_{1-x}N$*''*, Appl. Phys. Lett., **80**, 1210 (2002).

[Li03] J. Li, K. B. Nam, M. L. Nakarmi, J. Y. Lin, H. X. Jiang, P. Carrier and S. H. Wei, *''Band structure and fundamental optical transitions in wurtzite AlN''*, Appl. Phys. Lett., **83**(25), (2003)

[Lin04] Y. J. Lin, W.F. Liu, and C.T. Lee, *"Excimer-laser-induced activation of Mg-doped GaN layers"*, Appl. Phys. Lett. **84** (14), 2515 (2004).

[Lin06] K. L. Lin, E. Y. Chang, J. C. Huang, W. C. Huang, Y. L. Hsiao, C. H. Chiang, T. Li, D. Tweet, J. S. Maa, and Sheng-Teng Hsu, *"MOVPE high quality GaN film grown on Si (111) substrates using a multilayer AlN buffer"*, Phys. Stat. Sol. (C), **5** (6), 1536 (2008).

[Liu03] R. Liu, F. A. Ponce, A. Dadgar and A. Krost, *"Atomic arrangement at the AlN/Si (111) interface"*, Appl. Phys. Lett. **83** (5), 860 (2003).

[Loba08] A.V. Lobanova, E.V. Yakovlev, R.A Talalaev, S.B. Thapa, and F. Scholz, *"Growth conditions and surface morphology of AlN MOVPE"*, J. Cryst. Growth **310**, 4935 (2008).

[Lund04] V. V. Lundin, E. E. Zavarin, A. I. Besulkin, A. G. Gladyshev, A. V. Sakharov, M. F. Kokorev, N. M. Shmidt, A. F. Tsatsul'nikov, N. N. Ledentsov, Zh. I. Alferov, and R. Kakanakov, *"MOCVD-Grown AlGaN/GaN Heterostructures with High Electron Mobility"*, Semiconductors, **38** (11), 1323 (2004).

[Lui07] W. Liu, J. F. Wang, J. J. Zhu, D. S. Jiang and H. Yang, *"Influence of AlN thickness on strain evolution of GaN layer grown on high-temperature AlN interlayer"*, J. Phys. D: Appl. Phys., **40**, 5252 (2007).

[Luo08] W. Luo, X. Wang, L. Guo, H. Xiao, C. Wang, J. Ran, J. Li, and J. Li, *"The effect of low temperature AlN interlayers on the growth of GaN epilayer on Si (111) by MOCVD"*, Superlattices and Microstructures, **44**, 153 (2008).

M

[Maje04] J.A. Majewski, S. Hackenbuchner, G. Zandler, and P. Vogl, *"Nitride heterostructures: a system for high frequency electronics"*, Computational Materials Science **30**, 81 (2004).

[Mart96] G. Martin, A. Botchkarev, A. Rockett, and H. Morkoc, *"Valence-band discontinuities of wurtzite GaN, AlN, and InN heterojunctions measured by x-ray photoemission spectroscopy"*, Appl. Phys. Lett, **68** (18), 2541 (1996)

[Mast06] M.A. Mastro, C.R. Eddy Jr., D.K. Gaskill, N.D. Bassim, J. Casey, A. Rosenberg, R.T. Holm, R.L. Henry, and M.E. Twigg, *"MOCVD growth of thick AlN and AlGaN superlattice structures on Si Substrates"*, J. Cryst. Growth **287**, 610 (2006).

[Matt74] J.W. Matthews and A.E. Blakeslee, *"Defects in Epilaxial Multilayers: I. Misfit dislocations"*, J. Cryst. Growth **27**, 118 (1974).

[Maye04] K. Mayes, A. Yasan, R. McClintock, D. Shiell, S.R. Darvish, P. Kung and M. Razeghi, *"High-power 280 nm AlGaN light-emitting diodes based on an asymmetric single-quantum well"*, Appl. Phys. Lett. **84** (7), 1046 (2004)

[Mazu09] A.V. Mazur and M.M. Gasik, *"Thermal expansion of silicon at temperatures up to 1100°C"*, J. Mat. Proc. Tech. **209**, 723 (2009).

[McCl98] M. D. McCluskey, N. M. Johnson, C. G. Van de Walle, D. P. Bour, and M. Kneissl, *"Metastability of Oxygen Donors in AlGaN"*, Phys. Rev. Lett, **80** (18), 4008 (1998).

[Microweb] www.microscopyu.com

[Miho98] T.G. Mihopoulos, V. Gupta and K.F. Jensen, *"A reaction-transport model for AlGaN MOVPE growth"*, J. Cryst. Growth **195**, 733 (1998).

[Miho99] T. Mihopoulos, *"Reaction and Transport Processes in OMCVD: Selective and Group III-Nitride Growth"*, Dissertation, Massachusetts Institute of Technology (1999).

[Mira98] F. Mireles and S. E. Ulloa, *"Acceptor binding energies in GaN and AlN"*, Phys. Rev. B, 58, (7) 3879 (1998).

[Mitc08] W. C. Mitchel, S. Elhamri, G. Landis, R. Gaska, S. B. Schujman, and L. J. Schowalter, *"Electrical characterization of AlGaN/GaN on AlN substrates"*, Phys. Stat. Sol. (c), 5 (6), 1550 (2008)

[Miti99] V. V. Mitin, V. A. Kochelap and M. A. Stroscio, *“Quantum Heterostructures”*, Cambridge University Press, Cambridge (1999)

[Mork08] Hadis Morkoc, *‘‘Handbook of nitrides semiconductors and devices volume 1: materials properties, physics and growth’’*, Wiley-VCH Verlag, Weinheim (2008)

[Mura07] K. Murakawa, E. Niikura, F. Hasegawa, and H. Kawanishi, *“Reduction of Threading Dislocations in AlGaN/AlN/SiC Epitaxial Layers by Controlled Strain with (AlN/GaN) Multibuffer-Layer Structure”*, Jpn. J. Appl. Phys. 46 (6A), 3301 (2007).

[Murp01] D.B. Murphy, *“Fundamentals of light microscopy and electronic imaging”*, Wiley-Liss, New York (2001)

N

[Nagam08] M. Nagamori, S. Ito, H. Saito, K. Shiojima, S. Yamada, N. Shibata, and M. Kuzuhara, *‘‘Optimum Rapid Thermal Activation of Mg-Doped p-Type GaN’’*, Jpn. J. Appl. Phys., **47 (**4), 2865 (2008).

[Nagam09] K. Nagamatsu, K. Takeda, M. Iwaya, S. Kamiyama, H. Amano, and I. Akasaki, *“Activation energy of Mg in* $Al_{0.25}Ga_{0.75}N$ *and* $Al_{0.5}Ga_{0.5}N$*”*, Phys. Stat. Sol. C **6** (S2), S437 (2009).

[Nagat09] K. Nagata, K. Takeda, T. Ichikawa, K. Nagamatsu, M. Iwaya, S. Kamiyama, H. Amano, and I. Akasaki, *‘‘Activation of Mg-Doped p-Type* $Al_{0.17}Ga_{0.83}N$ *in Oxygen Ambient’’*, Jpn. J. Appl. Phys. **48**, 101002 (2009).

[Naka92a] S. Nakamura, N. Iwasa, M. Senoh, and T. Mukai, *‘‘Hole Compensation Mechanism of P-Type GaN Films’’*, Jpn. J. Appl. Phys., **31**, 1258 (1992).

[Naka92b] S. Nakamura, T. Mukai, M. Senoh, and N. Iwasa, *‘‘Thermal Annealing Effects on P-Type Mg-Doped GaN Films’’*, Jpn. J. Appl. Phys., **31**, L139 (1992).

[Naka94] S. Nakamura, T. Mukai, and M. senoh, *‘‘Candela-class high-brightness InGaN/AIGaN double-heterostructure blue-light-emitting’’*, Appl. Phys. Lett., **64** (13), 1687 (1994).

[Naka05] M.L. Nakarmi, K.H. Kim, M. Khizar, Z.Y. Fan, J.Y. Lin, and H.X. Jiang, *“Electrical and optical properties of Mg-doped* $Al_{0.7}Ga_{0.3}N$ *alloys”*, Appl. Phys. Lett. **86**, 092108 (2005).

[Naka09] M.L. Nakarmi, N. Nepal, J.Y. Lin, and H.X. Jiang, *“Photoluminescence studies of impurity transitions in Mg-doped AlGaN alloys”*, Appl. Phys. Lett. **94**, 091903 (2009).

[Nakag04] Y. Nakagawa, M. Haraguchi, M. Fukui, S. Tanaka, A. Sakaki, K. Kususe, N. Hosokawa, T. Takehara, Y. Morioka, H. Iijima, M. Kubota, M. Abe, T. Mukai, H. Takagi, and G. Shinomiya,*‘‘Hydrogen Dissociation from Mg-doped GaN’’*, Jpn. J. Appl. Phys., **43** , 23 (2004).

[Nam03] K.B. Nam, M.L. Nakarmi, J. Li, J.Y. Lin, and H.X. Jiang, *“Mg acceptor level in AlN probed by deep ultraviolet photoluminescence”*, Appl. Phys. Lett. **83** (5), 878 (2003).

[Neug95] J. Neugebauer and C. G. Van de Walle, *‘‘Hydrogen in GaN: Novel Aspects of a Common Impurity’’*, Phys. Rev. Lett., **75**, 4452 (1995).

[Niki03] S.A. Nikishin, V.V. Kuryatkov, A. Chandolu, B.A. Borisov, G.D. Kipshidze, I. Ahmad, M. Holtz and H. Temkin, *“Deep Ultraviolet Light Emitting Diodes Based on Short Period Superlattices of AlN/AlGa(In)N”*, Jpn. J. Appl. Phys. **42** (11B), L1362 (2003).

[Niki05] S. A. Nikishin, M. Holtz, and H. Temkim, *‘‘Digital Alloys of AlN/AlGaN for Deep UV Light Emitting Diodes’’*, Jpn. J. Appl. Phys. 44, 7221 (2005).

[Niik07] E. Niikura, K. Murakawa, F. Hasegawa, and H. Kawanishi, *“Improvement of crystal quality of AlN and AlGaN epitaxial layers by controlling the strain with the (AlN/GaN) multi-buffer layer”*, J. Cryst. Growth **298**, 345 (2007) 345

[Niki08] S. Nikishin, B. Borisov, V. Kuryatkov, M. Holtz, G. A. Garrett, W. L. Sarney, A. V. Sampath, H. Shen, M. Wraback, A. Usikov, and V. Dmitriev, *‘‘Deep UV light emitting diodes grown by gas source molecular beam epitaxy’’*, J Mater Sci: Mater Electron (2008) 19:764–769

[Nish99] T. Nishida and N. Kobayashi, *‘‘346 nm Emission from AlGaN Multi-Quantum-Well Light Emitting Diode’’*, Phys. Stat. Sol. (a) **176**, 45 (1999).

[Nish01a] T. Nishida, H. Saito, and N. Kobayashi, *‘‘Submilliwatt operation of AlGaN-based ultraviolet light-emitting diode using short-period alloy superlattice’’*, Appl. Phys. Lett., **78** (4), 399 (2001).

[Nish01b] T. Nishida, H. Saito, and N. Kobayashi, *‘‘Efficient and high-power AlGaN-based ultraviolet light-emitting diode grown on bulk GaN’’*, Appl. Phys. Lett., **79** (6), 711 (2001).

[Nish03] T. Nishida, T. Ban and N. Kobayashi,*“Highly Transparent Structure for Nitride Ultraviolet Light Emitting Diodes”*, Jpn. J. Appl. Phys. Part 1, **42** (4B), 2273 (2003).

[Nish04] T. Nishida, T. Makimoto, H. Saito, and T. Ban, *“AlGaN-based ultraviolet light-emitting diodes grown on bulk AlN substrates”*, Appl. Phys. Lett., 84, (6), 1002 (2004).

O

[Obat04] T. Obata, H. Hirayama, Y. Aoyagi, and K. Ishibashi, *‘‘Growth and annealing conditions of high Al-content p-type AlGaN for deep-UV LEDs’’***,** Phys. Status. Solidi. (a), **201**, 2803 (2004).

[Oblo98] H. Obloh, K. H. Bachem, U. Kaufmann, M. Kunzer, M. Maier, A. Ramakrishnan, and P. Schlotter, *“Self-compensation in Mg doped p-type GaN grown by MOCVD”*, J. Cryst. Growth **195**, 270 (1998).

[Ohba94] Y. Ohba and A. Hatano, *‘‘H-Atom Incorporation in Mg-Doped GaN Grown by Metalorganic Chemical Vapor Deposition’’*, Jpn.J .Appl.Phys., **33**, L1367 (1994).

[Oley06] N. Oleynik, *“MOVPE Growth and Characterisation of ZnO Properties for Optoelectronic Applications”*, Dissertation, Univ. Magdeburg (2006)

[Omar90] W.C. O’Mara, R. B. Herring, and L. P. Hunt, *‘‘Handbook semiconductor silicon technology’’*, Noyes Publications, New Jersey (1990)

P

[Pier96] R.F. Pierret, *‘‘Semiconductor device fundamentals’’*, Addison-Wesley, Reading, Massachusetts (1996)

[Piet04] U. Pietsch, V. Holy, and T. Baumbach, *“High-Resolution X-Ray Scattering: From Thin Films to Lateral Nanostructures”,* 2nd edition, Springer-Verlag, New York (2004).

[Pödö96] B. Pödör, *‘‘Acceptor ionization energies in gallium nitride: chemical trends and electronegativities’’*, Semicond. Sci. Technol., **11**(5), 827 (1996)

Q

[Quay08] R. Quay, *“Gallium Nitride Electronics”* , Springer-Verlag, Berlin, Heidelberg (2008)

R

[Ragh04] S. Raghavan and J. M. Redwing, *“Intrinsic stresses in AlN layers grown by metal organic chemical vapor deposition on (0001) sapphire and (111) Si substrates”*, J. Appl. Phys. **96** (5), 2995 (2004).

[Ragh05a] S. Raghavan and J. M. Redwing, *“Growth stresses and cracking in GaN films on (111)Si grown by metal-organic chemical-vapor deposition. I. AlN buffer layers”*, J. Appl. Phys. **98**, 023514 (2005).

[Ragh05b] S. Raghavan, X. Weng, E. Dickey, and J. M. Redwing, *“Effect of AlN interlayers on growth stress in GaN layers deposited on (111)Si”*, Appl. Phys. Lett., 87, 142101 (2005).

[Raja05] S. Rajan, M. Wong, Y. Fu, F. Wu, J. S. Speck, and U. K. Mishra, *“Growth and Electrical Characterization of N-face AlGaN/GaN Heterostructures”*, Jpn. J. Appl. Phys., **44**, (49), L1478 (2005)

[Reen08] O. Reentila, F. Brunner, A. Knauer, A. Mogilatenko, W. Neumann, H. Protzmann, M. Heuken, M. Kneissl, M. Weyers, and G. Tränkle, *“Effect of the AlN nucleation layer growth on AlN material quality”*, J. Cryst. Growth **310**, 4932 (2008)

[Reih03] A. Reiher, J. Bläsing, A. Dadgar, A. Diez, and A. Krost, *“Efficient stress relief in GaN heteroepitaxy on Si(111) using low-temperature AlN inter-layers”*, J. Crystal Growth **248**, 563 (2003)

[Reih08] F. Reiher, *‘‘Wachstum Galliumnitrid-basierten Bauelementen auf Silizium (100)–Substraten mittels metallorganischer Gasphasenepitaxie’’*, Dissertation, Univ. Magdeburg (2009)

[Reih09] F. Reiher, A. Dadgar, J. Bläsing, M. Wieneke, M. Müller, A. Franke, L. Reißmann, J. Christen and A. Krost, *‘‘InGaN/GaN light-emitting diodes on Si(110) substrates grown by metal–organic vapour phase epitaxy’’*, J. Phys. D: Appl. Phys., 42, 055107 (2009).

[Resh05] M. Reshchikov and H. Morkoc, *“Luminescence properties of defects in GaN”* , J. Appl. Phys. 97, 061301 (2005).

[Rode05] C. Roder, S. Einfeldt, S. Figge, and D. Hommel, *“Temperature dependence of the thermal expansion of GaN”*, Phy. Rev. B, **72**, 085218 (2005)

[Roma03] A. E. Romanov and J. S. Speck, *“Stress relaxation in mismatched layers due to threading dislocation inclination”*, Appl. Phys. Lett. **83** (13) 2569 (2003).

[Roma06] A. E. Romanov, G. E. Beltz, P. Cantu, F. Wu, S. Keller, S. P. DenBaars, and J. S. Speck *“Cracking of III-nitride layers with strain gradients”*, Appl. Phys. Lett., **89**, 161922 (2006).

[Rose02] E. Rosencher and B. Vinter, *“Optoelectronics”*, Cambridge University Press, Cambridge (2002).

S

[Saen09a] P. Saengkaew, A. Dadgar, J. Blaesing, B. Bastek, F. Bertram, F. Reiher, C. Hums, M. Noltemeyer, T. Hempel, P. Veit, J. Christen, and A. Krost, *“MOVPE growth of high-quality* $Al_{0.1}Ga_{0.9}N$ *on Si(111) substrates for UV-LEDs”*, Phys. Stat. Sol. (C), **6** (S2), S455 (2009).

[Saen09b] P. Saengkaew, A. Dadgar, J. Blaesing, T. Hempel, P. Veit, J. Christen, and A. Krost, *“Low-temperature/high-temperature AlN superlattice buffer layers for high-quality* $Al_xGa_{1-x}N$ *on Si(111)”*, J. Cryst. Growth, **311**, 3742 (2009).

[Safcweb] www.safcglobal.com

[Saxl99] A. Saxler, W. C. Mitchel, P. Kung and M. Razeghi, *“Aluminum gallium nitride short-period superlattices doped with magnesium”*, Appl. Phys. Lett., **74** (14), 2023 (1999)

[Schö07] J. Schörmann, *“Cubic AlGaN/GaN structures for device application”*, Dissertation, Univ. Paderborn (2007)

[Schu04] F. Schulze, A. Dadgar, J. Bläsing, and A. Krost, *“GaN heteroepitaxy on Si(001)”*, J. Cryst. Growth **272**, 496 (2004).

[Schu06] F. Schulze, A. Dadgar, J. Bläsing, A. Diez, and A. Krost, *‘‘Metalorganic vapor phase epitaxy grown InGaN/GaN light-emitting diodes on Si(001) substrate’’,*Appl. Phys. Lett.**88**, 121114 (2006).

[Schu07] F. Schulze, O. Kisel, A. Dadgar, A. Krtschil, J. Bläsing, M. Kunze, I. Daumiller, T. Hempel, A. Diez, R. Clos, J. Christen and A. Krost, *‘‘Crystallographic and electric properties of MOVPE-grown AlGaN/GaN-based FETs on Si(001) substrates’’*, J. Crys. Growth, **299** (2), 399 (2007).

[Schu08] F. Schulze, A. Dadgar, A. Krtschil, C. Hums, L. Reissmann, A. Diez, J. Christen, and A. Krost, *‘‘MOVPE growth of blue* In_xGa_{1-x}*N/GaN LEDs on 150 mm Si(001)’’*, Phys. Stat. Sol. (c), **5** (6), 2238 (2008).

[Schubweb] http://www.rpi.edu/~schubert/

[Schub96] E. F. Schubert, W. Grieshaber, and I. D. Goepfert, *“Enhancement of deep acceptor activation in semiconductors by superlattice doping”*, Appl. Phys. Lett., **69** (24), 3737 (1996)

[Schub03] E. F. Schubert, “Light-Emitting Diodes”, Cambridge University Press, Cambridge (2003)

[Semo01] F. Semond, P. Lorenzini, N. Grandjean, and J. Massies, *“High-electron-mobility AlGaN/GaN heterostructures grown on Si(111) by molecular-beam epitaxy”*, Appl. Phys. Lett. 78, (3), 335 (2001).

[Shat02] M. Shatalov, G. Simin, V. Adivarahan, A. Chitnis, S. Wu, R. Pachipulusu, V. Mandavilli, K. Simin, J. Zhang, J. Yang, and M. Khan, *‘‘Lateral Current Crowding in Deep UV Light Emitting Diodes over Sapphire Substrates”*, Jpn. J. Appl. Phys. 41, 5083 (2002).

[Shih05] Chaun-Feng Shih, Nie-Chuan Chen, Chin-An CHANG and Kuo-Shung Liu, **‘‘***Blue, Green and White InGaN Light-Emitting Diodes Grown on Si’’*, Jpn. J. Appl. Phys. 44, L140, (2005)

[Simb07] C. Simbrunner, M. Wegscheider, M. Quast, Tian Li, A. Navarro-Quezada, H. Sitter, A. Bonanni and R. Jakiela, *‘‘On the effect of periodic Mg distribution in GaN:*δ*-Mg’’*, Appl. Phys. Lett. **90**, 142108 (2007).

[Smit93] R. D. King-Smith and D. Vanderbilt, *“Theory of polarization of crystalline solids”*, Phys. Rev. B, 47, 1651 (1993)

[Stam98] C. Stampfl and C.G. Van de Walle, *“Doping of* $Al_xGa_{1-x}N$*”*, Appl. Phys. Lett. **72** (4), 459 (1998).

[Stri89] G. B. Stringfellow, “*Organometallic Vapor-Phase Epitaxy: theory and practice’’,* 2nd edition, Academic Press, San Diego, California (1989).

[Stut01] M. Stutzmann , O. Ambacher, M. Eickhoff, U. Karrer, A. Lima Pimenta, R. Neuberger, J. Schalwig, R. Dimitrov, P. J. Schuck, and R. D. Grober, *‘‘Playing with Polarity’’*, phys.stat.sol.(b), **228**(2), 505 (2001).

[Ston09] G.G. Stoney, *“The Tension of Metallic Films Deposited by Electrolysis*”**,** Proc. R. Soc. Lond., A **82**, 172 (1909)

[Sumi08] S. Sumiya, Y. Zhu, J. Zhang, K. Kosaka, M. Miyoshi, T. Shibata, M. Tanaka, and T. Egawa, *“AlGaN-Based Deep Ultraviolet Light-Emitting Diodes Grown on Epitaxial AlN/Sapphire Templates”*, Jpn. J. Appl. Phys. **47** (1), 43 (2008).

[Sun00] J. Sun, J.M. Redwing, and T.F. Kuech, *“Model Development of GaN MOVPE Growth Chemistry for Reactor Design”*, J. Electronic materials, **29** (1), (2000)

[Sun04a] W. H. Sun, J. P. Zhang, V. Adivarahan, A Chitnis, M. Shatalov, S. Wu, V. Mandavilli, J. W. Yang, and M. A. Khan, *‘‘AlGaN-based 280 nm light-emitting diodes with continuous wave powers in excess of 1.5 mW’’*, Appl. Phys. Lett., **85** (4), 531 (2004).

[Sun04b] W. H. Sun, V. Adivarahan, M. Shatalov, Y. Lee, S. Wu, J. W. Yang, J. P. Zhang, and M. Asif Khan, *‘‘Continuous Wave Milliwatt Power AlGaN Light Emitting Diodes at 280nm’’*, Jpn. J. Appl. Phys., **43** (11A), L1419, (2004).

[Sun05] W.H. Sun, J.P. Zhang, J.W. Yang, H.P. Maruska, M. Asif Khan, R. Liu and F.A. Ponce, *“Fine structure of AlN/AlGaN superlattice grown by pulsed atomic-layer epitaxy for dislocation filtering”*, Appl. Phys. Lett. **87**, 211915 (2005).

[Suzu98] M. Suzuki, J. Nishio, M. Onomura, and C. Hongo, *‘‘Doping characteristics and electrical properties of Mg-doped AlGaN grown by atmospheric-pressure MOCVD’’*, J. Cryst. Growth, **189/190**, 511(1998)

[Sze85] S. M. Sze, *“Semiconductor Devices: Physics and Technology”*, John Wiley & Sons, New Jersey (1985)

[Sze07] S. M. Sze and K. K. Ng, *“Physics of Semiconductor Devices”*, 3rd edition, John Wiley & Sons, Inc., **New** Jersey (2007)

T

[Take01] M. Takeya and M. Ikeda, *‘‘Novel Methods of p-type Activation in Mg-doped GaN’’*, Jpn. J. Appl. Phys., **40**, 6260 (2001).

[Tana94] T. Tanaka, A. Watanabe, H. Amano, Y. Kobayashi, I. Akasaki, S. Yamazaki, and M. Koike, *‘‘P-type conduction in Mg-doped GaN and* $Al_{0.08}Ga_{0.92}N$ *grown by metalorganic vapor phase epitaxy’’*, Appl. Phys. Lett. **65**, 593 (1994).

[Tani02] Y. Taniyasu, M. Kasu, and N. Kobayashi, *"Intentional control of n-type conduction for Si-doped AlN and* $Al_xGa_{1-x}N$ *(* $0.42 \le x \le 1$ *)"***,** Appl. Phys. Lett. **81** (7), 1255 (2002).

[Tani06] Y. Taniyasu, M. Kasu, and T. Makimoto, *''An aluminium nitride light-emitting diode with a wavelength of 210 nanometres''*, Nature **441**, 325 (2006).

[Tani08] Y. Taniyasu and M. Kasu,*''Aluminum nitride deep-ultraviolet light-emitting p–n junction diodes''*, Diamond & Related Materials, 17, 1273 (2008).

[Tasl10] P. Tasli, S. B. Lisesivdin, A. Yildiz, M. Kasap, E. Arslan, S. Özcelik, and E. Ozbay, *"Well parameters of two-dimensional electron gas in* $Al_{0.88}In_{0.12}N$*/AlN/GaN/AlN heterostructures grown by MOCVD"***,** Cryst. Res. Technol., **45** (2), 105 (2010)

[Thak07] J. S. Thakur, H. E. Prakasam, L. Zhang, E. F. McCullen, L. Rimai, V. M. García-Suárez, R. Naik, K. Y. S. Ng, and G. W. Auner, *"Characteristic jump in the electrical properties of a Pd/AlN/Si-based device on exposure to hydrogen"*, Phys. Rev. B **75**, 075308 (2007).

[Thap08] S. B. Thapa, J. Hertkorn, F. Scholz, G. M. Prinz, M. Feneberg, M. Schirra, K. Thonke, R. Sauer, J. Biskupek, and U. Kaiser, *"MOVPE growth of high quality AlN layers and effects of Si doping"*, Phys. Stat. Sol. C **5**, (6), 1774 (2008).

[Touz05] C. Touzi, F. Omnes, B. El Jani, P. Gibart, *"LP MOVPE growth and characterization of high Al content* $Al_xGa_{1-x}N$ *epilayers"*, J. Cryst. Growth **279**, 31 (2005).

[Tran99] C. A. Tran, A. Osinski, R. F. Karlicek, Jr., and I. Berishev, *''Growth of InGaN/GaN multiple-quantum-well blue light-emitting diodes on silicon by metalorganic vapor phase epitaxy''*, Appl. Phys. Lett. **75** (11), 1494 (1999).

[Trip07] S. Tripathy, V. K. X. Lin, S. L. Teo, A. Dadgar, A. Diez, J. Bläsing, and A. Krost, *''InGaN/GaN light emitting diodes on nanoscale silicon on insulator''*, Appl. Phys. Lett. **91**, 231109 (2007).

[Trip08] S. Tripathy, T. E. Sale, A. Dadgar, V. K. X. Lin, K. Y. Zang, S. L. Teo, S. J. Chua, J. Bläsing, and A. Krost, *''GaN-based microdisk light emitting diodes on (111)-oriented nanosilicon-on-insulator templates''***,** J. Appl. Phys. **104**, 053106 (2008).

V

[Vech92] J. A. van Vechten, J. D. Zook, R. D. Hornig, and B. Goldenberg,*''Defeating Compensation in Wide Gap Semiconductors by Growing in H that is Removed by Low Temperature De-Ionizing Radiation''*, Jpn. J. Appl. Phys. **31**, 3662 (1992).

[Vesc02] A. Vescan, J. D. Brown, J. W. Johnson, R. Therrien, T. Gehrke, P. Rajagopal, J. C. Roberts, S. Singhal, W. Nagy, R. Borges, E. Piner, and K. Linthicum, *"AlGaN/GaN HFETs on 100 mm Silicon Substrates for Commercial Wireless Applications"*, Phys. Stat. Sol. (C), **0** (1), (2002).

W

[Wang02] H.M. Wang, J.P. Zhang, C.Q. Chen, Q. Fareed, J.W. Yang and M. Asif Khan, *"AlN/AlGaN superlattices as dislocation filter for low-threading-dislocation thick AlGaN layers on sapphire"*, Appl. Phys. Lett. **81** (4), 604 (2002).

[Wang07] X. Wang, X. Wang, B. Wang, H. Xiao, H. Liu, J. Wang, Y. Zeng, and J. Li, *"High responsivity ultraviolet photodetector based on crack-free GaN on Si (111)"*, Phys. Stat. Sol. (c) **4** (5), 1613 (2007).

[Wald01] E. L. Waldron, J. W. Graff, and E. F. Schubert, *"Improved mobilities and resistivities in modulation-doped p-type AlGaN/GaN superlattices"*, Appl. Phys. Lett. **79** (17), 2737 (2001)

[Wall04] C.G. Van de Walle and J. Neugebauer, *"First-principles calculations for defects and impurities: Applications to III-nitrides"*, J. Appl. Phys. **95** (8), 3851 (2004)

[Walt00] P. Waltereit, O. Brandt, A. Trampert, H.T. Grahn, J. Menniger, M. Ramsteiner, M. Reiche and K.H. Ploog, "Nitride semiconductors free of electrostatic fields for efficient white light-emitting diodes", Nature **406**, 865 (2000).

[Weng07] X. Weng, S. Raghavan, J.D. Acord, A. Jain, E.C. Dickey, and J.M. Redwing,*''Evolution of threading dislocations in MOCVD-grown GaN films on (111) Si substrates''*, J. Crys. Growth, **300**, 217 (2007).

[Wikiweb] www.wikipedia.org

[Willi09] D. B. Williams and C. B. Carter, *"Transmission Electron Microscopy: A Textbook for Materials Science"*, 2nd edition, Springer Science + Business Media, New York (2009).

[Wong08] M. H. Wong, Y. Pei, R. Chu, S. Rajan, B. L. Swenson, D. F. Brown, S. Keller, S. P. DenBaars, J. S. Speck, and U. K. Mishra, *"N-Face Metal–Insulator–Semiconductor High-Electron-Mobility Transistors With AlN Back-Barrier"*, IEEE ELECTRON DEVICE LETTERS, 29 (10), 1101 (2008).

[Wrig02] A. F. Wright, *"Substitutional and interstitial carbon in wurtzite GaN"*, J. Appl. Phys. 92 (5), 2575 (2002).

[Wu04] S. Wu, V. Arahan, M. Shatalov, A. Chitnis, W. Sun, and M. A. Khan, *''Micro-pixel Design Milliwatt Power 254nm Emission Light Emitting Diodes''*, Jpn. J. Appl. Phys. 43, 1035 (2004).

[Wu04YF] Y. F. Wu, A. Saxler, M. Moore, R. P. Smith, S. Sheppard, P. M. Chavarkar, T. Wisleder, U. K. Mishra, and P. Parikh, *"30-W/mm GaN HEMTs by Field Plate Optimization"*, IEEE ELECTRON DEVICE LETTERS, **25**, (3), 117 (2004).

[Wu04J] J. Wu, D. Li, Y. Lu, X. Han, J. Li, H. Wei, T. Kang, X. Wang, X. Liu, Q. Zhu, and Z. Wang, *"Crack-free InAlGaN quaternary alloy films grown on Si(111) substrate by metalorganic chemical vapor deposition"*, J. Cryst. Growth **273**, 79 (2004).

[Wu06] S. Wu, S. Chhajed, L. Yan, W. Sun, M. Shatalov, V. Adivarahan, and M. A. Khan, *''Matrix Addressable Micro-Pixel 280nm Deep UV Light-Emitting Diodes''*, Jpn. J. Appl. Phys., **45** (12), L352 (2006).

[Wu07a] G.M. Wu, C.W. Tsai, N.C. Chen, and P.H. Chang, *"Investigation of GaN crystal quality on silicon substrates using GaN/AlN superlattice structures"*, Cryst. Res. Technol. **42** (12), 1276 (2007).

[Wu07b] G.M. Wu and T.H. Hsieh, *"Crystal quality and electrical properties of p-type GaN thin film on Si(111) substrate by metal-organic chemical vapor deposition MOCVD"*, J. Achievements in Materials and Manufacturing Engineering, **24** (1), 193 (2007).

X

[Xi07a] Y.A. Xi, K.X. Chen, F.W. Mont, J.K. Kim, W. Lee, E.F. Schubert, W. Liu, X. Li and J.A. Smart,*"Kinetic study of Al-mole fraction in AlxGa1-xN grown on c -plane sapphire and AlN bulk substrates by metal-organic vapor-phase epitaxy"*, Appl. Phys. Lett. **90**, 051104 (2007).

[Xi07b] Y.A. Xi, K.X. Chen, F.W. Mont, J.K. Kim, W. Lee, E.F. Schubert, W. Liu, X. Li and J.A. Smart,*"Kinetic study of Al-mole fraction in AlxGa1-xN grown on c -plane sapphire and AlN bulk substrates by metal-organic vapor-phase epitaxy"*, Appl. Phys. Lett. **90**, 209902 (2007).

[Xi07c] Y.A. Xi, K.X. Chen, F. Mont, J.K. Kim, E.F. Schubert, W. Liu, X. Li, and J.A. Smart, *"Comparative study of n-type AlGaN grown on sapphire by using a superlattice layer and a low-temperature AlN interlayer"*, J. Cryst. Growth **299**, 59 (2007).

[Xin04] H. P. Xin, J. S. Flynn, J. A. Dion, E. L. Hutchins, H. Antunes, L. Fieschi-Corso, R.Van Egas, G. R. Brandes, S. F. LeBoeuf, X. A. Cao, J. L. Garrett, and L. B. Rowland, *''Electrical and Optical Characteristics of Delta Doped AlGaN Cladding Layer Materials for Highly Efficient 340nm Ultra Violet LEDs''*, Mat. Res. Soc. Symp. Proc., **798**, Y3.10.1 (2004).

Y

[Yaco90] B.G. Yacobi and D.B. Holt**,** *"Cathodoluminescence microscopy of inorganic solids"*, Plenum Press, New York (1990)

[Yang00] J. W. Yang, A. Lunev, G. Simin, A. Chitnis, M. Shatalov, M. A. Khan, J. E. Van Nostarnd, and R. Gaska, *''Selective area deposited blue GaN–InGaN multiple-quantum well light emitting diodes over silicon substrates''*, Appl. Phys. Lett., **76**, 273 (2000).

[Yao08] J. Yao, P. Han, Z. L. Xie, B. Liu, R. Zhang, R. L. Jiang, Q. J. Liu, F. Xu, H. M. Gong, Y. Shi and Y. D. Zheng, *"MOCVD growth and annealing characteristics of Mg-doped AlGaN films"*, Proc. SPIE 6984, 69842N (2008).

[Yu05] P.Y. Yu, and M. Cardona, *"Fundamentals of Semiconductors"*, 3rd Edition, Springer-Verlag, Berlin, Heidelberg (2005)

[Yun02] F. Yun, F. Yun, M. A. Reshchikov, L. He, T. King, H. Morkoc, S. W. Novak, and L. Wei, *"Energy band bowing parameter in* $Al_xGa_{1-x}N$ *alloys"*, J. Appl. Phys., 92, (8),4837 (2002)

Z

[Zami00] S. Zamir, B. Meyler, E. Zolotoyabko and J. Salzman, *"The effect of AlN buffer layer on GaN grown on (111)-oriented Si substrates by MOCVD"*, J. Cryst. Growth **218**, 181 (2000).

[Zeis00] R. Zeisel, M.W. Bayerl, S.T.B. Goennenwein, R. Dimitrov, O. Ambacher, M.S. Brand, and M. Stutzmann, *"DX-behavior of Si in AlN"*, Phys. Rev. B **61**, R16283 (2000).

[Zimm04] T. Zimmermann, M. Neuburger, M. Kunze, I. Daumiller, A. Denisenko, A. Dadgar, A. Krost, and E. Kohn, *"P-Channel InGaN-HFET Structure Based on Polarization Doping"*, IEEE ELECTRON DEVICE LETTERS, **25** (7), 450 (2004)

[Zimm08] T. Zimmermann, *"Polarisationseffekte in Gruppe-(III)-Nitriden und deren Anwendung in p-Kanal FETs und elektromechanischen Strukturen"*, Dissertation, Univ. Ulm (2008)

[Zhan02a] J.P. Zhang, H.M. Wang, M.E. Gaevski, C.Q. Chen, Q. Fareed, J.W. Yang, G. Simin and M.A. Khan, *"Crack-free thick AlGaN grown on sapphire using AlN/AlGaN superlattices for strain management"*, Appl. Phys. Lett. **80** (19), 3542 (2002).

[Zhan02b] J. P. Zhang, A. Chitnis, V. Adivarahan, S. Wu, V. Madavilli, R. Pachipulusu, M. Shatalov, G. Simin, J. W. Yang, and M. Asif Khan, *''Milliwatt power deep ultraviolet light-emitting diodes over sapphire with emission at 278 nm''*, Appl. Phys. Lett. **81**, 4910 (2002).

[Zhang02] S. B. Zhang, *''The microscopic origin of the doping limits in semiconductors and wide-gap materials and recent developments in overcoming these limits: a review''*, J. Phys. Condens. Matter **14**, 881 (2002).

[Zhang07] B. Zhang, H. Liang, Y. Wang, Z. Feng, K. W. Ng, K. M. Lau, *''High-performance III-nitride blue LEDs grown and fabricated on patterned Si substrates''***,** J. Cryst. Growth **298**, 725 (2007).

[Zhou07] W. Zhou and Z. L. Wang, *“Scanning Microscopy for Nanotechnology: Techniques and Applications”*, Springer + Business Media, LLC, New York (2007)

[Zhu02] T. G. Zhu, J. C. Denyszyn, U. Chowdhury, M. M. Wong, and R. D. Dupuis, *‘‘AlGaN–GaN UV Light-Emitting Diodes Grown on SiC by Metal–Organic Chemical Vapor Deposition’’*, IEEE J. Sel. Top. Quant. Electron., **8** (2), 298 (2002).

[Zhu09a] D. Zhu, C. McAleese, K. K. McLaughlin, M. Häberlen, C. O. Salcianu, E. J. Thrush, M. J. Kappers, W. A. Phillips, P. Lane, D. J. Wallis, T. Martin, M. Astles, S. Thomas, A. Pakes, M. Heuken, and C. J. Humphreys, *‘‘GaN-based LEDs grown on 6-inch diameter Si (111) substrates by MOVPE’’*, Proc.SPIE7231, 723118 (2009).

[Zhu09b] D. Zhu, C. McAleese, M. Häberlen, C. O. Salcianu, E. J. Thrush, M. J. Kappers, W. A. Phillips, P. Lane, M. Kane, D. J. Wallis, T. Martin, M. Astles, and C. J. Humphreys, *‘‘InGaN/GaN LEDs grown on Si(111): Dependence of device performance on threading dislocation density and wavelength’’*, the 8th international conference on nitride semiconductors, ThP113, 1305 (2009).

[Zuka02] A. Zukauskas, M. S. Shur and R. Gaska, *‘‘Introduction to Solid-State Lighting’’*, Wiley, New York, (2002).

Appendix

In *Fig. A1*, PL measurements show UV-luminescence peaks at ~340 nm relating to AlGaN barrier layers since the UV-luminescence peaks at ~340 nm are emitted from sample QW1 and QW2 with ~20 nm AlGaN barrier layers and not from sample QW3 with ~10 nm AlGaN barrier layers. Moreover UV-luminescence peaks at ~360 nm relate to a GaN-well luminescence since they are emitted from sample QW1 and QW3 with a thicker GaN well. In case of a DAP luminescence at about 540-550 nm, sample QW1 shows a weak dominant intensity of the DAP luminescence and a high intensity of the GaN-QW luminescence. This means to a highly radiative recombination of this QW structure of sample QW1. As compared to sample QW3 with a thinner AlGaN barrier, sample QW1 has a higher efficiency of a radiative recombination in the QW. This implies to an important role of an AlGaN-barrier thickness to localize carriers in the QW.

Furthermore, cross-sectional CL measurements of sample QW2 in *Fig.A2* show only one dominant UV-luminescence at ~340 nm in the lower part of sample (~1.8 μm $Al_{0.1}Ga_{0.9}N$:Si layers) meaning to a good optical material. Addition to this UV-luminescence, the DAP luminescence at about 540-550 nm is observable in the upper part of sample (5 periods of GaN/$Al_{0.1}Ga_{0.9}N$). The sample material in this part is charged up by the electron beam as distorted optical data. However it can be concluded that with this QW structure of sample QW2, there are two dominant luminescence emissions in the QW part; UV-luminescence peak at ~340 nm from the AlGaN barrier layers and DAP luminescence at about 540-550 nm. As well these CL measurements agree with the results of PL measurements.

<u>Note</u> the sample QW3 is the sample W2 in *section 6.2.2* and details of a sample structure shown in *Fig 6.2.6* and *Table 6.8*.

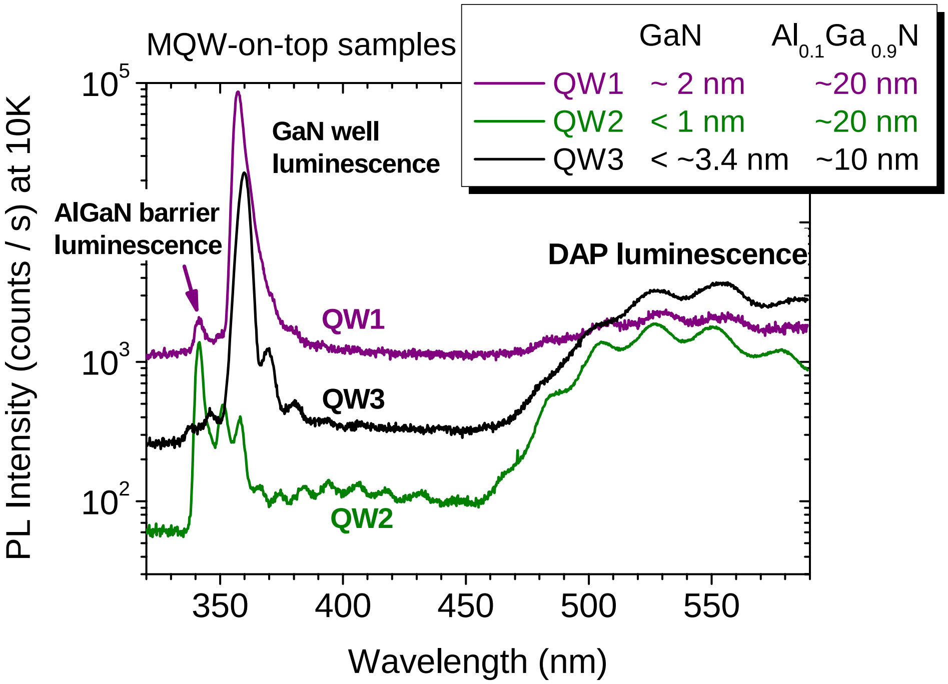

Figure A1 PL measurements on different GaN/AlGaN MQW structures at 10K

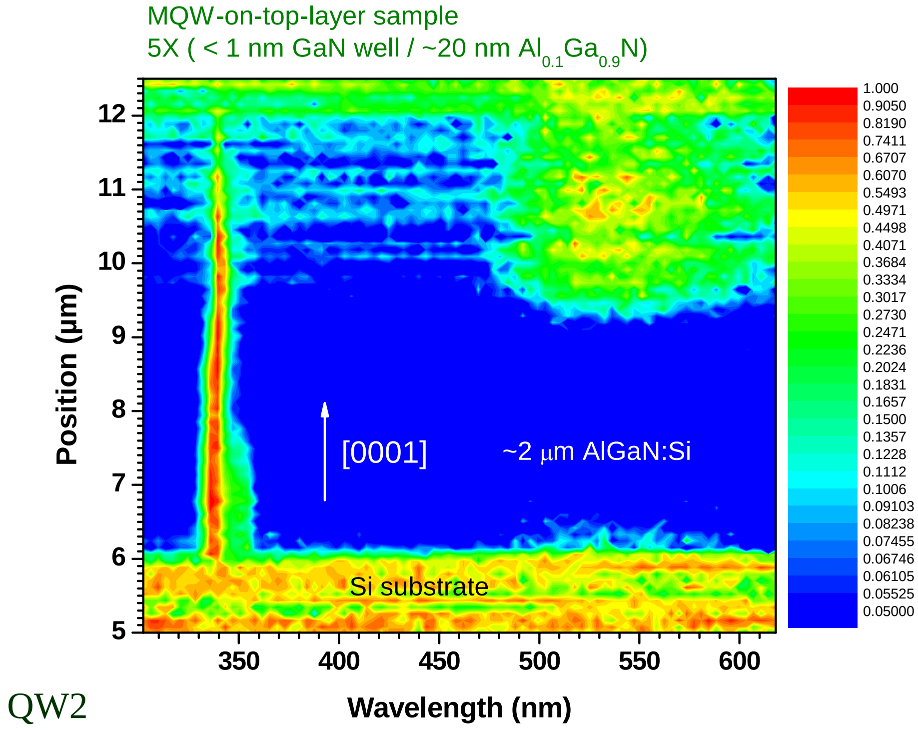

Figure A2 Cross-sectional CL measurements of the <1 nm GaN/ 20 nm AlGaN - MQW sample at 5K

Publications

Literature contributions

P. Saengkaew, A. Dadgar, J. Blaesing, B. Bastek, F. Bertram, F. Reiher, C. Hums, M. Noltemeyer, T. Hempel, P. Veit, J. Christen, and A. Krost, *"MOVPE growth of high-quality* $Al_{0.1}Ga_{0.9}N$ *on Si(111) substrates for UV-LEDs"*, Phys. Stat. Sol. (C), **6** (S2), S455 (2009).

P. Saengkaew, A. Dadgar, J. Blaesing, T. Hempel, P. Veit, J. Christen, and A. Krost, *"Low-temperature/high-temperature AlN superlattice buffer layers for high-quality* $Al_xGa_{1-x}N$ *on Si(111)"*, J. Cryst. Growth, **311**, 3742 (2009).

Conference contributions

Oral presentations

P. Saengkaew, A. Diez, M. Noltermeyer, J. Blaesing, B. Bastek, F. Bertram, A. Dadgar, J. Christen, and A. Krost, *"Impact of seed and buffer layer growth on the quality of AlGaN on Si(111)"*, DPG-Verhandlungen, Berlin, Germany, **HL 55.6**, (2008).

P. Saengkaew, A. Dadgar, J. Bläsing, B. Bastek, F. Bertram, F. Schulze, C. Hums, M. Noltemeyer, T. Hempel, P. Veit, J. Christen, and A. Krost, *"MOVPE growth of high-quality AlGaN on Si(111) substrates for UV LEDs"*, International Workshop on Nitride Semiconductors (IWN2008), Montreux, Switzerland, **We2b-B2**, (2008).

P. Saengkaew, A. Dadgar, J. Blaesing, B. Bastek, F. Bertram, T. Hempel, P. Veit, J. Christen, and A. Krost, *"Optimization of AlN-based seeding and superlattice buffer layers to grow high-quality* $Al_xGa_{1-x}N$ *with Al content up to* $x=0.66$ *on Si (111) substrates"*, DPG-Verhandlungen, Dresden, Germany, **HL 16.7**, (2009).

P. Saengkaew, A. Dadgar, J. Blaesing, B. Bastek, H. Witte, P. Veit, R. Clos, J. Christen, and A. Krost, *"MOVPE Growth of AlGaN-Based UV LEDs on Si(111) Substrate"*, The 8th International Conference on Nitride Semiconductors (ICNS 2009), Jeju, Korea, **W6** (2009).

P. Saengkaew, A. Dadgar, J. Bläsing, H. Witte, M. Müller, K. M. Günther, T. Fey, B. Bastek, F. Bertram, M.v. Kurnatowski, M. Wieneke, T. Hempel, P. Moser, P. Veit, R. Clos, J. Christen, and A. Krost, *"MOVPE grown crack-free AlGaN-based UV LED structures on Si(111) substrate"*, 24. DGKK Workshop "Epitaxie von III/V Halbleitern", Berlin, Germany, **A 1.6**, (2009).

K.-M. Günther, H. Witte, P. Saengkaew, J. Bläsing, A. Dadgar and A. Krost, *"Untersuchung von Raumladungen in AlN/AlGaN Strukturen für LEDs auf Si(111)"*, 24. DGKK Workshop "Epitaxie von III/V Halbleitern", Berlin, Germany, **A 3.8**, (2009).

K.-M. Günther, H. Witte, A. Rohrbeck, P. Saengkaew, J. Bläsing, A. Dadgar and A. Krost, *"Elektrische Untersuchungen an AlN/AlGaN-Strukturen für LEDs auf Si(111)"*, DPG-Verhandlungen, Regensburg, Germany, **HL 56.9**, (2010).

L. Groh, C. Hums, M. Wieneke, P. Saengkaew, J. Bläsing and A. Krost, *"Charakterisierung von AlGaInN mittels Röntgenbeugung und –fluoreszenz"*, DPG-Verhandlungen, Regensburg, Germany, **HL 27.5**, (2010).

Poster presentations

K.-M. Günther, H. Witte, P. Saengkaew, A. Dadgar, J. Bläsing, and A. Krost, *"Detailed electrical characterization of AlN/AlGaN multilayer structures on Si(111)"*, 25th International conference on defects in semiconductors (ICDS-25), St. Petersburg, Russia, **Tue-2.37po**, (2009).

P. Saengkaew, A. Dadgar, J. Bläsing, H. Witte, M. Müller, K. M. Günther, T. Fey, B. Bastek, F. Bertram, M.v. Kurnatowski, M. Wieneke, T. Hempel, P. Veit, R. Clos, J. Christen, and A. Krost, *"Crack-free AlGaN-based UV LED on Si(111) substrate"*, DPG-Verhandlungen, Regensburg, Germany, **HL 31.10**, (2010).

* * *

Curriculum Vitae

Personal data

Family name	Saengkaew
Fist name	Phannee
Earlier names	Satiansri
Date of birth	07.03.1974
Place of birth	Phrae, Thailand
Sex	Female
Correspondence address	19/121 Kritsana 1 Village, Bangkok-Pathum Road, Bangprok, Muang, Pathumthani, Thailand. 12000
Nationality	Thai
Family status	Married
Current Occupation	Lecturer
Office	Department of Industrial Physics and Medical Instrumentation, Faculty of Applied Science, King Mongkut's University of Technology North Bangkok, 1518 Piboolsongkram Road, Bangkok, Thailand. 10800
E-mail:	phns@kmutnb.ac.th , s_phannee@hotmail.com

Education

05.1980 - 03.1986	Phacharajpithaya School, Bangkok, Thailand
05.1986 - 03.1989	Benjamarachalai School, Bangkok, Thailand
05.1989 - 03.1991	Satrinonthaburi School, Nonthaburi, Thailand

06.1991- 03.1995	Prince of Songkla University, Songkla, Thailand Academic degree: B.Sc. in Physics Bachelor project: *"Quantitative analysis of K-40, uranium and thorium in sand used in construction in Hat Yai area"*
06.1997 - 05.2000	Chulalongkorn University, Bangkok, Thailand Academic degree: M.Sc. in Nuclear Technology Master thesis: *"In situ analysis of some major elements in soil using neutron techniques"*
10.2006 - 07.2010	Otto-von-Guericke University Magdeburg, Magdeburg, Germany Academic degree: Dr. rer. nat. in Physics Dissertation: *"Epitaxial growth and properties of AlGaN-based UV-LEDs on Si(111) substrates"*

Work experience

04.1995 - 12.1995	Technician (Laboratory instruments) Gammaco (Thailand) Co.,Ltd. Bangkok, Thailand
02.1996 - 05.1997	Technical translator (English-Thai documents) Thai Yarnyon Co.,Ltd. Bangkok, Thailand
10.1997 - 10.1999	Teaching Assistant Chulalongkorn University, Bangkok, Thailand
06.2000- present	Lecturer King Mongkut's University of Technology North Bangkok, Bangkok, Thailand

* * *

Eidesstattliche Erklärung

Hiermit erkläre ich, dass ich die von mir eingereichte Dissetation zum dem Thema “Epitaxial growth and properties of AlGaN-based UV-LEDs on Si(111) substrates” selbstaendig erfasst, nicht schon als Dissetation verwendet habe und bei benutzten Hilfsmittel und Quellen vollständig angegeben wurden.

Weiterhin erkläre ich, dass ich werde dieser noch eine andere Arbeit zur Erlangung des akademischen Grades doctor reum naturalium (Dr. rer. nat.) an anderen Einrichtungen eingereicht habe.

Magdeburg, den 24.03.2010

M. Sc. Phannee Saengkaew